The Dissertation Committee for Bryan William Reuter certifies that this is the approved version of the following dissertation:

A Reacting Jet Direct Numerical Simulation for Assessing Combustion Model Error

Committee:

Robert D. Moser, Supervisor

Fabrizio Bisetti

Clint Dawson

Omar Ghattas

Todd Oliver

A Reacting Jet Direct Numerical Simulation for Assessing Combustion Model Error

by

Bryan William Reuter

Dissertation

Presented to the Faculty of the Graduate School
of the University of Texas at Austin
in Partial Fulfillment
of the Requirements
for the Degree of

Doctor of Philosophy

The University of Texas at Austin
May 2021

Dedicated to my parents

Acknowledgments

Firstly, I would like to thank my advisor, Dr. Robert Moser, for your wisdom and guidance throughout my time at the Oden Institute. Your trust helped me push through the unknown that is academic research. I will carry the principles you have instilled in me throughout my scientific career. Thank you to Dr. Todd Oliver, who effectively served as a second advisor for this work. I am grateful for your mentorship academically, professionally, and personally. Your thoughtful perspective turned quick questions into long discussions, which shaped much of this work and reminded me to distill seemingly complicated problems to their basics first. Thank you to my committee members, particularly Dr. Fabrizio Bisetti for many lively conversations about combustion modeling and numerics.

Thanks to Gopal and Prakash for being my sounding board for many of the trickier points in this thesis and reliable friends. Thank you to all my friends that I met in Austin and kept my work-life balance in check – especially Melissa, Sam, Sid, Tim, Keith, Sameer, and Travis. To my family, your trust, love, and support shaped my resiliency needed to get to this point. I see my curiosity in my father who was always interested in the fine details of my work. I see my work ethic in my mother who always does whatever needs doing.

Finally, I owe so much to Teresa. Nearly all of the effort reflected by this document was made with you by my side (literally). We have been partners, maturing intellectually and growing together since meeting our first year. Your laughter and enthusiasm is infectious, your encouragement unending, and your trust inspiring.

Computational resources were provided by the Texas Advanced Computing Center (TACC). Thank you to Dr. Antonio Attili for supplying datasets from the reference DNS in this thesis.

A Reacting Jet Direct Numerical Simulation for Assessing Combustion Model Error

by

Bryan William Reuter, Ph.D.

The University of Texas at Austin, 2021

SUPERVISOR: Robert D. Moser

The simulation of turbulent combustion systems is a vital tool in the design and development of new technologies for power generation, transportation, defense applications, and industrial heating. In an engineering design cycle, modeling realistic device configurations in a cost- and time-effective manner is required. Due to their flexibility and computational tractability, Reynolds-Averaged Navier-Stokes (RANS)-based models are most commonly used for these purposes. However, these models are known to be inadequate. Turbulent combustion is the coupling of two multiscale, nonlinear phenomena which individually have many modeling challenges. Hence, it is unsurprising that the modeling ansatzes and simplifying assumptions which lead to these practical RANS-based models are suspect. Since RANS-based models will continue to be the dominant tool for turbulent combustion simulation, it is necessary to improve their predictivity through a better understanding of their deficiencies.

The are three main modeling issues for turbulent combustion: modeling the turbulent flow, representing the chemical reactions, and capturing the interaction between the turbulence and the chemistry. Model errors can easily be conflated when attempting to quantify deficiencies in this multiphysics context where many individual models are coupled. This

work introduces a new technique for isolating these errors through the creation of a flamelet-based direct numerical simulation (DNS) of a nonpremixed, temporally-evolving, planar, reacting jet. DNS is a technique which resolves all lengthscales and timescales of the turbulent flow, providing high-quality data for model development but at a significant computational cost. In the turbulent combustion context, the turbulence-chemistry interaction is also fully resolved. By closing the DNS with a steady laminar flamelet representation, a typical chemical reactions model for RANS-based simulations, RANS turbulence closures and turbulence-chemistry interaction models can be evaluated in isolation through *a priori* testing. Conversely, by comparing the flamelet DNS to a second DNS employing a higher-fidelity chemistry model, the flamelet closure and its impact on the flame's evolution can be interrogated directly. To obtain the DNS data, a novel algorithm for solving the variable-density, low-Mach Navier-Stokes equations extending the method of Kim, Moin, and Moser [1] for incompressible flow is detailed here. It is a pseudospectral Fourier/B-spline collocation approach which obtains second order accuracy in time and numerical stability for large density ratios with an efficient, matrix-free, iterative treatment of the scalar equations.

The *a posteriori* comparisons of the flamelet DNS and the complex chemistry DNS suggest the flamelet model can significantly alter the evolution of the mean state of the reacting jet; however, violations of global conservation were identified in the complex chemistry DNS. Therefore, no strong conclusions can be made about the chemical reactions model from the comparisons. Significant shortcomings have been identified in the *a priori* evaluations of the aforementioned RANS closures for turbulent transport, scalar mixing, and turbulence-chemistry interaction, where the flamelet model is taken to be exact. Finally, a flawed assumption in the steady laminar flamelet approach has been directly linked to nonphysical behavior of the density for small values of the scalar dissipation rate.

Contents

List of Tables

List of Figures

Chapter 1

Introduction

1.1 Motivation

Turbulent combustion is a technologically critical phenomenon relevant to transportation, weapons systems, and energy generation. Despite the increasing importance of alternate energy sources, the burning of hydrocarbons remains the dominant source for power generation and propulsion [2–4]. In these systems, nearly all fluid flows are turbulent; hence, turbulent combustion is a topic of significant engineering interest and importance. There are many complicated participating physical processes including chemical reactions, turbulent mixing and transport, and thermodynamics. A realistic chemical reaction may include hundreds of species and elementary reactions. Additionally, both turbulence and combustion occur over a large range of timescales and lengthscales [4] and are complex phenomena whose modeling has seen limited success even individually. The turbulent combustion problem is inherently multiscale, nonlinear, and multiphysics, and development of reliable models is an ongoing research challenge [5]. Practical models are highly uncertain and have been invalidated even in scenarios much less complex than industrially-relevant systems for which predictions of performance and environmental impact are needed. As the combination of many complex physical phenomena, there are many potential sources of modeling error. Predictions require modeling of three main aspects of the turbulent combustion process: the chemical reactions, the turbulence, and the interaction between the two.

Currently, Reynolds-Averaged Navier-Stokes (RANS) models are the predominant tool used in the modeling of turbulent combustion for engineering design [6]. In a recent review of RANS closures for turbulence, Durbin notes higher-fidelity approaches are still not feasible due to computational time and grid requirements, despite advances in computing resources [7]. Those resources instead enable more realistic configurations for RANS-based analyses. In a study comparing RANS-based computations and higher-fidelity Large Eddy Simulation (LES)-based models for a swirled flow, a methane flame, and a turbulent diffusion flame, Sadiki *et al.* required a timestep ten times smaller for the LES calculations [8]. Results from the International Workshop on Measurement and Computation of Turbulent Nonpremixed Flames (TNF) often show grid requirements are two orders of magnitude less for RANS-based simulations versus LES for the same configuration with a similar reduction in computational cost (see, e.g., [9, 10]). In addition to removing the computational burden of tracking the detailed turbulent fields, RANS-based methods offer flexibility in simulating complex geometries with realistic flow conditions [4]. For these reasons, RANS-based turbulent combustion simulations are the only tractable approach in an engineering context. However this tractability is gained at the cost of many simplifying assumptions to address each of the three modeling challenges, so the reliability of these RANS-based simulations remains poor [3–5, 11].

A model of turbulent combustion must include appropriate closure relationships for turbulent and molecular transport of momentum, species, and energy, as well as a description of the relevant chemical reaction processes and a representation of boundary and initial conditions. Typical RANS-based combustion models employ turbulence closures developed for constant-density, nonreacting flows, rewritten in terms of Favre (density-weighted) averages and coupled with a representation of mean reaction rates or a precomputed mean thermochemical state. Turbulent transport terms are modeled with eddy-viscosity, gradient-diffusion closures [4]. The description of the chemistry is often based on a steady laminar

flamelet assumption [12]. Laminar flamelet models are predicated on the assumption that combustion occurs rapidly in flame sheets that are thin relative the scales of the turbulence. These thin sheets, or "flamelets," are assumed to behave like local one-dimensional, laminar counterflow flames whose composition falls on a low-dimensional manifold. Under these assumptions, a chemical reaction involving hundreds of species and many subreactions can be described by tracking only a few conserved scalars and the flow and the chemical kinetics are effectively decoupled. This makes them attractive for practical engineering calculations, but strong assumptions about the flame structure and species transport are needed to make these simplifications. To complete the closure the mean thermochemical properties relevant to the RANS equations must be related to the instantaneous thermochemical state described by the flamelets. This is accomplished by assuming a convenient probability density function (PDF) *a priori*, to describe the fluctuations of the thermochemical state [3].

Due to their prominence in the engineering-design and decision-making process, this study will focus on evaluating these flamelet-based RANS models for turbulent combustion in the context of a canonical flow: a nonpremixed, turbulent jet flame. Given the necessary simplifying assumptions, it is unsurprising that these methods are known to be inadequate. For example, they struggle to predict diffusion flames [13–16] as well as more complicated configurations such as a swirling burner flow [17], burners with hot coflow [18], and bluff body stabilized flames [19]. One avenue to improving the reliability of these engineering turbulent combustion models is to develop a better understanding of their errors. However, the multiphysics nature of the underlying problem makes it challenging to assess the various errors in isolation.

1.2 Exploiting model hierarchies to probe errors

Much more reliable than RANS simulations are direct numerical simulations (DNS). However, the computational cost of DNS is orders of magnitude greater than RANS because in DNS all the scales of turbulence must be resolved, where as in RANS, only the mean need be resolved. Direct numerical simulations of turbulent combustion are limited to moderate Reynolds numbers and simple configurations, but are an invaluable tool to provide high-quality data for model development and evaluation and for answering questions about combustion physics [5]. In RANS the Navier-Stokes conservation equations are averaged, necessitating closure relations for the turbulent fluxes, the higher moments of the velocity field, and the mean chemical source terms or mean thermodynamic properties [3,4]. However, because chemical reactions occur at the smallest scales [2, 11], their effects must be entirely modeled in RANS along with the interaction between the chemistry and the turbulence.

When simulating turbulence alone, there is a natural hierarchy of models in which DNS can be trusted as a high-fidelity representation of reality and RANS models are lowest fidelity. Hence, any discrepancies between DNS and RANS can be attributed directly to the deficiencies of the RANS model once numerical errors are accounted for. However, for the combustion problem there are additional model hierarchies associated with the chemistry and turbulence-chemistry interaction. A DNS-based turbulent combustion model will always require some form of chemistry closure as the chemical source terms are unknown. However, the turbulence and the interaction between the turbulence and chemistry are represented without further modeling. To represent a turbulent flame as accurately as possible, many DNS employ a complex chemistry model that represents many intermediate chemical species and their associated elementary reactions as well as complex multispecies diffusion models. Using such DNS to evaluate RANS model error is difficult because the composite RANS-based turbulent combustion model will differ in all three modeling areas. Discrepancies

between flamelet-based RANS models and the complex chemistry DNS could arise from any one of the model simplifications or as a result of their interaction.

Examples of nonpremixed combustion DNS are prevalent in the literature (see [20] for a recent review of combustion DNS). For example, Hawkes *et al.* simulated a planar, temporally-evolving CO/H_2 jet to study mixing fields while employing a skeletal chemical mechanism which retained 11 species [21]. Yoo *et al.* simulated a spatially-evolving, lifted ethylene jet and observed flame stabilization, tracking 22 species and 18 reactions [22]. Attili *et al.* used a n-heptane planar jet DNS to study soot formation and Damköhler number effects, carrying nearly 50 species and 300 reactions in their chemical mechanism [23, 24]. Lignell *et al.* were also interested in Damköhler number effects in the context of flame extinction and reignition when simulating a planar ethylene jet and used another skeletal mechanism [25]. Missing from these studies is a DNS of turbulent combustion which will enable the examination of decoupled modeling errors in this multiphysics context.

For this reason, a DNS study has been designed which will allow for the investigation of the impact of the different modeling assumptions in steady flamelet-based RANS models for nonpremixed turbulent combustion without conflating the sources of error. In this work, a "flamelet DNS" is introduced, whose chemistry model matches that of common RANS combustion models (steady laminar flamelet) while representing the turbulence and the turbulence-chemistry interactions without further modeling. A reference "complex chemistry DNS" (CC DNS) employs a more detailed, higher fidelity chemistry closure. This allows for two distinct sets of model evaluations, both of which serve to isolate errors in different aspects of the combustion problem. The model assessment framework is shown in table 1.1, where the columns are three differing multiphysics combustion models and the rows indicate the closures introduced (if necessary). Note that the underlying chemical mechanism (the description of the participating species and the reactions between them) on which the chemistry closures are based must be common among the models. That is, the flamelet model

gives a representation of the mechanism used in the complex chemistry DNS; however, the flamelet assumptions are much more aggressive in reducing the complexity of the chemistry model.

	RANS		Flamelet DNS		Complex chemistry DNS
Chemistry	Laminar flamelet		Laminar flamelet	$\leftrightarrow$	Complex chemistry
Turbulence	Transport and mixing models	$\leftrightarrow$	Fully resolved		Fully resolved
Turbulence-chemistry interaction	Presumed PDF	$\leftrightarrow$	Fully resolved		Fully resolved

Table 1.1: Model hierarchies in turbulent combustion with three simulation frameworks. Arrows show where consecutive composite models differ.

On one hand, the flamelet DNS data can be compared to the complex chemistry DNS in an *a posteriori* sense. In both DNS cases, the turbulence and the turbulence-chemistry interaction are fully resolved, so any discrepancies between the quantities of interest can be directly attributed to the shortcomings of the steady laminar flamelet model. Alternatively, *a priori* evaluations for the RANS closures for turbulence and the presumed PDF models can be performed once the flamelet DNS data is appropriately averaged. The flamelet DNS can be viewed as the true solution to the turbulence and mixing problem of the nonpremixed jet under the assumption that the flamelet model is valid. Hence, the related RANS closures can be assessed independent of any errors introduced from the chemistry modeling.

1.3 Numerical challenges for simulating variable-density flows

To perform the proposed flamelet DNS, an efficient numerical algorithm to solve the low-Mach-number, variable-density Navier-Stokes equations with high-order spatial and temporal

discretization is needed, which can interface with flamelet-like chemistry models. Low-speed flows with significant density changes are common in engineering and nature, such as in turbulent combustion, nonreacting mixing problems, the atmosphere, and the oceans. In the low-Mach-number limit, the pressure fluctuations are decoupled from the density fluctuations. The pressure can then be decomposed into a uniform background, thermodynamic pressure and a mechanical, or dynamic, pressure. The mechanical pressure fluctuates in space and time and acts to enforce continuity as in incompressible flow. Unlike constant-density incompressible flow, in variable-density flow, there is a time derivative term in the continuity constraint which presents additional numerical challenges, particularly in cases of large density ratios.

It is natural to adapt algorithms designed for constant-density, incompressible flows to the low-Mach-number, variable-density case due to the similar role of the mechanical pressure. Fully compressible algorithms perform poorly at low Mach numbers, since the Navier-Stokes equations are formally singular as $\mathrm{Ma} \to 0$. Furthermore, compressible solvers are built to handle often severe stability constraints imposed by acoustic timescales which are removed by the low-Mach assumption. Therefore, most numerical methods for solving the low-Mach equations are based on traditional incompressible fractional-step, projection approaches [26, 27]. These formulations differ based on a choice to enforce either the divergence of the momentum or the divergence of the velocity, resulting in a constant-coefficient or variable-coefficient pressure Poisson equation, respectively. In both cases, the time dependence of the constraint necessitates particular care in enforcing the constraint in the context of the time discretization scheme.

1.3.1 Treatment of the mechanical pressure in fractional step methods

Fundamental to the low-Mach Navier-Stokes equations is the time-dependent divergence constraint on the momentum and the role of the mechanical pressure in enforcing that constraint. Fractional-step approaches for incompressible flows solve for an intermediate velocity or momentum field by neglecting or lagging the pressure in the momentum equations and then projecting the result onto a divergence-free basis through the solution of a Poisson equation derived from the governing equations. Since the momentum field is not divergence-free for variable-density flows, standard incompressible projection methods must be modified. Within the class of fractional-step methods for the low-Mach equations, two formulations are commonly employed. One option is to take the divergence of the momentum equations, giving a constant-coefficient Poisson equation for the pressure. Upon temporal discretization, the divergence of the momentum is related to the time derivative of the density through the mass conservation equation. The second option involves manipulating the advective form of the momentum equations after dividing through by the density to give a variable-coefficient Poisson equation. The velocity divergence is then related to the material derivative of the density by reformulating the mass conservation equation.

The first approach has the advantage of being much easier to solve, but the evaluation of the density time derivative can lead to instability, especially when density ratios are larger than three [26, 28, 29]. To help alleviate this issue, predictor-corrector schemes or implicit formulations have shown some success [30–32]. Predictor-corrector methods are attractive in scenarios where only explicit or segregated time-stepping is practical (e.g. when spectral methods are employed). The second approach [27, 33] does allow for higher density ratios, but cannot take advantage of the progress made in efficiently solving the pressure Poisson equation in incompressible flows. The solution of the variable-coefficient Poisson equation

generally requires an iterative scheme, can be an order of magnitude slower, and convergence can be hampered by large density ratios [34]. As always with such projection methods, both approaches must specify boundary conditions for the pressure which are not formally specified *a priori* and can introduce inconsistencies with the velocity field [35]. A third option, in which the pressure is eliminated entirely from the dynamic equations, is used in this work. This is advantageous because only a cheap, constant-coefficient Poisson solve for the momentum, rather than the pressure, is required. Furthermore, all boundary conditions are well defined.

1.3.2 The redundant nature of the low-Mach equations and its impact on numerical stability

Formally, the low-Mach Navier-Stokes equations are a partial differential-algebraic system (coupled partial differential equations along with the continuity constraint and an equation of state). However, there is a redundancy in the equations since the density must simultaneously obey the equation of the state and the mass conservation equation. Inconsistencies between the scalar fields, the equation of state, and the momentum field have been identified as numerically destabilizing as kinetic energy can be incorrectly injected into the system nonlocally through the continuity constraint [36]. Work by Shunn and Ham [37] suggests that scenarios where the equation of state is sufficiently nonlinear can introduce prohibitive resolution requirements on the density even when the scalar fields are well resolved. In turn, these underresolved features can produce a nonphysical velocity field. More generally, instability can occur due to inconsistencies that arise when using a segregated time-advancement scheme. Knikker [26] notes that the structure of the low-Mach equations leads to redundancies that make it impossible to both advance them in conservative form and satisfy the equation of state without resorting to a temporally implicit scheme, which can be cost prohibitive (certainly in a DNS context). Instead predictor-corrector approaches are com-

mon, since they presumably can lessen, but not eliminate, the degree of the discrepancies and provide additional stability while remaining computationally cheaper. Stability is not guaranteed as these methods are still susceptible when density gradients are steep [29].

To address these challenges of the mechanical pressure and stability in a DNS context, where highly accurate numerics are necessary, a novel algorithm has been developed. It is the extension of a pseudospectral method for incompressible flow [1] (recently employed for a state-of-the-art channel DNS [38]) to variable-density scenarios. By recasting the momentum equations as evolution equations for the density-weighted vorticity and the Laplacian of the momentum, the need to solve for the pressure is removed. Additionally, a second-order time-advancement scheme is introduced which improves robustness for flows with high density ratios, without losing the wavenumber-by-wavenumber decoupling which makes pseudospectral methods efficient.

1.4 Objectives

This thesis will investigate the validity of flamelet-based RANS models for turbulent combustion through the creation and analysis of a DNS database. The configuration chosen is a nonpremixed, temporally-evolving, turbulent jet.

To assess model error in this multiphysics context, a novel combustion DNS is needed. A laminar flamelet model is used to represent the chemical reactions, the same as is employed in RANS models. This allows for the isolation of the flamelet-based RANS model error due to turbulence and turbulence-chemistry interaction closures by using the flamelet model in the parameter regimes for which it is assumed to be valid. This isolation is possible because in DNS there are no further modeling assumptions, beyond the chemistry model. Separately, by comparing with a DNS of the same problem but coupled with a complex chemistry closure [23, 24], the flamelet approximations can be assessed, since the simulations

will only differ in the fidelity of the chemistry model.

To generate high-quality data, an efficient, reliable DNS method for flows with large density variations is required. Hence, the design and implementation of a new DNS algorithm for the low-Mach-number, variable-density Navier-Stokes equations is introduced. The algorithm employs a Fourier/B-spline pseudospectral spatial scheme and an efficient, matrix-free iterative scheme that allows for second-order convergence in time and numerical stability for higher density ratios while retaining the parallelizability of a purely explicit method.

In what follows, chapter 2 describes the mathematical models used here. Chapter 3 details the development of the novel variable-density DNS algorithm used for the flamelet DNS. In chapter 4 the impact of the laminar flamelet assumptions of the RANS quantities of interest is examined by way of an *a posteriori* comparison of the flamelet DNS and a reference DNS with high fidelity chemistry. Further, *a priori* evaluations of RANS closures for turbulence and presumed PDF models for turbulence-chemistry interaction are performed. Finally, chapter 5 provides conclusions and potential avenues for future work.

Chapter 2

Mathematical models for nonpremixed turbulent combustion

Given the model hierarchy established in section 1.2, this chapter provides descriptions of the three mathematical models relevant to this work: the complex chemistry DNS [23], the flamelet DNS, and a flamelet-based RANS model. The complex chemistry DNS and flamelet DNS solve the low-Mach-number, variable-density Navier-Stokes equations for chemically reacting flows, introducing a higher or lower fidelity thermochemistry model, respectively, along with molecular transport models to close the system. *A posteriori* comparisons of the complex chemistry and flamelet DNS will reveal the effect of the steady laminar flamelet model on the evolution of a jet flame. The averaging procedure applied to the governing equations to obtain the RANS model introduces the need for closures for the turbulence and turbulence-chemistry interaction as well as the chemistry. After defining the Favre average and presenting the RANS equations, the closures which will be examined in chapter 4 are detailed with key assumptions and ansatzes highlighted. These direct *a priori* evaluations are possible because the flamelet DNS and the RANS models of interest share the same representation of the chemistry.

2.1 Complex chemistry direct numerical simulation

The temporally evolving, planar n-heptane/air jet DNS of Attili, Bisetti, *et al.* [23] was obtained by solving the low-Mach-number, variable-density Navier-Stokes equations for chemi-

cally reacting flows as is appropriate for a low-speed combustion configuration. The thermochemical state in this complex chemistry DNS is described by the temperature, the species mass fractions, the density, and a constant background thermodynamic pressure. The equations representing conservation of mass and momentum for a viscous fluid are

$$\frac{\partial \rho}{\partial t} + \frac{\partial \rho u_i}{\partial x_i} = 0 \tag{2.1}$$

$$\frac{\partial \rho u_i}{\partial t} + \frac{\partial \rho u_i u_j}{\partial x_j} = -\frac{\partial p}{\partial x_i} + \frac{\partial \tau_{ij}}{\partial x_j} \tag{2.2}$$

where u_i is the fluid velocity, ρ the density, p the mechanical pressure, τ_{ij} the viscous stress tensor. For a Newtonian fluid the stress tensor is

$$\tau_{ij} = -\frac{2}{3}\mu \frac{\partial u_k}{\partial x_k}\delta_{ij} + \mu\left(\frac{\partial u_i}{\partial x_j} + \frac{\partial u_j}{\partial x_i}\right) \tag{2.3}$$

where μ is the fluid dynamic viscosity and δ_{ij} is the Kronecker delta. Conservation of species and energy are expressed as

$$\frac{\partial \rho Y_\beta}{\partial t} + \frac{\partial}{\partial x_i}\left(\rho u_i Y_\beta\right) = -\frac{\partial}{\partial x_i}\left(\rho V_{\beta,i}\frac{\partial Y_\beta}{\partial x_i}\right) + \dot{\omega}_\beta \tag{2.4}$$

and

$$c_p\left[\frac{\partial \rho T}{\partial t} + \frac{\partial}{\partial x_i}\left(\rho u_i T\right)\right] = -\frac{\partial}{\partial x_i}\left(\lambda\frac{\partial T}{\partial x_i}\right) - \sum_{\beta=1}^{N_s} c_{p,\beta}\rho Y_\beta V_{\beta,i}\frac{\partial T}{\partial x_i} + \dot{\omega}_T \tag{2.5}$$

where Y_β is the mass fraction of one of the N_s participating species, $\boldsymbol{V}_\beta$ is its diffusion velocity, $c_{p,\beta}$ is its specific heat at constant pressure ($c_p = \sum_{\beta=1}^{N_s} c_{p,\beta}Y_\beta$), λ is the mixture's thermal conductivity, and $\dot{\omega}_\beta$ and $\dot{\omega}_T = -\sum_{\beta=1}^{N_s} h_\beta \dot{\omega}_\beta$ are source terms for the species and temperature equations, respectively, where h_β is the enthalpy per unit mass of species β. In the complex chemistry DNS, the following modeling assumptions close the equations above:

1. the Hirschfelder-Curtiss approximation of the diffusion velocity with correction (see

section 1.1.4 in [4]) is used:

$$\boldsymbol{V}_\beta \approx -\mathcal{D}_\beta \frac{\nabla X_\beta}{X_\beta} + \boldsymbol{V}^c \,, \tag{2.6}$$

where X_β is the mole fraction of species β, $\mathcal{D}_\beta$ is the mixture-averaged diffusion coefficient of species β, and

$$\boldsymbol{V}^c = \sum_{\beta=1}^{N_s} \mathcal{D}_k \frac{W_\beta}{W} \nabla X_\beta \,, \tag{2.7}$$

where W_β is the molecular weight of species β and $W = \sum_{\beta=1}^{N_s} X_\beta W_\beta$. The correction velocity $\boldsymbol{V}^c$ ensures that overall mass conservation is satisfied.

2. The mixture-averaged diffusion coefficients $\mathcal{D}_\beta$ are given by

$$\mathcal{D}_\beta \approx \frac{1 - Y_\beta}{\sum_{\substack{\gamma=1 \\ \gamma \neq \beta}}^{N_s} \frac{X_\gamma}{\mathcal{D}_{\beta\gamma}}} \tag{2.8}$$

where $\mathcal{D}_{\gamma\beta}$ is the binary diffusion coefficient of species γ into species β.

3. Transport properties ($\mathcal{D}_{\gamma\beta}$, μ, λ) are obtained from Chapman-Enskog kinetic theory (see chapter 11 in [39] for details and resulting models).

4. Thermodynamic properties ($c_{p,\beta}$, h_β, etc.) are polynomial functions of temperature as specified in [40].

5. The chemical source terms are obtained from a reaction mechanism describing the oxidation of n-heptane whose reaction rates are described by the Arrhenius law (see section H.3). The mechanism contains 47 species and 290 reactions and is detailed in [41].

6. The ideal-gas equation of state

$$\rho = \frac{p_0 W}{\mathcal{R} T} \tag{2.9}$$

relates the density, temperature, and mass fractions to the thermodynamic pressure p_0. In eq. (2.9) $\mathcal{R}$ is the universal gas constant.

2.2 Flamelet direct numerical simulation

The flamelet DNS uses a low-dimensional description of the thermochemical state derived from the steady laminar flamelet assumptions for nonpremixed combustion. As with the complex chemistry DNS, no models are introduced for the turbulence or turbulence-chemistry interaction.

2.2.1 Steady laminar flamelet approximation for nonpremixed combustion

In a nonpremixed flame, the fuel and oxidizer are initially either wholly separated or not perfectly premixed upon entering the combustion chamber. Entrainment of the reactants occurs at large lengthscales and micromixing occurs at the molecular diffusion scale, bringing together fuel and oxidizer in a reaction zone where the combustion occurs [11, 42]. Typically, the mixing time controls the rate of reaction in nonpremixed combustion [4, 43]. Relevant lengthscales associated with these flames are the diffusion layer thickness ℓ_d, the reaction zone thickness ℓ_r, and the turbulent integral and Kolmogorov scales (ℓ_t, η). The diffusion layer thickness is the length over which reactants are molecularly mixed and the reaction zone thickness describes the region within the diffusion layer where the reaction takes place [4]. Relevant timescales are the turbulent transport timescales and the reaction timescale.

Broadly, steady laminar flamelet models [12] for turbulent nonpremixed combustion presume a thermochemical state which is fully determined by two variables describing the mixing with no explicit dependence on time. This is valid under strong assumptions about the nature of the species transport and the scales of the problem. Key assumptions are:

1. the species experience Fickian diffusion and share the same diffusion coefficient $\mathcal{D}$;

2. the thermal diffusion coefficient α is equal to $\mathcal{D}$;

3. $\ell_d \approx \eta$ and $\ell_r \ll \ell_d$;

4. the reaction timescale is much shorter than the timescales of the turbulence;

5. gradients normal to the flame are much larger than those along the flame front;

6. the flame evolution is quasi-steady.

The first assumption about the simplified nature of molecular transport implies that there exists a conserved quantity z, known as the mixture fraction, that obeys the following equation:

$$\frac{\partial \rho z}{\partial t} + \frac{\partial}{\partial x_i}\left(\rho u_i z\right) = \frac{\partial}{\partial x_i}\left(\rho \mathcal{D}_z \frac{\partial z}{\partial x_i}\right) \tag{2.10}$$

where $\rho\mathcal{D}_z = \rho\mathcal{D}$ is its' effective diffusivity. This is the first thermochemical state variable under the flamelet approximation. The mixture fraction is a linear combination of the species mass fractions which is zero in the oxidizer stream and one in the fuel stream (see section H.1 for the exact definition of z and derivation of eq. (2.10)). The second thermochemical state variable is

$$\chi \equiv 2\mathcal{D}_z \left(\frac{\partial z}{\partial x_i}\frac{\partial z}{\partial x_i}\right) , \tag{2.11}$$

which is known as the scalar dissipation rate. It is an inverse timescale characterizing molecular diffusion and mixing [12]. Under the steady flamelet approximation, the full thermochemical state space (Y_β, p_0, ρ, T) is projected onto a two-dimensional manifold parameterized by z and χ, providing a convenient, low-dimensional description of the reactions.

Assuming the reaction lengthscale is small compared to the turbulence lengthscales implies that the local flowfield surrounding the reaction zone is laminar. So, one can imagine the turbulent flame as an ensemble of small laminar flame elements known as flamelets [12].

Additionally, assuming the reaction timescales are much shorter than those of the turbulence implies that the chemistry is quasi-steady and adjusts immediately to the local turbulent flow [44]. With the final two assumptions, the so-called steady flamelet equations [4, 12] govern the local turbulent flame structure. Their solution is a function of z parameterized by χ, where χ is sensitive to characteristics of the surrounding flowfield. In practice, the flamelet equations are solved as a preprocessing step, generating an equation of state $\rho(z;\chi)$ as well as all other thermochemical and transport properties as functions of z and χ. See Appendix H for the flamelet equations and details on their solution.

2.2.2 Flamelet DNS governing equations

The flamelet DNS need only solve the mixture fraction transport equation in addition to the low-Mach, variable-density Navier-Stokes equations for conservation of mass and momentum. Consistent with the steady laminar flamelet model, the density, viscosity, and mixture fraction diffusivity are known functions of z and χ. The flamelet DNS system is therefore

$$\begin{aligned}
\frac{\partial \rho}{\partial t}+\frac{\partial \rho u_i}{\partial x_i} &= 0 \\
\frac{\partial \rho u_i}{\partial t}+\frac{\partial \rho u_i u_j}{\partial x_j} &= -\frac{\partial p}{\partial x_i}+\frac{\partial \tau_{ij}}{\partial x_j} \\
\frac{\partial \rho z}{\partial t}+\frac{\partial}{\partial x_i}\left(\rho u_i z\right) &= \frac{\partial}{\partial x_i}\left(\rho \mathcal{D}_z \frac{\partial z}{\partial x_i}\right) \\
\rho &= f(z;\chi) \\
\mu &= g(z;\chi) \\
\mathcal{D}_z &= h(z;\chi)
\end{aligned} \tag{2.12}$$

where f, g, and h are precomputed functions determined from solutions to the flamelet equations.

2.2.3 Assessing model error with the flamelet DNS

Both the flamelet DNS and complex chemistry DNS provide a complete description of the temporally-evolving, reacting n-heptane jet. Even though not explicitly carried as a state variable in the flamelet DNS, the species mass fractions and the temperature are known functions of mixture fraction so the entire thermochemical state (and any derived quantities) can be reconstructed in the flamelet DNS as well. On the other hand, z and χ can be computed from the species mass fractions in the complex chemistry DNS. However, instantaneous comparisons between the full three-dimensional DNS fields are not meaningful due to the chaotic nature of turbulence. Instead, comparisons of statistical quantities of interest can be made to discern the effects of the flamelet assumptions on the evolution of the jet. More specifically, an appropriately resolved flamelet DNS provides a highly reliable representation of a canonical nonpremixed combustion configuration under the assumptions underlying the steady laminar flamelet model. Hence, the validity of any additional assumptions introduced by flamelet-based RANS turbulent combustion models can be assessed in an *a priori* analysis using the flamelet DNS data.

2.3 Flamelet-based Reynolds-Averaged Navier-Stokes models

Currently only RANS methods are practical for the wide range of geometries and flow conditions encountered in realistic engineering configurations involving turbulent combustion [4, 6, 7]. RANS models make the turbulence problem tractable by performing a statistical average of the governing equations. However, the averaged equations are unclosed, necessitating turbulent combustion models for turbulent momentum and species transport, molecular diffusion, and mean thermodynamic properties.

2.3.1 Reynolds and Favre averaging

The RANS equations for nonpremixed combustion under the steady laminar flamelet assumptions are obtained by averaging the flamelet DNS equations (system (2.12)). Consider a variable $f = f(\mathbf{x}, t)$ in a turbulent flow. The standard Reynolds decomposition is

$$f = \overline{f} + f' \tag{2.13}$$

where $\overline{f} \equiv \langle f \rangle$ is the expected value of f over the probability space of uncontrolled initial conditions and external perturbations. This is commonly considered to be an ensemble average

$$\overline{f} = \lim_{N \to \infty} \frac{1}{N} \sum_{i=1}^{N} f_i \tag{2.14}$$

where each of the f_i is from an independent instance of the turbulent flow. $\overline{f}$ is the called the Reynolds average of f. For turbulent flows in which the turbulence is statistically homogeneous in one or more spatial directions, an assumption of ergodicity allows the Reynolds average to be determined as

$$\overline{f} = \lim_{L_i \to \infty} \frac{1}{L_i} \int_0^{L_i} f \, dx_i \,, \tag{2.15}$$

where x_i is the coordinate in a spatially homogeneous direction. The fluctuations about the mean f' has the property $\overline{f'} = 0$. For variable-density flows, a density-weighted or Favre average is commonly used:

$$\widetilde{f} = \frac{\overline{\rho f}}{\overline{\rho}} \tag{2.16}$$

because it simplifies the evolution equations for the average quantity. In this case, f is decomposed as

$$f = \widetilde{f} + f'' \,, \tag{2.17}$$

where $\widetilde{f''} = 0$, and one should note that $\overline{f''} \neq 0$. Favre averaging results in averaged governing equations that appear similar to those for incompressible flow; however, mean quantities cannot be interpreted in the same way. It follows from the definitions of the different averages that

$$\begin{aligned} \rho f = (\overline{\rho} + \rho')\left(\widetilde{f} + f''\right) &= \overline{\rho}\widetilde{f} + \overline{\rho} f'' + \rho'\widetilde{f} + \rho' f'' \\ \implies \overline{\rho}\widetilde{f} &= \overline{\rho f} = \overline{\rho}\widetilde{f} + \overline{\rho' f''}\,. \end{aligned} \tag{2.18}$$

Hence, Reynolds averaging in the context of variable-density flows would introduce density fluctuation correlations like $\overline{\rho' f''}$ which would need to be modeled. Note that if the density is constant, the Reynolds and Favre averages are equivalent.

Decomposing the state variables as in eq. (2.17) and averaging the flamelet DNS equations gives the Favre-Averaged Navier-Stokes (FANS) continuity, momentum, and mixture fraction equations as follows:

$$\frac{\partial \overline{\rho}}{\partial t} + \frac{\partial}{\partial x_i}\left(\overline{\rho}\widetilde{u}_i\right) = 0 \tag{2.19}$$

$$\frac{\partial \overline{\rho}\widetilde{u}_i}{\partial t} + \frac{\partial}{\partial x_i}\left(\overline{\rho}\widetilde{u}_i\widetilde{u}_j\right) = -\frac{\partial \overline{p}}{\partial x_i} + \frac{\partial \overline{\tau}_{ij}}{\partial x_j} - \frac{\partial}{\partial x_j}\left(\widetilde{\overline{\rho} u_i'' u_j''}\right) \tag{2.20}$$

$$\frac{\partial \overline{\rho}\widetilde{z}}{\partial t} + \frac{\partial}{\partial x_i}\left(\overline{\rho}\widetilde{u}_i\widetilde{z}\right) = \frac{\partial}{\partial x_i}\left(\overline{\rho \mathcal{D}_z \frac{\partial z}{\partial x_i}}\right) - \frac{\partial}{\partial x_i}\left(\widetilde{\overline{\rho} u_i'' z''}\right)\,. \tag{2.21}$$

While the steady laminar flamelet model provides the complete instantaneous thermochemical state as a function of z and χ, the Reynolds averaged thermochemical state is unknown. Typical RANS models for nonpremixed combustion represent the mean thermochemical state in therms of a presumed PDF (see section 2.3.2) of the z fluctuations that is parameterized in terms of the mixture fraction variance $\widetilde{z''z''}$, which then becomes part of the mean state.

The transport equation for $\widetilde{z''z''}$ is

$$\begin{aligned}\frac{\partial \overline{\rho}\widetilde{z''z''}}{\partial t} + \frac{\partial}{\partial x_i}\left(\overline{\rho}\widetilde{u}_i\widetilde{z''z''}\right) = &-\frac{\partial}{\partial x_i}\left(\overline{\rho u_i'' z'' z''}\right) + \frac{\partial}{\partial x_i}\left(\overline{\rho \mathcal{D}_z \frac{\partial z'' z''}{\partial x_i}}\right) \\ &+ 2\overline{z''\frac{\partial}{\partial x_i}\left(\rho \mathcal{D}_z \frac{\partial \widetilde{z}}{\partial x_i}\right)} \\ &- 2\overline{\rho u_i'' z''}\frac{\partial \widetilde{z}}{\partial x_i} - 2\overline{\rho \mathcal{D}_z \frac{\partial z''}{\partial x_i}\frac{\partial z''}{\partial x_i}}\,.\end{aligned} \tag{2.22}$$

In the literature, it is common to refer to models which solve Favre-averaged equations as RANS models so this nomenclature is adopted in this text with the implicit understanding that density-weighted averaging is appropriate in the combustion context. The averaged equations (eqs. (2.19) to (2.22)) are exact and highly reliable in the sense that they are only a manipulation of conservation laws; however, they are unclosed with respect to

- the Reynolds stress tensor $\widetilde{u_i'' u_j''}$,
- the mean density $\overline{\rho}$,
- the mean viscous stress tensor $\overline{\tau}_{ij}$,
- the turbulent scalar fluxes $\langle \rho u_i'' z'' \rangle$ and $\langle \rho u_i'' z'' z'' \rangle$,
- the three molecular diffusion terms in eq. (2.21) and eq. (2.22),
- the dissipation term $2\langle \rho \mathcal{D}_z \partial z''/\partial x_i \partial z''/\partial x_i \rangle$.

The remainder of this section discusses a set of modeling assumptions commonly used to close the system, which will be the subject of the *a priori* testing in chapter 4.

2.3.2 Determining the mean thermochemical state

Under the laminar flamelet description the density, for example, is a highly nonlinear function of the mixture fraction [45]. As a consequence, applying the RANS averaging operator to a Taylor expansion of ρ and closing with only the first few moments is likely to result in large errors. Including more terms in the expansion is impractical, requiring additional

modeling efforts for higher and mixed moments. Instead, ρ can be modeled as a random variable depending on z and χ, and taking its expectation with respect to the joint density, $f_{z,\chi}(z,\chi)$, gives the mean density $\langle\rho\rangle$. The hope is the nature of the mixture fraction and scalar dissipation rate fluctuations can be sufficiently captured by the presumed shape of the PDF, $f_{z,\chi}(z,\chi)$. The modeling focus is thus shifted to prescribing the form of the PDF for which

$$\langle\rho\rangle = \int_0^\infty \int_0^1 \rho(z,\chi) f_{z,\chi}(z,\chi) dz d\chi \,. \tag{2.23}$$

The typical presumed PDF model which is evaluated in this work assumes z and χ are independently distributed and the individual PDFs are fully characterized by two parameters [3, 4, 46]. Consistent with Favre averaging, the density-weighed mixture fraction PDF

$$\widetilde{f}_z(z) = \frac{\rho f_z(z)}{\langle\rho\rangle} \tag{2.24}$$

is taken as a β-distribution (first introduced in [47]) which is dependent on $\widetilde{z}$ and $\widetilde{z''z''}$ [1]. Specifically,

$$\begin{aligned} \widetilde{f}_z(z) &= \frac{\Gamma(a+b)}{\Gamma(a)\,\Gamma(b)} z^{a-1}(1-z)^{b-1} \\ a = \widetilde{z}\left\{\frac{\widetilde{z}(1-\widetilde{z})}{\widetilde{z''z''}} - 1\right\} &\qquad b = \frac{a}{\widetilde{z}} - a \,. \end{aligned} \tag{2.25}$$

In eq. (2.25), $\widetilde{z}$ and $\widetilde{z''z''}$ are obtained as the solutions of eqs. (2.21) and (2.22) respectively, with additional modeling required to close the equations (see section 2.3.3). The PDF for χ, $f_\chi(\chi)$, is not density weighted and is taken as log-normal [48, 49]:

$$f_\chi(\chi) = \frac{1}{\chi\sigma\sqrt{2\pi}} \exp\left(-\frac{(\log\chi - \mu_\chi)^2}{2\sigma^2}\right) . \tag{2.26}$$

[1] There is an inconsistency introduced by modeling $\widetilde{f}_z(z)$. $\rho f_z(z)$ should formally have a χ dependence from the flamelet density.

In eq. (2.26), σ is assumed to be constant, which implies the variance of the scalar dissipation rate $\widetilde{\chi''^2}$ is linearly proportional to the square of its mean, i.e.

$$\widetilde{\chi''^2} = \widetilde{\chi}^2 \left(\exp\left(\sigma^2\right) - 1\right) , \tag{2.27}$$

and $\mu_\chi = \log\left(\widetilde{\chi}\right) - \sigma^2/2$. The Favre average of $\widetilde{\chi} \equiv 2/\overline{\rho} \times \langle \rho \mathcal{D}_z \partial z/\partial x_i \partial z/\partial x_i \rangle$ is the "total" mean scalar dissipation rate [4] and is unknown. The particular model studied here assumes that only the gradients of the mixture fraction fluctuations contribute to the mean scalar dissipation rate, as is typical in these flamelet-based RANS models [4, 50]. That is,

$$\overline{\rho}\widetilde{\chi} \approx 2\overline{\rho \mathcal{D}_z \frac{\partial z''}{\partial x_i} \frac{\partial z''}{\partial x_i}} \equiv \overline{\rho}\widetilde{\chi}_p \, , \tag{2.28}$$

which means the "total" mean scalar dissipation rate is taken to be the same as $\widetilde{\chi}_p$, the dissipation of the scalar variance, $\widetilde{z''z''}$. The quantity $\widetilde{\chi}_p$ appears in the mixture fraction variance equation as a sink and the discussion of its modeling is deferred to the following section (see section 2.3.3.3).

2.3.3 Determining the mean mixture fraction and its variance

The mean mixture fraction and its variance are computed from their respective transport equations. Models for unclosed terms in these equations are needed, one of which is the mean scalar dissipation rate due to the fluctuations of z $\left(\widetilde{\chi}_p\right)$. As discussed in section 2.3.2, $\widetilde{z}$, $\widetilde{z''z''}$, and $\widetilde{\chi}_p$ are needed as inputs into the presumed PDF models.

2.3.3.1 Gradient diffusion models for the turbulent scalar fluxes

The turbulent scalar fluxes $\langle \rho u_i'' z'' \rangle$ and $\langle \rho u_i'' z'' z'' \rangle$ which appear in the $\widetilde{z}$ and $\widetilde{z''z''}$ equations are modeled using gradient diffusion closures [4, 46]. The basis for these models is the

assumption that the turbulent transport of a conserved quantity ζ is given by

$$\langle \rho u_i'' \zeta'' \rangle \approx -D_t \frac{\partial \widetilde{\zeta}}{\partial x_i} \tag{2.29}$$

where D_t is the turbulent diffusivity of ζ [51]. The standard model for $\langle \rho u_i'' z'' \rangle$ is

$$\langle \rho u_i'' z'' \rangle \approx -\overline{\rho} \frac{\nu_t}{\mathrm{Sc}_t} \frac{\partial \widetilde{z}}{\partial x_i} \tag{2.30}$$

where

$$\nu_t = -C_\mu \frac{k^2}{\varepsilon} \tag{2.31}$$

is the turbulent kinematic viscosity (as assumed by the k-ε turbulence model [52]) and Sc_t is the turbulent Schmidt number (assumed to be a constant) [4]. $k \equiv 1/2\widetilde{u_l'' u_l''}$ is the turbulent kinetic energy and ε is the turbulent dissipation rate defined by

$$\overline{\rho}\varepsilon \equiv \overline{\mu \left[\left(\frac{\partial u_j}{\partial x_i} + \frac{\partial u_i}{\partial x_j} \right) \frac{\partial u_i''}{\partial x_j} - \frac{2}{3} \frac{\partial u_l}{\partial x_l} \frac{\partial u_m''}{\partial x_m} \right]}. \tag{2.32}$$

As summarized by Haering *et al.* [53], the turbulent viscosity used for the momentum flux ν_t can be interpreted as the product of an isotropic approximation of the velocity covariance and the turbulent timescale k/ε. Hence, eq. (2.30) implicitly assumes a simple relationship between these scales and the turbulent diffusivity D_t. An alternative model which uses the mixing timescale $\widetilde{z''z''}/\widetilde{\chi}_p$

$$\langle \rho u_i'' z'' \rangle \approx -\overline{\rho} C_{mix} \frac{\widetilde{z''z''}}{\widetilde{\chi}_p} k \frac{\partial \widetilde{z}}{\partial x_i} \tag{2.33}$$

and one which relaxes the isotropy assumption

$$\langle \rho u_i'' z'' \rangle \approx -\overline{\rho} \frac{C_{ani}}{\mathrm{Sc}_{ani}} \frac{k}{\varepsilon} \widetilde{u_i'' u_j''} \frac{\partial \widetilde{z}}{\partial x_j} \tag{2.34}$$

are also proposed and evaluated in chapter 4. The standard closure for $\langle \rho u_i'' z'' z'' \rangle$ is obtained by simply applying the model form in eq. (2.30) to $z''z''$:

$$\langle \rho u_i'' z'' z'' \rangle \approx -\overline{\rho} \frac{\nu_t}{\mathrm{Sc}_t} \frac{\partial \widetilde{z''z''}}{\partial x_i} \,. \tag{2.35}$$

The two alternative forms of the turbulent diffusivity shown in eqs. (2.33) and (2.34) are also tested in the context of this term.

2.3.3.2 Models for the molecular diffusion terms

In the $\widetilde{z''z''}$ equation, the two molecular diffusion terms are neglected under the assumption that they are negligible in comparison to the turbulent transport term [4]. The molecular diffusion term in the $\widetilde{z}$ equation is typically modeled [4] by assuming

$$\overline{\rho \mathcal{D}_z \frac{\partial z}{\partial x_i}} \approx \overline{\rho}\, \overline{\mathcal{D}_z} \frac{\partial \widetilde{z}}{\partial x_i} \tag{2.36}$$

which neglects the contributions of z fluctuations and takes $\langle \rho \mathcal{D}_z \rangle \approx \langle \rho \rangle \langle \mathcal{D}_z \rangle$.

2.3.3.3 Modeling the scalar dissipation rate

The interpretation of $\widetilde{\chi}_p$ as the dissipation rate of the mixture fraction variance is directly analogous to viewing ε as the dissipation rate of k. An algebraic relationship [54,55] following this reasoning

$$\widetilde{\chi}_p \approx C_{\widetilde{\chi}} \frac{\varepsilon}{k} \widetilde{z''z''} \tag{2.37}$$

is commonly used [4]. The assumption behind this model is that the turbulent timescale k/ε and the mixing timescale $\widetilde{z''z''}/\widetilde{\chi}_p$ are proportional.

With a model for the scalar dissipation rate specified, the mean mixture fraction and

mixture fraction variance equations are (standard turbulent scalar flux models shown)

$$\begin{aligned}\frac{\partial \overline{\rho}\widetilde{z}}{\partial t}+\frac{\partial}{\partial x_i}\left(\overline{\rho}\widetilde{u}_i\widetilde{z}\right)&=\frac{\partial}{\partial x_i}\left(\overline{\rho\mathcal{D}_z}\frac{\partial \widetilde{z}}{\partial x_i}\right)-\frac{\partial}{\partial x_i}\left(\frac{\mu_t}{\mathrm{Sc}_t}\frac{\partial \widetilde{z}}{\partial x_i}\right)\\ \frac{\partial \overline{\rho}\widetilde{z''z''}}{\partial t}+\frac{\partial}{\partial x_i}\left(\overline{\rho}\widetilde{u}_i\widetilde{z''z''}\right)&=-\frac{\partial}{\partial x_i}\left(\frac{\mu_t}{\mathrm{Sc}_t}\frac{\partial \widetilde{z''z''}}{\partial x_i}\right)-2\frac{\mu_t}{\mathrm{Sc}_t}\frac{\partial \widetilde{z}}{\partial x_i}\frac{\partial \widetilde{z}}{\partial x_i}-\overline{\rho}C_{\widetilde{\chi}}\frac{\varepsilon}{k}\widetilde{z''z''}\end{aligned} \tag{2.38}$$

and are fully closed when paired with a k-ε-based model.

2.3.4 Eddy Viscosity Models (EVMs) for the Reynolds stress

The most popular RANS closures for the Reynolds stress are based on the Boussinesq assumption [4], wherein the Reynolds stresses are related to the mean velocity gradients by

$$\overline{\rho}\widetilde{u_i''u_j''}=-\overline{\rho}\nu_t\left(\frac{\partial \widetilde{u}_i}{\partial x_j}+\frac{\partial \widetilde{u}_j}{\partial x_i}-\frac{2}{3}\delta_{ij}\frac{\partial \widetilde{u}_l}{\partial x_l}\right)+\frac{2}{3}\delta_{ij}\overline{\rho}k\,. \tag{2.39}$$

This assumption implies the anisotropic stress tensor, $\widetilde{u_i''u_j''}-2/3\delta_{ij}k$, is aligned with the anisotropic mean strain rate tensor and thus, the Reynolds stress responds immediately to local changes in the mean strain. Clearly, this form is similar to models derived from the gradient diffusion hypothesis (section 2.3.3.1). This work is concerned primarily with the modeling which is unique to the nonpremixed combustion problem, but a brief discussion of the widely employed k-ε EVM which provides the turbulent viscosity in some of the turbulent scalar flux models studied in this work follows.

The k-ε model includes transport equations for these turbulence statistics. Exact equations for k and ε can be derived but are unclosed due the presence of higher moments. In practice, the k equation is closed with various ansatzes based on a mixture of physical intuition, dimensional analysis, and convenience (see [52] for a summary). The resulting

transport equation is

$$\frac{\partial \overline{\rho} k}{\partial t} + \frac{\partial}{\partial x_i}\left(\overline{\rho} k \widetilde{u}_i\right) = -\overline{\rho}\widetilde{u_i'' u_j''}\frac{\partial \widetilde{u}_i}{\partial x_j} - \overline{\rho}\varepsilon + \frac{\partial}{\partial x_i}\left[\left(\overline{\mu} + \overline{\rho}\frac{\nu_t}{\sigma_k}\right)\frac{\partial k}{\partial x_i}\right] \tag{2.40}$$

where σ_k is a model constant. This is a standard transport equation with a convection, diffusion, sink, and source term. The ε equation is engineered to mimic the structure of the closed k equation rather than through term-by-term modeling [56] such that

$$\frac{\partial \overline{\rho} \varepsilon}{\partial t} + \frac{\partial}{\partial x_i}\left(\overline{\rho} \widetilde{u}_i \varepsilon\right) = -C_{\varepsilon 1}\frac{\varepsilon}{k}\overline{\rho}\widetilde{u_i'' u_j''}\frac{\partial \widetilde{u}_i}{\partial x_j} - C_{\varepsilon 2}\overline{\rho}\frac{\varepsilon^2}{k} + \frac{\partial}{\partial x_i}\left[\left(\overline{\mu} + \overline{\rho}\frac{\nu_t}{\sigma_\varepsilon}\right)\frac{\partial \varepsilon}{\partial x_i}\right]. \tag{2.41}$$

σ_k, σ_ε, $C_{\varepsilon 1}$, and $C_{\varepsilon 2}$ are model constants. The modeling required to close the k and ε equations will not be evaluated herein.

2.3.5 Mean stress tensor

The mean stress tensor is commonly closed by assuming

$$\overline{\tau}_{ij} \approx \overline{\mu}\left(\frac{\partial \widetilde{u}_i}{\partial x_j} + \frac{\partial \widetilde{u}_j}{\partial x_i}\right) - \frac{2}{3}\delta_{ij}\overline{\mu}\frac{\partial \widetilde{u}_l}{\partial x_l}, \tag{2.42}$$

thereby neglecting fluctuations in viscosity [52]. This hypothesis is not evaluated in this thesis but highlights that obtaining the mean viscosity is also necessary for these flamelet-based RANS models.

2.3.6 The complete flamelet-based RANS model for nonpremixed turbulent combustion

The model described above is summarized by tabulating the different ingredients of a RANS model of nonpremixed combustion employing the steady laminar flamelet closure:

1. Conservation of mass and momentum, represented by eqs. (2.19) and (2.20), for which a representation of the Reynolds stress $\widetilde{u_i'' u_j''}$ and the mean stress tensor is needed.

2. A model for the turbulent viscosity ν_t, supplemented with additional transport equations for the turbulence statistics k and ε which themselves require multiple closure models.

3. A scalar transport equation for the mean mixture fraction $\widetilde{z}$ and a transport equation for its variance $\widetilde{z''z''}$, represented by eqs. (2.21) and (2.22), which require further modeling, including a closure for the mean scalar dissipation rate $\widetilde{\chi}$ and turbulent scalar fluxes.

4. An instantaneous flame structure model which is obtained from the steady laminar flamelet assumptions.

5. A model mapping the instantaneous flame structure to mean thermodynamic quantities. Presumed PDF models relate mixture fraction statistics $\widetilde{z}$, $\widetilde{z''z''}$, and $\widetilde{\chi}_p$ to $\overline{\rho}$, $\overline{\mu}$, and $\overline{\mathcal{D}_z}$, thereby closing the flow problem.

The analysis in chapter 4 will assess the validity of the ansatzes and modeling decisions used in ingredients 2, 3, and 5, through the use the flamelet DNS in which all modeled terms are resolved exactly. This is done without the conflation of errors from modeling ingredient 4, since the DNS employs the same chemistry assumptions to capture the instantaneous flame structure. The impact of the assumptions in ingredient 4 on the evolution of the reacting jet can be examined separately by comparison of the flamelet DNS with the complex chemistry DNS. Reynolds stress closures and the modeling of the k and ε equations are not a focus of this work.

Chapter 3

Numerical method and DNS algorithm

This chapter details the development of a novel numerical scheme to solve the variable-density, low-Mach-number Navier-Stokes equations and the associated DNS algorithm. With the understanding that the method extends to the more general case of N_s species and an energy equation, the following discussion will be limited to a formulation in which a single conserved scalar is used to characterize the thermochemical state. This is the relevant case for the flamelet DNS which is formulated in terms of a mixture fraction.

3.1 Outline of the present approach

Most algorithms for the incompressible or the low-Mach-number, variable-density Navier-Stokes equations employ fractional-step or other projection methods, but the formulation presented here is an extension of the scheme of Kim, Moin, and Moser (KMM) [1] developed for incompressible flows. In their scheme, equations for one component of the vorticity and the Laplacian of the velocity are advanced, eliminating the need to solve for the pressure. Herein the momentum is decomposed into divergence-free and curl-free parts. The divergence-free momentum plays a role that is similar to the incompressible velocity in the original KMM algorithm, and the curl-free momentum is reconstructed through the mass conservation equation. A similar decomposition was used in the work of Almagro *et al.* [57]. Their scheme, however, is only first-order accurate in time despite using three Runge-Kutta

(RK) stages and assumes constant fluid viscosity, thermal conductivity, and specific heat. The algorithm presented here relaxes these restrictive assumptions, achieves a higher order temporal accuracy in two stages, and *a priori* guarantees discrete conservation of mass. Additionally, the scheme is made more robust to large density variations by considering the impact of the divergence constraint on numerical stability.

As shown in section 3.4.1, the redundancy between the equation of state and the mass conservation equation places constraints on the conserved scalar equation. Because of this, the convective term depends on the time derivative of the conserved scalar z. The mathematical structure of the scalar equation is that of an implicit PDE which is linear in the time derivative on the right-hand side. A numerical scheme accounting for this structure thus requires the solution of an equation of the following form:

$$\frac{\partial z}{\partial t} = \mathcal{L}(z)\frac{\partial z}{\partial t} + \mathcal{R}_z \tag{3.1}$$

where $\mathcal{L}(z)$ is a z-dependent linear operator acting on $\partial z/\partial t$ and $\mathcal{R}_z$ is a convection-diffusion operator with convection velocity defined by the divergence-free momentum. If $\mathcal{I} - \mathcal{L}$ is nonsingular, eq. (3.1) can be written

$$\frac{\partial z}{\partial t} = \{\mathcal{I} - \mathcal{L}(z)\}^{-1}\,\mathcal{R}_z\,, \tag{3.2}$$

and time-discretized using a convenient time-discretization scheme, such as an explicit RK2 scheme can be used. However, inverting $\mathcal{I} - \mathcal{L}$ is not practical, especially in a DNS, as $\mathcal{L}$ is nonlinear in z and dense. Instead, a matrix-free iterative scheme is introduced with the following properties:

1. assuming the spectral radius $\rho(\mathcal{L}) < 1$, the iterations converge to the solution of eq. (3.2) after it has been discretized by the explicit RK2 method;

2. the temporal order of the scheme is independent of the number of iterations;

3. iterations can be performed efficiently on massively parallel high performance computers.

In general, it is not necessary to fully converge the scheme for stability, so the iterations can be stopped early to minimize computational costs without sacrificing second-order accuracy in time.

The algorithm is designed for DNS scenarios with two statistically homogeneous directions that can be simulated with periodic boundary condition and one inhomogeneous direction. Spatially, Fourier bases are employed in the homogeneous directions with a B-spline basis [58] in the inhomogeneous direction. The equations are discretized using a mixed Fourier/B-spline-collocation method. Special care is taken to ensure the discrete divergence operator is exact, guaranteeing conservation of mass. Time is discretized using an explicit, low-storage, second-order Runge-Kutta method.

This chapter is organized as follows. Section 3.2 introduces the decomposition of the momentum used to eliminate the pressure. Details of the spatial discretization are given in section 3.3. Section 3.4 describes the temporal discretization, its second-order convergence, and its numerical stability. Finally, section 3.5 lays out the complete DNS algorithm and demonstrates its efficacy for flows with large density ratios via a single-mode Rayleigh-Taylor test case.

3.2 Decomposition of the low-Mach-number, variable-density equations

This thesis employs a DNS formulation based on a transformation which eliminates the pressure from the governing equations. A Helmholtz decomposition of the momentum $\boldsymbol{m} =$

$\rho \boldsymbol{u}$ is used:

$$\boldsymbol{m} = \boldsymbol{m}^d + \boldsymbol{m}^c \tag{3.3}$$

where $\boldsymbol{m}^d$ is divergence free and $\boldsymbol{m}^c$ is curl free, so that $\boldsymbol{m}^c = \nabla\psi$ for some scalar potential ψ.

Inspired by the formulation of Kim, Moin, and Moser [1] (for incompressible flow), define

$$\boldsymbol{\phi} \equiv \nabla^2 \boldsymbol{m}^d \qquad \boldsymbol{\Omega} \equiv \nabla \times \boldsymbol{m}^d \,. \tag{3.4}$$

The 2-component of the curl and double curl of the momentum equations, eq. (2.2), are then given by

$$\begin{cases} \dfrac{\partial \Omega_2}{\partial t} &= \dfrac{\partial^2}{\partial x_3 \partial x_j}\left(C_{1j} + \tau_{1j}\right) - \dfrac{\partial^2}{\partial x_1 \partial x_j}\left(C_{3j} + \tau_{3j}\right) \\ \dfrac{\partial \phi_2}{\partial t} &= \dfrac{\partial^3}{\partial x_l \partial x_l \partial x_j}\left(C_{2j} + \tau_{2j}\right) - \dfrac{\partial^3}{\partial x_2 \partial x_l \partial x_j}\left(C_{lj} + \tau_{lj}\right) \\ \Omega_2 &= \dfrac{\partial m_1^d}{\partial x_3} - \dfrac{\partial m_3^d}{\partial x_1} \\ \phi_2 &= \nabla^2 m_2^d \end{cases} \tag{3.5}$$

with $C_{ij} \equiv -\rho u_i u_j$, the nonlinear convective terms. The 2-component is used here because it is the x_1 and x_3 directions that are assumed to be statistically homogeneous and treated with Fourier spectral methods as in KMM. Conservation of mass relates the curl-free momentum to the density

$$\frac{\partial \rho}{\partial t} = -\nabla \cdot \boldsymbol{m}^c = -\nabla^2 \psi \,. \tag{3.6}$$

Additionally, the scalar transport equation for z is expressed in nonconservative form

$$\frac{\partial z}{\partial t} = -u_i \frac{\partial z}{\partial x_i} + \frac{1}{\rho}\frac{\partial \rho \mathcal{D}_z}{\partial x_i}\frac{\partial z}{\partial x_i} + \mathcal{D}_z \frac{\partial^2 z}{\partial x_i \partial x_i} \,. \tag{3.7}$$

This avoids an unnecessary coupling with the equation of state which would arise from the material derivative even with explicit time-stepping and simplifies the formulation of $\mathcal{L}(z)$

in eq. (3.1). The density, viscosity, and scalar diffusion coefficient, $\mathcal{D}_z$, are known functions of z, as in system (2.12) but the χ dependence is dropped for simplicity.

Finally, since system (3.5) was obtained through applications of derivative operations to the momentum equations, they leave $\boldsymbol{m}^d$ averaged in the homogeneous directions undetermined. Averaging the momentum equation over the homogeneous directions and denoting such averages as $\overline{\cdot}^{x_1x_3}$ gives for $\overline{m}_1^{x_1x_3}$ and $\overline{m}_3^{x_1x_3}$:

$$\begin{aligned}\frac{\partial \overline{m}_1^{x_1x_3}}{\partial t} &= \frac{\partial}{\partial x_2}\left(\overline{C}_{12}^{x_1x_3} + \overline{\tau}_{12}^{x_1x_3}\right)\\ \frac{\partial \overline{m}_3^{x_1x_3}}{\partial t} &= \frac{\partial}{\partial x_2}\left(\overline{C}_{23}^{x_1x_3} + \overline{\tau}_{23}^{x_1x_3}\right)\end{aligned} \tag{3.8}$$

where $\overline{m}_1^{x_1x_3} = \overline{m^d}_1^{x_1x_3}$, $\overline{m}_3^{x_1x_3} = \overline{m^d}_3^{x_1x_3}$, and $\overline{m^d}_2^{x_1x_3} = 0$. The fact that $\partial\overline{\tau}_{ij}^{x_1x_3}/\partial x_j$ collapses to $\partial\overline{\tau}_{i2}^{x_1x_3}/\partial x_2$ has also been used.

3.3 Spatial discretization

The computational domain is $\mathcal{V} = [-L_1/2, L_1/2]\times[-L_2/2, L_2/2]\times[-L_3/2, L_3/2]$. Assuming periodicity in the homogeneous directions, the discrete representation of a flow variable f is expressed as a Fourier series in x_1 and x_3 and a B-spline series of order p, $\{B_s^p\}$, in x_2, to yield

$$\begin{aligned} f^h(x_1,x_2,x_3,t) &= \sum_{l=-\frac{N_1}{2}+1}^{\frac{N_1}{2}-1}\sum_{n=-\frac{N_3}{2}+1}^{\frac{N_3}{2}-1} \widehat{f}_{ln}(x_2,t)e^{\mathrm{i}k_1x_1}e^{\mathrm{i}k_3x_3}\\ &= \sum_{l=-\frac{N_1}{2}+1}^{\frac{N_1}{2}-1}\sum_{j=0}^{N_2-1}\sum_{n=-\frac{N_3}{2}+1}^{\frac{N_3}{2}-1} f_{ljn}(t)e^{\mathrm{i}k_1x_1}B_j^p(x_2)e^{\mathrm{i}k_3x_3}\\ k_1 &= \frac{2\pi l}{L_1} \qquad k_3 = \frac{2\pi n}{L_3}\end{aligned} \tag{3.9}$$

with $(N_1-1)\times N_2\times(N_3-1)$ total degrees of freedom. Note that the dependence of k_1 and k_3 on l and n is assumed, though not explicitly indicated. For a selected B-spline order

p, all variables use a B-spline basis of order p with the exception of the x_2 component of momentum, which is represented with B-splines of order $p+1$ (discussed in section 3.3.3) and therefore includes one additional degree of freedom:

$$\begin{aligned} m_2^h(x_1,x_2,x_3,t) &= \sum_{l=-\frac{N_1}{2}+1}^{\frac{N_1}{2}-1} \sum_{n=-\frac{N_3}{2}+1}^{\frac{N_3}{2}-1} \widehat{m_2}_{,ln}(x_2,t) e^{\mathrm{i}k_1x_1} e^{\mathrm{i}k_3x_3} \\ &= \sum_{l=-\frac{N_1}{2}+1}^{\frac{N_1}{2}-1} \sum_{j=0}^{N_2} \sum_{n=-\frac{N_3}{2}+1}^{\frac{N_3}{2}-1} m_{2,ljn}(t) e^{\mathrm{i}k_1x_1} B_j^{p+1}(x_2) e^{\mathrm{i}k_3x_3} \,. \end{aligned} \tag{3.10}$$

B-splines of order p are piecewise polynomials of degree $p-1$ defined by the selection of knot points (ξ_i) which partition the domain into intervals and determine the degree of continuity of the basis. They have minimal local support and have up to $p-2$ continuous derivatives at interval boundaries. They are attractive for the simulation of turbulent flows [38, 59–62] due to their flexibility near boundaries and on nonuniform grids, and their ability to achieve high spatial resolution while being computationally efficient [59, 63]. A standard reference on B-splines is de Boor [58] and for specifics about the use of B-splines with maximal continuity (which are chosen in this work) for fluid flows see [59].

The equations in section 3.2 are spatially discretized with a weighted residual method [64, 65]. A mixed Fourier/B-spline-collocation pseudospectral approach with approximate quadrature is used where test functions are of the form

$$\varphi = e^{-\mathrm{i}k_1x_1} \delta(x_2 - x_2') e^{-\mathrm{i}k_3x_3} \tag{3.11}$$

where δ is the Dirac delta function and which exploit orthogonality of the Fourier bases with respect to the L^2 inner product. This requires selecting a set of 'collocation points' $\mathcal{Y}_{coll}^p \equiv \{x_{2,i}'\}$ of size N_2 at which the weighted residual is enforced [63], the Greville abscissae

[59, 66] are used here:

$$x'_{2,i} = \frac{1}{p-1}\left(\xi_i + \xi_{i-1} + \cdots + \xi_{i+p-1}\right) \qquad x'_{2,i} \in \mathcal{Y}^p_{coll}\,. \tag{3.12}$$

The result is $(N_1 - 1) \times (N_3 - 1)$ systems of N_2 equations for each governing equation – one system for each wavenumber pair. Spectral methods commonly employ numerical quadrature with $3/2N$ uniformly spaced quadrature points [67] to compute the weighted residual integrals because it is sufficient to entirely eliminate quadrature error for quadratic nonlinearities which appear in the incompressible Navier-Stokes equations [64]. Higher order nonlinearities are present in the variable-density system, but empirical tests have found that most of the quadrature error can be controlled with a number of quadrature points only modestly larger than N [32]. Additionally, $3/2N$ quadrature was successfully employed in a variable-density, compressible DNS [61]. Based on these findings, $3/2N$ quadrature is used here. The spatially discrete equations obtained by applying the weighted residual method are shown in section 3.3.2.

3.3.1 B-spline collocation matrices

Consider a linear differential operator $\mathcal{D}$ and let $f^h = f^h(x_2)$. The B-spline collocation method approximates the action of $\mathcal{D}$ on $f^h(x_2) = \sum_j f_j B^p_j(x_2)$ by requiring

$$g^h(x_2) = \mathcal{D}\left(f^h\right) = \sum_j g_j B^{p'}_j = \sum_j f_j \mathcal{D}\left(B^p_j\right) \tag{3.13}$$

at the specified collocation points [63]. In general, the B-spline orders p and p' may be different. Define the B-spline collocation matrix

$$\left(B^d_{r,s}\right)_{ij} \equiv \left.\frac{\partial^d B^{p+s}_j}{\partial x_2^d}\right|_{x_2 = x'_{2,i}} \tag{3.14}$$

where $x'_{2,i}$ are the $p+r$ order collocation points, $\mathcal{Y}^{p+r}_{coll}$ where s and r are either 0 or 1 to account for the use of order p and $p+1$ splines (see eqs. (3.9) and (3.10)). Let $c^f_i = f_i$, then, for example, if f^h is of order $p+1$ and g^h order p, applying the first derivative operator requires solving

$$\boldsymbol{B}^0_{0,0}\boldsymbol{c}^g = \boldsymbol{B}^1_{0,1}\boldsymbol{c}^f \tag{3.15}$$

for $\boldsymbol{c}^g$. In this case, the collocation points must be chosen as $\mathcal{Y}^p_{coll}$ ($r = 0$), corresponding with the order of the unknown function g^h, for well-posedness. Other discrete derivative operators (in the x_2 direction) are formed analogously.

3.3.2 Spatially discrete equations

The result of applying the weighted residual method to the variable-density Navier-Stokes equations (see section 3.2) is summarized below. The vector of Fourier coefficients is denoted $\boldsymbol{c}^{\widehat{f}_{ln}}$ for modes with k_1 or k_3 nonzero and $\boldsymbol{c}^{\overline{f}^{x_1x_3}} \equiv \{f_{0j0}\}$ is the vector of coefficients of the plane-averaged quantity. Since each system of equations is associated with a unique wavenumber pair, the subscripts l and n will be suppressed for simplicity of notation from this point, where appropriate. The semi-discrete Ω_2 equation is

$$\begin{aligned}\boldsymbol{B}^0_{0,0}\frac{\partial \boldsymbol{c}^{\widehat{\Omega}_2}}{\partial t} = {} & k_1k_3\boldsymbol{B}^0_{0,0}\left(\boldsymbol{c}^{\widehat{C}_{33}} - \boldsymbol{c}^{\widehat{C}_{11}}\right) + \mathrm{i}k_3\boldsymbol{B}^1_{0,0}\boldsymbol{c}^{\widehat{C}_{12}} - \left(k_3^2 - k_1^2\right)\boldsymbol{B}^0_{0,0}\boldsymbol{c}^{\widehat{C}_{13}} \\ & - \mathrm{i}k_1\boldsymbol{B}^1_{0,0}\boldsymbol{c}^{\widehat{C}_{23}} + \left(\mathrm{i}k_3\boldsymbol{B}^0_{0,0}\boldsymbol{c}^{\widehat{F^\tau}_1} - \mathrm{i}k_1\boldsymbol{B}^0_{0,0}\boldsymbol{c}^{\widehat{F^\tau}_3}\right)\end{aligned} \tag{3.16}$$

where $\boldsymbol{F}^\tau = \nabla\cdot\boldsymbol{\tau}$ is the divergence of the stress tensor which is nonlinear like $\boldsymbol{C}$. Details of how these nonlinear coefficients are obtained are deferred to section 3.5; see procedure 2 in

particular. The ϕ_2 equation is

$$\begin{aligned}\boldsymbol{B}^0_{0,0}\frac{\partial \boldsymbol{c}^{\widehat{\phi}_2}}{\partial t} &= k_1^2\boldsymbol{B}^1_{0,0}\left(\boldsymbol{c}^{\widehat{C}_{11}} - \boldsymbol{c}^{\widehat{C}_{22}}\right) - \mathrm{i}\left\{k_1\boldsymbol{B}^2_{0,0} + \boldsymbol{B}^0_{0,0}\left(k_1^3 + k_1k_3^2\right)\right\}\boldsymbol{c}^{\widehat{C}_{12}} \\ &\quad + 2k_1k_3\boldsymbol{B}^1_{0,0}\boldsymbol{c}^{\widehat{C}_{13}} - \mathrm{i}\left\{k_3\boldsymbol{B}^2_{0,0} + \boldsymbol{B}^0_{0,0}\left(k_1^2k_3 + k_3^3\right)\right\}\boldsymbol{c}^{\widehat{C}_{23}} \\ &\quad + k_3^2\boldsymbol{B}^2_{0,0}\left(\boldsymbol{c}^{\widehat{C}_{33}} - \boldsymbol{c}^{\widehat{C}_{22}}\right) \\ &\quad - \left(\mathrm{i}k_1\boldsymbol{B}^1_{0,0}\boldsymbol{c}^{\widehat{F^\tau}_1} + \left(k_1^2 + k_3^2\right)\boldsymbol{B}^0_{0,0}\boldsymbol{c}^{\widehat{F^\tau}_2} + \mathrm{i}k_3\boldsymbol{B}^1_{0,0}\boldsymbol{c}^{\widehat{F^\tau}_3}\right).\end{aligned} \tag{3.17}$$

The discrete plane-averaged momentum equations are

$$\begin{aligned}\boldsymbol{B}^0_{0,0}\frac{\partial \boldsymbol{c}^{\overline{m}_1^{x_1x_3}}}{\partial t} &= \boldsymbol{B}^1_{0,0}\boldsymbol{c}^{\overline{C}_{12}^{x_1x_3}} + \boldsymbol{B}^0_{0,0}\boldsymbol{c}^{\overline{F^\tau}_1^{x_1x_3}} \\ \boldsymbol{B}^0_{0,0}\frac{\partial \boldsymbol{c}^{\overline{m}_3^{x_1x_3}}}{\partial t} &= \boldsymbol{B}^1_{0,0}\boldsymbol{c}^{\overline{C}_{23}^{x_1x_3}} + \boldsymbol{B}^0_{0,0}\boldsymbol{c}^{\overline{F^\tau}_3^{x_1x_3}}\end{aligned} \tag{3.18}$$

where $\overline{F^\tau}_1^{x_1x_3} = \partial\overline{\tau}_{12}^{x_1x_3}/\partial x_2$ and $\overline{F^\tau}_3^{x_1x_3} = \partial\overline{\tau}_{23}^{x_1x_3}/\partial x_2$. The scalar transport equation for z is comprised entirely of nonlinear products so it is of the form

$$\boldsymbol{B}^0_{0,0}\frac{\partial \boldsymbol{c}^{\widehat{z}}}{\partial t} = \boldsymbol{B}^0_{0,0}\boldsymbol{c}^{\widehat{RHS_z}} \tag{3.19}$$

and it is further manipulated as detailed in section 3.4. For forming the nonlinear terms in this equation, as well as $\boldsymbol{C}$ and $\boldsymbol{F}^\tau$, the discrete gradient and discrete Laplacian are block-diagonal operators acting on coefficients of order p B-spline expansions and are defined as

$$\nabla^h_{ln}\{\cdot\} = \begin{bmatrix} \mathrm{i}k_1\{\cdot\} \\ \boldsymbol{B}^1_{0,0}\{\cdot\} \\ \mathrm{i}k_3\{\cdot\} \end{bmatrix} \tag{3.20}$$

$$\nabla^{2,h}_{ln}\{\cdot\} = \left\{-\left(k_1^2 + k_3^2\right)\boldsymbol{B}^0_{0,0} + \boldsymbol{B}^2_{0,0}\right\}\{\cdot\}.$$

The mass conservation equation (eq. (3.6)) can be handled in two ways. A straightforward

discretization of the Poisson operator would give

$$\boldsymbol{B}^0_{0,0}\frac{\partial \widehat{\boldsymbol{c}^{\rho}}}{\partial t} = \left\{\left(k_1^2 + k_3^2\right)\boldsymbol{B}^0_{0,0} - \boldsymbol{B}^2_{0,0}\right\}\widehat{\boldsymbol{c}^{\psi}} \tag{3.21}$$

and the coefficients for $\boldsymbol{m}^c$ would be obtained by taking the gradient of ψ. Then $\boldsymbol{m}^c$ would be discretely curl free. However, because the discrete second derivative operator is not equal to the first derivative applied twice, $\partial\rho/\partial t + \nabla\cdot\boldsymbol{m}^c = 0$ would not be satisfied discretely anywhere in the domain. Instead, consider the operator $\mathcal{C} : \partial\rho/\partial t \to \boldsymbol{m}^c$ such that $\nabla\times\boldsymbol{m}^c = 0$. In the continuous setting $\mathcal{C} = \nabla\left(\nabla^2\right)^{-1}$ with consistent boundary conditions. Discretizing this operator gives

$$\boldsymbol{B}^0_{0,0}\widehat{\boldsymbol{c}^{\partial\rho/\partial t}} = -\boldsymbol{B}^0_{0,0}\left(\mathrm{i}k_1\widehat{\boldsymbol{c}^{m_1^c}} + \mathrm{i}k_3\widehat{\boldsymbol{c}^{m_3^c}}\right) - \boldsymbol{B}^1_{0,1}\widehat{\boldsymbol{c}^{m_2^c}} \tag{3.22}$$

with the curl-free conditions

$$\begin{aligned}\boldsymbol{B}^1_{1,0}\widehat{\boldsymbol{c}^{m_3^c}} - \mathrm{i}k_3\boldsymbol{B}^0_{1,1}\widehat{\boldsymbol{c}^{m_2^c}} &= 0\\ k_3\widehat{\boldsymbol{c}^{m_1^c}} - k_1\widehat{\boldsymbol{c}^{m_3^c}} &= 0\end{aligned} \tag{3.23}$$

enforced explicitly (for $k_3 \neq 0$). It follows that the third curl-free condition

$$\mathrm{i}k_1\boldsymbol{B}^0_{1,1}\widehat{\boldsymbol{c}^{m_2^c}} - \boldsymbol{B}^1_{1,0}\widehat{\boldsymbol{c}^{m_1^c}} = 0 \tag{3.24}$$

is satisfied automatically. If $k_3 = 0$, eq. (3.24) is enforced instead of the first condition in eq. (3.23). Using this discrete operator ensures global conservation of mass in addition to $\boldsymbol{m}^c$ satisfying the conservation of mass equation at all interior collocation points. This is contingent on expanding m_2 with order $p+1$ B-splines.

3.3.3 Discrete conservation of mass

By expanding m_2 with order $p+1$ B-splines, the discrete divergence of $\boldsymbol{m}$ can be exactly represented in the mixed p^{th}-order B-spline/Fourier basis. Differentiation in the homogeneous directions results in multiplication by the imaginary unit and wavenumber components and therefore results in an exact projection onto the discrete basis in x_1 and x_3. Then define the discrete first derivative associated with the discrete divergence operator as in eq. (3.15):

$$\sum_{j=0}^{N_2-1} m_{2,j}^1 B_j^p(x'_{2,i}) = \sum_{j=0}^{N_2} m_{2,j} \frac{\partial B_m^{p+1}}{\partial x_2}\bigg|_{x_2=x'_{2,i}} \qquad \forall\ x'_{2,i} \in \mathcal{Y}_{coll}^p \tag{3.25}$$

where $m_{2,j}^1$ are the B-spline coefficients of $\partial m_2/\partial x_2$. The splines represented by both the left-hand and right-hand side coefficients are piecewise polynomials of the same order on the same set of knots used to partition the domain. With the appropriate number of equations relative to the degrees of freedom, using the Greville abscissae ensures a unique spline interpolant as each basis function has at least one collocation point within its interval of support [68]. It follows that the equality in eq. (3.25) holds everywhere,

$$\sum_{j=0}^{N_2-1} m_{2,j}^1 B_m^p(y) = \sum_{j=0}^{N_2} m_{2,j} \frac{\partial B_m^{p+1}}{\partial x_2}\bigg|_{x_2=y} \qquad \forall\ y \in [-L_2/2, L_2/2] \tag{3.26}$$

and, therefore, $\nabla \cdot \boldsymbol{m}$ is exactly represented.

With this divergence operation, global conservation of mass is always satisfied. Firstly, it must be true that $\nabla \cdot \boldsymbol{m}^d = 0$ discretely so that $\nabla \cdot \boldsymbol{m} = \nabla \cdot \boldsymbol{m}^c$. This is trivially satisfied upon the reconstruction of $\boldsymbol{m}^d$ from ϕ_2 and Ω_2 (shown in eq. (3.98)), akin to the guarantee of a divergence-free velocity in KMM for incompressible Navier-Stokes [1]. Secondly, recognize

$$\frac{1}{L_1 L_3}\int_{\mathcal{V}} \left(\frac{\partial \rho}{\partial t} + \nabla \cdot \boldsymbol{m}^c\right)\, dx_1 dx_2 dx_3 = \int_{-\frac{L_2}{2}}^{\frac{L_2}{2}} \left(\frac{\partial \overline{\rho}^{x_1 x_3}}{\partial t} + \frac{\partial \overline{m}_2^{x_1 x_3}}{\partial x_2}\right)\, dx_2 \tag{3.27}$$

and periodicity of the Fourier bases in $\mathcal{V}$ implies

$$\begin{aligned}\int_{\mathcal{V}} \sum_{l=-\frac{N_1}{2}+1}^{\frac{N_1}{2}-1} \sum_{n=-\frac{N_3}{2}+1}^{\frac{N_3}{2}-1} \widehat{f}_{ln}(x_2,t) e^{\mathrm{i}k_1 x_1} e^{\mathrm{i}k_3 x_3}\, dx_1 dx_2 dx_3 \\ = \int_{-\frac{L_2}{2}}^{\frac{L_2}{2}} \widehat{f}_{00}(x_2,t)\, dx_2 = \int_{-\frac{L_2}{2}}^{\frac{L_2}{2}} \overline{f}^{x_1 x_3}(x_2,t)\, dx_2\,.\end{aligned} \tag{3.28}$$

Then for $k_1 = k_3 = 0$ eq. (3.22) simplifies to

$$\boldsymbol{B}^0_{0,0} \boldsymbol{c}^{\overline{\partial\rho/\partial t}^{x_1 x_3}} = -\boldsymbol{B}^1_{0,1} \boldsymbol{c}^{\overline{m}_2^{x_1 x_3}} \tag{3.29}$$

where $\overline{m}_2^{x_1 x_3} = \overline{m^c}_2^{x_1 x_3}$. This is a system of size N_2 and needs to be supplemented with one boundary condition. Therefore, $\partial\overline{\rho}^{x_1 x_3}/\partial t + \partial\overline{m}_2^{x_1 x_3}/\partial x_2 = 0$ is satisfied at all collocation points and by eq. (3.25) it is satisfied everywhere. Combining this with eq. (3.27) implies

$$\frac{\partial}{\partial t}\int_{-\frac{L_2}{2}}^{\frac{L_2}{2}} \overline{\rho}^{x_1 x_3}\, dx_2 = -\int_{-\frac{L_2}{2}}^{\frac{L_2}{2}} \frac{\partial \overline{m}_2^{x_1 x_3}}{\partial x_2}\, dx_2 = -\left(\overline{m}_2^{x_1 x_3}(L_2/2) - \overline{m}_2^{x_1 x_3}(-L_2/2)\right) \tag{3.30}$$

ensuring global conservation of mass.

3.4 Temporal discretization

Fourier spectral methods rely on a wavenumber-by-wavenumber decoupling to make computation tractable. In the variable-density case, few operators in the governing equations are linear, so explicit time integration or linearly-implicit schemes that avoid prohibitively expensive nonlinear solves are attractive. This work focuses on the DNS of flows in unbounded domains where the timestep required for accuracy is similar to the timestep required for stability when using an explicit method [69]. For this reason, it is based on an explicit, low-storage, second-order Runge-Kutta scheme. Explicit time discretization also allows the

equations for Ω_2, ϕ_2, and z to be advanced independently. However, treatment of the z equation is complicated by the mass conservation constraint, which is particularly challenging to enforce for large density ratios. A new, robust numerical formulation for solving the z equation is introduced below.

3.4.1 Reframing the scalar transport equation

The variable-density Navier-Stokes equations from section 3.2 are a system of partial differential equations along with the equation of state that makes the mass conservation equation redundant. The equation of state relating ρ and z, $\rho = f(z)$, and the mass conservation equation imply

$$\frac{\partial \rho}{\partial t} = \frac{\partial f}{\partial z}\frac{\partial z}{\partial t} = -\nabla \cdot \boldsymbol{m}^c \,. \tag{3.31}$$

The curl-free momentum $\boldsymbol{m}^c$ can be written as the gradient of a scalar potential $\boldsymbol{m}^c = \nabla\psi$ which obeys

$$\frac{\partial \rho}{\partial t} = -\nabla^2\psi \,, \tag{3.32}$$

with appropriate boundary conditions. This implies

$$\boldsymbol{m}^c = -\nabla\left(\nabla^2\right)^{-1}\left[\frac{\partial f}{\partial z}\frac{\partial z}{\partial t}\right] \tag{3.33}$$

where $\left(\nabla^2\right)^{-1}$ is the inverse Laplacian (equivalently, $\mathcal{C}^{-1}$ can be used as discussed in section 3.3.2). When explicitly time advancing the equations, the conserved scalar z and the momentum will not satisfy eq. (3.33) in general. As noted in section 1.3.2, such inconsistencies are destabilizing, especially when large density gradients are present.

Evaluating the convective term (including the contribution from $\boldsymbol{m}^c$) in the z equation

purely explicitly can result in numerical instability. Consider the evolution equation for z:

$$\frac{\partial z}{\partial t} = -\frac{1}{\rho}\left(\boldsymbol{m}^d + \boldsymbol{m}^c\right) \cdot \nabla z + \frac{1}{\rho}\nabla\rho\mathcal{D}_z \cdot \nabla z + \mathcal{D}_z\nabla^2 z\,. \tag{3.34}$$

From eq. (3.33) $\boldsymbol{m}^c$ is determined directly from $\partial z/\partial t$; therefore, treating $\boldsymbol{m}^c$ explicitly is equivalent to lagging the dependence of $\partial z/\partial t$ on the right-hand side with respect to the derivative on the left-hand side. This effective lagging of the time derivative leads to instabilities.

To remove the potential for numerical instability, the z equation can be reformulated as follows: let

$$\mathcal{L}(z)\,\{\cdot\} \equiv -\frac{1}{\rho}\nabla z \cdot \nabla\left(\nabla^2\right)^{-1}\left[\frac{\partial f}{\partial z}\{\cdot\}\right]. \tag{3.35}$$

$\mathcal{L}$ is linear in $\partial z/\partial t$ and has a dependence on z. Then the scalar transport equation, eq. (3.7), can be rewritten as

$$\frac{\partial z}{\partial t} = \mathcal{L}(z)\frac{\partial z}{\partial t} - \frac{1}{\rho}\boldsymbol{m}^d \cdot \nabla z + \frac{1}{\rho}\nabla\rho\mathcal{D}_z \cdot \nabla z + \mathcal{D}_z\nabla^2 z\,. \tag{3.36}$$

This makes explicit the dependence of the right-hand side on $\partial z/\partial t$ due to the $\boldsymbol{m}^c$ portion of the convective term. Further, define

$$\mathcal{R}_z \equiv -\frac{1}{\rho}\boldsymbol{m}^d \cdot \nabla z + \frac{1}{\rho}\nabla\rho\mathcal{D}_z \cdot \nabla z + \mathcal{D}_z\nabla^2 z \tag{3.37}$$

and the z equation is of the form presented previously in eq. (3.1), rewritten here:

$$\frac{\partial z}{\partial t} = \mathcal{L}(z)\frac{\partial z}{\partial t} + \mathcal{R}_z\,.$$

If $\mathcal{I} - \mathcal{L}$ is nonsingular, eq. (3.1) can be manipulated into explicit form, eq. (3.2), again

rewritten:

$$\frac{\partial z}{\partial t} = \{\mathcal{I} - \mathcal{L}(z)\}^{-1} \mathcal{R}_z \,.$$

Time advancing eq. (3.2) would ensure consistency in the equation of state, the mass conservation equation, and the scalar transport equation, avoiding potential instability because the redundant equations have been eliminated. However, inverting $\mathcal{I} - \mathcal{L}$ directly is not practical as it is nonlocal in Fourier space and dense.

Instead eq. (3.1) is solved using a fixed-point iteration which, upon convergence, would effectively solve eq. (3.2) and mitigate the stability problems. Recognizing that full convergence will not be necessary for stability, the method is designed such that z will be temporally second order, consistent with the temporal discretization of the momentum equations, regardless of the number of iterations. Hence, the number of iterations is selected to reduce the destabilizing inconsistencies between the equation of state, the mass conservation equation, and the scalar transport equation to an appropriate level. This allows for stability while minimizing cost.

3.4.2 Iterative, matrix-free, second-order scheme

To analyze the time discretization issues described above, consider the following system of ODEs, designed to exhibit the challenges arising in the low-Mach-number, variable-density equations:

$$\begin{cases} \dfrac{dz}{dt} = \mathcal{M}_1(z)\dfrac{dz}{dt} + \mathcal{M}_2(z) \\ \dfrac{dr}{dt} = \mathcal{M}_3(r, m^c) \\ \dfrac{d\rho}{dt} = \mathcal{G}(m^c) \\ \rho = f(z) \end{cases} \tag{3.38}$$

where $\mathcal{M}_1$ is a potentially z-dependent operator which is linear in dz/dt, $\mathcal{M}_2$ has no dz/dt dependence but also is generally nonlinear in z – this equation has the same structure

as eq. (3.1). $\mathcal{M}_3(r, m^c)$ is potentially nonlinear in both r and m^c and is a surrogate for the transformed momentum equations. $\mathcal{G}$ is a linear operator acting on m^c akin to the divergence operator in the mass conservation equation. Although m^c is not strictly needed to advance the z equation, it participates in the r equation, therefore its reconstruction from $d\rho/dt = \mathcal{G}(m^c)$ must be compatible with the temporal discretization of the r equation in order to achieve the desired temporal order of convergence.

The advancement of the evolution equations is built on an explicit, low-storage RK2 scheme which is described here first. Two substeps are needed to advance u where $du/dt = f(u)$ from time level n to $n+1$:

$$\begin{aligned} u' &= u^n + \frac{1}{2}\Delta t f(u^n) \\ u^{n+1} &= u' + \Delta t \left\{ f(u') - \frac{1}{2} f(u^n) \right\} \end{aligned} \tag{3.39}$$

where the prime notation indicates the value taken at the intermediate stage and u^{n+1} is the estimation of $u(t_{n+1}) = u(t_n + \Delta t)$. Starting with $u^n = u(t_n)$, an evaluation of $f(u)$ at t_n,

$$f(u^n) = f\left(u\left(t_n\right)\right) , \tag{3.40}$$

gives an approximation of u at $t_{n+1/2} = t + 1/2\Delta t$ which is

$$u' = u^n + \frac{1}{2}\Delta t f(u^n) = u(t_n) + \frac{1}{2}\Delta t f\left(u\left(t_n\right)\right) . \tag{3.41}$$

This is used to estimate $f(u)$ at $t_{n+1/2}$,

$$\begin{aligned} f(u') &= f\left(u(t_n) + \frac{1}{2}\Delta t f(u(t_n)) \right) \\ &= f\left(u(t_n)\right) + \frac{1}{2}\Delta t \left.\frac{df}{dt}\right|_{u(t_n)} + \mathcal{O}\left(\Delta t^2\right) , \end{aligned} \tag{3.42}$$

and obtain a second order accurate u^{n+1}:

$$\begin{aligned} u^{n+1} &= u' + \Delta t\left\{ f(u') - \frac{1}{2}f(u^n) \right\} \\ &= u(t_n) + \frac{1}{2}\Delta t f\left(u\left(t_n\right)\right) \\ &\quad + \Delta t \left\{ f\left(u(t_n)\right) + \frac{1}{2}\Delta t \frac{df}{dt}\bigg|_{u(t_n)} - \frac{1}{2}f\left(u\left(t_n\right)\right) + \mathcal{O}\left(\Delta t^2\right) \right\} \\ &= u(t_n) + \Delta t f\left(u\left(t_n\right)\right) + \frac{1}{2}\Delta t^2 \frac{df}{dt}\bigg|_{u(t_n)} + \mathcal{O}\left(\Delta t^3\right) \\ &\implies u^{n+1} - u^n = \Delta t \frac{du}{dt}\bigg|_{u(t_n)} + \frac{1}{2}\Delta t^2 \frac{d^2u}{dt^2}\bigg|_{u(t_n)} + \mathcal{O}\left(\Delta t^3\right) . \end{aligned} \tag{3.43}$$

The time discretization strategy of system (3.38) is formulated to match the zeroth, first, and second order terms of this RK2 scheme as appropriate so the entire state is second-order accurate in time.

3.4.2.1 Advancing the z equation

For the z equation,

$$\frac{dz}{dt} = \mathcal{M}_1(z)\frac{dz}{dt} + \mathcal{M}_2(z) \tag{3.44}$$

is equivalent to

$$\frac{dz}{dt} = \left\{\mathcal{I} - \mathcal{M}_1(z)\right\}^{-1}\mathcal{M}_2(z) \tag{3.45}$$

assuming $\{\mathcal{I} - \mathcal{M}_1(z)\}$ is nonsingular. However, practically eq. (3.45) cannot be solved in this form. Instead, applying the RK2 discretization to eq. (3.44) gives

$$z' - z^n = \mathcal{M}_1(z^*)\left(z' - z^n\right) + \frac{1}{2}\Delta t \mathcal{M}_2(z^n) \tag{3.46}$$

for the first stage, with z^* representing a potentially intermediate value. This is equivalent to applying the same time derivative approximation on both sides of the equation with the

caveat being the state at which $\mathcal{M}_1$ is evaluated. This equation is solved with a fixed-point iteration, where for iterate i the following is evaluated:

$$z'^{,i} - z^n = \mathcal{M}_1(z^*)\left(z'^{,i-1} - z^n\right) + \frac{1}{2}\Delta t \mathcal{M}_2(z^n)\,. \tag{3.47}$$

This will converge if the spectral radius of $\mathcal{M}_1$ is less than one. This can be seen by rewriting the i^{th} iterate in terms of repeated application of eq. (3.47) to the initial guess, $i = 0$:

$$z'^{,k} - z^n = \mathcal{M}_1^k(z^*)\left(z'^{,0} - z^n\right) + \sum_{j=0}^{k-1} \mathcal{M}_1^j(z^*)\frac{1}{2}\Delta t \mathcal{M}_2(z^n)\,. \tag{3.48}$$

For $\rho(\mathcal{M}_1) < 1$,

$$\{\mathcal{I} - \mathcal{M}_1\}^{-1} = \mathcal{I} + \mathcal{M}_1 + \mathcal{M}_1^2 + \cdots = \sum_{j=0}^{\infty} \mathcal{M}_1^j\,. \tag{3.49}$$

Hence, in the limit of large k the solution to the fixed-point problem approaches a standard RK step applied to eq. (3.45) since

$$\mathcal{M}_1^k(z^*)\left(z'^{,0} - z^n\right) + \sum_{j=0}^{k-1} \mathcal{M}_1^j(z^*)\frac{1}{2}\Delta t \mathcal{M}_2(z^n) \xrightarrow[k\to\infty]{} \frac{1}{2}\Delta t \left\{\mathcal{I} - \mathcal{M}_1\right\}^{-1} \mathcal{M}_2\,. \tag{3.50}$$

Since RK methods are zero stable, linear stability is then governed solely by the eigenvalues of the Jacobian of the right-hand side of the modified problem, eq. (3.45). Practically, a large number of iterations is expensive; however, for an arbitrary initial guess the scheme becomes first order if the iterations are terminated. To avoid this, a backwards differentiation formula- (BDF)-like approximation is used to generate the initial guess. With an appropriate selection of the intermediate stage, z^*, it can then be shown that the desired truncation error is recovered regardless of the number of iterations.

We desire a second-order z and assume $z^n = z(t_n)$. If the BDF-like approximation

producing $z'^{,0}$ is such that

$$z'^{,0} - z^n = \frac{1}{2}\Delta t \frac{dz}{dt}\bigg|_{z(t_n)} + \mathcal{O}\left(\Delta t^3\right) \tag{3.51}$$

and $z^* = z^n$ then

$$\begin{aligned} z'^{,k} - z^n &= \mathcal{M}_1^k(z^n)\left(z'^{,0} - z^n\right) + \frac{1}{2}\Delta t \sum_{j=0}^{k-1} \mathcal{M}_1^j(z^n)\mathcal{M}_2(z^n) \\ &= \frac{1}{2}\Delta t \left[\mathcal{M}_1^k \frac{dz}{dt}\right]_{z(t_n)} + \frac{1}{2}\Delta t \sum_{j=0}^{k-1} \left[\mathcal{M}_1^j \mathcal{M}_2\right]_{z(t_n)} + \mathcal{O}\left(\Delta t^3\right) . \end{aligned} \tag{3.52}$$

Then splitting the sum and factoring $\mathcal{M}_1^{k-1}$ reveals

$$\begin{aligned} &\frac{1}{2}\Delta t \left[\mathcal{M}_1^k \frac{dz}{dt}\right]_{z(t_n)} + \frac{1}{2}\Delta t \sum_{j=0}^{k-1} \left[\mathcal{M}_1^j \mathcal{M}_2\right]_{z(t_n)} \\ &= \frac{1}{2}\Delta t \mathcal{M}_1^{k-1} \left\{ \left[\mathcal{M}_1 \frac{dz}{dt}\right]_{z(t_n)} + \mathcal{M}_2(z(t_n)) \right\} + \frac{1}{2}\Delta t \sum_{j=0}^{k-2} \left[\mathcal{M}_1^j \mathcal{M}_2\right]_{z(t_n)} \\ &= \frac{1}{2}\Delta t \left[\mathcal{M}_1^{k-1} \frac{dz}{dt}\right]_{z(t_n)} + \frac{1}{2}\Delta t \sum_{j=0}^{k-2} \left[\mathcal{M}_1^j \mathcal{M}_2\right]_{z(t_n)} . \end{aligned} \tag{3.53}$$

By recursion it follows that

$$\begin{aligned} z'^{,k} - z^n &= \frac{1}{2}\Delta t \left[\mathcal{M}_1 \frac{dz}{dt}\right]_{z(t_n)} + \frac{1}{2}\Delta t \mathcal{M}_2(z(t_n)) + \mathcal{O}\left(\Delta t^3\right) \\ &= \frac{1}{2}\Delta t \frac{dz}{dt}\bigg|_{z(t_n)} + \mathcal{O}\left(\Delta t^3\right) , \end{aligned} \tag{3.54}$$

which recovers eq. (3.41) up to $\mathcal{O}\left(\Delta t^3\right)$ as required to maintain the desired accuracy of the scheme.

The next step is a bit more involved due to the second order term. Starting with

$$z^{n+1} - z' = \mathcal{M}_1(z^*)\left(z^{n+1} - z'\right) + \Delta t \mathcal{M}_2(z') - \frac{1}{2}\Delta t \mathcal{M}_2(z^n) \tag{3.55}$$

gives the fixed-point iteration

$$z^{n+1,i} - z' = \mathcal{M}_1(z^*)\left(z^{n+1,i-1} - z'\right) + \Delta t \mathcal{M}_2(z') - \frac{1}{2}\Delta t \mathcal{M}_2(z^n)\,. \tag{3.56}$$

To obtain the desired error, $\mathcal{M}_1$ is evaluated at an intermediate stage which satisfies

$$z^* = z(t_n) + \Delta t \left.\frac{dz}{dt}\right|_{z(t_n)} + \mathcal{O}\left(\Delta t^2\right) \tag{3.57}$$

such that

$$\mathcal{M}_1\left(z(t_n) + \Delta t \left.\frac{dz}{dt}\right|_{z(t_n)} + \mathcal{O}\left(\Delta t^2\right)\right) = \mathcal{M}_1(z(t_n)) + \Delta t \left[\frac{d\mathcal{M}_1}{dz}\frac{dz}{dt}\right]_{z(t_n)} + \mathcal{O}\left(\Delta t^2\right)\,. \tag{3.58}$$

Then if the BDF-like approximation produces

$$z^{n+1,0} - z' = \frac{1}{2}\Delta t \left.\frac{dz}{dt}\right|_{z(t_n)} + \frac{1}{2}\Delta t^2 \left.\frac{d^2 z}{dt^2}\right|_{z(t_n)} + \mathcal{O}\left(\Delta t^3\right)\,, \tag{3.59}$$

it follows that, for the first iteration,

$$\begin{aligned} z^{n+1,1} - z' = &\left\{\mathcal{M}_1(z(t_n)) + \Delta t \left[\frac{d\mathcal{M}_1}{dz}\frac{dz}{dt}\right]_{z(t_n)}\right\} \times \left\{\frac{1}{2}\Delta t \left.\frac{dz}{dt}\right|_{z(t_n)} + \frac{1}{2}\Delta t^2 \left.\frac{d^2 z}{dt^2}\right|_{z(t_n)}\right\} \\ &+ \Delta t \mathcal{M}_2(z') - \frac{1}{2}\Delta t \mathcal{M}_2(z^n) + \mathcal{O}\left(\Delta t^3\right)\,. \end{aligned} \tag{3.60}$$

Expanding out the product and further simplification reveals

$$
\begin{aligned}
z^{n+1,1} - z' &= \frac{1}{2}\Delta t \left[\mathcal{M}_1 \frac{dz}{dt}\right]_{z(t_n)} + \frac{1}{2}\Delta t^2 \left[\frac{d\mathcal{M}_1}{dz}\left(\frac{dz}{dt}\right)^2\right]_{z(t_n)} + \frac{1}{2}\Delta t^2 \left[\mathcal{M}_1 \frac{d^2 z}{dt^2}\right]_{z(t_n)} \\
&\quad + \Delta t \left\{\mathcal{M}_2(z(t_n)) + \frac{1}{2}\Delta t \left[\frac{d\mathcal{M}_2}{dz}\frac{dz}{dt}\right]_{z(t_n)}\right\} - \frac{1}{2}\Delta t \mathcal{M}_2(z(t_n)) \\
&\quad + \mathcal{O}\left(\Delta t^3\right) \\
&= \frac{1}{2}\Delta t \left\{\left[\mathcal{M}_1 \frac{dz}{dt}\right]_{z(t_n)} + \mathcal{M}_2(z(t_n))\right\} \\
&\quad + \frac{1}{2}\Delta t^2 \left\{\left[\mathcal{M}_1 \frac{d^2 z}{dt^2}\right]_{z(t_n)} + \left[\frac{d\mathcal{M}_1}{dz}\left(\frac{dz}{dt}\right)^2\right]_{z(t_n)} + \left[\frac{d\mathcal{M}_2}{dz}\frac{dz}{dt}\right]_{z(t_n)}\right\} \\
&\quad + \mathcal{O}\left(\Delta t^3\right) \\
&= \frac{1}{2}\Delta t \frac{dz}{dt}\bigg|_{z(t_n)} + \frac{1}{2}\Delta t^2 \frac{d^2 z}{dt^2}\bigg|_{z(t_n)} + \mathcal{O}\left(\Delta t^3\right) .
\end{aligned}
\tag{3.61}
$$

Combining this and the result of eq. (3.52) gives

$$
z^{n+1,1} = z(t_n) + \Delta t \frac{dz}{dt}\bigg|_{z(t_n)} + \frac{1}{2}\Delta t^2 \frac{d^2 z}{dt^2}\bigg|_{z(t_n)} + \mathcal{O}\left(\Delta t^3\right) \tag{3.62}
$$

which indicates $z^{n+1,1}$ is accurate to $\mathcal{O}\left(\Delta t^3\right)$ as in eq. (3.43). As with the first stage, continuing to iterate will not affect the lower order terms. Hence, for any k

$$
z^{n+1,k} - z^n = \Delta t \frac{dz}{dt}\bigg|_{z(t_n)} + \frac{1}{2}\Delta t^2 \frac{d^2 z}{dt^2}\bigg|_{z(t_n)} + \mathcal{O}\left(\Delta t^3\right) , \tag{3.63}
$$

such that z is second order in time.

To get the correct order at each RK stage, the initial guess for the fixed-point iteration and the intermediate stage, z^*, must be selected appropriately. The coefficients for constructing these approximations from four available evaluations of z are shown below.

3.4.2.2 Coefficients for fixed-point problem

Inspired by BDF methods, we seek an approximation which satisfies eq. (3.51) to initialize the fixed-point iteration eq. (3.47). The condition on z^* is trivial for the first stage. At this stage, $z^n, z^{n-1,\prime}, z^{n-1}, z^{n-2,\prime}$ are available. Let

$$\begin{aligned}\left(z^{\prime,0} - z^n\right) &= \alpha'_1 z^n + \alpha'_2 z^{n-1,\prime} + \alpha'_3 z^{n-1} + \alpha'_4 z^{n-2,\prime} = \frac{1}{2}\Delta t \left.\frac{dz}{dt}\right|_{z(t_n)} + \mathcal{O}\left(\Delta t^3\right) \\ z^{*\prime} &= \beta'_1 z^n + \beta'_2 z^{n-1,\prime} + \beta'_3 z^{n-1} + \beta'_4 z^{n-2,\prime} = z(t_n)\end{aligned} \tag{3.64}$$

then Taylor expansions show

$$\begin{aligned}&\alpha'_1 = 1 \quad \alpha'_2 = -1 \quad \alpha'_3 = 0 \quad \alpha'_4 = 0 \\ &\beta'_1 = 1 \quad \beta'_2 = 0 \qquad \beta'_3 = 0 \quad \beta'_4 = 0\,.\end{aligned} \tag{3.65}$$

For the second stage, $z', z^n, z^{n-1,\prime}, z^{n-1}$ are available and approximations which satisfy eq. (3.59) and eq. (3.57) are required to solve eq. (3.47). Similarly, letting

$$\begin{aligned}\left(z^{n+1,0} - z'\right) &= \alpha_1^{n+1} z' + \alpha_2^{n+1} z^n + \alpha_3^{n+1} z^{n-1,\prime} + \alpha_4^{n+1} z^{n-1} \\ &= \frac{1}{2}\Delta t \left.\frac{dz}{dt}\right|_{z(t_n)} + \frac{1}{2}\Delta t^2 \left.\frac{d^2 z}{dt^2}\right|_{z(t_n)} + \mathcal{O}\left(\Delta t^3\right) \\ z^{*n+1} &= \beta_1^{n+1} z' + \beta_2^{n+1} z^n + \beta_3^{n+1} z^{n-1,\prime} + \beta_4^{n+1} z^{n-1} \\ &= z(t_n) + \Delta t \left.\frac{dz}{dt}\right|_{z(t_n)} + \mathcal{O}\left(\Delta t^2\right)\end{aligned} \tag{3.66}$$

and expanding gives

$$\begin{aligned}&\alpha_1^{n+1} = 3 \quad \alpha_2^{n+1} = -4 \quad \alpha_3^{n+1} = 0 \quad \alpha_4^{n+1} = 1 \\ &\beta_1^{n+1} = 2 \quad \beta_2^{n+1} = -1 \quad \beta_3^{n+1} = 0 \quad \beta_4^{n+1} = 0\,.\end{aligned} \tag{3.67}$$

3.4.2.3 Advancing r and obtaining a consistent m^c

The r equation in system (3.38),

$$\frac{dr}{dt} = \mathcal{M}_3\left(r, m^c\right) , \tag{3.68}$$

is time discretized by the RK2 method (eq. (3.39)). The solution for r will be second order if evaluations of $dr/dt = \mathcal{M}_3\left(r, m^c\right)$ match eqs. (3.40) and (3.42) up to $\mathcal{O}\left(\Delta t^2\right)$. If so, the intermediate r' and final r^{n+1} will match eqs. (3.41) and (3.43) up to $\mathcal{O}\left(\Delta t^3\right)$, obtaining the desired accuracy. If m^c was obtained from time advancing an ODE $dm^c/dt = h(m^c)$ by the RK2 scheme, this would be trivially satisfied as eq. (3.39) extends to systems of ODEs. However, m^c is not time advanced but rather reconstructed from $d\rho/dt$. This means the approximations $d\rho/dt'$ and $d\rho/dt^{n+1}$ need only produce $m^{c,'} = \mathcal{G}^{-1}d\rho/dt'$ and $m^{c,n+1} = \mathcal{G}^{-1}d\rho/dt^{n+1}$ which are consistent with eqs. (3.41) and (3.43) up to $\mathcal{O}\left(\Delta t^2\right)$ so they provide the required approximations of dr/dt. The local error is the relevant error for the accuracy of m^c because the curl-free momentum is obtained at each substep via the continuity constraint rather than marched in time.

Differentiating the equation of state with respect to time gives

$$\frac{d\rho}{dt} = \frac{df}{dz}\frac{dz}{dt} . \tag{3.69}$$

In the context of the model problem above, let

$$\mathcal{M}_4(z)\left\{\cdot\right\} = \mathcal{G}^{-1}\frac{df}{dz}\left\{\cdot\right\} \tag{3.70}$$

so that

$$m^c = \mathcal{M}_4(z)\frac{dz}{dt} . \tag{3.71}$$

Now, requiring $m^{c,'}$ matches eq. (3.41) up to $\mathcal{O}\left(\Delta t^2\right)$ means

$$\begin{aligned} m^{c,'} &= m^c(t_n) + \frac{1}{2}\Delta t \frac{dm^c}{dt}\bigg|_{t_n} + \mathcal{O}\left(\Delta t^2\right) \\ &= \left[\mathcal{M}_4 \frac{dz}{dt}\right]_{z(t_n)} + \frac{1}{2}\Delta t \left\{ \left[\mathcal{M}_4 \frac{d^2z}{dt^2}\right]_{z(t_n)} + \left[\frac{d\mathcal{M}_4}{dz}\left(\frac{dz}{dt}\right)^2\right]_{z(t_n)} \right\} \\ &\quad + \mathcal{O}\left(\Delta t^2\right) . \end{aligned} \tag{3.72}$$

An approximation for $\dfrac{dz}{dt}$ at $t_{n+1/2}$ which satisfies

$$\frac{dz'}{dt} = \frac{dz}{dt}\bigg|_{z(t_n)} + \frac{1}{2}\Delta t \frac{d^2z}{dt^2}\bigg|_{z(t_n)} + \mathcal{O}\left(\Delta t^2\right) \tag{3.73}$$

will produce

$$\begin{aligned} \mathcal{M}_4\left(z'\right)\frac{dz'}{dt} &= \mathcal{M}_4\left(z(t_n) + \frac{1}{2}\Delta t \frac{dz}{dt}\bigg|_{z(t_n)} + \mathcal{O}\left(\Delta t^2\right)\right) \times \\ &\quad \left\{ \frac{dz}{dt}\bigg|_{z(t_n)} + \frac{1}{2}\Delta t \frac{d^2z}{dt^2}\bigg|_{z(t_n)} + \mathcal{O}\left(\Delta t^2\right) \right\} \\ &= \left\{ \mathcal{M}_4(z(t_n)) + \frac{1}{2}\Delta t \left[\frac{d\mathcal{M}_4}{dz}\frac{dz}{dt}\right]_{z(t_n)} + \mathcal{O}\left(\Delta t^2\right) \right\} \times \\ &\quad \left\{ \frac{dz}{dt}\bigg|_{z(t_n)} + \frac{1}{2}\Delta t \frac{d^2z}{dt^2}\bigg|_{z(t_n)} + \mathcal{O}\left(\Delta t^2\right) \right\} \\ &= \left[\mathcal{M}_4 \frac{dz}{dt}\right]_{z(t_n)} + \frac{1}{2}\Delta t \left\{ \left[\mathcal{M}_4 \frac{d^2z}{dt^2}\right]_{z(t_n)} + \left[\frac{d\mathcal{M}_4}{dz}\left(\frac{dz}{dt}\right)^2\right]_{z(t_n)} \right\} \\ &\quad + \mathcal{O}\left(\Delta t^2\right) \end{aligned} \tag{3.74}$$

which is what is needed. Similarly, the second stage requires

$$\begin{aligned} m^{c,n+1} &= m^c(t_n) + \Delta t \frac{dm^c}{dt}\bigg|_{t_n} + \mathcal{O}\left(\Delta t^2\right) \\ &= \left[\mathcal{M}_4 \frac{dz}{dt}\right]_{z(t_n)} + \Delta t \left\{ \left[\mathcal{M}_4 \frac{d^2 z}{dt^2}\right]_{z(t_n)} + \left[\frac{d\mathcal{M}_4}{dz}\left(\frac{dz}{dt}\right)^2\right]_{z(t_n)} \right\} + \mathcal{O}\left(\Delta t^2\right) . \end{aligned} \tag{3.75}$$

Therefore, if

$$\frac{dz}{dt}^{n+1} = \frac{dz}{dt}\bigg|_{z(t_n)} + \Delta t \frac{d^2 z}{dt^2}\bigg|_{z(t_n)} + \mathcal{O}\left(\Delta t^2\right) \tag{3.76}$$

then

$$\begin{aligned} \mathcal{M}_4\left(z^{n+1}\right)\frac{dz}{dt}^{n+1} &= \mathcal{M}_4\left(z + \Delta t \frac{dz}{dt}\bigg|_{z(t_n)} + \frac{1}{2}\Delta t^2 \frac{d^2 z}{dt^2}\bigg|_{z(t_n)} + \mathcal{O}\left(\Delta t^3\right)\right) \times \\ &\quad \left\{ \frac{dz}{dt}\bigg|_{z(t_n)} + \Delta t \frac{d^2 z}{dt^2}\bigg|_{z(t_n)} + \mathcal{O}\left(\Delta t^2\right) \right\} \\ &= \left\{ \mathcal{M}_4(z(t_n)) + \Delta t \left[\frac{d\mathcal{M}_4}{dz}\frac{dz}{dt}\right]_{z(t_n)} + \mathcal{O}\left(\Delta t^2\right) \right\} \times \\ &\quad \left\{ \frac{dz}{dt}\bigg|_{z(t_n)} + \Delta t \frac{d^2 z}{dt^2}\bigg|_{z(t_n)} + \mathcal{O}\left(\Delta t^2\right) \right\} \\ &= \left[\mathcal{M}_4 \frac{dz}{dt}\right]_{z(t_n)} + \Delta t \left\{ \left[\mathcal{M}_4 \frac{d^2 z}{dt^2}\right]_{z(t_n)} + \left[\frac{d\mathcal{M}_4}{dz}\left(\frac{dz}{dt}^n\right)^2\right]_{z(t_n)} \right\} \\ &\quad + \mathcal{O}\left(\Delta t^2\right) . \end{aligned} \tag{3.77}$$

This also implies m^c itself is second order accurate.

For both stages, a specially constructed intermediate z^* is not needed when evaluating $\mathcal{M}_4$, the current stage is sufficient. The coefficients for constructing these approximations from the four available evaluations of z are shown below.

3.4.2.4 Coefficients for final m^c reconstruction

To form $\dfrac{dz'}{dt}$, $z', z^n, z^{n-1,'}, z^{n-1}$ are available. Then requiring

$$\Delta t \frac{dz'}{dt} = \gamma_1' z' + \gamma_2' z^n + \gamma_3' z^{n-1,'} + \gamma_4' z^{n-1} = \Delta t \frac{dz}{dt}\bigg|_{z(t_n)} + \frac{1}{2}\Delta t^2 \frac{d^2 z}{dt^2}\bigg|_{z(t_n)} + \mathcal{O}\left(\Delta t^3\right) \tag{3.78}$$

gives

$$\gamma_1' = 4 \qquad \gamma_2' = -5 \qquad \gamma_3' = 0 \qquad \gamma_4' = 1\,. \tag{3.79}$$

To form $\dfrac{dz}{dt}^{n+1}$, $z^{n+1}, z', z^n, z^{n-1,'}$ are available. Then requiring

$$\Delta t \frac{dz}{dt}^{n+1} = \gamma_1^{n+1} z^{n+1} + \gamma_2^{n+1} z' + \gamma_3^{n+1} z^n + \gamma_4^{n+1} z^{n-1,'} = \Delta t \frac{dz}{dt}\bigg|_{z(t_n)} + \Delta t^2 \frac{d^2 z}{dt^2}\bigg|_{z(t_n)} + \mathcal{O}\left(\Delta t^3\right) \tag{3.80}$$

gives

$$\gamma_1^{n+1} = 2 \qquad \gamma_2^{n+1} = -2 \qquad \gamma_3^{n+1} = 0 \qquad \gamma_4^{n+1} = 0\,. \tag{3.81}$$

3.4.2.5 Initial timestep

Without the appropriate time history of z at the initial timestep it is assumed the right-hand side of eq. (3.44) can be evaluated directly (this is certainly the case in the underlying low-Mach-number system) to obtain $z'^{,0}$ for the fixed-point iteration. Then

$$\frac{z'^{,0} - z^0}{\Delta t} = \frac{dz}{dt}\bigg|_{z(t_0)} \tag{3.82}$$

is taken and the iterative method proceeds normally. To obtain $z^{1,0}$ for the second stage fixed-point problem, a first-order approximation is used:

$$\frac{z^{1,0} - z'}{\Delta t} = \frac{2}{\Delta t}\left(z' - z^0\right) . \tag{3.83}$$

For the final m^c reconstruction for the initial timestep, only the first stage needs modification. Again, a first-order approximation is used:

$$\Delta t \frac{dz'}{dt} = 2\left(z' - z^0\right) . \tag{3.84}$$

3.4.3 Temporal convergence tests

To verify the order of accuracy of the temporal scheme detailed in section 3.4, numerical solutions of system (3.38) are sought with

$$\begin{gathered} \mathcal{M}_1(z) = c_1\left(1 + \sin(z)\right) , \quad \mathcal{M}_2(z) = c_2 \exp(z) , \quad \mathcal{M}_3(r, m^c) = c_3 r m_c^3 , \\ \mathcal{G}(m^c) = c_4 m^c , \quad f(z) = z , \end{gathered} \tag{3.85}$$

where $c_1 = .6\text{i}$, $c_2 = -1$, $c_3 = 2 - .8\text{i}$, $c_4 = -3 + .5\text{i}$, and $z_0 = r_0 = .5$. A reference solution is obtained by integrating with a fine $\Delta t = 1 \times 10^{-9}$, an order of magnitude lower than the final case shown here. Additionally, instead of approximating $d\rho/dt$ as shown in section 3.4.2.2, it is obtained directly by evaluating

$$\frac{d\rho}{dt} = \frac{d\rho}{dz}\frac{\mathcal{M}_2}{1 - \mathcal{M}_1} \tag{3.86}$$

and the z equation is solved in the modified form

$$\frac{dz}{dt} = \frac{\mathcal{M}_2}{1 - \mathcal{M}_1} \tag{3.87}$$

for the reference solution. Hence, the momentum reconstruction can be checked for consistency and the reference z is obtained without employing the iterative scheme. Equation (3.86) is also used to obtain m_0^c to ensure consistency of the initial condition for all solutions.

Figure 3.1 shows the convergence rate of z and r of the test problem for both double and extended (long double) precision by comparing the solution at $t = .1$ to the reference solution. Four iterations are used to solve the z equation at each substep. Some noise in the error is expected close to machine precision; however, the behavior seen for small Δt needs further explanation. Round-off errors in z are amplified during the estimation of dz/dt from the time history of z. A linear combination of the four previous evaluations is scaled by $1/\Delta t$ (e.g. eq. (3.78)). These errors feed into m^c through the mass conservation equation and, in turn, can start to degrade the apparent convergence rate of r or they feed into z during the iterative solve. This is inevitable and is of no practical concern. The error in extended precision calculations continues to decay at a second-order rate (fig. 3.1), which demonstrates the behavior of the double precision result is solely a consequence of round-off error. Hence, the approximation of m^c is confirmed to be consistent with the standard RK2 scheme and the convergence of the entire state is second order.

3.4.4 Linear stability analysis

To assess the stability of this algorithm, consider a linearized system modeling the characteristics of the z equation in system (3.38)

$$\frac{dz}{dt} = h\left(z, \frac{dz}{dt}\right) = \lambda_1 \frac{dz}{dt} + \lambda_2 z \tag{3.88}$$

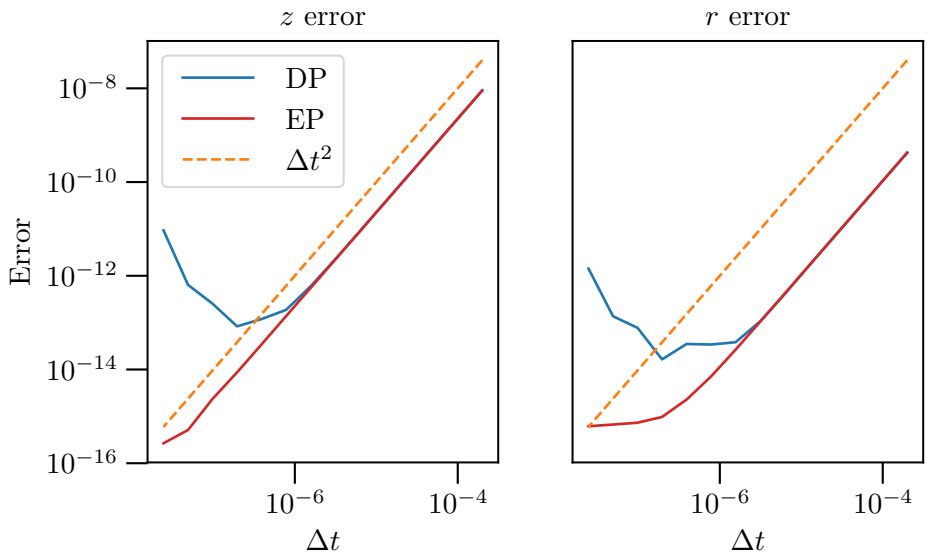

Figure 3.1: Temporal convergence of the iterative scheme. z (left), r (right). Solution error at $t = .1$ defined against the reference case. Shown for both double precision (DP) and extended precision (EP).

where λ_1,$\lambda_2 \in \mathbb{C}$. Additionally, define

$$\lambda^* = \frac{\lambda_2}{1 - \lambda_1} \tag{3.89}$$

so that

$$\frac{dz}{dt} = \lambda^* z \tag{3.90}$$

is the underlying modified ODE (assuming $\lambda_1 \neq 1$). In this context, setting $\lambda_2 = 0$ in eq. (3.88) gives the appropriate test problem for zero stability.

Applying the temporal scheme with k fixed-point iterations to eq. (3.88) gives

$$\begin{aligned} z'^{,k} - z^n &= \lambda_1^k \left(z^n - z^{n-1,'} \right) + \frac{1}{2}\Delta t \sum_{j=0}^{k-1} \lambda_1^j \lambda_2 z^n \\ z^{n+1,k} - z' &= \lambda_1^k \left(3z' - 4z^n + z^{n-1} \right) + \Delta t \sum_{j=0}^{k-1} \lambda_1^j \lambda_2 \left(z' - \frac{1}{2} z^n \right) . \end{aligned} \tag{3.91}$$

Taking inspiration from linear differential equation analysis [70], this can be written as

$$\begin{aligned} \boldsymbol{z}' &= \boldsymbol{A}'\boldsymbol{z}^n \\ \boldsymbol{z}^{n+1} &= \boldsymbol{A}^{n+1}\boldsymbol{z}' \\ \implies \boldsymbol{z}^{n+1} &= \boldsymbol{A}^{n+1}\boldsymbol{A}'\boldsymbol{z}^n = \boldsymbol{A}\boldsymbol{z}^n \end{aligned} \tag{3.92}$$

where

$$\begin{aligned} \boldsymbol{z}^n &= \begin{bmatrix} z^n & z^{n-1,'} & z^{n-1} & z^{n-2,'} \end{bmatrix}^T \\ \boldsymbol{z}' &= \begin{bmatrix} z' & z^n & z^{n-1,'} & z^{n-1} \end{bmatrix}^T . \end{aligned} \tag{3.93}$$

Let $S = \sum_{j=0}^{k-1} \lambda_1^j \lambda_2$. Then

$$\boldsymbol{A}' = \begin{bmatrix} 1 + \lambda_1^k + \frac{1}{2}\Delta t S & -\lambda_1^k & 0 & 0 \\ 0 & 1 & 0 & 0 \\ 0 & 0 & 1 & 0 \\ 0 & 0 & 0 & 1 \end{bmatrix} \tag{3.94}$$

$$\boldsymbol{A}^{n+1} = \begin{bmatrix} 1 + 3\lambda_1^k + \Delta t S & -4\lambda_1^k - \frac{1}{2}\Delta t S & 0 & \lambda_1^k \\ 0 & 1 & 0 & 0 \\ 0 & 0 & 1 & 0 \\ 0 & 0 & 0 & 1 \end{bmatrix} . \tag{3.95}$$

Then for $\rho(\boldsymbol{A}) < 1$, the scheme is linearly stable. Unlike traditional explicit Runge-Kutta methods applied to ODEs of the form $dz/dt = f(z)$ (like eq. (3.89)), the scheme is not zero stable. The zero stability is instead like that of a linear multistep method due to the parasitic modes introduced by the data required to obtain the initial guesses $z^{',0}$ and $z^{n+1,0}$. In this case, λ_1 has a direct impact on zero stability. As shown in fig. 3.2, the size of the zero stability regions grows with the number of iterations. When fully converged, the zero

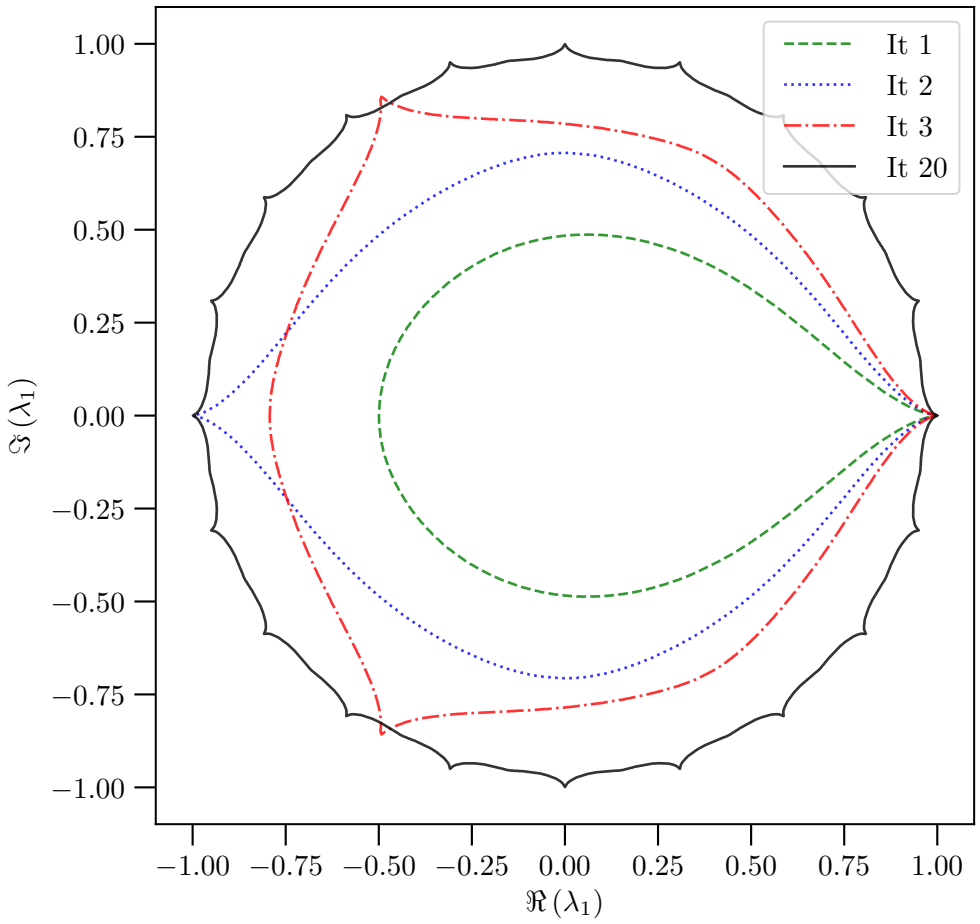

Figure 3.2: Zero stability of the iterative scheme for the first few k iterations. Iteration 20 shows a nearly converged region.

stability region is a circle of radius 1, which is consistent with the scheme diverging for $\rho(\mathcal{M}_1) \geq 1$ and recovering the stability of the RK2 scheme otherwise.

The absolutely stability region is defined in terms of the "true" eigenvalue, λ^*, and is plotted for different values of λ_1 which are growing in magnitude, see fig. 3.3. As expected, when fully converged the absolute stability region coincides with the standard RK2 result. For small $\|\lambda_1\|$ this convergence happens quickly so that only two to three iterations would be required to get a stability region that approaches that of RK2. As the eigenvalue magnitude approaches one, as in fig. 3.3.d, the stability region does not approximate that of RK2

even after twenty iterations. Figure 3.4 shows the effect of the phase of λ_1 on the stability region. In particular, there is a symmetry about the imaginary axis when $\mathbb{I}[\lambda_1]$ changes sign. Additionally, a 180° phase change can produce dramatic changes in stability as the eigenvalues which have large imaginary parts tend to exhibit much more erratic behavior. One thus needs an estimate for the spectral radius of $\mathcal{M}_1$ to determine an appropriate number of iterations *a priori*.

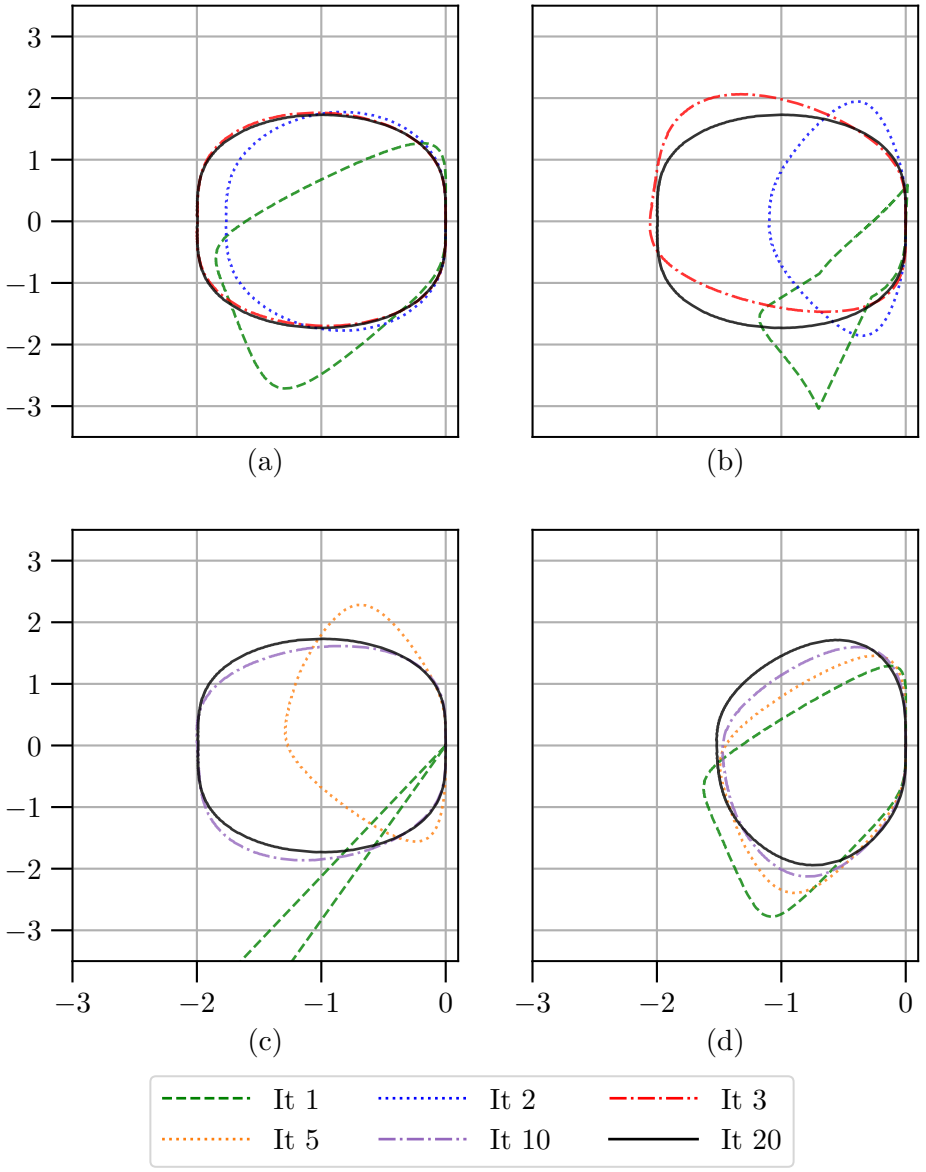

Figure 3.3: Absolute stability as a function of the number of iterations for varying λ_1. *Top left*: $\lambda_1 = 2\mathrm{i}$, *top right*: $\lambda_1 = -.02 + .42\mathrm{i}$, *lower left*: $\lambda_1 = .5 + .5\mathrm{i}$, *lower right*: $\lambda_1 = .7 + .25\mathrm{i}$.

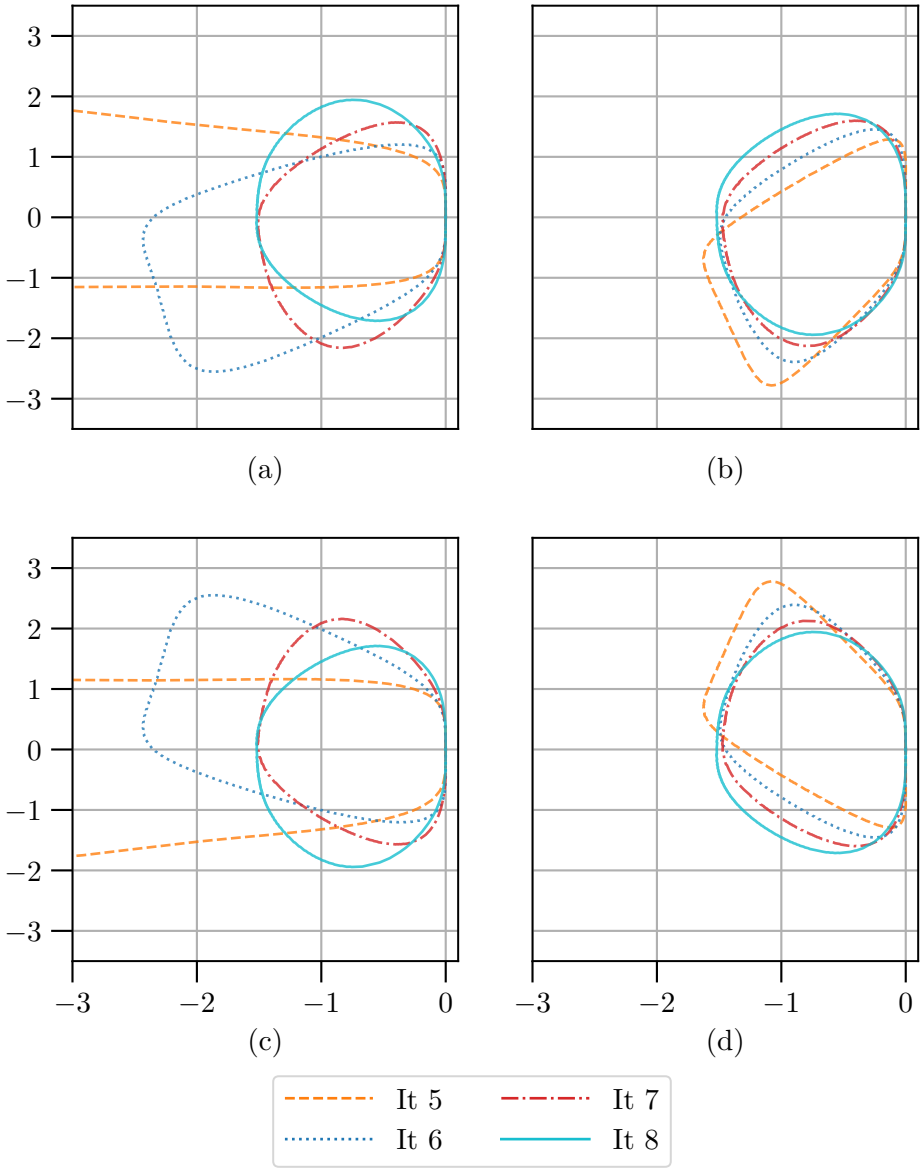

Figure 3.4: Absolute stability as a function of the number of iterations of the for λ_1 of equal magnitude but different phase. *Top left*: $\lambda_1 = .25 + .7\text{i}$, *top right*: $\lambda_1 = .7 + .25\text{i}$, *lower left*: $\lambda_1 = .25 - .7\text{i}$, *lower right*: $\lambda_1 = .7 - .25\text{i}$.

3.5 Low-Mach-number Navier-Stokes algorithm

This section details the time advance of the spatially discrete equations (section 3.3.2) with the temporal scheme established in section 3.4. Given the decomposition presented in section 3.2, the overall algorithm can be broken into two main stages:

1. a reconstruction of the momentum from its Laplacian and curl ($\boldsymbol{\phi}$ and $\boldsymbol{\Omega}$, respectively) and the mass conservation equation.

2. A time advance of the momentum equations and the conserved scalar equation.

Throughout the calculation, operations are performed on the data in either 'wavespace', when it is ordered by wavenumber pair and the values of the Fourier coefficients on the B-spline collocation grid are stored, or in 'realspace', when it is evaluated on a physical grid via discrete Fourier transforms. Time advancement and linear algebra (including differentiation) is performed in wavespace, and nonlinear operators are computed in realspace to avoid costly convolution sums.

A natural parallel decomposition is the so-called 'pencil' decomposition. In wavespace, operations are performed wavenumber pair by wavenumber pair on lines of data in the x_2 direction. Transforming to realspace requires two sets of a global transpose followed by a discrete Fourier transform. Transforming back to wavespace essentially reverses this process. For many more details on the parallel decomposition see Lee *et al.* [71] who developed the decomposition for a DNS of incompressible channel flow. It served as a basis for this work which also uses Lee's custom linear algebra package. The Fourier transform and associated data transpose were shown to account for most of the cost of a timestep; therefore, the following algorithm was designed to minimize the total number of these operations. Additional design constraints arise from a desire to avoid representing second derivatives in diffusion

terms as a repeated application of the first derivative operator in the inhomogeneous direction as this can lead to an underrepresentation of the physical dissipation as well as stability issues[1]. Hence, the divergence of the stress tensor, $F_i^\tau = \partial\tau_{ij}/\partial x_j$, needed to advance the momentum equations, and the molecular diffusion term in the z equation are expanded by the chain rule and must be assembled from products of the flow variables and their derivatives. The number of fields required for this step sets the minimum memory requirements, so the algorithm is designed to make this requirement as low as possible. See procedure 2 and eq. (3.99) for details of the assembly of these quantities.

3.5.1 Momentum reconstruction

For the continuous DNS equations described in section 3.2 the minimum state has dimension three and is taken to be $\boldsymbol{\mathcal{S}} = (\phi_2, \Omega_2, z, \overline{m}_1^{x_1x_3}, \overline{m}_3^{x_1x_3})$. Note that $\overline{\phi}_2^{x_1x_3} = \overline{\Omega}_2^{x_1x_3} = 0$, so the state only requires storage for three full 3-D fields. For the purposes of the discrete problem, approximating $\partial z/\partial t$ for the fixed-point problem and curl-free momentum reconstruction requires that three previous evaluations of z are available. The computational algorithm begins each stage with this minimal state in wavespace.

In advancing from stage $s \to s+1$, the first step is to reconstruct the momentum. To do so, the following steps are required:

1. construct $\partial\rho/\partial t$ and obtain $\boldsymbol{m}^c$ (note again $\overline{m}_2^{x_1x_3} = \overline{m^c}_2^{x_1x_3}$);

2. solve the Poisson problem to obtain m_2^d from ϕ_2 and enforce the divergence-free condition to obtain $\boldsymbol{m}^d$.

[1] See, for example, the modified wavenumber analysis of Kwok *et al.* [63] which demonstrates the damping of the highest wavenumbers by numerical first differentiation

3.5.1.1 Obtaining the curl-free momentum and $\overline{m}_2^{x_1 x_3}$

Firstly, $\partial\rho/\partial t$ must be formed. As discussed in section 3.4.2.3, $\partial z/\partial t$ is approximated from a time history of z in wavespace. For optimization purposes, derivatives of the scalar variable (i.e. ∇z and $\nabla^2 z$) needed for the z equation are computed and moved to realspace. Procedure 1 details the formation of the density derivative along with the evaluation of the thermodynamic state and preparation for future computations.

Procedure 1 Evaluating the density derivative and preparing for z solve

---

1: Starting in wavespace, form fields needed for $\dfrac{\partial \rho}{\partial t}$ from time history of z (section 3.4.2.4):

$\underbrace{\dfrac{\partial z}{\partial t}}_{\text{1 field}}$

2: Form fields needed for $\mathcal{R}_z$:

$\underbrace{\nabla z}_{\text{3 fields}}$ $\underbrace{\nabla^2 z}_{\text{1 field}}$

3: Fourier transform 6 fields Wave $\rightarrow$ Real

$\dfrac{\partial z}{\partial t}$, z, ∇z, $\nabla^2 z$

4: Evaluate thermodynamic and transport properties from known functions of z:

$\underbrace{\rho}_{\text{2 copies}}$ $\underbrace{\rho^{-1}}_{\text{To stay in realspace}}$ $\underbrace{\rho\mathcal{D}_z}_{\text{2 copies}}$ $\underbrace{\mu}_{\text{2 copies}}$ $\underbrace{\dfrac{\partial f}{\partial z}}_{\text{Needed in next step}}$

5: Form nonlinear product:

$\underbrace{\dfrac{\partial f}{\partial z}\dfrac{\partial z}{\partial t}}_{\text{1 field}} = \dfrac{\partial \rho}{\partial t}$

6: Fourier transform 4 fields Real $\rightarrow$ Wave

ρ, $\rho\mathcal{D}_z$, μ, $\dfrac{\partial \rho}{\partial t}$

Leave a copy of ρ, $\rho\mathcal{D}_z$, μ; leave z derivatives; leave ρ^{-1} in realspace.

Then a coupled system composed of the mass conservation equation and the curl-free

constraint, eqs. (3.22) and (3.23), is solved for the fluctuating modes of $\boldsymbol{m}^c$ if $k_3 \neq 0$ (when $k_3 = 0$, eqs. (3.22) and (3.24) are solved instead). The x_2 component of the plane-averaged momentum is determined by solving

$$\begin{cases} \boldsymbol{B}^0_{0,0}\boldsymbol{c}^{\overline{\partial\rho/\partial t}^{x_1x_3}} & = -\boldsymbol{B}^1_{0,1}\boldsymbol{c}^{\overline{m}_2^{x_1x_3}} \\ \texttt{BC:} \qquad c_{N_2}^{\overline{m}_2^{x_1x_3}} & = 0 \end{cases} . \tag{3.96}$$

In this case, the homogeneous Dirichlet boundary condition does not replace one of the collocation equations but rather is needed for well-posedness since m_2 carries an additional degree of freedom. The solution is then offset to obey boundary conditions, if appropriate. Since $\overline{m}_1^{x_1x_3}$ and $\overline{m}_3^{x_1x_3}$ are already known, the plane-averaged momentum reconstruction is now complete.

3.5.1.2 The Poisson problem for m_2^d

To reconstruct m_2^d the Poisson problem $\nabla^2 m_2^d = \phi_2$ is solved. In terms of the discretization scheme, this is

$$\boldsymbol{B}^0_{1,0}\boldsymbol{c}^{\widehat{\phi}_2} = -k^2\boldsymbol{B}^0_{1,1}\boldsymbol{c}^{\widehat{m_2^d}} + \boldsymbol{B}^2_{1,1}\boldsymbol{c}^{\widehat{m_2^d}} \tag{3.97}$$

where $k = \sqrt{k_1^2 + k_3^2}$. Once m_2^d is known, the divergence-free condition and the definition of Ω_2 are invoked to solve for m_1^d and m_3^d:

$$\begin{aligned} \boldsymbol{B}^0_{0,0}\boldsymbol{c}^{\widehat{m_1^d}} &= \frac{1}{k^2}\left(\mathrm{i}k_1\boldsymbol{B}^1_{0,1}\boldsymbol{c}^{\widehat{m_2^d}} - \mathrm{i}k_3\boldsymbol{B}^0_{0,0}\boldsymbol{c}^{\widehat{\Omega}_2}\right) \\ \boldsymbol{B}^0_{0,0}\boldsymbol{c}^{\widehat{m_3^d}} &= \frac{1}{k^2}\left(\mathrm{i}k_3\boldsymbol{B}^1_{0,1}\boldsymbol{c}^{\widehat{m_2^d}} + \mathrm{i}k_1\boldsymbol{B}^0_{0,0}\boldsymbol{c}^{\widehat{\Omega}_2}\right) . \end{aligned} \tag{3.98}$$

This completely determines the momentum.

3.5.2 Advancing the evolution equations

With the momentum known, next is advancing the Ω_2, ϕ_2, $\overline{m}_1^{x_1 x_3}$, $\overline{m}_3^{x_1 x_3}$, and z equations. To minimize the total number of fields needed when forming the residual for the transformed momentum equations (Ω_2 and ϕ_2), the velocity is required in wavespace. For the matrix-free iterative solve of the z equation, the velocity from the divergence-free momentum is needed for $\mathcal{R}_z$. The curl-free momentum is readily available after solving eqs. (3.22) to (3.24) and is used along with the three components of the total momentum and the density to obtain these fields. The following step involves mapping derivatives of the flow variables to realspace and returning with the nonlinear terms for the ϕ_2, Ω_2, $\overline{m}_1^{x_1 x_3}$, $\overline{m}_2^{x_1 x_3}$, and z equations. This is outlined in procedure 2. In procedure 2, the divergence of the stress tensor is constructed as follows:

$$\begin{aligned}
\nabla \cdot \boldsymbol{u} &= \left(\nabla \boldsymbol{u} + \nabla \boldsymbol{u}^T\right)_{11} + \left(\nabla \boldsymbol{u} + \nabla \boldsymbol{u}^T\right)_{22} + \left(\nabla \boldsymbol{u} + \nabla \boldsymbol{u}^T\right)_{33} \\
F_i^{\tau} &= 2\left(\nabla \boldsymbol{u} + \nabla \boldsymbol{u}^T\right)_{i1} \frac{\partial \mu}{\partial x_1} + 2\left(\nabla \boldsymbol{u} + \nabla \boldsymbol{u}^T\right)_{i2} \frac{\partial \mu}{\partial x_2} + 2\left(\nabla \boldsymbol{u} + \nabla \boldsymbol{u}^T\right)_{i3} \frac{\partial \mu}{\partial x_3} \\
&\quad + \mu\left(\nabla^2 \boldsymbol{u} + 1/3\, \nabla(\nabla \cdot \boldsymbol{u})\right)_i - \frac{2}{3}\left(\nabla \cdot \boldsymbol{u}\right) \frac{\partial \mu}{\partial x_i}
\end{aligned} \tag{3.99}$$

and eqs. (3.16) and (3.17) indicate only five independent combinations of C_{ij} are required,

$$(C_{11} - C_{22}) \quad (C_{33} - C_{22}) \quad C_{12} \quad C_{13} \quad C_{23}\,, \tag{3.100}$$

so one fewer field is carried.

Appropriate derivatives are applied to $\widehat{F^{\tau}}_i$ and $\widehat{C}_{ij}$ to form their contributions to the momentum equations (eqs. (3.16) to (3.18)), which are then advanced as in eq. (3.39). Then the iterative scheme is applied to advance z as demonstrated in procedure 3. This shows how $\mathcal{L}$ is applied practically, in stages. At this point, a RK substep is considered completed. Throughout the computation, current and old evaluations of the right-hand side

Procedure 2 Computing the nonlinear terms for ϕ_2, Ω_2, $\overline{m}_1^{x_1x_3}$, $\overline{m}_2^{x_1x_3}$, $\mathcal{R}_z$ residuals

1: Starting in wavespace, form fields needed for $\boldsymbol{u}$ and $\boldsymbol{m}^d/\rho$:

$$\underbrace{\boldsymbol{m}}_{\text{3 fields}} \quad \underbrace{\boldsymbol{m}^c}_{\text{3 fields}} \quad \underbrace{\rho^{-1}}_{\text{Already in realspace}}$$

2: Fourier transform 6 fields Wave $\rightarrow$ Real
As listed above in step 1

3: Form nonlinear products

$$\underbrace{\boldsymbol{u}}_{\text{3 fields, 2 copies}} \quad \underbrace{\boldsymbol{m}^d/\rho}_{\text{To stay in realspace}}$$

4: Fourier transform 3 fields Real $\rightarrow$ Wave
Leave a copy of $\boldsymbol{u}$; leave $\boldsymbol{m}^d/\rho$ in realspace.

5: Form fields needed for $\nabla \cdot \boldsymbol{\tau}$:

$$\underbrace{\left(\nabla \boldsymbol{u} + \nabla \boldsymbol{u}^T\right)}_{\text{6 fields}} \quad \underbrace{\nabla \mu}_{\text{3 fields}} \quad \underbrace{\mu}_{\text{Already in realspace}} \quad \underbrace{\nabla^2 \boldsymbol{u} + 1/3\, \nabla(\nabla \cdot \boldsymbol{u})}_{\text{3 fields}} \quad \underbrace{\nabla \cdot \boldsymbol{u}}_{\text{Can be formed from}(\nabla \boldsymbol{u} + \nabla \boldsymbol{u}^T)}$$

6: Fields needed for C_{ij}:

$$\underbrace{\rho}_{\text{Already in realspace}} \quad \underbrace{\boldsymbol{u}}_{\text{Already in realspace}}$$

7: Form fields needed for $\mathcal{R}_z$ equation (if necessary):

$$\underbrace{\nabla z}_{\text{Already in realspace}} \quad \underbrace{\nabla^2 z}_{\text{Already in realspace}} \quad \underbrace{\nabla \rho \mathcal{D}_z}_{\text{3 fields}} \quad \underbrace{\boldsymbol{m}^d/\rho}_{\text{Already in realspace}} \quad \underbrace{\rho^{-1}}_{\text{Already in realspace}}$$

8: Fourier transform 15 fields Wave $\rightarrow$ Real
As listed above in steps 5 and 7

9: Form nonlinear products:

$$\underbrace{\nabla \cdot \boldsymbol{\tau}}_{\text{3 fields}} \quad \underbrace{C_{ij}}_{\text{5 fields}} \quad \underbrace{-\frac{1}{\rho}\boldsymbol{m}^d \cdot \nabla z + \frac{1}{\rho}\nabla \rho \mathcal{D}_z \cdot \nabla z + \mathcal{D}_z \nabla^2 z}_{\text{1 field}}$$

10: Fourier transform 9 fields Real $\rightarrow$ Wave
Nonlinear products listed in step 9

and the scalar fields are stored and reused per section 3.4. Although this formulation has formally eliminated the pressure, it can be computed consistently during runtime or as a post-processing step. See Appendix E for details.

Procedure 3 Advancing z with the iterative scheme

1: $i = 0$

2: Form initial guess $\partial z/\partial t^0 = (z^{s,0} - z^{s-1})/\Delta t$ and z^* from z history (section 3.4.2.2). Form fields for the application of $\mathcal{L}(z^*)$:

$$\underbrace{\frac{\partial z}{\partial t}^0}_{\text{BDF-like approx.}} \qquad \underbrace{z^*}_{\text{BDF-like approx.}} \qquad \underbrace{\nabla z^*}_{\text{To stay in realspace}}$$

3: **while** $i < i_{iters}$ **do**

4: Fourier transform 1 field, $\partial z/\partial t^i$ Wave $\rightarrow$ Real

5: **if** $i = 0$ **then**

6: Fourier transform 4 fields, z^* ∇z^* Wave $\rightarrow$ Real

7: Evaluate and store fields for the application of $\mathcal{L}(z^*)$:

$$\underbrace{\rho(z^*)^{-1}}_{\text{To stay in realspace}} \qquad \underbrace{\frac{\partial f}{\partial z}(z^*)}_{\text{To stay in realspace}}$$

8: **end if**

9: Form nonlinear product, $\partial f/\partial z \, \partial z/\partial t^i$

10: Fourier transform 1 field, $\partial \rho/\partial t^i$ Real $\rightarrow$ Wave

11: Compute $\boldsymbol{m}^{c,i}$ as in section 3.5.1.1

12: Fourier transform 3 fields, $\boldsymbol{m}^{c,i}$ Wave $\rightarrow$ Real

13: Form nonlinear product, $\mathcal{L}(z^*)\,\partial z/\partial t^i$:

$$\underbrace{-\frac{1}{\rho}\boldsymbol{m}^{c,i} \cdot \nabla z^*}_{\text{1 field}}$$

14: Fourier transform 1 field, $\mathcal{L}(z^*)\,\partial z/\partial t^i$ Real $\rightarrow$ Wave

15: Update $z^{s,i} \rightarrow z^{s,i+1}$, $\partial z/\partial t^i \rightarrow \partial z/\partial t^{i+1}$

16: **end while**

3.5.3 Boundary conditions

Unbounded domains which must be truncated for computational purposes are commonly encountered in the simulation of turbulent flows. Herein, it is assumed the domain is formally infinite in the inhomogeneous direction. In the homogeneous directions, periodic boundary conditions are employed consistent with the choice of Fourier expansions. In the inhomogeneous direction, the momentum boundary condition is an extension of the potential-matching condition of Corral and Jiménez originally developed for incompressible flows [72]. This is based on the assumption that the vorticity decays rapidly as $x_2 \to \pm\infty$, so at the boundary of the computational domain the potential part of the velocity is consistent with an exterior decaying irrotational field. In the variable-density case this means, for L_2 sufficiently large, $\rho \to \rho_\infty$, $\nabla \times \boldsymbol{m} \to 0$, and $\nabla \cdot \boldsymbol{m} \to 0$.

Consider a potential-only momentum field valid for $x_2 > L_2/2$:

$$\boldsymbol{m}^p = \nabla\phi\,. \tag{3.101}$$

$\phi = \sum_{ln} \widehat{\phi}_{ln}(x_2) e^{\mathrm{i}k_1 x_1} e^{\mathrm{i}k_3 x_3}$ obeys $\nabla^2\phi = 0$ such that $\widehat{\phi}_{ln} \sim e^{-\sqrt{k_1^2+k_3^2}x_2} = e^{-kx_2}$ for consistency with the vanishing condition at infinity. Hence, the following relationships are satisfied for each wavenumber pair except $(0,0)$:

$$\begin{aligned} \widehat{m_2^p}\big|_{\frac{L_2}{2}} &= -k\widehat{\phi}\big|_{\frac{L_2}{2}} \\ \implies \widehat{m_1^p}\big|_{\frac{L_2}{2}} &= -\frac{\mathrm{i}k_1}{k}\widehat{m_2^p}\big|_{\frac{L_2}{2}} \\ \implies \widehat{m_3^p}\big|_{\frac{L_2}{2}} &= -\frac{\mathrm{i}k_3}{k}\widehat{m_2^p}\big|_{\frac{L_2}{2}}\,. \end{aligned} \tag{3.102}$$

Furthermore, $\nabla \times \boldsymbol{m}^p = 0$ gives:

$$\begin{aligned} \frac{\partial \widehat{m_2^p}\big|_{\frac{L_2}{2}}}{\partial x_1} - \frac{\partial \widehat{m_1^p}\big|_{\frac{L_2}{2}}}{\partial x_2} &= 0 \\ \implies \widehat{m_2^p}\big|_{\frac{L_2}{2}} + \frac{1}{k}\frac{\partial \widehat{m_2^p}}{\partial x_2}\bigg|_{\frac{L_2}{2}} &= 0\,. \end{aligned} \tag{3.103}$$

The result is similar for $x_2 < -L_2/2$:

$$\begin{aligned} \widehat{m_1^p}\big|_{-\frac{L_2}{2}} &= \frac{\mathrm{i}k_1}{k}\widehat{m_2^p}\big|_{-\frac{L_2}{2}} \\ \widehat{m_3^p}\big|_{-\frac{L_2}{2}} &= \frac{\mathrm{i}k_3}{k}\widehat{m_2^p}\big|_{-\frac{L_2}{2}} \\ \widehat{m_2^p}\big|_{-\frac{L_2}{2}} - \frac{1}{k}\frac{\partial \widehat{m_2^p}}{\partial x_2}\bigg|_{\frac{-L_2}{2}} &= 0\,. \end{aligned} \tag{3.104}$$

Requiring both the divergence-free and curl-free parts to obey the potential-matching condition separately clearly guarantees the entire momentum does so as well. This choice is natural and does not introduce an unnecessary coupling between the two parts through the boundary condition.

Recall $\nabla^2 m_2^d = \phi_2$. Two additional boundary conditions on m_2^d are needed since system (3.5) is formally fourth order in m_2^d. From the potential-matching condition, it follows that

$$\begin{aligned} \frac{\partial^2 \widehat{m_2^d}}{\partial x_2^2}\bigg|_{\frac{L_2}{2}} &= -k^3\widehat{\phi}\big|_{\frac{L_2}{2}} = k^2\widehat{m_2^d}\big|_{\frac{L_2}{2}} \\ \implies \widehat{m_2^d}\big|_{\frac{L_2}{2}} - \frac{1}{k^2}\frac{\partial^2 \widehat{m_2^d}}{\partial x_2^2}\bigg|_{\frac{L_2}{2}} &= 0\,. \end{aligned} \tag{3.105}$$

Similarly,

$$\widehat{m_2^d}\big|_{-\frac{L_2}{2}} - \frac{1}{k^2}\frac{\partial^2 \widehat{m_2^d}}{\partial x_2^2}\bigg|_{-\frac{L_2}{2}} = 0\,. \tag{3.106}$$

This is consistent with a divergence-free and curl-free condition at the boundaries. Given the spatial discretization, eq. (3.106) and eq. (3.105) imply ϕ_2 must obey homogeneous Dirichlet

conditions for consistency. Hence, when m_2^d is reconstructed from ϕ_2 via the Poisson equation eq. (3.97), only the Robin conditions of eq. (3.103) and eq. (3.104) are explicitly enforced by replacing the first and last equations. A homogeneous Dirichlet condition is enforced on Ω_2 which is consistent with a curl-free momentum.

Averaging the mass conservation equation over x_1 and x_3 implies a homogeneous Neumann condition on $\overline{m}_2^{x_1 x_3}$ at the boundary, since the flow is essentially incompressible there. This means there is one remaining degree of freedom when determining $\overline{m}_2^{x_1 x_3}$ which is used to enforce a symmetry condition or set the value at a location in the domain, for example. For the Rayleigh-Taylor problem, cases are stopped well before the front nears the boundary so a homogeneous Dirichlet condition is used at the top of the domain as the fluid remains at rest.

Homogeneous Neumann conditions are imposed on the streamwise and spanwise plane-averaged momentum as well as the plane-averaged and fluctuating components of the transported scalar, z. Numerical imposition of Neumann boundary conditions is nontrivial with explicit schemes because strong enforcement can introduce artificial discontinuities in the solution as boundary degrees of freedom are forced to satisfy the given condition while interior degrees of freedom are set independently. This can introduce numerical discontinuities and cause instability. Methods based on weak formulations circumvent this naturally. Here the Neumann conditions are imposed "weakly" by building them directly into the discrete differential operators and solving the governing equations at all collocation points, including those on the boundary. The boundary condition then only explicitly appears during the computation of the residual. Canuto has a relevant discussion in [73] for the interested reader. With a sufficiently large domain, a weak Neumann condition is appropriate since the flow is allowed to relax to the freestream outflow condition. See Appendix A for full details.

3.5.4 Results and verification

This section contains numerical results which demonstrate the algorithm described above. A sweep over Atwood numbers (density ratios) for the single-mode Rayleigh-Taylor (RT) instability serves as a verification exercise for the variable-density Navier-Stokes algorithm and demonstrates its stability. Additionally, the implementation has been verified (results not shown) with a manufactured solution created with MASA [74], a C++ library which can generate source terms for arbitrary differential equations by automatic differentiation. A solution which specifies the curl-free and divergence-free momentum separately was created, eliminating the need to decompose the momentum field which cannot be done without inversion of the Laplacian operator. See Appendix B for the created solution.

3.5.4.1 Single-mode Rayleigh-Taylor test problem

Following He *et al.* [75] who simulate a single-mode Rayleigh-Taylor instability in a rectangular box with square cross section, the configuration is that of two miscible fluids of varying density with the heavier fluid on top under the influence of gravity which is aligned with the vertical direction (x_2). In this case, the kinematic viscosity ν for both fluids is the same. The computational domain is $\mathcal{V}_{RT} = [0, W] \times [0, 7W] \times [0, W]$. The box is seven times as tall as it is wide to mitigate boundary effects, and periodicity is assumed in the x_1 and x_3 directions. The initial perturbation is given by

$$\frac{h(x_1, x_3)}{W} = 0.05 \left[\cos\left(\frac{2\pi x_1}{W}\right) + \cos\left(\frac{2\pi x_3}{W}\right) \right] \tag{3.107}$$

with h being the interface height. This occurs slightly above the center plane at $x_2 = 4W$ since the structures bias in the direction of gravity.

There is a slight change in the governing equations due to the presence of gravity as a

source term in the momentum equations. The momentum equations become

$$\frac{\partial \rho u_i}{\partial t} + \frac{\partial \rho u_i u_j}{\partial x_j} = -\frac{\partial p}{\partial x_i} + \frac{\partial \tau_{ij}}{\partial x_j} - \rho g \delta_{i2} \tag{3.108}$$

which slightly alters the equation for ϕ_2,

$$\frac{\partial \phi_2}{\partial t} = \frac{\partial^3}{\partial x_l \partial x_l \partial x_j}\left(C_{2j} + \tau_{2j}\right) - \frac{\partial^3}{\partial x_2 \partial x_l \partial x_j}\left(C_{lj} + \tau_{lj}\right) - \left(\frac{\partial^2 \rho g}{\partial {x_1}^2} + \frac{\partial^2 \rho g}{\partial {x_3}^2}\right). \tag{3.109}$$

To track the mixture, define

$$z = \frac{\rho_h Y_l + \rho_l Y_h - \rho_h}{\rho_l - \rho_h} \tag{3.110}$$

where Y_l and Y_h are the species mass fractions of the light and heavy fluid, respectively. Then z obeys a scalar transport equation like eq. (2.10):

$$\frac{\partial \rho z}{\partial t} + \frac{\partial}{\partial x_i}\left(\rho u_i z\right) = \frac{\partial}{\partial x_i}\left(\rho \mathcal{D}_z \frac{\partial z}{\partial x_i}\right) \tag{3.111}$$

with $\rho\mathcal{D}_z$ defined as the dynamic viscosity. The potential-matching condition is specified at the top and bottom boundary for the fluctuating momentum, and the plane-averaged momentum obeys a homogeneous Neumann condition for the spanwise and streamwise components and a homogeneous Dirichlet condition for the vertical component at the top of the box. A homogeneous Neumann condition is used for z as well. See section 3.5.3 for more details on applying boundary conditions within the algorithm presented here. The reference length is the box width, W, and the reference timescale is $\sqrt{W/g}$. The density of the lighter fluid, ρ_l, is taken to be the reference density. This leads to a Reynolds number and Atwood number which parameterize the problem:

$$\mathrm{Re} = \frac{\sqrt{W g}\, W}{\nu} \qquad \mathrm{A} = \frac{\rho_h - \rho_l}{\rho_h + \rho_l}. \tag{3.112}$$

Note that the density ratio is

$$\frac{\rho_h}{\rho_l} = \frac{1 + \mathrm{A}}{1 - \mathrm{A}} \tag{3.113}$$

and

$$\frac{\rho}{\rho_l} = \frac{1 + \mathrm{A}}{1 + \mathrm{A} - 2\mathrm{A}z} \tag{3.114}$$

is then the equation of state. Taking the Schmidt number to be one implies

$$\frac{\mu}{\rho_l \nu} = \frac{1 + \mathrm{A}}{1 + \mathrm{A} - 2\mathrm{A}z} \tag{3.115}$$

as well.

The single-mode RT instability experiences different stages: an initial acceleration when viscous effects dominate, followed by a period of constant "bubble" velocity predicted by potential theory before a reacceleration occurs. For validation we compare to the result of Goncharov [76] which gives the bubble velocity, or the rate at which the light fluid penetrates the heavy, during the potential growth as

$$v_b = \sqrt{\frac{2A}{1 + A}\frac{g}{Ck}} \tag{3.116}$$

where $C = 1$ or 3 in three- or two-dimensional flows, respectively, and k is the perturbation wave number. Figure 3.5 shows a comparison of this theoretical result with the computation. The Reynolds number is 512 for all runs. The simulated bubble velocity is similar to the theoretical result. Most importantly, this demonstrates the algorithm's stability over a wide range of density ratios. For the three-dimensional simulations shown here, the highest Atwood number case was .875, which corresponds to a density ratio of 15.

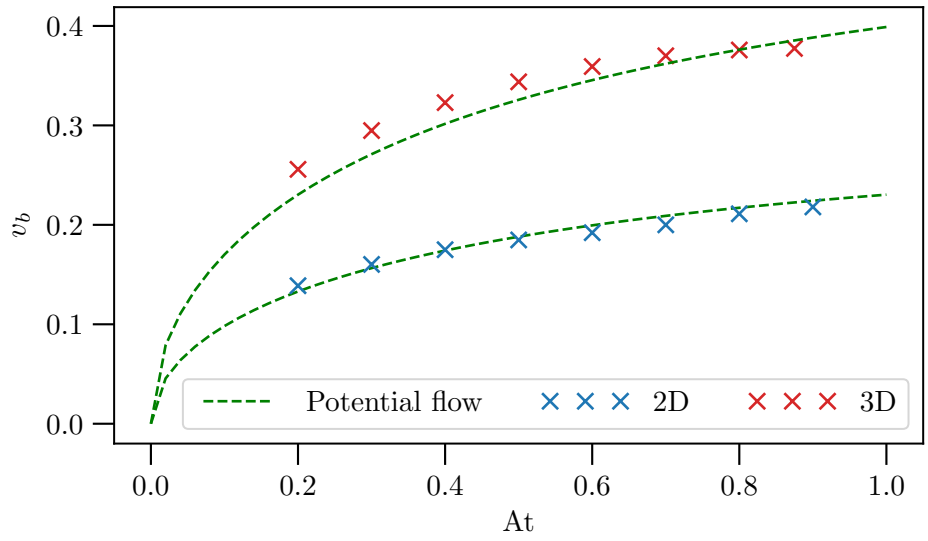

Figure 3.5: v_b versus Atwood number for the RT problem. Goncharov's theoretical result is also shown.

Chapter 4

Modeling a nonpremixed, reacting, planar jet

In this chapter we apply the numerical methods described in chapter 3 to perform a direct numerical simulation of a nonpremixed, temporally-evolving, reacting planar jet coupled with a steady laminar flamelet model to represent the thermochemical state. The results are used for *a posteriori* comparisons to a DNS of the same configuration with a higher fidelity chemistry model as well as *a priori* evaluations of flamelet-based RANS closure models. This analysis framework, as shown in section 1.2, allows for errors from the three modeling focuses (turbulence, chemical reactions, turbulence-chemistry interaction) to be cleanly isolated.

4.1 Complex chemistry reference DNS

The DNS of Attili, Bisetti, *et al.* [23] serves as the complex chemistry reference simulation discussed previously. It is a temporally-evolving, reacting, planar jet of a n-heptane fuel stream in co-flowing air. The chemical mechanism is described in [41] and is used here to generate the flamelets. Forty seven species and 290 reactions are included. The reference DNS implements this mechanism directly, solving the species and temperature equations, whereas the flamelet DNS only queries the tabulated thermochemical state as a function of the mixture fraction z. The complex chemistry DNS equations and assumptions are detailed in section 2.1.

4.2 Simulation details

The configuration of the flamelet DNS is the same as the complex chemistry DNS and is illustrated in fig. 4.1 which shows the temperature field in the streamwise (x_1) and inhomogeneous (x_2) directions early on in the flame's evolution. The computational domain is rectangular ($\mathcal{V} = [-L_1/2, L_1/2] \times [-L_2/2, L_2/2] \times [-L_3/2, L_3/2]$) and periodic in the x_1 and x_3 directions. The domain extent is 105 mm in the inhomogeneous (x_2) direction, 94 mm in the x_1 direction, and 47 mm in the x_3 direction. The number of grid points ($N_1 \times N_2 \times N_3$) are selected to be the same as in the reference DNS. The collocation points are uniformly spaced ($\Delta = .091$ mm) in most of the domain (for $|x_2/H| \lesssim 2.8$) with a slight stretching in the x_2 direction otherwise, mimicking the distribution of points in the complex chemistry DNS which employs a high-order finite difference spatial discretization. The B-spline order is $p = 8$ and the knots and collocation points are explicitly defined in Appendix C.

To ensure consistency, the initial velocity field and mixture fraction are taken directly from Attili, Bisetti, *et al.* and projected onto the mixed Fourier/B-spline basis. There are no fluctuations in the initial mixture fraction field and the fuel stream and oxidizer stream have equal and opposite mean streamwise velocity (fig. 4.2). There are turbulent fluctuations in the velocity field which are generated from a turbulent channel flow (see [23] for details). In the reference data, the mixture fraction is stored at cell centers and the velocity field is staggered. Therefore, the u_2, u_3, and z data needs to be shifted by $-\Delta/2$ in the x_1 direction. This is accomplished by a forward FFT, applying the shift theorem (multiplying the l^{th} coefficient by $\exp(-\mathrm{i}k_l\Delta/2)$), and an inverse FFT. In the x_3 direction, the u_1, u_2, and z data is shifted analogously. Finally, lines of the shifted data are interpolated in the x_2 direction with fifth order splines using SciPy [77] and evaluated at the collocation points. This is required for all fields.

Details of the boundary conditions and their application are described in section 3.5.3. As

noted earlier, there is one remaining degree of freedom in the boundary conditions associated with the mean momentum in the x_2 direction, whose specification is problem dependent. In the case of shear flows like the jet, it is specified as:

$$\overline{m}_2\left(L_2/2\right) = -\overline{m}_2\left(-L_2/2\right) \ . \tag{4.1}$$

This expresses the symmetry of the configuration about the constant x_2 plane at the center of the jet. This condition is enforced numerically by obtaining a solution with one homogeneous boundary condition and correcting by an appropriate offset. Here a particular solution $\overline{m}_2^p$ is found satisfying $\overline{m}_2\left(L_2/2\right) = 0$, then the solution satisfying eq. (4.1) is obtained as

$$\overline{m}_2 = \overline{m}_2^p - \frac{1}{2}\overline{m}_2^p\left(-L_2/2\right) \ . \tag{4.2}$$

The temporally-evolving jet is characterized by a Reynolds number based on the initial jet width, H, and velocity difference, ΔU, which is the difference between the initial centerline velocity and the co-flow velocity. This gives a jet Reynolds number $\mathrm{Re} = 15,000$, using the kinematic viscosity of the fuel stream. The reference chemical timescale is $1/\chi_{ext} = 650\ s^{-1}$, the inverse scalar dissipation rate at extinction. Extinction is possible, but rare due to the relatively high Damköhler number, in the complex chemistry DNS.

Three iterations per Runge-Kutta step were chosen to solve the fixed-point problem, which is outlined in procedure 3. By obtaining an estimate for the largest eigenvalues of $\mathcal{L}$, the absolute stability region as a function of iteration number was analyzed (see section 3.4.4). One of these analyses is shown in fig. 3.3.a, which demonstrates the stability region nearly completely coincides with the fully converged target region after three iterations. To obtain the eigenvalue estimate, a two-dimensional (x_1-x_2) simulation was performed and snapshots were used to determine the spectrum of $\mathcal{L}$ by employing an eigenvalue solver built with SLEPc [78]. The two-dimensional initial condition was simply a plane taken from the full

Domain size, $(L_1 \times L_2 \times L_3)$ (mm)	$94 \times 105 \times 47$
Reference velocity, ΔU (m/s)	17.48
Reference kinematic viscosity, ν_R (m^2/s)	1.7×10^{-5}
Initial jet width, H (mm)	15
Reference scalar dissipation rate, χ_{ext} $(1/s)$	650
Stoichiometric mixture fraction, z_{st}	.147
Reference mixture fraction diffusion coefficient, $\mathcal{D}_R$ (m^2/s)	1.8×10^{-5}
Reference temperature, T_R (K)	400
Reference density, ρ_R (kg/m^3)	1.17
Final simulation time, t_f (ms)	20
Reynolds number, Re	$15,000$
Grid points, $(N_1 \times N_2 \times N_3)$	$1024 \times 1024 \times 512$
Mesh spacing before stretching, Δ (mm)	.091
B-spline order, p	8

Table 4.1: Simulation parameters.

three-dimensional initial condition. The eigenvalues did not vary substantially throughout the test run, so the number of iterations was fixed for the three-dimensional simulation.

Relevant simulation parameters are summarized in table 4.1.

Figure 4.1: Temperature contours in a n-heptane jet in co-flowing air.

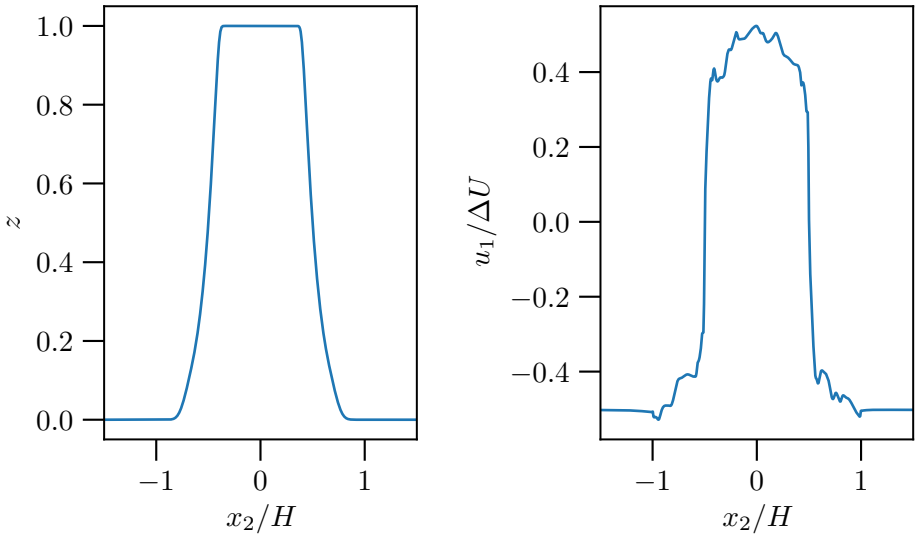

Figure 4.2: Initial profiles of mixture fraction and streamwise velocity for the flamelet DNS ($x_1/H = 0$, $x_3/H = 0$).

4.3 Laminar flamelet closure generation

Practically, flamelet closures are obtained from precomputed libraries. The steady laminar flamelet equations, system (H.32), are solved for different χ_{lam} profiles and the relevant thermochemical and transport properties are obtained as functions of the mixture fraction. Essentially, this results in a family of flames, $\boldsymbol{\phi}^i = \boldsymbol{\phi}\left(z; \chi^i_{\text{lam,st}}\right)$, where $\boldsymbol{\phi}$ is the thermochemical state and the flames are parameterized by the scalar dissipation rate at the stoichiometric point ($\chi_{\text{lam,st}}$). For this work, the flames are obtained through the use of Cantera's [79] one-dimensional counterflow diffusion flame solver with different inlet mass flow rates. Cantera does not use the flamelet equations directly but rather solves the governing equations for axisymmetric stagnation flow in physical space. By assuming unity Lewis numbers, a unique mixture fraction can be defined (which, in general, is not possible) and the solutions translated into mixture fraction space. This work uses Bilger's definition of the mixture fraction which is a normalized, weighted sum of the elemental mass fractions. The definition is provided in section H.1.

The data obtained by this procedure cannot cover the entire (z, χ) space relevant to these simulations. For example, for z values away from 0 or 1, there is no data with low χ since it is only small when approaching the freestreams of the counterflowing flame ($\|\nabla z\| \to 0$). Additionally, high instantaneous spikes in χ can exceed the values found in the limiting "extinction" flamelet, which corresponds with the laminar flame with the highest imposed strain rate before extinction occurs. With the presumed PDF models, both of these situations are assigned a low probability so that the mean thermodynamic properties are insensitive to the extrapolation used to fill in this missing data. This is not the case for the flamelet DNS which is dynamically simulating the underlying assumed instantaneous turbulent flame, making the extrapolation important. Discontinuities in the flamelet representation of the density will

also introduce noise into the calculation via the divergence constraint on the momentum which, as discussed in section 1.3.2, can quickly lead to instabilities. Even with care taken to ensure a $\mathcal{C}^1$ flamelet representation, it was found that the steady flamelet assumptions themselves produce an unrealistic density response which causes numerical issues independent of any artifacts of extrapolation. This is discussed in the following section and details of the extrapolations are described in Appendix G.

To avoid these problems, the family of flames generated by Cantera is averaged in χ to create a representative mean flamelet thermochemical equation of state which only retains the mixture fraction dependence. This is justified by the observation that the density has a much stronger dependence on z than on χ. To do the averaging, a PDF of the conditional scalar dissipation rate at the stoichiometric point ($f_{\chi_{st}}$) is obtained from the reference complex chemistry DNS data and projected onto an interpolating spline. As indicated above, the stoichiometric scalar dissipation rate is often used to parameterize flamelet solutions so this is a natural choice. The PDF is taken from a point in the simulation at which the mixture fraction field is highly turbulent ($t = 15\ ms$). As with the PDF, the χ_{st} dependence of the Cantera flames is projected onto splines for interpolation. The averaged density, ρ_z, is then computed as

$$\rho_z(z) = \int_{\Omega_s} \rho\left(z; \chi_{\mathrm{st}}\right) f_{\chi_{st}}\left(\chi_{\mathrm{st}}\right)\ d\chi_{\mathrm{st}}\,, \tag{4.3}$$

where Ω_s is the support of $f_{\chi_{st}}$. Other properties are obtained similarly. The average thermochemical state dependence on z from the flamelet is then represented with a B-spline interpolant for use in the flamelet DNS. Evaluation is accomplished using GSL's B-spline functionality [80] paired with a set of Fortran wrappers, FGSL[1].

[1] https://github.com/reinh-bader/fgsl/

4.4 A fundamental limitation of the steady laminar flamelet formulation

As alluded to above, flamelet-based DNS of a planar, reacting jet using a flamelet formulation with a dependence on χ experienced numerical instabilities. The instability originated from sharp gradients in the density which led to jumps in the momentum through the mass conservation equation. The sharp gradients occurred near local extrema in the mixture fraction where $\chi \to 0$ (recall $\chi \sim \|\nabla z\|^2$). To investigate further, the χ-dependent flamelet was used as the chemistry closure in a one-dimensional, steady, diffusion flame whose solution featured local extrema in the mixture fraction. As shown in fig. 4.3, the density exhibits a bump in a narrow region centered on a minimum in z. Resolving this feature in the flamelet DNS would require an order of magnitude finer grid than in the complex chemistry DNS. This indicates that there is a flaw in the flamelet assumptions that produces these anomalously fine-scale density features, despite a smooth mixture fraction field. In a real flame, as the scalar dissipation rate decreases, times for relaxation to the steady thermochemical state implied by the local (z, χ) become longer. However, this relaxation is assumed to occur instantaneously in the steady laminar flamelet model. The breakdown of this assumption manifests itself as anomalous small-scale features in the density field. This is of little consequence in flamelet-based RANS combustion modeling because the underlying instantaneous turbulent flame is never directly simulated. However, local extrema in z are common in the turbulent shear layer, resulting in the anomalous small-scale density features and stability problems described above.

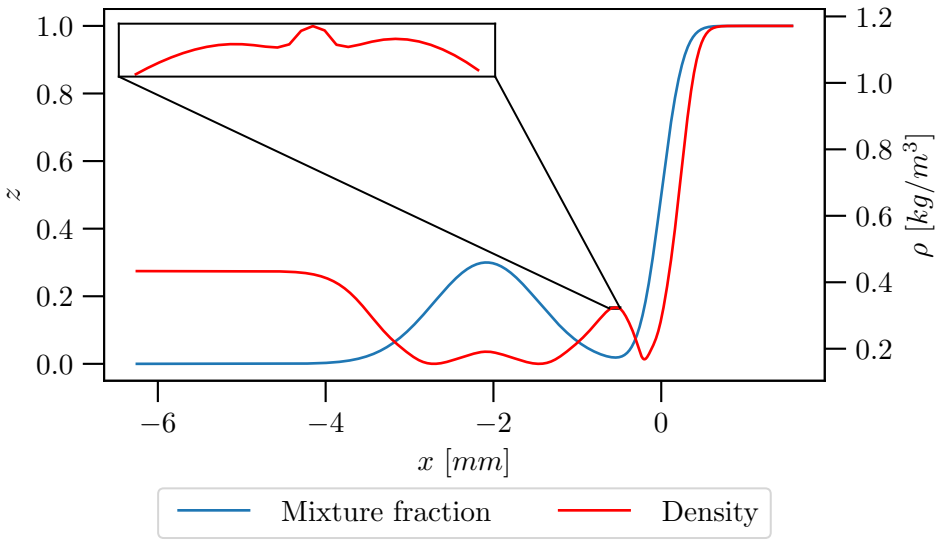

Figure 4.3: Mixture fraction (left axis) and density (right axis) for a 1D diffusion flame coupled with the χ-dependent flamelet. The density profile is magnified near a local minimum in the mixture fraction.

4.5 Results and analysis

The flamelet DNS described above was run for 20 ms, the same simulation time as the complex chemistry DNS (hereafter CC DNS) of Attili, Bisetti, *et al.* [23]. During the calculation, solution snapshots were taken for each millisecond of simulation time. Statistics are collected twice as often. Since the DNS configuration is time-evolving, averaging occurs over the homogeneous directions and by applying statistical symmetries in the x_2 direction. The data collected is sufficient to reproduce the terms in the Favre-averaged equations shown in Appendix D. One-dimensional energy spectra for the state variables were also collected each millisecond and used to ensure sufficient resolution of the turbulence (Appendix F provides computational details and an example is shown in the appendices, fig. I.1).

To illustrate the planar jet's development, fig. 4.4 shows the evolution of a x_1-x_2 plane of the mixture fraction field at several times during the simulation. Additionally, the evolution

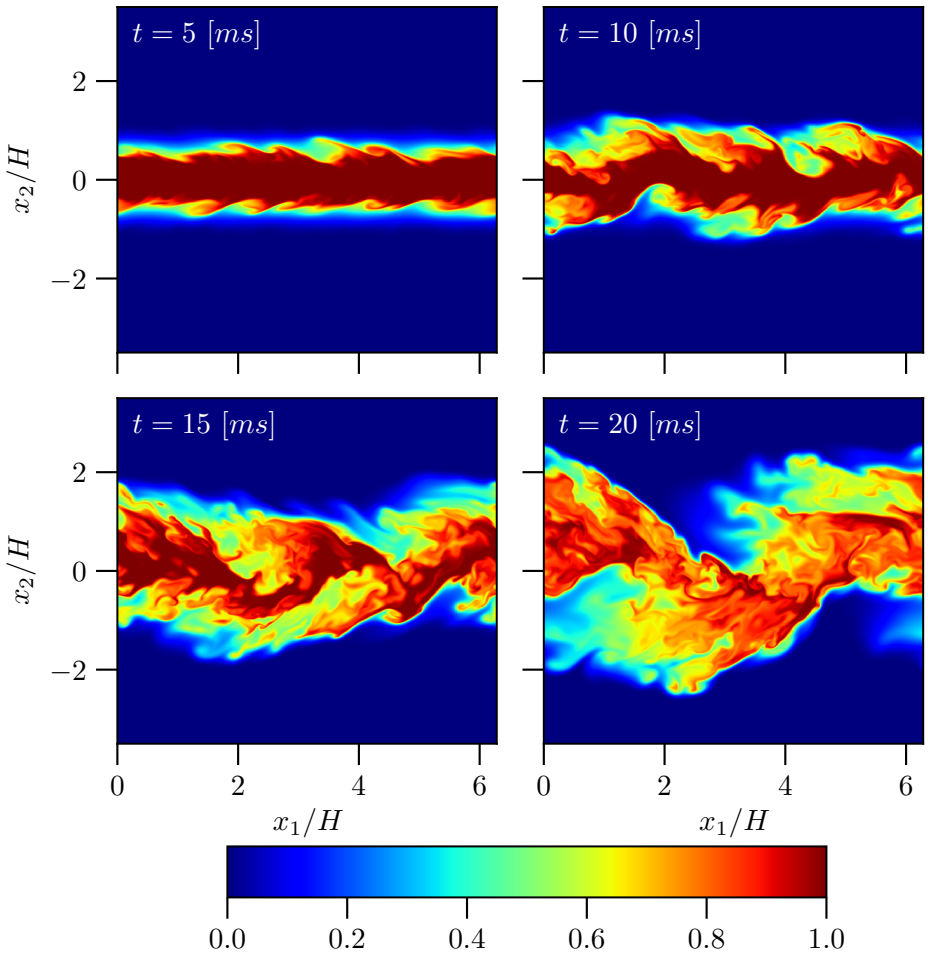

Figure 4.4: Contours of mixture fraction in a x_1-x_2 plane of the flamelet DNS.

of profiles of the mean state appear in fig. 4.5. There are no fluctuations in the initial z field but fluctuations develop due to the turbulence in the velocity. These are dominated by the rollers that arise from the Kelvin-Helmholtz instability, and they lead to enhanced mixing of the fuel jet with the co-flowing air. The jet width grows rapidly near the end of the simulation (from 15 to 20 ms) and increasingly fine features are apparent. As the mean mixture fraction profile broadens, the flame becomes more spatially intermittent, including at the centerline. Any further simulation in time past 20 ms would be contaminated by boundary effects as the flame encompasses over four-fifths of the domain's extent in the

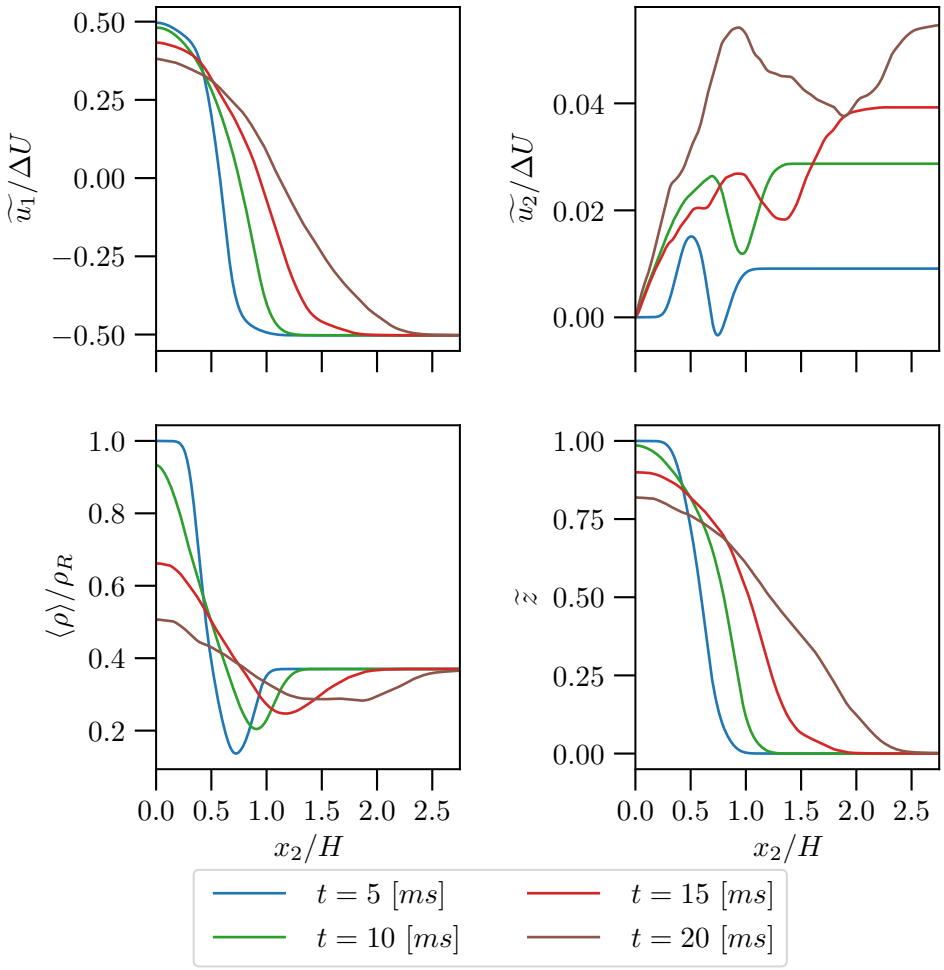

Figure 4.5: Evolution of the mean state variables of the flamelet DNS.

inhomogeneous direction.

4.5.1 *A posteriori* comparisons with complex chemistry DNS

In this section, we consider an *a posteriori* comparison between the flamelet DNS and the reference CC DNS to assess the impact that the laminar flamelet approximation has on quantities of interest in RANS. Most of the CC DNS data shown below is available at 5, 10, 15, and 20 ms but some quantities were not given for all times. First, consider the

conditionally averaged density, and molecular diffusivity of z, figs. 4.6 and 4.7, respectively[2]. Conditioned on z, the flamelet DNS density and mixture fraction diffusivity are independent of time by construction, but this is not so for the CC DNS. None-the-less the conditionally averaged quantities change only slightly over time in the latter, with an L^2 variation of only 4% in the density. Further, the conditionally averaged density and mixture fraction diffusivity are in good agreement between the flamelet and CC DNS. The largest discrepancy ($\sim 5\%$) being in the diffusivity around the stoichiometric value of z ($z_{st} = 0.147$). One key approximation of the steady laminar flamelet model is the projection of the thermochemical state onto a low-dimensional manifold parameterized by z and χ. These results suggest that this approximation may be justified on average.

The conditionally averaged scalar dissipation rate evolves quantitatively similarly in both DNS, with $\langle \chi | z \rangle$ increasing over time until 10 ms, and then decreasing (fig. 4.8). However, the variation in time is larger in the complex chemistry DNS. Additionally, the dissipation rate is larger on average for fuel rich conditions ($z > 0.147$) in the CC DNS for all times. The mean z profiles (e.g. at 20 ms in fig. 4.9) are fuller for the flamelet DNS (see figs. I.3 to I.5 in Appendix I for comparisons at other times) while matching closely at the centerline and reaching oxidizer freestream values at nearly the same location. This indicates that the mean mixture fraction gradient is larger in the CC DNS, which may be leading to the larger scalar dissipation rate. The mean density and velocity, also shown in fig. 4.9, are consistent with a lower overall heat release in the flamelet DNS. The mean density is higher, which conversely means the mean temperature is lower, the centerline streamwise velocity deficit is larger, and the velocity in the inhomogeneous direction is lower at the boundary, all indicating less expansion of the jet compared to the CC DNS.

To investigate the discrepancies in the evolution of the mixture fraction between the two simulations, an analysis of the mean mixture fraction budgets was performed. The

[2]The complex chemistry DNS data for $\langle \rho \mathcal{D}_z | z \rangle$ was not available for 15 and 20 ms. The conditional mean temperature, which is not carried as part of the RANS state, is included in Appendix I, see fig. I.2.

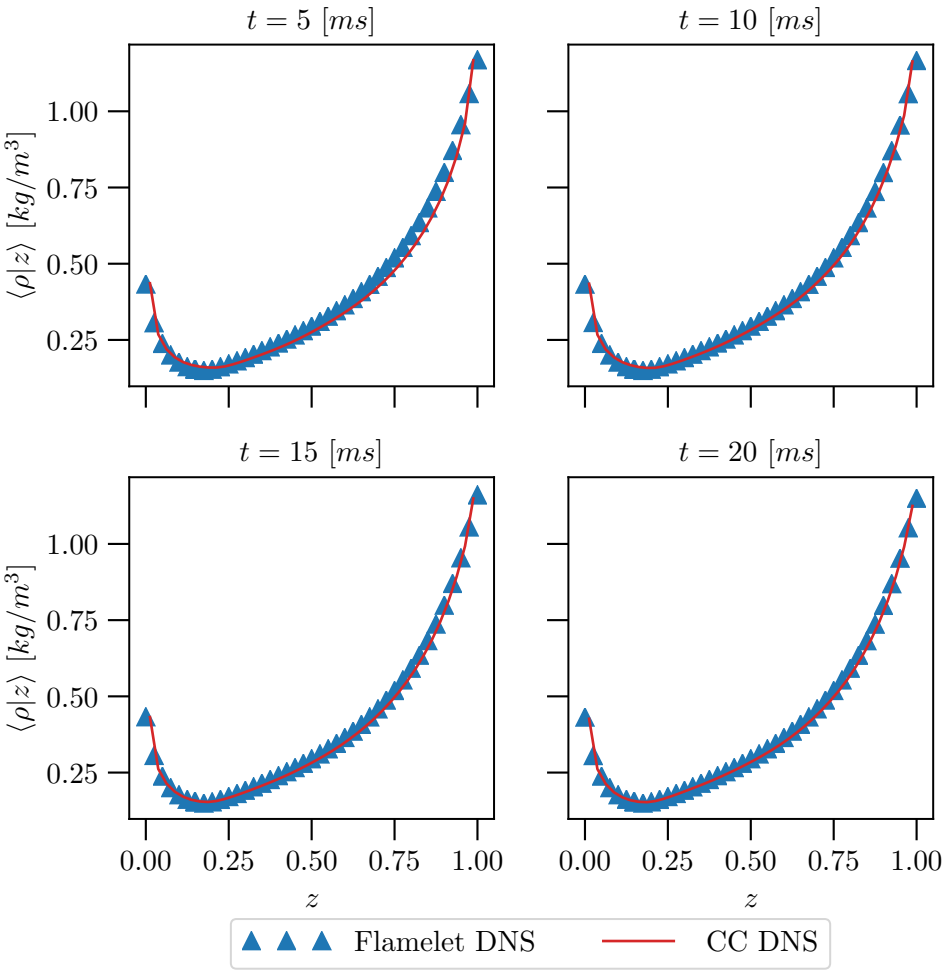

Figure 4.6: Conditionally averaged density, conditioned on mixture fraction for the flamelet DNS conducted here and the complex chemistry DNS (CC DNS) of [23].

conservation equation for $\overline{\rho}\widetilde{z} = \overline{\rho z}$, the mean density-weighted mixture fraction, eq. (H.27) is derived in Appendix H for the CC DNS. This differs from eq. (2.21) in the diffusion terms due to the simplified transport assumptions in the steady laminar flamelet model. The integral in time of the mean convection and turbulent transport terms in eq. (2.21) or eq. (H.27) yields the total contribution of these terms to the temporal change in $\overline{\rho}\widetilde{z}$. At $t = 20\ ms$ (fig. 4.10), these are in good agreement between the two DNS, with the discrepancy between them much smaller than the discrepancy in $\overline{\rho}\widetilde{z}$ (also shown in fig. 4.10). Because the initial $\overline{\rho}\widetilde{z}$ is nearly identical in the two simulations, the only other potential source of this discrepancy in $\overline{\rho}\widetilde{z}$

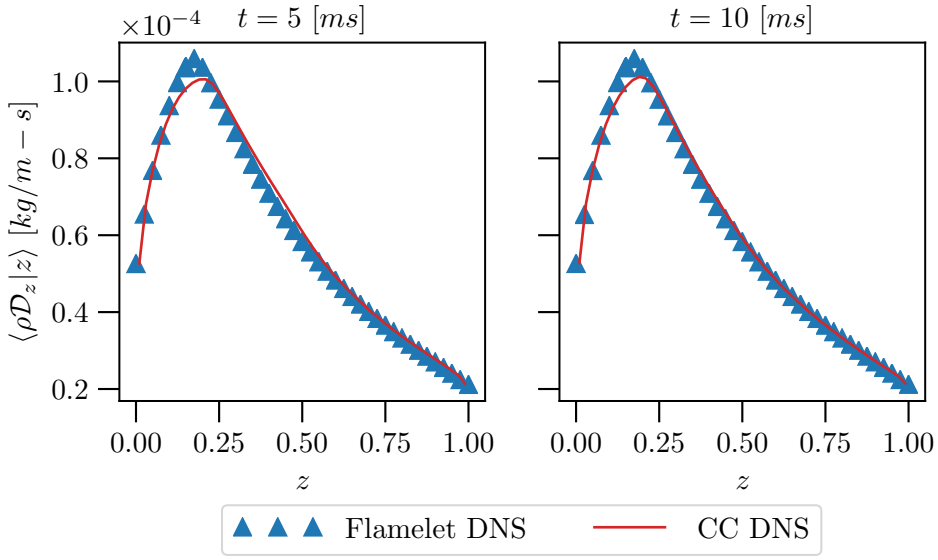

Figure 4.7: Conditionally averaged molecular diffusivity of z, conditioned on z for the flamelet DNS conducted here and the complex chemistry DNS (CC DNS) of [23].

is the molecular diffusion term. However, in the flamelet DNS, this makes an insignificant contribution (fig. 4.10) so this is an unlikely explanation for the difference.

The mean density-weighted mixture fraction $\overline{\rho}\widetilde{z}$ is a conserved quantity for both the complex chemistry and flamelet models. Thus the integral $\int \overline{\rho}\widetilde{z}\, dx_2$ should be time independent, since $\overline{\rho}\widetilde{z}$ and its derivatives are zero at the domain boundary. However, as shown in fig. 4.11, $\int \overline{\rho}\widetilde{z}\, dx_2$ drops off by nearly 25% over time in the CC DNS, far larger than would be expected due to nonconservative numerics in a DNS. Due to this discrepancy, it is not possible to determine whether differences between the two DNS can be attributed to the steady laminar flamelet approximation or the loss of z conservation in the CC DNS.

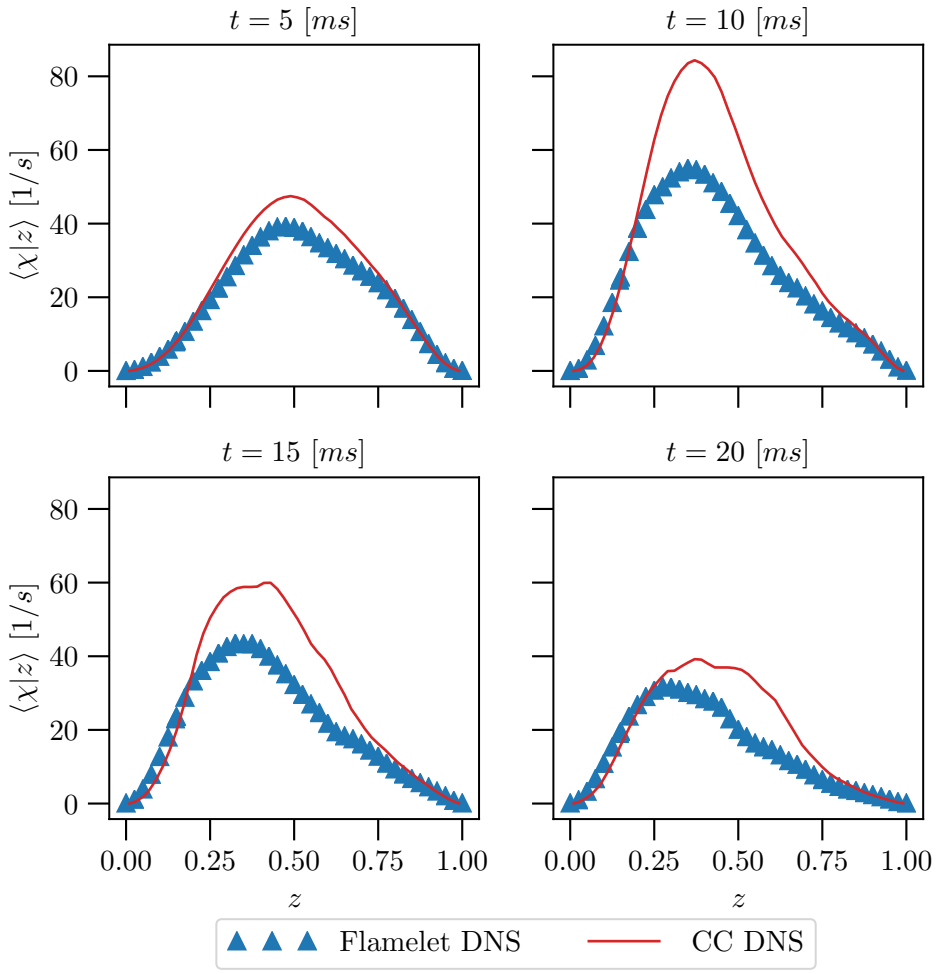

Figure 4.8: Conditionally averaged scalar dissipation rate, conditioned on the mixture fraction z for the flamelet DNS conducted here and the complex chemistry DNS (CC DNS) of [23].

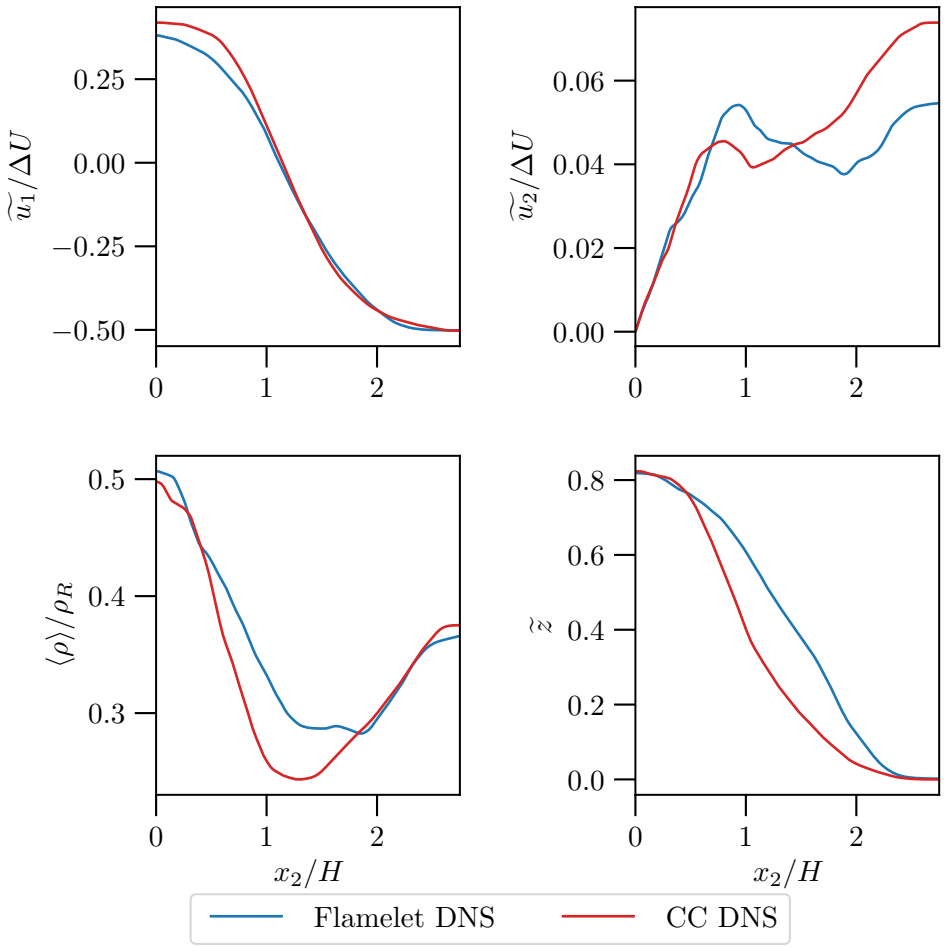

Figure 4.9: Profiles of the flamelet DNS mean state variables at 20 ms as a function of the crosswise coordinate x_2/H for the flamelet DNS conducted here and the complex chemistry DNS (CC DNS) of [23].

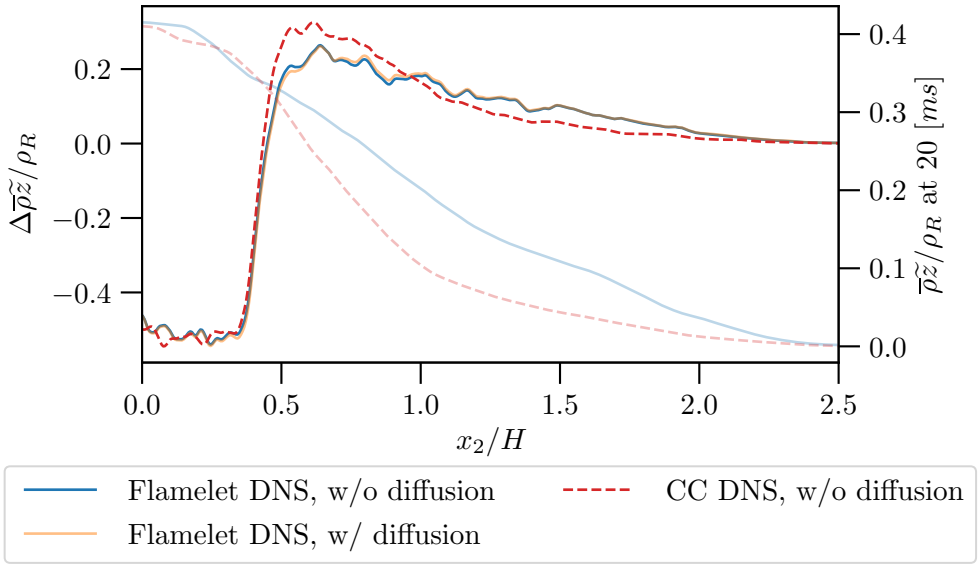

Figure 4.10: Change in the conserved quantity $\overline{\rho}\widetilde{z}$ due to turbulent transport, convection, and, for the flamelet DNS, with or without the molecular diffusion at $t = 20\ ms$ as a function of x_2/H (left axis). Also shown are profiles of $\overline{\rho}\widetilde{z}$ at $t = 20\ ms$ (right axis). The complex chemistry DNS (CC DNS) is from [23].

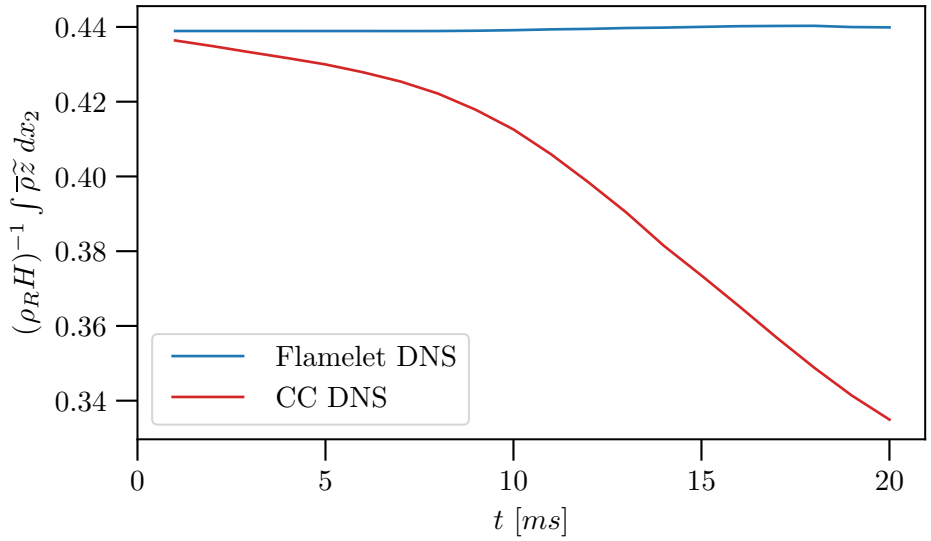

Figure 4.11: Integral of $\overline{\rho}\widetilde{z}$ as a function of time for the flamelet DNS conducted here and the complex chemistry DNS (CC DNS) of [23].

4.5.2 *A priori* evaluations of RANS closures

In this section, relevant RANS models for the nonpremixed combustion problem (see section 2.3) are assessed in the *a priori* sense. That is, closure models are evaluated using quantities from the flamelet DNS as inputs and compared to the exact terms also determined from the flamelet DNS. Many of the models assume the scalar dissipation and turbulent dissipation timescales (τ_{mix} and τ_{turb}, respectively) are proportional, either explicitly or implicitly. To assess the validity of this assumption, the evolution of the statistics of the turbulent velocity field (k and ε) and turbulent mixing field ($\widetilde{z''z''}$ and $\widetilde{\chi}_p$) in the flamelet DNS are compared in fig. 4.12. These are the quantities that define the aforementioned timescales:

$$\begin{aligned} \tau_{mix} &= \frac{\widetilde{z''z''}}{\widetilde{\chi}_p} \\ \tau_{turb} &= \frac{k}{\varepsilon}\,. \end{aligned} \tag{4.4}$$

The turbulent kinetic energy, turbulent dissipation rate, and scalar dissipation rate evolve similarly, peaking halfway through the simulation and broadening throughout. On the other hand, the mixture fraction variance continues to grow both in magnitude and breadth during the entirety of the calculation. For additional context, the evolution of the nonzero components of the Reynolds stress tensor appear in fig. 4.13, which indicates that there is significant anisotropy. These figures will be relevant for much of the discussion below.

In the flamelet-based RANS context, a presumed PDF depending on the first two moments of the mixture fraction is used to obtain the mean thermochemical and transport properties from the underlying flamelet model. In the following, closures for the mean z equation are evaluated in section 4.5.2.1 followed by closures for the mixture fraction variance equation in section 4.5.2.2. The presumed PDF model is tested in section 4.5.2.3. Finally, the model constants used in these comparisons are provided in table 4.2.

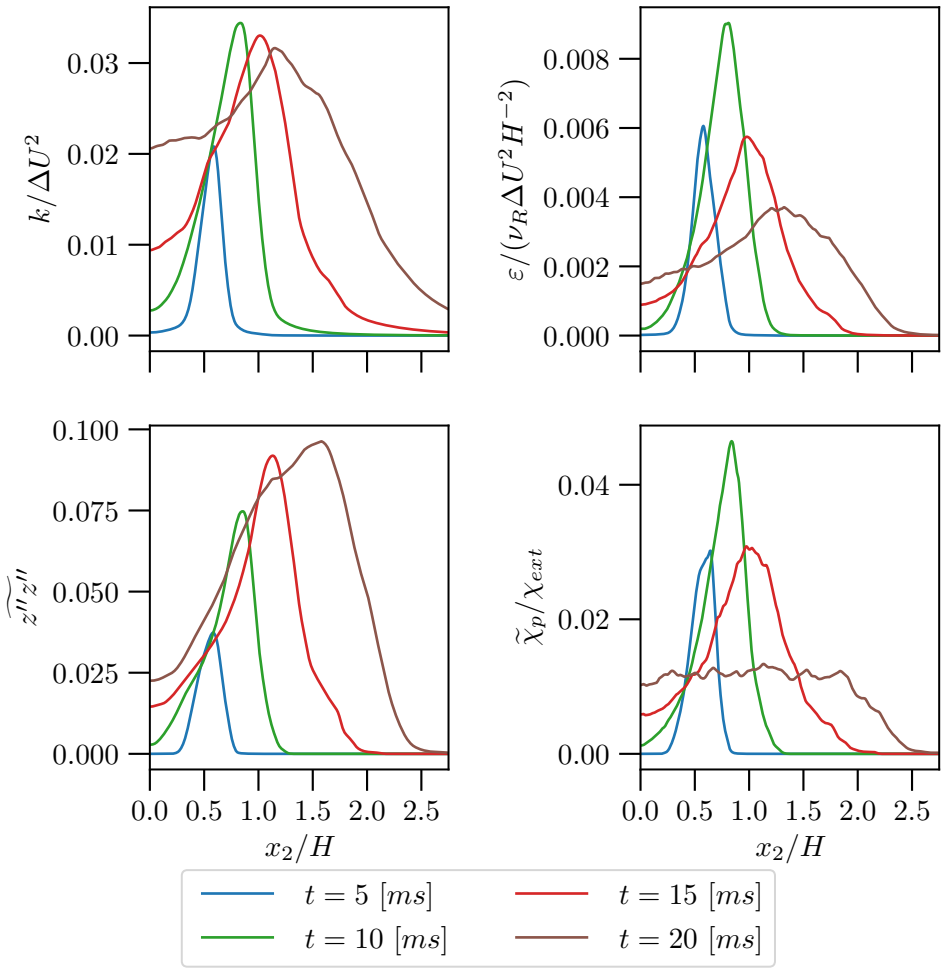

Figure 4.12: Evolution of statistics of the turbulent velocity field and turbulent mixing field.

C_μ	0.09
Sc_t	0.85
C_{mix}	2.35 C_μ
C_{ani}	2 C_μ
C_χ	2.0
σ	1.0

Table 4.2: RANS model constants.

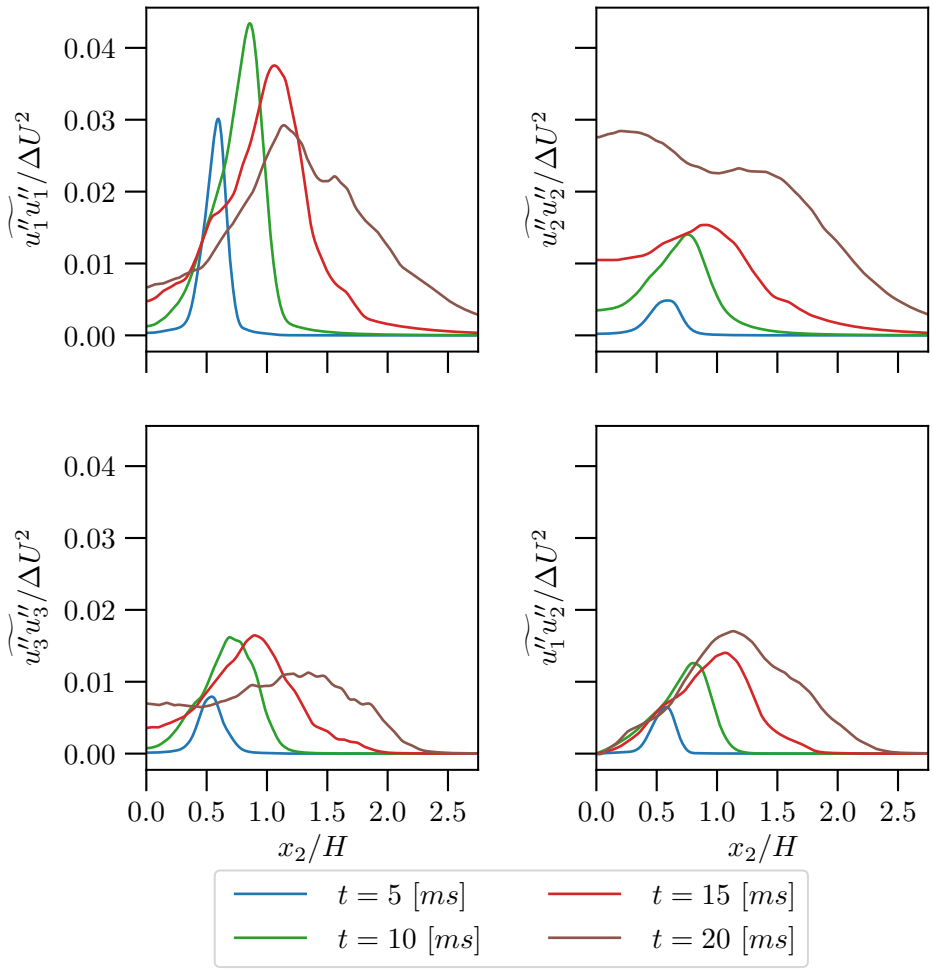

Figure 4.13: Profiles of the Reynolds stress components as the jet evolves.

4.5.2.1 Mean z equation

For the planar, reacting jet the mean mixture fraction equation, eq. (2.21), simplifies to

$$\underbrace{\frac{\partial \overline{\rho}\widetilde{z}}{\partial t}}_{\text{temporal}} + \underbrace{\frac{\partial}{\partial x_2}\left(\overline{\rho}\widetilde{u}_2\widetilde{z}\right)}_{\text{convection}} = \underbrace{\frac{\partial}{\partial x_2}\left(\overline{\rho\mathcal{D}_z\frac{\partial z}{\partial x_2}}\right)}_{\text{molecular diffusion}} - \underbrace{\frac{\partial}{\partial x_2}\left(\overline{\rho}\widetilde{u_2''z''}\right)}_{\text{turbulent transport}} . \tag{4.5}$$

The two unclosed terms in this equation are the turbulent transport term,

$$-\frac{\partial\langle\rho u_2''z''\rangle}{\partial x_2}, \tag{4.6}$$

and the molecular diffusion term,

$$\frac{\partial}{\partial x_2}\left(\overline{\rho\mathcal{D}_z\frac{\partial z}{\partial x_2}}\right) . \tag{4.7}$$

The standard model for the turbulent flux

$$\overline{\rho}\widetilde{u_2''z''} = \langle\rho u_2''z''\rangle \approx -\overline{\rho}\frac{\nu_t}{\mathrm{Sc}_t}\frac{\partial\widetilde{z}}{\partial x_2} \tag{4.8}$$

is evaluated below. The turbulent viscosity $\nu_t = C_\mu k^2/\varepsilon$ is from the k-ε model and Sc_t, the turbulent Schmidt number, is a model constant. Additionally, two alternatives are tested. Rather than assuming a constant turbulent Schmidt number is sufficient to obtain the appropriate diffusivity D_t from ν_t as in eq. (4.8), the first is a gradient-diffusion model which uses the mixing timescale (τ_{mix}) directly instead of the turbulent timescale (τ_{turb}) such that

$$\begin{aligned} D_t &= \overline{\rho}C_{mix}\frac{\widetilde{z''z''}}{\widetilde{\chi}_p}k \\ \langle\rho u_2''z''\rangle &\approx -\overline{\rho}C_{mix}\frac{\widetilde{z''z''}}{\widetilde{\chi}_p}k\frac{\partial\widetilde{z}}{\partial x_2} \end{aligned} \tag{4.9}$$

where C_{mix} is a constant. The second accounts for an anisotropic turbulent diffusivity in the style of Daly and Harrow [81], i.e.

$$\langle \rho u_2'' z'' \rangle \approx -\overline{\rho} \frac{C_{ani}}{\mathrm{Sc}_t} \frac{k}{\varepsilon} \widetilde{u_2'' u_2''} \frac{\partial \widetilde{z}}{\partial x_2} \,, \tag{4.10}$$

where C_{ani} is a constant. For the molecular diffusion closure, the standard model for the molecular diffusive flux

$$\langle \rho \mathcal{D}_z \frac{\partial z}{\partial x_2} \rangle \approx \langle \rho \rangle \langle \mathcal{D}_z \rangle \frac{\partial \widetilde{z}}{\partial x_2} \tag{4.11}$$

is tested along with an alternative model which uses the appropriate leading order term,

$$\langle \rho \mathcal{D}_z \rangle \frac{\partial \widetilde{z}}{\partial x_2} \,. \tag{4.12}$$

To start, terms in the evolution equation for the mean mixture fraction eq. (4.5) are shown in fig. 4.14. The convective term,

$$- \frac{\partial \overline{\rho} \widetilde{u}_2 \widetilde{z}}{\partial x_2} \,, \tag{4.13}$$

and the turbulent transport term (eq. (4.6)) dominate over molecular diffusion throughout the evolution of the jet. Though, diffusion does make a small contribution during the initial stages. Of the unclosed terms in eq. (4.5), modeling the turbulent flux is the primary concern for this configuration.

As seen in fig. 4.15, the standard gradient-diffusion model (eq. (4.8)) overpredicts the turbulent flux for most of the simulation then underpredicts it after 15 ms. The anisotropic model (eq. (4.10)) performs best out of the three, matching the flamelet DNS well at 5 ms and more closely capturing the behavior from the centerline to the peak at 10 and 15 ms. None of the models are in particularly good agreement with the DNS at $t = 20$ ms. Figure 4.13 indicates a significant Reynolds stress anisotropy which invalidates the isotropy

ansatz which leads to the standard k^2/ε scaling of the turbulent viscosity. The anisotropic model (eq. (4.10)) is intended to address this deficiency. Additionally, while the standard model (eq. (4.8)) has a dependence on the strength of the velocity fluctuation $u_2''u_2''$ via $k = 1/2\ \widetilde{u_i''u_i''}$ in the turbulent diffusivity, there is no explicit dependence on the fluctuating mixture fraction. The scalar variance and the scalar flux are reasonably well correlated so one might expect that the scalar variance would be a missing dependence in the standard model. However, including this dependence in the manner of eq. (4.9) does not yield a significant improvement.

It is appropriate to ask how the closure for the Reynolds shear stress

$$\widetilde{u_1''u_2''} \approx -C_\mu \frac{k^2}{\varepsilon} \frac{\partial \widetilde{u}_2}{\partial x_2} \tag{4.14}$$

performs since the turbulent timescale more naturally applies to the momentum flux. An *a priori* evaluation is shown in fig. 4.16. The model does a good job of capturing the breadth of the profile throughout the calculation but severely overpredicts the peak during the first half of the jet's development. As the flame becomes increasingly turbulent, improvement is seen until there is good agreement with the DNS at 20 ms. However, there is no evidence that the model would continue to perform well at later times. Certainly, it is unsatisfactory for most of the observed flame evolution.

In fig. 4.17, the standard model for mean molecular diffusion of z (eq. (4.11)) tends to overpredict the peak flux by roughly a factor of two. This includes early in the jet evolution when the mixture fraction field has only weak fluctuations and the molecular diffusion is nonnegligible. The alternative model (eq. (4.12)) can be derived directly by simply neglecting the fluctuating contributions to the molecular diffusion term. However, for this configuration, it only performs marginally better and molecular diffusion contributions are small. Regardless, it seems that the alternative is preferable, since it requires fewer

assumptions.

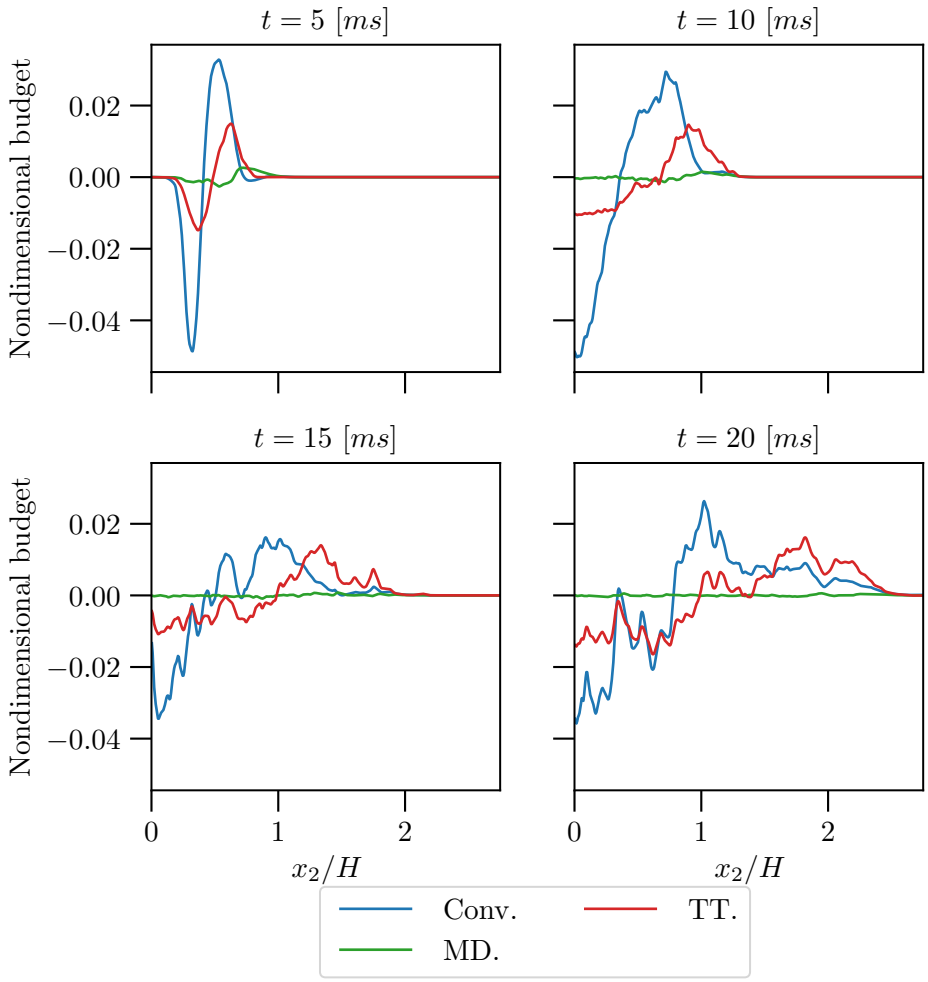

Figure 4.14: Terms in the mean mixture fraction equation over the course of the simulation. Time derivative term not shown. TT is turbulent transport, MD is molecular diffusion. The terms are nondimensionalized by $\rho_R \Delta U H^{-1}$.

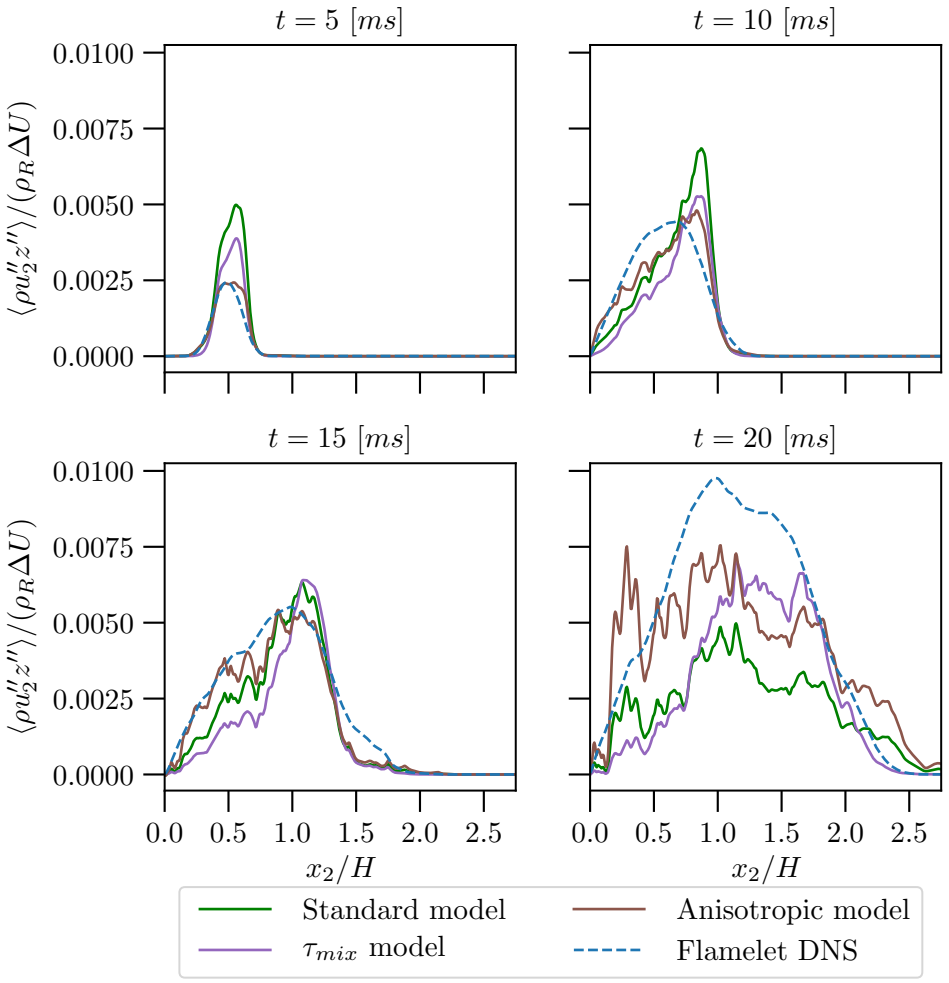

Figure 4.15: *A priori* comparison of closures for the turbulent flux $\langle \rho u_2'' z'' \rangle$: standard (eq. (4.8)), τ_{mix} (eq. (4.9)), and anisotropic (eq. (4.10)).

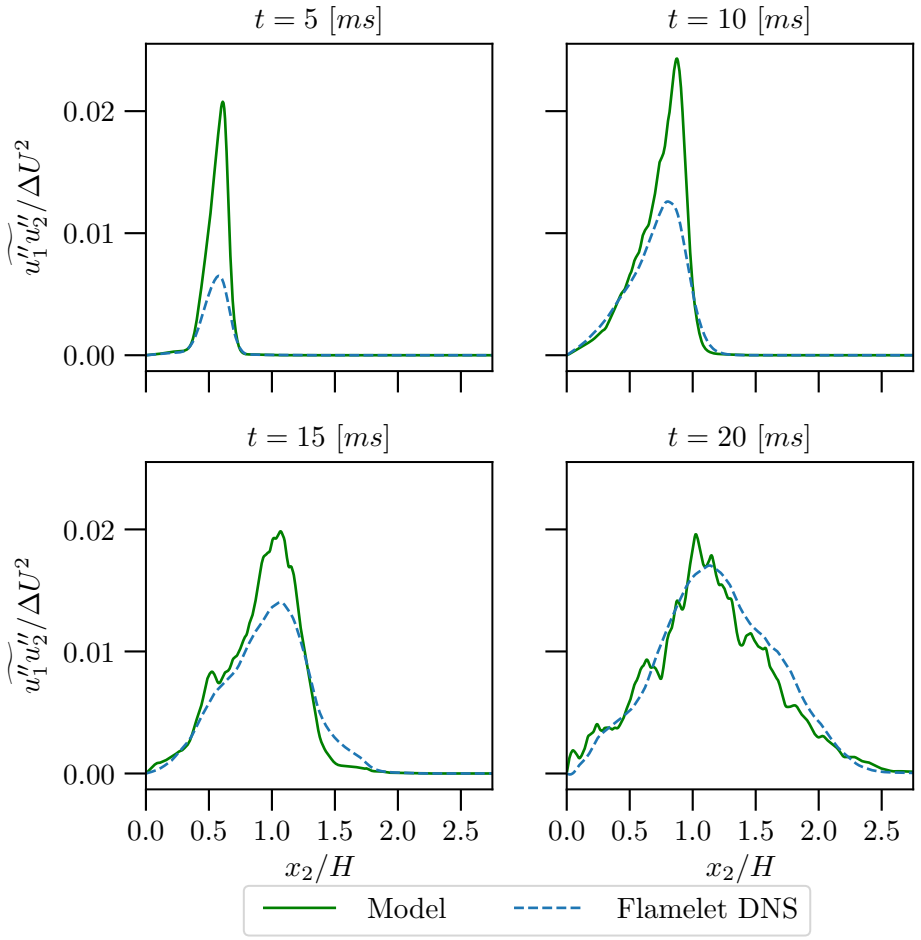

Figure 4.16: *A priori* comparison of the closure (eq. (4.14)) for the Reynolds shear stress $\widetilde{u_1''u_2''}$.

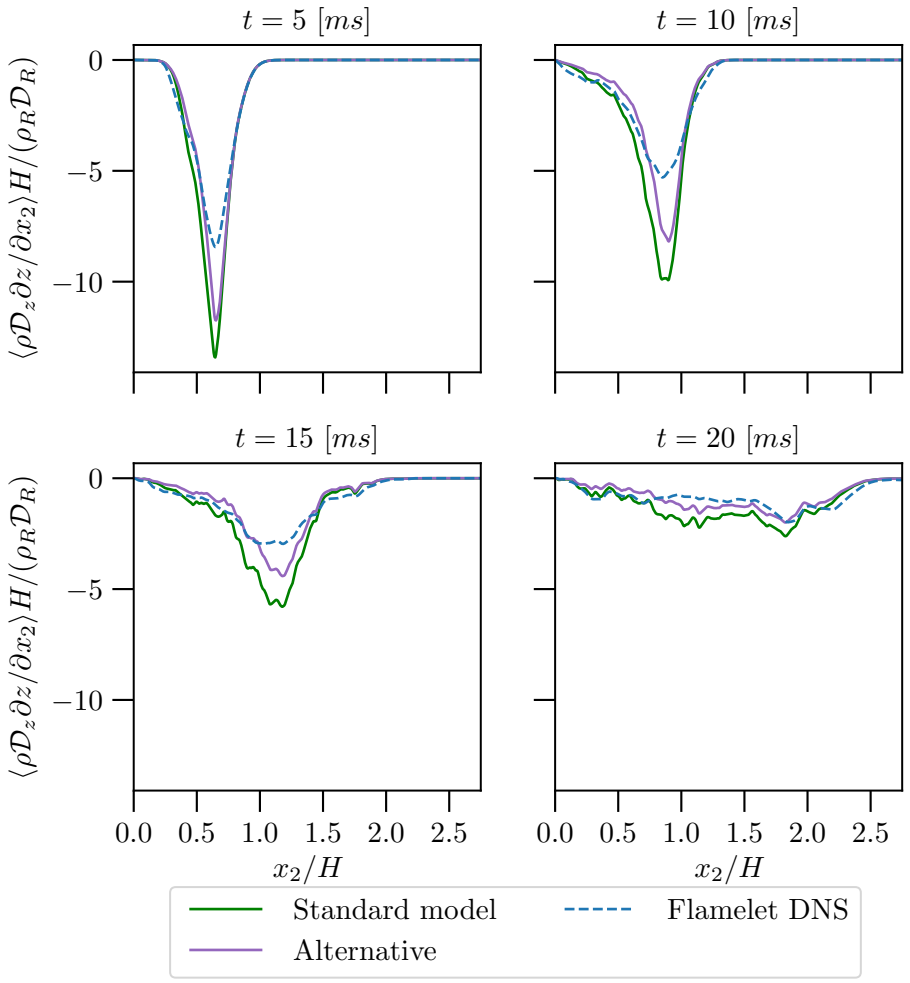

Figure 4.17: *A priori* comparison of the closures for molecular diffusive flux $\langle \rho \mathcal{D}_z \partial z / \partial x_2 \rangle$: standard (eq. (4.11)), alternative (eq. (4.12)).

4.5.2.2 Mixture fraction variance equation

For the planar, reacting jet the mixture fraction variance equation, eq. (2.22), simplifies to

$$\underbrace{\frac{\partial \overline{\rho}\widetilde{z''z''}}{\partial t}}_{\text{temporal}} + \underbrace{\frac{\partial}{\partial x_2}\left(\overline{\rho}\widetilde{u}_2\widetilde{z''z''}\right)}_{\text{convection}} = -\underbrace{\frac{\partial}{\partial x_2}\left(\overline{\rho u_2'' z'' z''}\right)}_{\text{turbulent transport}} + \underbrace{\frac{\partial}{\partial x_2}\left(\overline{\rho \mathcal{D}_z \frac{\partial z'' z''}{\partial x_2}}\right)}_{\text{molecular diffusion 1}} + \underbrace{\overline{2z''\frac{\partial}{\partial x_2}\left(\rho \mathcal{D}_z \frac{\partial \widetilde{z}}{\partial x_2}\right)}}_{\text{molecular diffusion 2}} - \underbrace{2\overline{\rho u_2'' z''}\frac{\partial \widetilde{z}}{\partial x_2}}_{\text{production}} - \underbrace{2\overline{\rho \mathcal{D}_z \frac{\partial z''}{\partial x_2}\frac{\partial z''}{\partial x_2}}}_{\text{dissipation}}, \tag{4.15}$$

The unclosed terms are the turbulent transport term, the two molecular diffusion terms, production, and dissipation. The evolution of terms in the mixture fraction variance equation over time are shown in fig. 4.18. Similar to the $\widetilde{z}$ equation, the turbulent transport term plays a much larger role than the molecular diffusion terms, especially as the mixture fraction field becomes fully turbulent. Production and dissipation are both significant throughout the flame's evolution.

The unclosed portion of the production is $\langle \rho u_2'' z'' \rangle$ whose modeling is evaluated in section 4.5.2.1. RANS models neglect the contribution of molecular diffusion, assuming it is negligible relative to turbulent transport. The standard model for the turbulent scalar flux is

$$\langle \rho u_2'' z'' z'' \rangle \approx -\overline{\rho}\frac{\nu_t}{\mathrm{Sc}_t}\frac{\partial \widetilde{z''z''}}{\partial x_2}, \tag{4.16}$$

akin to eq. (4.8). As with $\langle \rho u_2'' z'' \rangle$, it is reasonable to use the mixing timescale to define the

turbulent diffusivity, which gives

$$\langle \rho u_2'' z'' z'' \rangle \approx -\overline{\rho} C_{mix} \frac{\widetilde{z'' z''}}{\widetilde{\chi}_p} k \frac{\partial \widetilde{z'' z''}}{\partial x_2} \,, \tag{4.17}$$

or an anisotropic turbulent diffusivity,

$$\langle \rho u_2'' z'' z'' \rangle \approx -\overline{\rho} \frac{C_{ani}}{\mathrm{Sc}_t} \frac{k}{\varepsilon} \widetilde{u_2'' u_2''} \frac{\partial \widetilde{z'' z''}}{\partial x_2} \,, \tag{4.18}$$

so both of these options are tested as well. Finally, the fluctuating portion of the scalar dissipation rate $\widetilde{\chi}_p$ closes the dissipation. The standard model, which assumes τ_{turb} is proportional to τ_{mix},

$$\widetilde{\chi}_p \approx c_\chi \widetilde{z'' z''} \frac{\varepsilon}{k} \,, \tag{4.19}$$

will be evaluated.

The sum of the molecular diffusion contributions to the mixture fraction budget are plotted along with the turbulent transport contribution in fig. 4.19. Generally, the RANS assumption of negligible molecular diffusion holds except at early time when the mean shear is greatest and z fluctuations are weak. Hence, the major modeling challenge lies in representing the turbulent flux $\langle \rho u_2'' z'' z'' \rangle$, $\langle \rho u_2'' z'' \rangle$ in production (see fig. 4.15 and the discussion in section 4.5.2.1), and the fluctuating scalar dissipation rate $\widetilde{\chi}_p$.

An *a priori* comparison of the evolution of the RANS closures for the turbulent scalar flux with the flamelet DNS appears in fig. 4.20. The standard model (eq. (4.16)) does well to capture the maxima and minima of the true profile for the first three snapshots before breaking down at late time. Using the mixing timescale in the turbulent diffusivity (eq. (4.17)) does not significantly change the result. The anisotropic eddy diffusivity model (eq. (4.18)) arguably agrees best with the DNS, as it appears to capture the minima of the profile most closely at late time, though none of the models is particularly accurate. The better late-time

behavior of the anisotropic model is presumably due to the evolving anisotropy of the turbulent fluctuations as the large-scale jet instabilities dominate the turbulence at late time.

An *a priori* comparison of the evolution of the RANS closure for $\widetilde{\chi}_p$ (eq. (4.19)) with the flamelet DNS is shown in fig. 4.21. The model consistently overpredicts the scalar dissipation rate but tends to capture the width of the profile. The latter is unsurprising given the jet width defined by the mixture fraction is similar to the jet width defined by the streamwise velocity (fig. 4.22). During the first half of the calculation, the ratio of the mixing to turbulent timescale varies throughout the jet and does not match well with the model constant C_χ (fig. 4.23). This assumption breaks down further as the flame becomes more turbulent and the mixing timescale grows more rapidly than the turbulent timescale. At the final snapshot, the timescale ratio varies by almost an order of magnitude. All of this is consistent with fig. 4.12 which demonstrates that the scalar mixing continues to intensify throughout the course of the flame's evolution whereas k peaks early on. Note also that the timescale ratio at the center of the jet is consistent lower than near the edge of the jet. This is presumably due to the intermittency and dominance of large scale fluctuations arising from the Kelvin-Helmholtz instability at the edge of the jet.

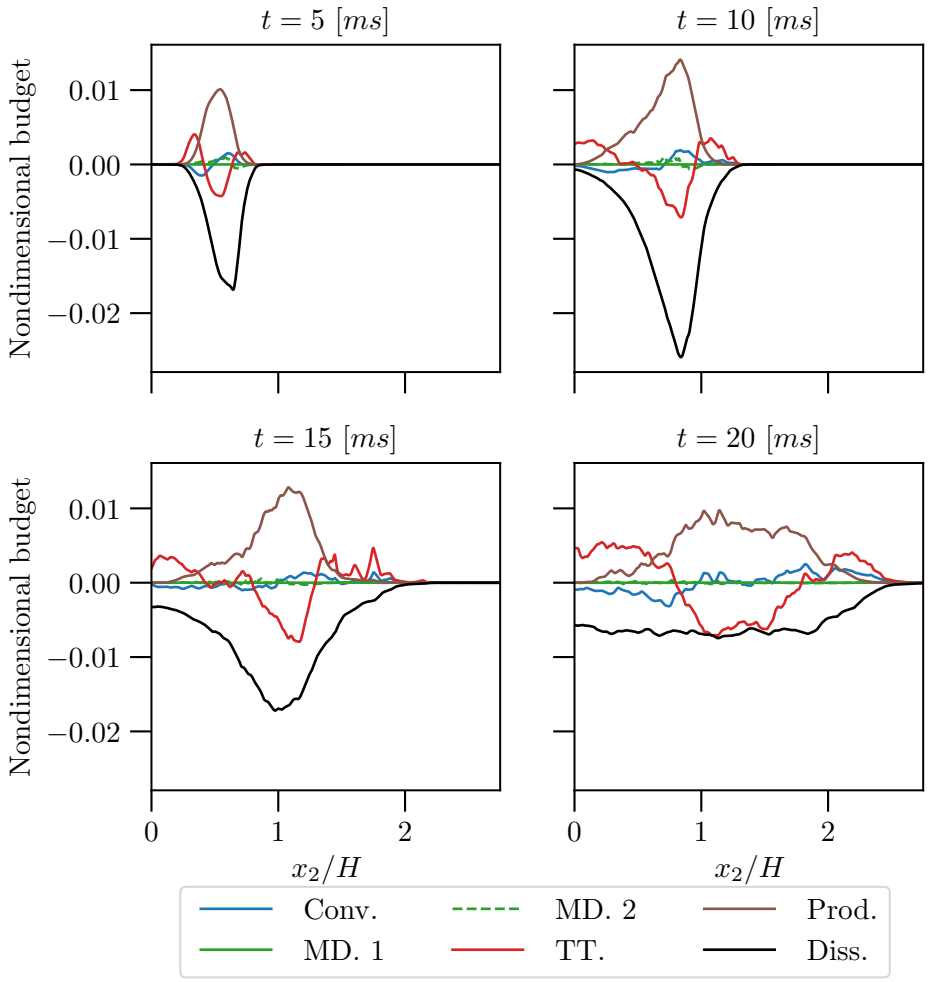

Figure 4.18: Terms in the mixture fraction variance equation over the course of the simulation. Time derivative term not shown. TT is turbulent transport, MD is molecular diffusion. The terms are nondimensionalized by $\rho_R \Delta U H^{-1}$.

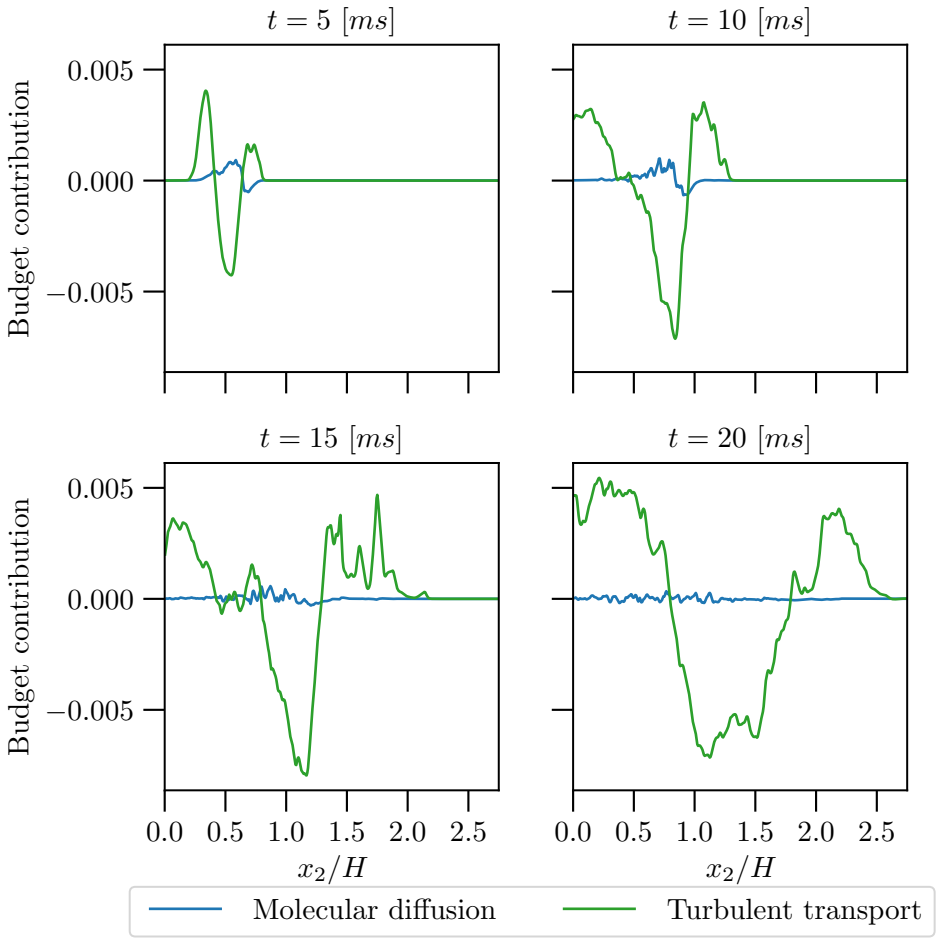

Figure 4.19: The sum of the molecular diffusion terms along with the turbulent transport contribution to mixture fraction variance equation, eq. (2.22). The terms are nondimensionalized by $\rho_R \Delta U H^{-1}$.

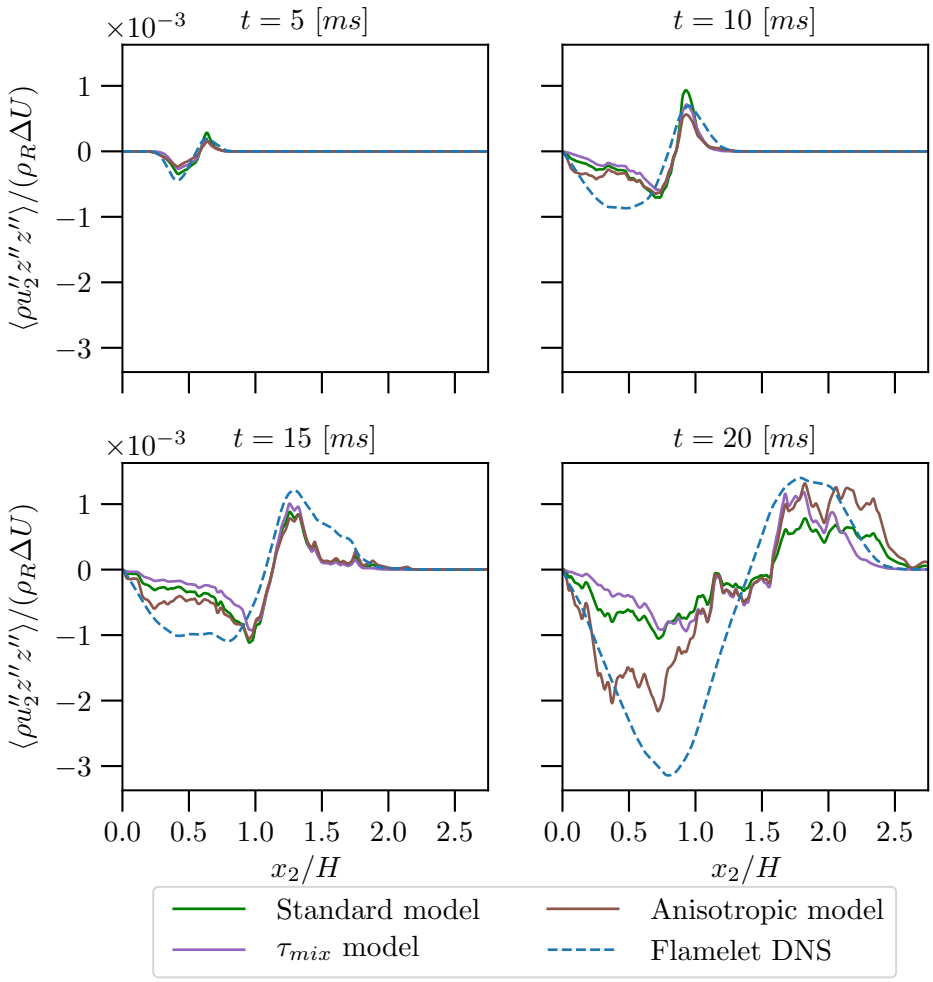

Figure 4.20: *A priori* comparison of the RANS-based closures for the turbulent flux $\langle \rho u_2'' z'' z'' \rangle$: standard model (eq. (4.16)), τ_{mix} model (eq. (4.17)), and anisotropic model (eq. (4.18)).

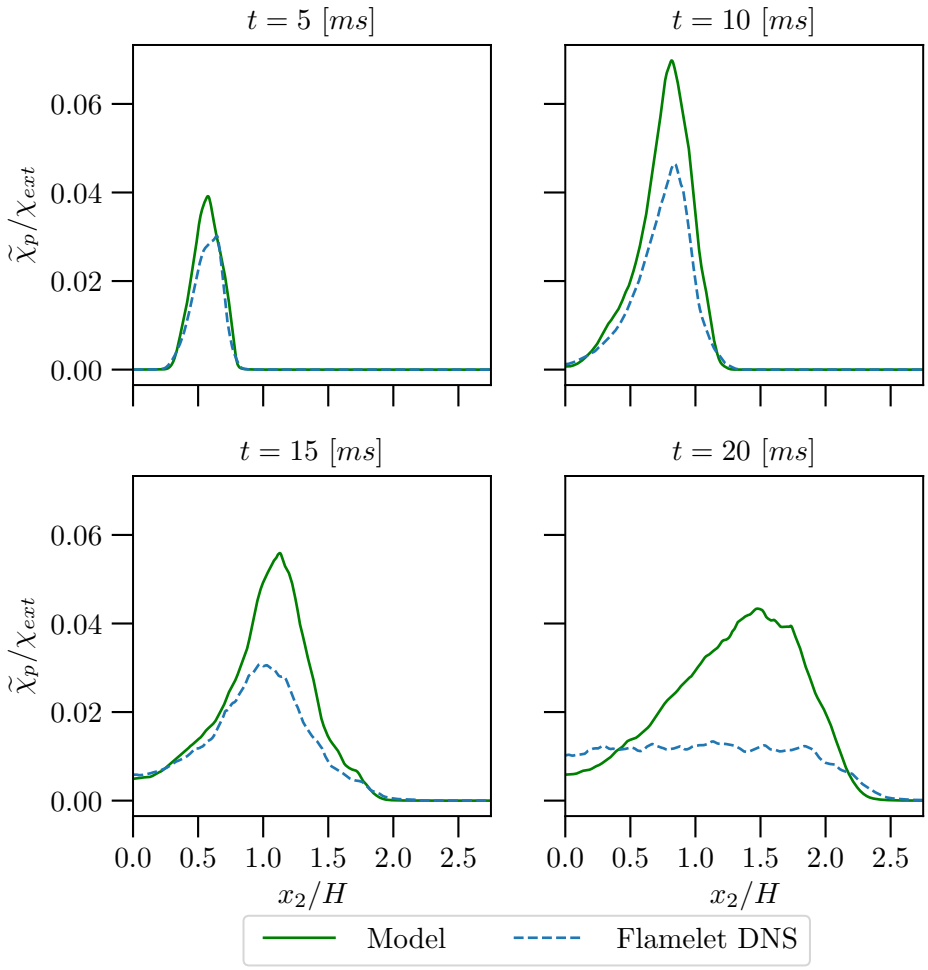

Figure 4.21: *A priori* comparison of the RANS-based closure with the flamelet DNS for the fluctuating scalar dissipation rate $\widetilde{\chi}_p$ (see eq. (4.19)).

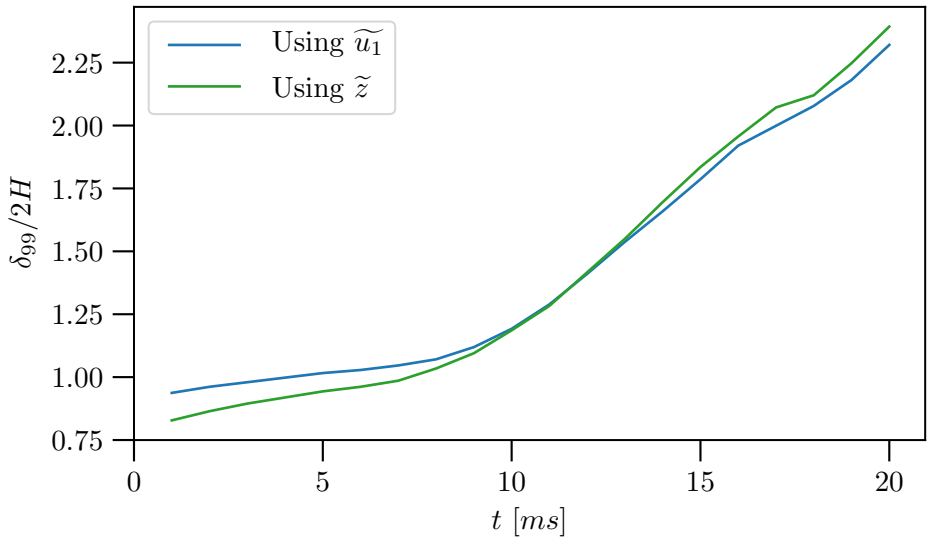

Figure 4.22: Jet width (δ_{99}) defined by the mean streamwise velocity and mean mixture fraction profiles as a function of time. The widths are based on the location at which 99% of the freestream value is obtained.

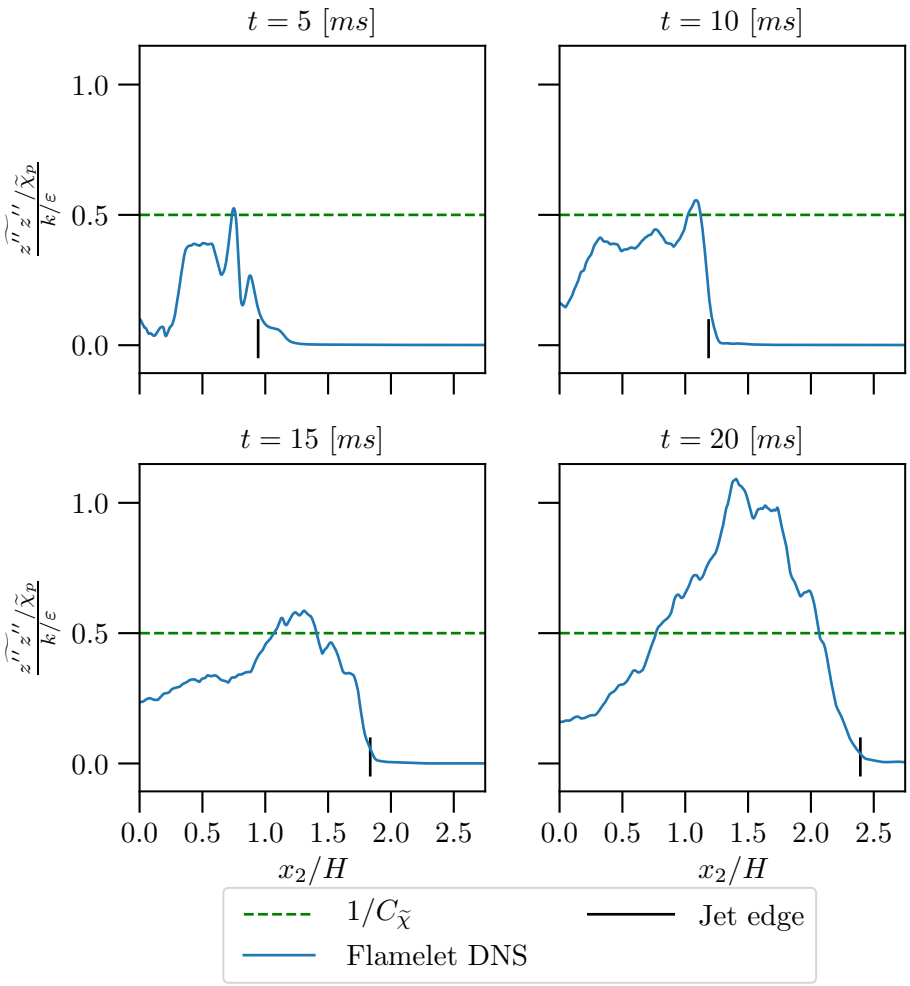

Figure 4.23: *A priori* comparison of the closure for the ratio of mixing and turbulent timescales $1/c_\chi = \frac{\widetilde{z''z''}\varepsilon}{\widetilde{\chi}_p k}$ over the course of the simulation. The ratio falls to zero in the freestream.

4.5.2.3 Presumed PDF models

The presumed PDF models used to determine mean thermochemical and transport quantities from the statistics of z as described in section 2.3.2 are analyzed below. The χ PDF is assumed to be

$$\begin{aligned} f_\chi(\chi) &= \frac{1}{\chi\sigma\sqrt{2\pi}} \exp\left(-\frac{\left(\log\chi - \mu_\chi\right)^2}{2\sigma^2}\right) \\ \mu_\chi = \log\left(\widetilde{\chi}\right) - \frac{\sigma^2}{2} \qquad & \sigma = \log\left(\frac{\widetilde{\chi''^2}}{\widetilde{\chi}^2} + 1\right) \end{aligned} \tag{4.20}$$

where the parameters μ_χ and σ are obtained from moments of χ. The presumed z PDF (eq. (2.25), repeated here for convenience) is

$$\begin{aligned} \widetilde{f}_z(z) &= \frac{\Gamma(a+b)}{\Gamma(a)\,\Gamma(b)} z^{a-1}(1-z)^{b-1} \\ a = \widetilde{z}\left\{\frac{\widetilde{z}(1-\widetilde{z})}{\widetilde{z''z''}} - 1\right\} \qquad & b = \frac{a}{\widetilde{z}} - a\,. \end{aligned}$$

Beyond the assumption of a log-normal scalar dissipation rate PDF, two further ansatzes are posed about the turbulent fluctuations to simplify the modeling. First the contribution of the mean gradients to the total mean scalar dissipation rate $\widetilde{\chi}$ is negligible. This appears to be justified except at early times (5 ms) when the mixture fraction fluctuations have not yet fully developed (fig. 4.24). The second assumption is that the variance of χ is proportional to $\widetilde{\chi}^2$. This assumption is poorly supported by the *a priori* comparison of the two quantities (fig. 4.25) where it is clear that the ratio of these quantities is neither constant in x_2 nor time. Even if this discrepancy is accounted for by constructing a log-normal PDF whose first two moments match the mean and the variance of χ from the flamelet DNS as shown in fig. 4.26, the modeled scalar dissipation rate PDF compares poorly with that of the flamelet DNS for small χ. This is problematic since these are the highest probability events. Also included in fig. 4.26 are sample PDFs of χ conditioned on z from the flamelet DNS. The model has

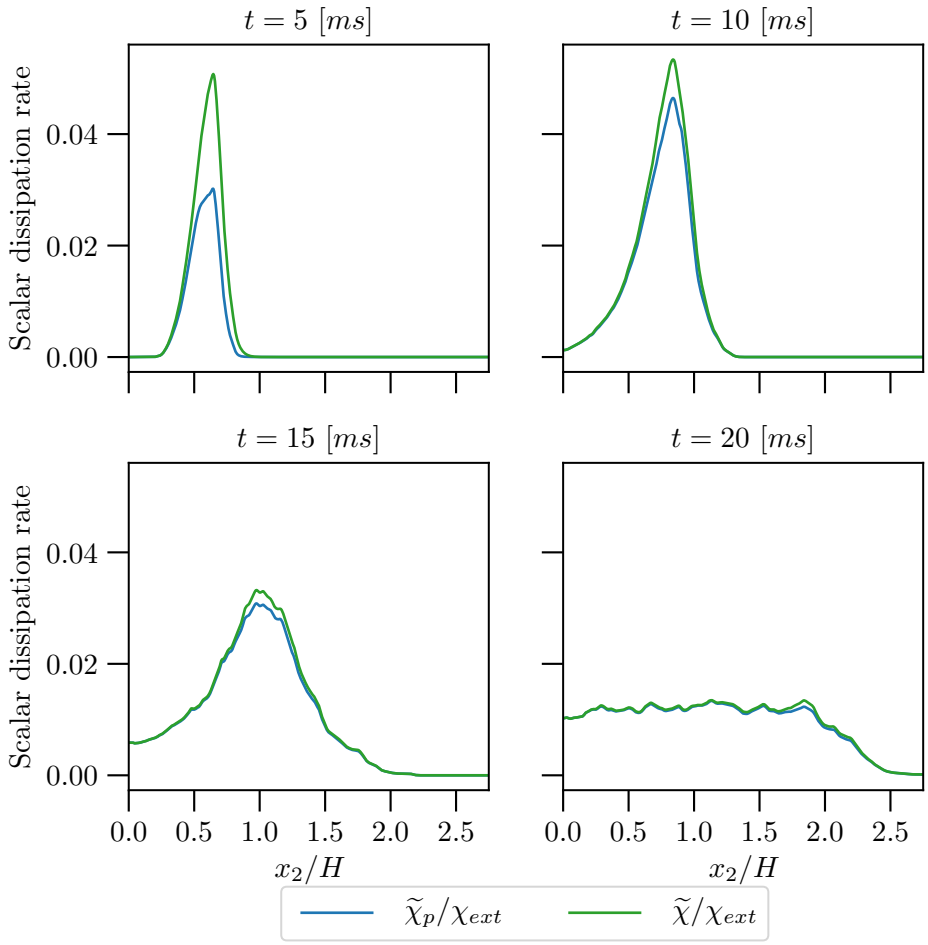

Figure 4.24: Evolution of the mean scalar dissipation rate. $\widetilde{\chi}_p$ is solely due to the z fluctuations whereas $\widetilde{\chi}$ includes the mean gradients.

no dependence on z but the conditional PDFs invalidate this assumption for $\chi < 1\ s^{-1}$, especially when fluctuations in mixture fraction are small ($t = 5\ ms$).

Another important modeling assumption is the presumed β-PDF of the mixture fraction fluctuations. From fig. 4.27 it is clear that at $t = 15\ ms$ a β-PDF parameterized to match the mean and variance of z is a good representation of the mixture fraction PDF from the flamelet DNS in the core of the jet (smaller x_2) but cannot represent the multi-modal structure that occurs for large x_2 – presumably due to intermittency at the edge of the jet, a known challenge in the modeling of free shear flows [82–85]. At later times, the entirety of the

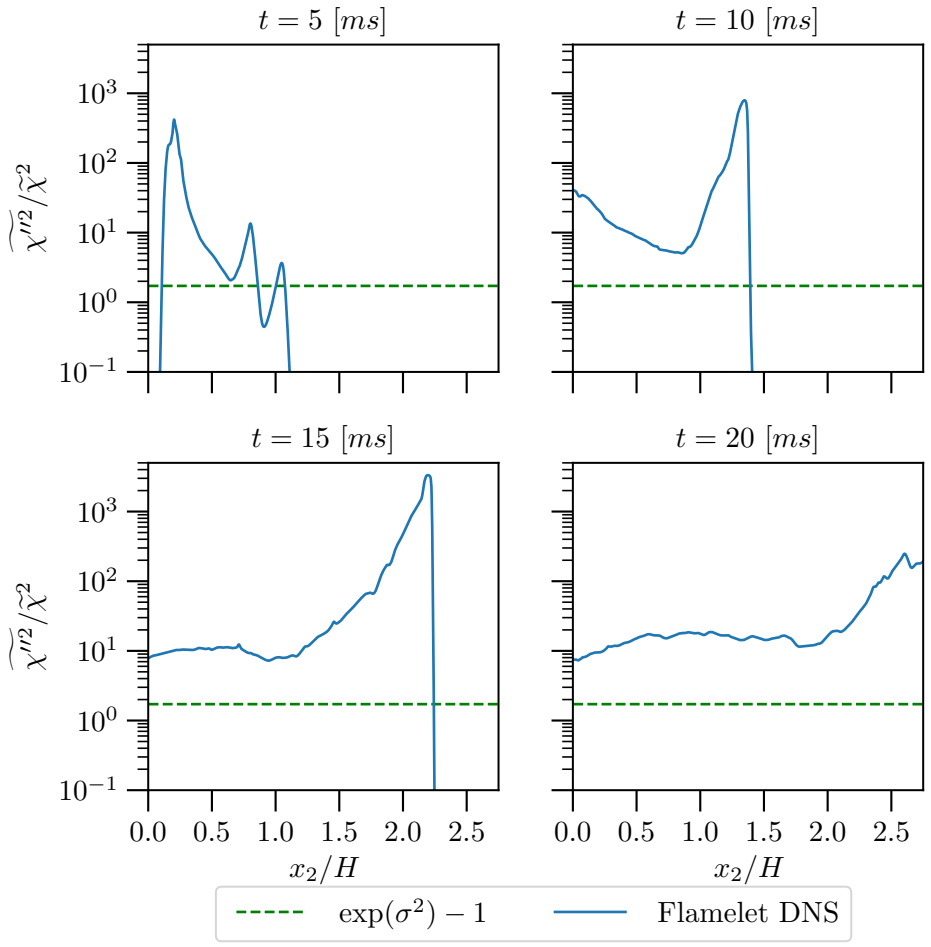

Figure 4.25: *A priori* comparison of the closure for the scalar dissipation rate variance from eq. (2.26).

jet is becoming more spatially intermittent, leading to a general breakdown of the β-PDF, as indicated by comparisons of the third moment obtained from the assumed PDF and from the flamelet DNS (fig. 4.28), since the third moment is not forced to agree. Appendix I contains *a priori* comparisons of the mixture fraction PDF at other times. The PDF model agrees most poorly with the DNS at 20 ms and best at 10 ms, perhaps because it is late enough to have well developed mixture fraction fluctuations, while early enough that intermittency does not dominate.

The mean density, mean mixture fraction diffusivity, and mean viscosity close the RANS

equations for nonpremixed combustion and are determined from the presumed β-PDF model. The mean density and mean mixture fraction diffusivity (see figs. 4.29 and 4.30) match very well with the DNS at 10 ms but the density is underpredicted at 15 ($\sim$10%) and 20 ms ($\sim$20%) in regions where the assumed PDFs are poor representations (figs. 4.27 and 4.28). The mixture fraction diffusivity is more sensitive to the errors in the β-PDF representation, showing discrepancies at 5 ($\sim$20%) and 15 ms ($\sim$20%) and vastly underperforming ($\sim$ 50%) at 20 ms. The comparison of the mean viscosity to the DNS is very similar to that of $\langle \rho \mathcal{D}_z \rangle$ (fig. 4.31). The inconsistencies in the thermodynamic and transport properties correlate to how well the assumed PDF matches $\widetilde{z''^3}$ from the flamelet DNS as this is an indicator of the inadequacy of the assumed PDF. Since molecular diffusion is only significant at early time, the inability of the model to reproduce the mixture fraction diffusivity when the mixing field is fully turbulent may not be an issue. Because of this and because the mean density is relatively well represented, one might be tempted to conclude the β-PDF is sufficient. However, the implied mean temperature, which does not directly enter this type of flamelet-based RANS model, suggests there is reason for concern. As seen in fig. 4.6, the density is lowest near the stoichiometric point and varies most rapidly with respect to mixture fraction on the fuel lean side. Conversely, the temperature (fig. I.2) is highest near the stoichiometric point, but also varies rapidly on the fuel lean side. These regions are near the edge of the jet where the model struggles to represent the increasingly turbulent, intermittent behavior as the flame evolves. Throughout the latter half of the simulation, the mean temperature implied by the β-PDF is significantly lower than in the flamelet DNS, underestimating by about 40% at 20 ms (fig. 4.32). Hence, the presumed PDF's inability to map to the correct mean state could have a large effect on predicted flame temperature, which is important in many applications.

As the flamelet used here is only z dependent, a similar analysis using the log-normal χ PDF is not possible. However, as noted in section 4.3, the equation of state has a much

stronger dependence on mixture fraction so it is likely the errors in the β-PDF modeling are most impactful.

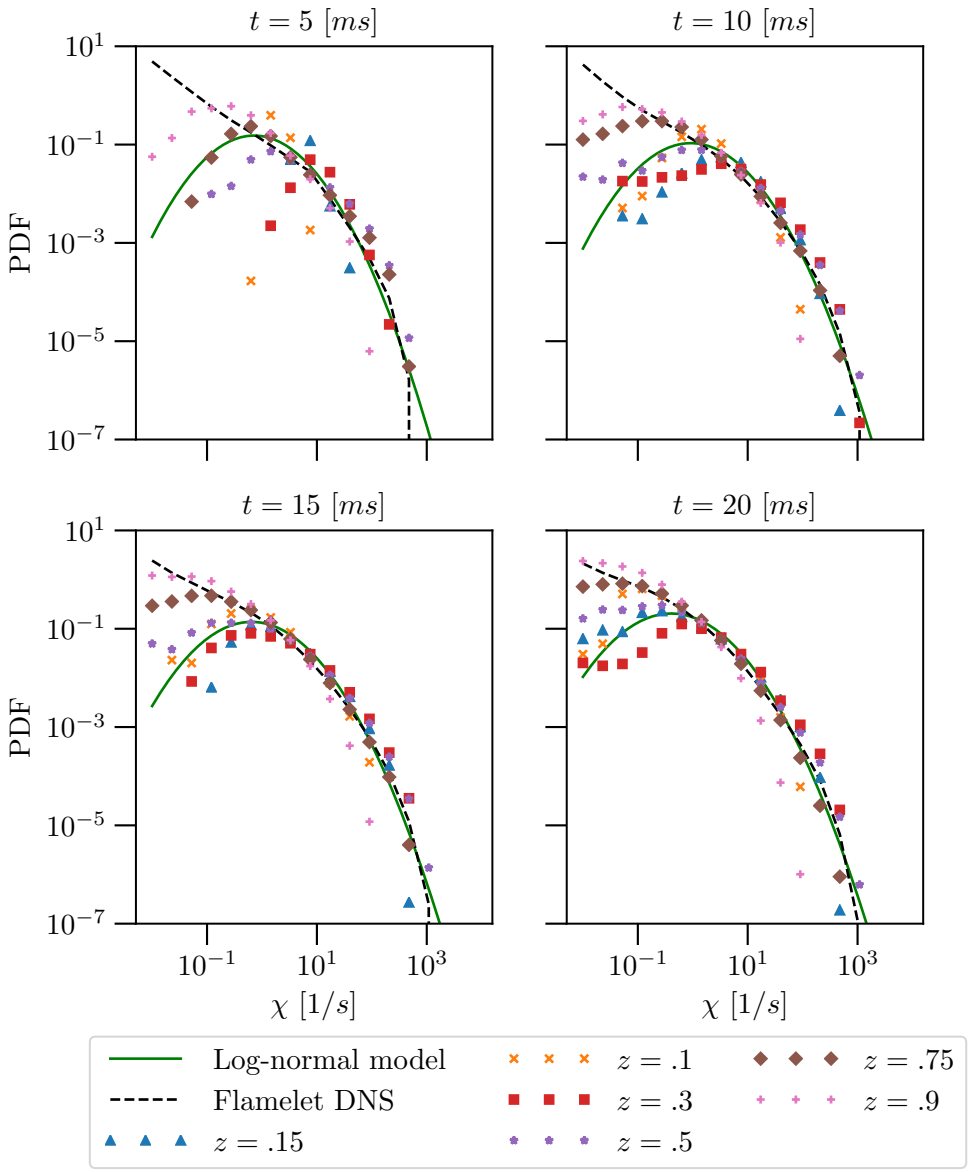

Figure 4.26: Sample PDFs of scalar dissipation rate. Also shown are log-normal PDFs (eq. (2.26)) matching the first two moments of χ and sampled PDFs of χ conditioned on mixture fraction for various values of z.

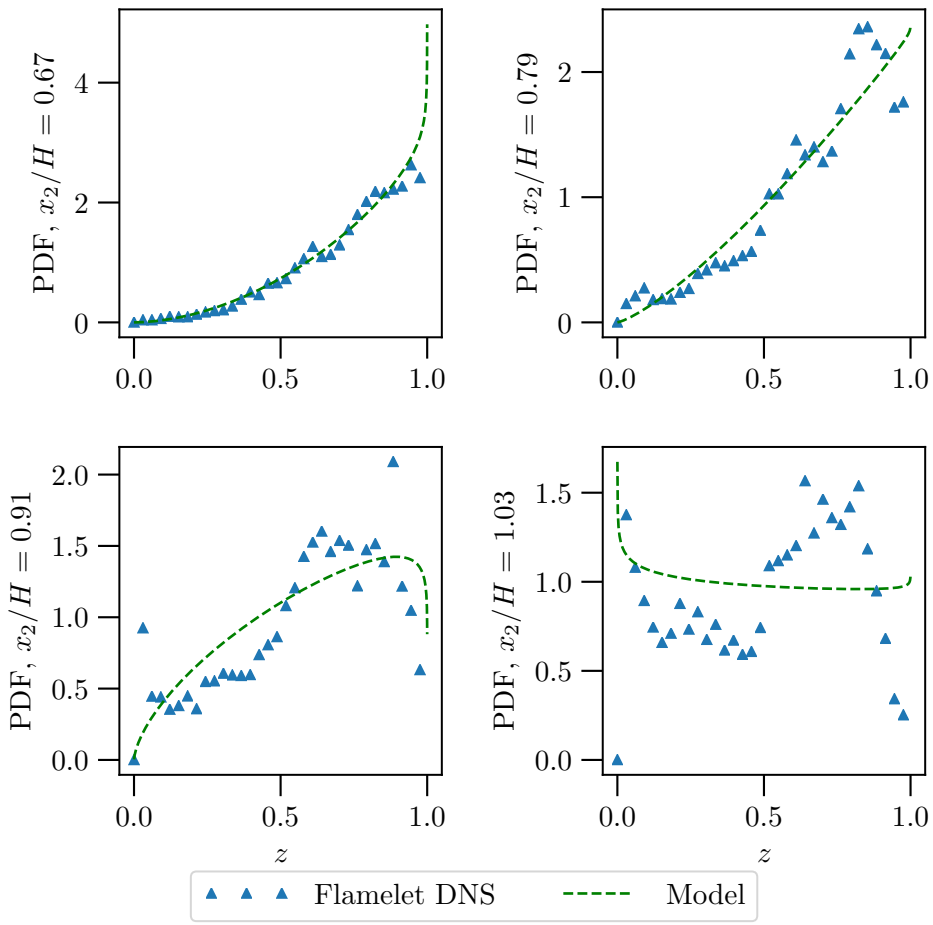

Figure 4.27: Sample PDFs of mixture fraction at various x_2 locations at 15 ms. Also shown is the β-PDF (eq. (2.25)) matching the first two sample moments of z at each location.

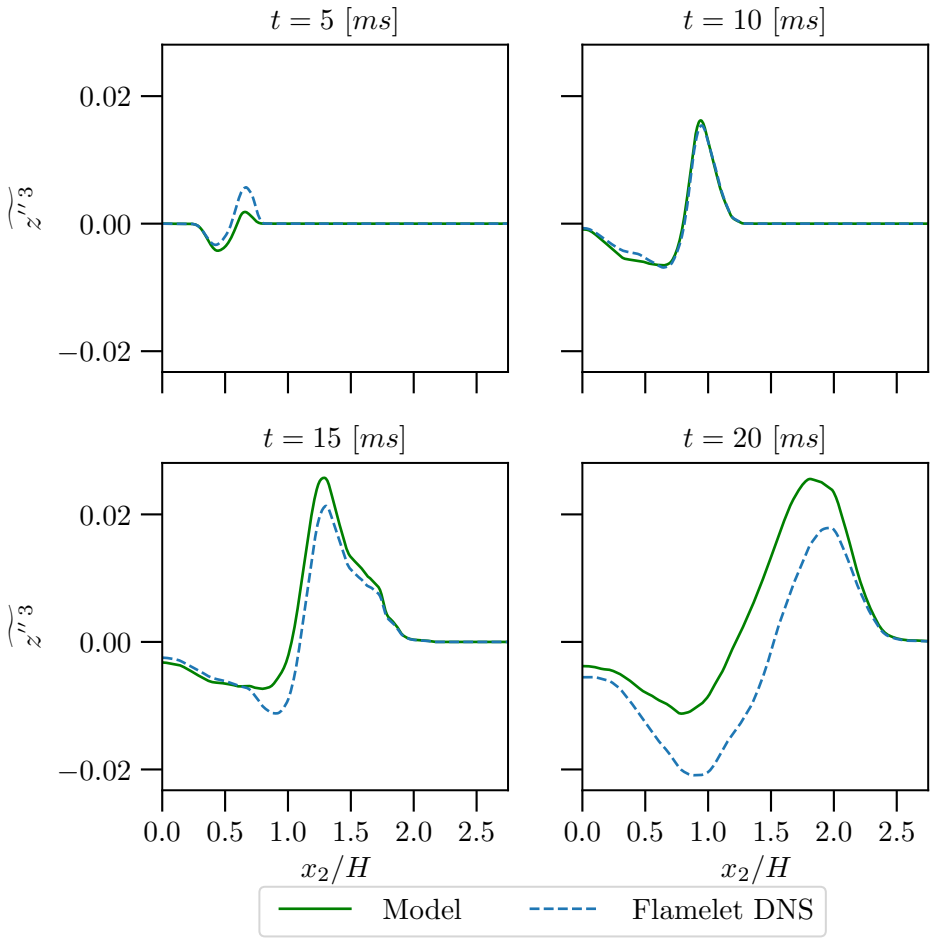

Figure 4.28: *A priori* comparison of the Favre-averaged third central moment of mixture fraction, $\widetilde{z''^3}$, from the β-PDF model (eq. (2.25)).

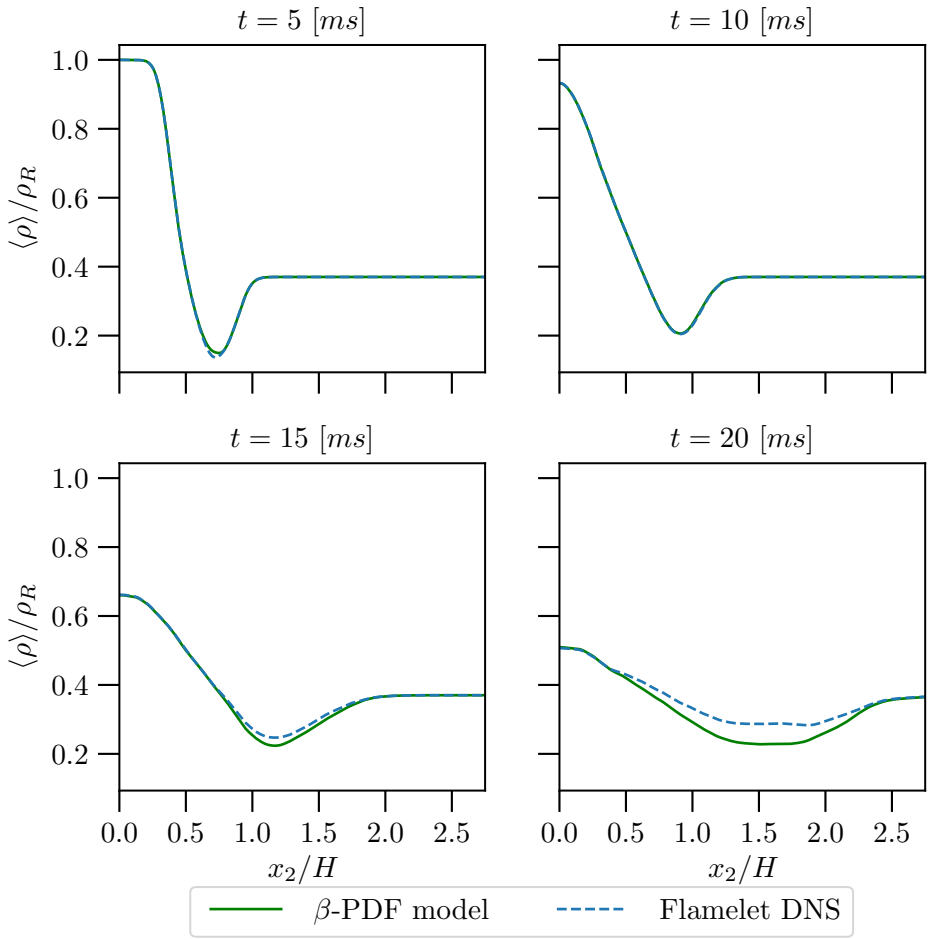

Figure 4.29: *A priori* comparison of the mean density determined from the presumed β-PDF (eq. (2.25)) with that from the flamelet DNS.

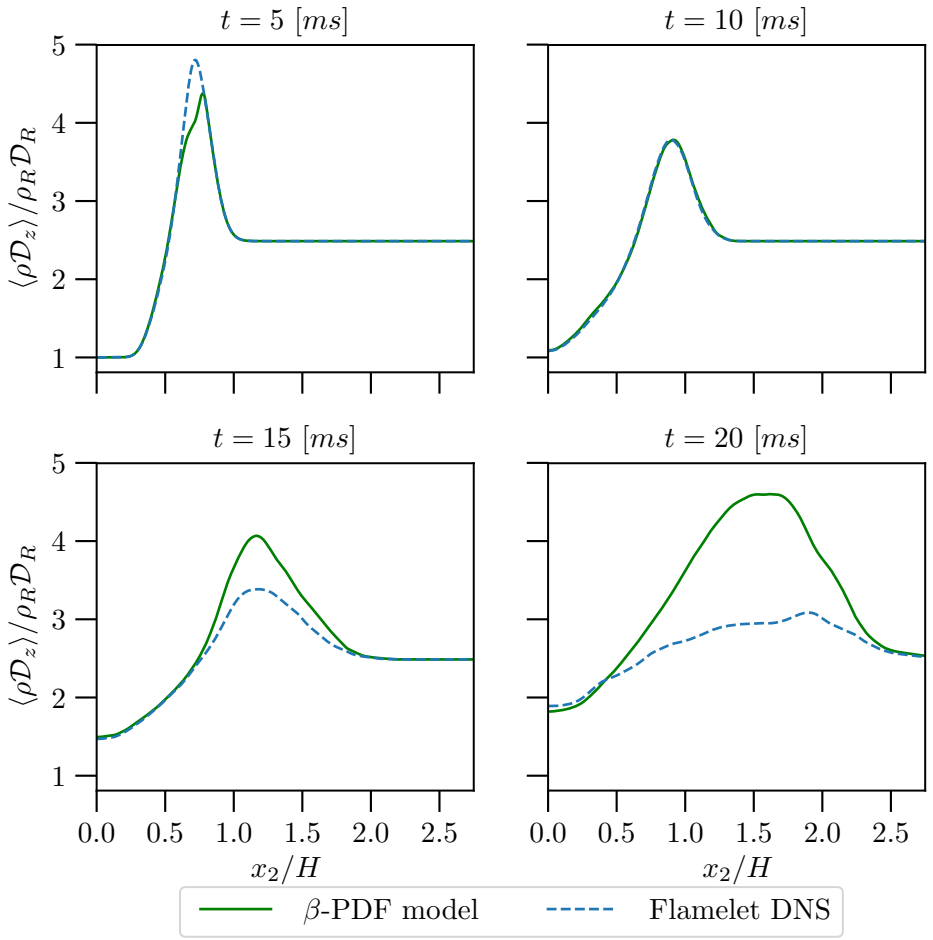

Figure 4.30: *A priori* comparison of the mean mixture fraction diffusivity determined from the presumed β-PDF (eq. (2.25)) with that from the flamelet DNS.

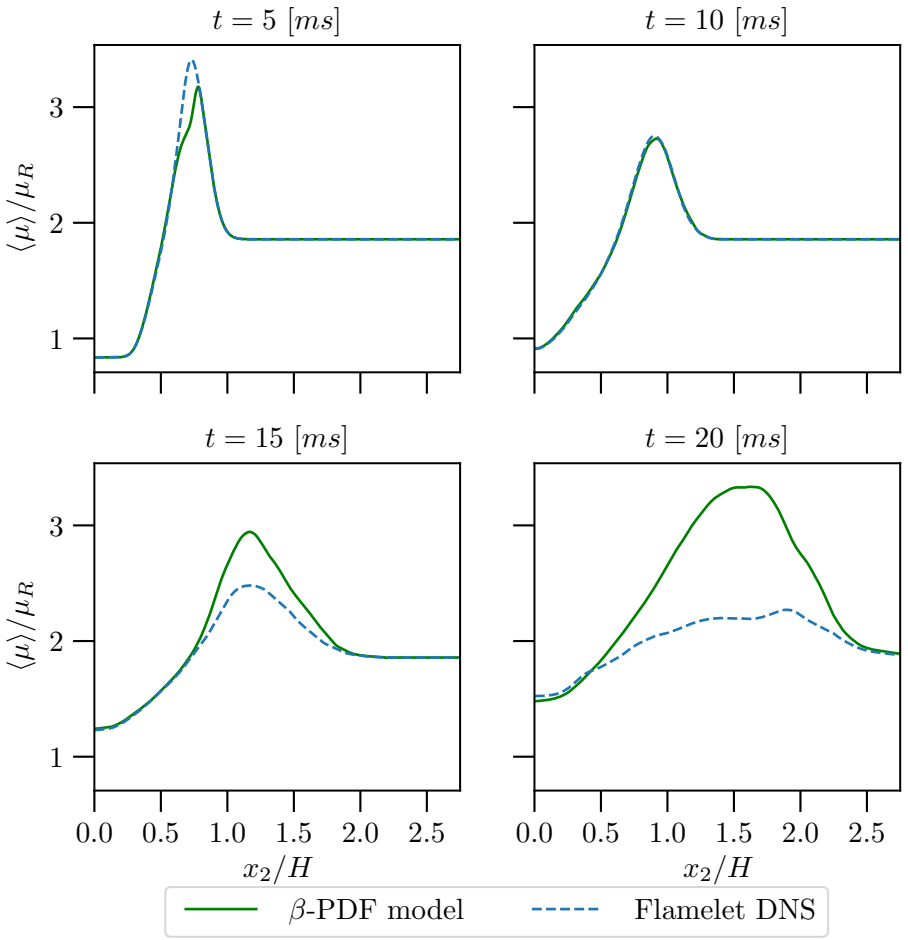

Figure 4.31: *A priori* comparison of the mean dynamic viscosity determined from the presumed β-PDF (eq. (2.25)) with that from the flamelet DNS. $\mu_R = \rho_R \nu_R$.

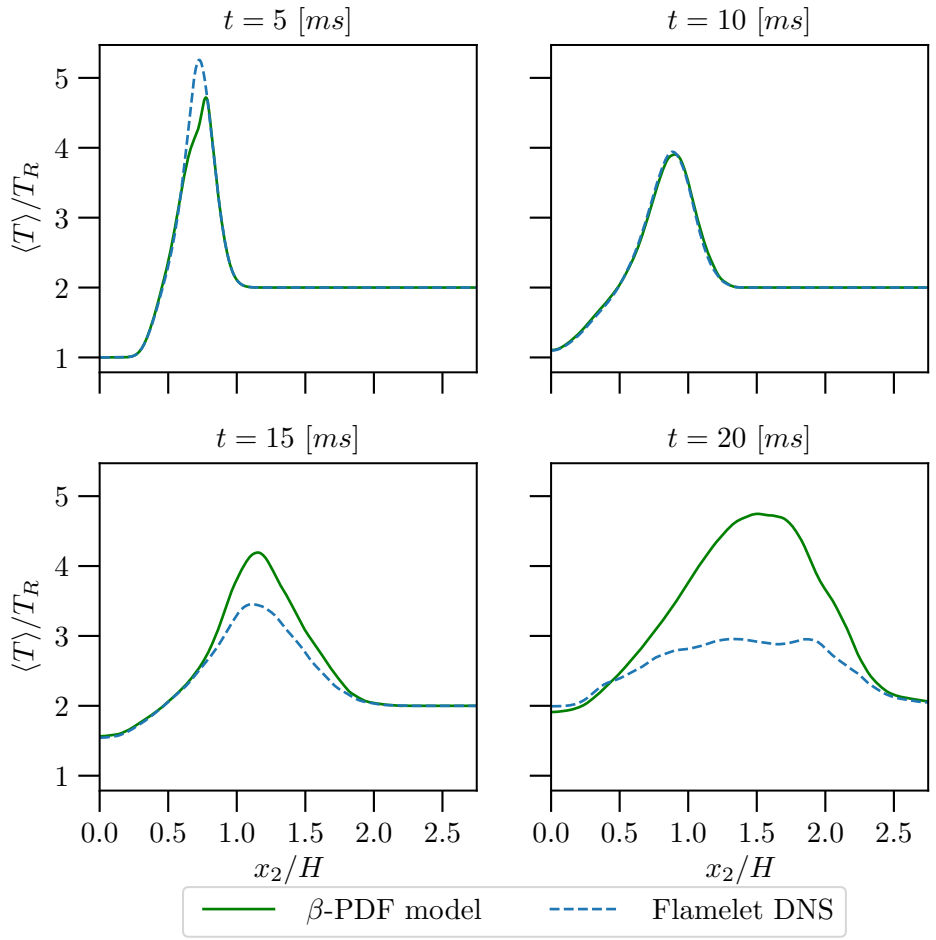

Figure 4.32: *A priori* comparison of the mean temperature determined from the presumed β-PDF (eq. (2.25)) with that from the flamelet DNS.

Chapter 5

Conclusions

The goal of this work was to evaluate the fidelity of steady laminar flamelet-based RANS models for nonpremixed turbulent combustion in a manner which respected the multiphysics nature of the modeling problem, thereby allowing for the assessment of errors from each of the three modeling focuses (turbulence, chemical reactions, turbulence-chemistry interaction) in isolation. To do so, a new DNS of the temporal, reacting jet of Attili, Bisetti, *et al.* [23] was performed using a laminar flamelet equation of state to close the governing equations instead of the complex chemistry model they employed.

To generate the flamelet DNS, a new pseudospectral method for the direct numerical simulation of low-Mach-number, variable-density flows with two statistically homogeneous directions was introduced. Based on a Helmholtz decomposition of the momentum, the approach recasts the momentum equations to eliminate the pressure. The introduction of a matrix-free, iterative scheme for solving the resulting scalar equation allows for second-order convergence in time and numerical stability for higher density ratios while retaining computational tractability. It was designed to address the implications of the redundancy among the equation of state, the mass conservation equation, and the scalar transport equation.

The algorithm is optimized to minimize storage and limit data transpose and Fourier transform operations. The novel temporal discretization scheme preserves some of the stability benefits of nonsegregated methods, without sacrificing the simple parallelizability of purely explicit schemes, and without requiring convergence to obtain the desired truncation

error. Additionally, the method discretely conserves mass by representing the component of the momentum in the inhomogeneous direction with higher order B-splines, guaranteeing the discrete divergence operation is exact. It was applied successfully to both a single-mode Rayleigh-Taylor test problem, where the density ratio could be controlled directly, and the temporally-evolving, reacting, planar jet. The test problem demonstrated the method was stable for density ratios up to about 15. In the flamelet DNS, the ratio of the maximum to minimum density is approximately 8.

A fundamental flaw in the steady laminar flamelet assumptions was identified when the use of a flamelet representation including a dependence on χ led to instabilities. For the chemical mechanism studied in this work, the behavior of the flamelet density as scalar dissipation rate tends to zero is nonphysical, leading to anomalous sharp features in the density field near local extrema in the mixture fraction. These anomalous small-scale density variations introduce instability into the calculation through the mass conservation equation and the resulting momentum field. Instead, a χ-averaged flamelet was used to simulate the reacting jet. Since the density varies weakly with scalar dissipation rate, this simplification does not significantly impact the model assessment conducted here.

Since the flamelet DNS employs the same chemistry closure as typical RANS composite models for nonpremixed, turbulent combustion, an *a posteriori* comparison with the reference complex chemistry DNS reveals the impact of the laminar flamelet assumptions. On the other hand, *a priori* evaluations of the RANS turbulence closures and associated presumed PDF models using the flamelet DNS allows these models to be evaluated without the conflation of errors from the chemical modeling. The comparisons with the complex chemistry DNS showed the mean thermodynamic properties conditioned on mixture fraction agreed well, especially for the density. However, the mean velocity and density were consistent with the flamelet DNS burning at a lower temperature and expanding less than the complex chemistry DNS. Discrepancies in the temporal evolution of the mean mixture fraction

between the flamelet and complex chemistry DNS were traced to violations of conservation discovered in the complex chemistry DNS. Hence, differences between the two simulations cannot definitively be attributed to deficiencies in the steady laminar flamelet model.

The *a priori* tests cataloged errors in closures for the turbulent and molecular diffusive fluxes in the mean mixture fraction and mixture fraction variance equations, a model for the scalar dissipation rate, and standard presumed PDF models. Gradient-diffusion models with an anisotropic turbulent diffusivity performed marginally better than other closures for the turbulent fluxes, but no model was satisfactory over the entire jet evolution. The scalar dissipation rate model performed poorly due to an invalid assumption that the turbulent and mixing timescales are proportional. The log-normal χ PDF assumption was not accurate for low values of scalar dissipation rate and the β-PDF for mixture fraction failed in regions with significant intermittency, resulting in a large discrepancy in the flame's mean temperature.

The analysis framework proposed and executed in this work is application and model specific. However, a composite multiphysics model with a representation of the coupling between different physics is common. Therefore, the ideas behind developing an "intermediate" fidelity model for turbulent combustion by employing a combination of low- and high-fidelity closures can serve as inspiration for analyzing model error in other multiphysics contexts.

5.1 Recommendations for future work

The most pressing need for further work is to resolve the conservation issue in the reference complex chemistry DNS of Attili, Bisetti, *et al.* [23]. It may be necessary to rerun this simulation. It will then be possible to unambiguously evaluate the impact of the flamelet approximation as originally envisioned for this study. This would also provide an opportunity to apply the new DNS algorithm in a context with many reacting scalars. It seems likely that the stability properties of the algorithm would be similar to that of the flamelet DNS

as both share the same underlying chemical mechanism.

A new complex chemistry DNS would provide an opportunity to more closely probe the specific steady laminar flamelet ansatzes which lead to deficiencies, using an *a priori* interrogation of the complex chemistry DNS. A place to start is by characterizing the projection error that results from representing the true thermochemical state on a low-dimensional manifold, as well as the model form error that arises from the simplified diffusive transport. Some insight on these ideas is included in section H.2.

Ultimately, a model is not deemed adequate or inadequate without an understanding of how deficiencies propagate to quantities of interest [86–88]. Hence, RANS simulations of the same reacting jet using the steady laminar flamelet model are needed. In addition to a standard *a posteriori* comparison to the flamelet DNS, sensitivity analysis can be performed to rank the closure models based on their impact on the outputs. This would identify models that require the most attention. The model errors detailed in this work could be used to directly improve closure or, since that is not always possible or practical, to inform and train model inadequacy representations which enhance the model's utility for prediction by representing uncertainty (see [86] for an overview, [87, 88] for recent examples).

The *a priori* analysis of flamelet-based RANS closures was primarily limited to aspects unique to nonpremixed combustion. It would also be worthwhile to investigate the rest of the RANS closures (i.e. models which appear in the k and ε equations) and evaluate the performance of several turbulence models (e.g. k-ω) which have been tuned and developed for incompressible flows and extended to variable-density and reacting flows through Favre averaging. Additionally, the methodology used to evaluate models for the turbulence and the turbulence-chemistry interaction is not limited to the closures discussed here. For example, transported PDF models [2] solve additional PDEs instead of fixing the PDF structure beforehand. Extensions to the standard presumed β-PDF to account for intermittency [82, 85, 89] require an indicator γ (the intermittency factor) which may be determined using

additional transport equations [83, 84] or described by moments of z [90]. Finally, large eddy simulations, which filter the governing equations rather than averaging, require models for the unresolved, subfilter terms and are becoming increasingly prevalent in turbulent combustion simulation [5, 11]. Studies similar to those pursued here could be conducted using the data from the current flamelet DNS.

Appendices

Appendix A

Enforcing Neumann boundary conditions in a weak sense

Consider a fully explicit time-stepping method advancing the equation $\partial f/\partial t = h(x_2, t)$ by the B-spline-collocation approach. Let $\mathcal{Y}^p_{coll}$ be the collocation points associated with the basis of order p. Let $\mathcal{Y}^p_{int}$ be the interior collocation points. See section 3.3.1 for more notation and details. The value of the solution at the interior points is advanced without any direct influence of the boundary conditions. Hence, strong enforcement of a Neumann condition can result in large jumps in the solution near the boundary if the gradient implied by the new interior values differs sufficiently from the boundary value. A weak or implicit enforcement can hopefully alleviate this issue and the numerical instability it can cause. This can be done by advancing the boundary points in a similar manner to the interior points using the PDE but substituting the Neumann condition when forming the residual. This is straightforward for the discrete first derivative operator where one can simply replace the resultant boundary values with the boundary conditions. Things are more complicated for the second derivative. Most simply, one could form the second derivative by applying another first derivative to the modified vector; however, the approach in this work specifically avoids repeated differentiation. Instead, the second derivative operator must be modified separately to account for the Neumann condition.

The unmodified second derivative is formed by solving

$$f'' = \sum_j f_j'' B_j^p(x'_{2,i}) = \sum_j f_j \frac{\partial^2 B_j^p}{\partial {x_2}^2}(x'_{2,i}) \qquad \forall x'_{2,i} \in \mathcal{Y}_{coll}^p \,. \tag{A.1}$$

Consider first mapping f to a second function g which respects the Neumann condition, then obtaining the second derivative by requiring the collocation rule holds for all points, including at the boundaries. The mechanics are the same as a strong enforcement but this occurs only for the purposes of forming the derivative; f itself will only feel the effect through the residual. Formally, take

$$\begin{aligned} g = \sum_j g_j B_j^p(y_i) &= \sum_m f_m B_m^k(x'_{2,i}) \qquad \forall x'_{2,i} \in \mathcal{Y}_{int}^p \\ \sum_j g_j \frac{\partial B_j^p}{\partial x_2}\bigg|_{-L_2/2} &= \frac{\partial f}{\partial x_2}\bigg|_{-L_2/2} \\ \sum_m g_j \frac{\partial B_j^p}{\partial x_2}\bigg|_{L_2/2} &= \frac{\partial f}{\partial x_2}\bigg|_{L_2/2} \end{aligned} \tag{A.2}$$

and allow

$$f'' = \sum_j f_j'' B_j^p(x'_{2,i}) = \sum_j g_j \frac{\partial^2 B_j^p}{\partial {x_2}^2}(x'_{2,i}) \qquad \forall x'_{2,i} \in \mathcal{Y}_{coll}^p \,. \tag{A.3}$$

Practically, the second derivative which weakly enforces an zero Neumann condition is constructed by solving

$$\boldsymbol{B}_{0,0}^0 \boldsymbol{c}^{f''} = \boldsymbol{B}_{0,0}^2 \boldsymbol{B}_N^{-1} \boldsymbol{I}_0 \boldsymbol{c}^f \tag{A.4}$$

where $\boldsymbol{I}_0$ is the identity matrix with the first and last rows zeroed out and $\boldsymbol{B}_N$ is $\boldsymbol{B}_{0,0}^0$ with the first and last rows replaced with their corresponding rows in $\boldsymbol{B}_{0,0}^1$.

Appendix B

Manufactured solutions

For the purpose of code verification, a manufactured solution was created using MASA [74], a C++ library which can easily generate sources terms for arbitrary equations by automatic differentiation. Respecting the pseudospectral nature of the algorithm, the spatial component of the flow variables are taken to be combinations of functions like

$$\begin{aligned} f_{ln}(x_1, x_2, x_3) &= \alpha_{ln}(x_2)\zeta_{ln}(x_1, x_3) \\ &= 2\alpha_{ln}(x_2)\{ \cos(k_l x_1)\cos(k_n x_3) - \sin(k_l x_1)\sin(k_n x_3) \\ &\qquad - \sin(k_l x_1)\cos(k_n x_3) - \cos(k_l x_1)\sin(k_n x_3)\}. \end{aligned} \tag{B.1}$$

These are purely real functions which excite one wavenumber pair (k_l, k_n) and $(-k_l, -k_n)$ with $\alpha_{ln} \in \mathbb{R}$ selected appropriately. The computational domain is $[-1, 1]$ in the inhomogeneous direction.

Take

$$\begin{gathered} \psi_{ln}(x_2) = \frac{1}{4}ax_2^4 + \frac{1}{2}cx_2^2 + e \\ a = 4ek\frac{k+1}{k^2+5k+8} \qquad c = -4ek\frac{k+3}{k^2+5k+8} \end{gathered} \tag{B.2}$$

for $k = \sqrt{k_l^2 + k_n^2} \neq 0$ then let $\boldsymbol{m}^c = \nabla\psi_{ln}(x_2)\zeta_{ln}(x_1, x_3)T(t)$.

$$\boldsymbol{m}_{ln}^c = \begin{pmatrix} \dfrac{\partial\zeta_{ln}}{\partial x_1}\psi_{ln} \\ \zeta_{ln}\dfrac{\partial\psi_{ln}}{\partial x_2} \\ \dfrac{\partial\zeta_{ln}}{\partial x_3}\psi_{ln} \end{pmatrix} T(t)\,. \tag{B.3}$$

The divergence-free momentum comes from

$$\begin{gathered} \phi_{ln} = x_2^5 + ax_2^4 + bx_2^3 + x_2^2 + x_2 \\ a = -\frac{2+k}{4+k} \qquad b = -\frac{8+3k}{3+k} - a\frac{k+4}{k+3} \end{gathered} \tag{B.4}$$

with

$$\begin{aligned} \boldsymbol{m}_{ln}^d &= \nabla \times \begin{pmatrix} \zeta_{ln}\phi_{ln} \\ 0 \\ \zeta_{ln}\phi_{ln} \end{pmatrix} T(t) \\ &= \begin{pmatrix} \zeta_{ln}\dfrac{\partial\phi_{ln}}{\partial x_2} \\ \left[\dfrac{\partial\zeta_{ln}}{\partial x_3} - \dfrac{\partial\zeta_{ln}}{\partial x_1}\right]\phi_{ln} \\ -\zeta_{ln}\dfrac{\partial\phi_{ln}}{\partial x_2} \end{pmatrix} T(t)\,. \end{aligned} \tag{B.5}$$

These solutions are curl-free and divergence-free, respectively, by construction and obey the boundary conditions which are explicitly enforced. For the mean,

$$\langle\boldsymbol{m}\rangle = \begin{pmatrix} 5x_2^4 + 4x_2^3 - 10x_2^2 - 12x_2 \\ -x_2^3 + 3x_2 \\ -5x_2^4 - 4x_2^3 + 10x_2^2 + 12x_2 \end{pmatrix} T(t)\,. \tag{B.6}$$

The manufactured solution carries a mixture fraction, z, which specifies the thermodynamic

properties. To respect the divergence constraint, it follows that

$$\begin{aligned}\frac{\partial \rho}{\partial z}\frac{\partial z}{\partial t} &= \frac{\partial \rho}{\partial z}\left(Z(x_1,x_2,x_3)T_z(t)\right) \times \left\{ Z(x_1,x_2,x_3)\frac{\partial T_z}{\partial t}(t) \right\} \\ &= -\nabla \cdot \boldsymbol{m}^c = -\sum_{ln} \nabla \cdot \left(\nabla \phi_{ln}(x_2)\zeta_{ln}(x_1,x_3)\right) T(t)\,.\end{aligned} \tag{B.7}$$

For simplicity, take $\rho(z) = Az + B$, then

$$Z(x_1,x_2,x_3) = -\frac{1}{A}\sum_{ln} \nabla \cdot \left(\nabla \phi_{ln}(x_2)\zeta_{ln}(x_1,x_3)\right) \qquad T_z = \int T dt + C\,. \tag{B.8}$$

Selecting $T(t) = \exp(Dt)$ and $T_z(t) = 1/D\exp(Dt)$ completes the specification of the mixture fraction. This ensures no sources are needed to reconstruct the curl-free momentum through the continuity constraint. Finally, it is assumed $\mu = \rho = \rho\mathcal{D}_z$. Creating a manufactured solution in terms of the momentum decomposition allows for much more flexibility when unit testing portions of the code.

Appendix C

Collocation points for flamelet DNS

The collocation points, $\mathcal{Y}^8_{coll}$, for the eighth order B-splines ($p = 8$) used in the flamelet DNS are computed by first selecting breakpoints ($b_j, j = 0, \cdots, n_b - 1$) which define the endpoints of the set of intervals which partition the x_2 axis. Let $n_b = N_2 - p + 2$ be the number of breakpoints required for p^{th} order splines with N_2 basis functions. Define a growth factor $G = 1.034$, then the breakpoints are specified as shown in procedure 4.

Procedure 4 Breakpoint specification

$b_{n_b/2} = \Delta/2$, $b_{n_b/2-1} = -\Delta/2$, $\delta = \Delta$
for $j = n_b/2 + 1$ to $n_b - 1$ **do**
  if $b_{j-1} > 2.8H$ **then**
    $\delta = \delta \times G$
  end if
  $b_j = b_{j-1} + \delta$, $b_{n_b-1-j} = -b_j$
end for

The knot vector ($\xi_j, j = 0, \cdots, N_2 + p - 1$) includes repeats of the breakpoints at the boundary so the underlying B-splines have the appropriate regularity there. Hence,

$$\xi_j = \begin{cases} b_0 & j = 0, \cdots, p-1 \\ b_{n_b-1} & j = N_2, \cdots, N_2 + p - 1 \\ b_{j-p+1} & \text{else.} \end{cases} \tag{C.1}$$

The collocation points are computed as the Greville abscissae:

$$x'_{2,i} = \frac{1}{p-1}\left(\xi_i + \xi_{i-1} + \cdots + \xi_{i+p-1}\right) . \tag{C.2}$$

The collocation grid is homogeneous for $|x_2/H| \lesssim 2.8$ and gradually stretched otherwise, akin to the grid of reference complex chemistry DNS.

Appendix D

Favre-averaged equations and statistics

The basis of Reynolds and Favre averaging techniques are described in section 2.3. During a calculation various quantities can be stored and later recombined to recover statistics of interest. Specifically, the terms in the Favre-averaged conservation equations for mass, momentum, mixture fraction, mixture fraction variance, turbulent kinetic energy, and turbulent dissipation rate, as well as PDFs of mixture fraction and scalar dissipation rate are of interest. Collecting these terms directly will allow for model error assessment with both *a priori* and *a posteriori* techniques.

D.1 Nondimensional Favre-averaged equations

The simulations are characterized by the jet initial velocity difference (ΔU), height (H), and kinematic viscosity ($\nu_R = \mu_R/\rho_R$) and the scalar dissipation rate at extinction (χ_{ext}). The mixture fraction transport additionally introduces a reference thermal diffusion coefficient, $\mathcal{D}_R$. For clarity, add a D superscript to indicate a dimensional quantity and consider quantities without a subscript as dimensionless for the purposes of the following derivations. As

an example, the spatial variables $x_i^D = x_i H$. Starting with eqs. (2.19) to (2.21),

$$\begin{aligned} \frac{\partial \overline{\rho^D}}{\partial t^D} + \frac{\partial}{\partial x_i^D}\left(\overline{\rho^D}\widetilde{u^D}_i\right) &= 0 \\ \frac{\partial \overline{\rho^D}\widetilde{u^D}_i}{\partial t^D} + \frac{\partial}{\partial x_j^D}\left(\overline{\rho^D}\widetilde{u^D}_i\widetilde{u^D}_j\right) &= -\frac{\partial \overline{p^D}}{\partial x_i^D} + \frac{\partial}{\partial x_j^D}\left(\overline{\tau^D}_{ij} - \widetilde{\overline{\rho^D} u^{D\prime\prime}_i u^{D\prime\prime}_j}\right) \end{aligned} \tag{D.1}$$

substitute

$$\begin{aligned} \left\{\frac{\rho_R \Delta U}{H}\right\}\frac{\partial \overline{\rho}}{\partial t} + \left\{\frac{\rho_R \Delta U}{H}\right\}\frac{\partial}{\partial x_i}\left(\overline{\rho}\widetilde{u}_i\right) &= 0 \\ \implies \frac{\partial \overline{\rho}}{\partial t} + \frac{\partial}{\partial x_i}\left(\overline{\rho}\widetilde{u}_i\right) &= 0 \end{aligned} \tag{D.2}$$

$$\begin{aligned} \left\{\frac{\rho_R \Delta U^2}{H}\right\}\left[\frac{\partial \overline{\rho}\widetilde{u}_i}{\partial t} + \frac{\partial}{\partial x_j}\left(\overline{\rho}\widetilde{u}_i\widetilde{u}_j\right)\right] &= -\left\{\frac{\rho_R \Delta U^2}{H}\right\}\frac{\partial \overline{p}}{\partial x_i} \\ &\quad + \left\{\frac{1}{H}\right\}\frac{\partial}{\partial x_j}\left(\left\{\mu_R \Delta U\right\}\overline{\tau}_{ij} - \left\{\rho \Delta U^2\right\}\widetilde{\overline{\rho} u^{\prime\prime}_i u^{\prime\prime}_j}\right) \end{aligned} \tag{D.3}$$

$$\implies \frac{\partial \overline{\rho}\widetilde{u}_i}{\partial t} + \frac{\partial}{\partial x_j}\left(\overline{\rho}\widetilde{u}_i\widetilde{u}_j\right) = -\frac{\partial \overline{p}}{\partial x_i} + \frac{1}{\mathrm{Re}}\frac{\partial \overline{\tau}_{ij}}{\partial x_j} - \frac{\partial}{\partial x_j}\left(\widetilde{\overline{\rho} u^{\prime\prime}_i u^{\prime\prime}_j}\right) .$$

Moving onto eq. (2.21)

$$\frac{\partial \overline{\rho^D}\widetilde{z}}{\partial t^D} + \frac{\partial}{\partial x_i^D}\left(\overline{\rho^D}\widetilde{u^D}_i\widetilde{z}\right) = \frac{\partial}{\partial x_i^D}\left(\overline{\rho^D \mathcal{D}_z^D \frac{\partial z}{\partial x_i^D}} - \widetilde{\overline{\rho^D} u_i^{D\prime\prime} z^{\prime\prime}}\right) \tag{D.4}$$

$$\begin{aligned} \left\{\frac{\rho_R \Delta U}{H}\right\}\left[\frac{\partial \overline{\rho}\widetilde{z}}{\partial t} + \frac{\partial}{\partial x_i}\left(\overline{\rho}\widetilde{u}_i\widetilde{z}\right)\right] &= \left\{\frac{1}{H}\right\}\frac{\partial}{\partial x_i}\left(\left\{\frac{\rho_R \mathcal{D}_R}{H}\right\}\overline{\rho \mathcal{D}_z \frac{\partial z}{\partial x_i}} - \left\{\rho_R \Delta U\right\}\widetilde{\overline{\rho} u_i^{\prime\prime} z^{\prime\prime}}\right) \\ \implies \frac{\partial \overline{\rho}\widetilde{z}}{\partial t} + \frac{\partial}{\partial x_i}\left(\overline{\rho}\widetilde{u}_i\widetilde{z}\right) &= \frac{1}{\mathrm{RePr}}\frac{\partial}{\partial x_i}\left(\overline{\rho \mathcal{D}_z \frac{\partial z}{\partial x_i}}\right) - \frac{\partial}{\partial x_i}\left(\widetilde{\overline{\rho} u_i^{\prime\prime} z^{\prime\prime}}\right) \end{aligned} \tag{D.5}$$

and eq. (2.22)

$$\begin{aligned} \frac{\partial \overline{\rho^D}\widetilde{z^{\prime\prime} z^{\prime\prime}}}{\partial t^D} + \frac{\partial}{\partial x_i^D}\left(\overline{\rho^D}\widetilde{u^D}_i\widetilde{z^{\prime\prime} z^{\prime\prime}}\right) &= -\frac{\partial}{\partial x_i^D}\left(\overline{\rho^D u_i^{D\prime\prime} z^{\prime\prime} z^{\prime\prime}}\right) + \frac{\partial}{\partial x_i^D}\left(\overline{\rho^D \mathcal{D}_z^D \frac{\partial z^{\prime\prime} z^{\prime\prime}}{\partial x_i^D}}\right) \\ &\quad + 2\overline{z^{\prime\prime} \frac{\partial}{\partial x_i^D}\left(\rho^D \mathcal{D}_z^D \frac{\partial \widetilde{z}}{\partial x_i^D}\right)} \\ &\quad - 2\overline{\rho^D u_i^{D\prime\prime} z^{\prime\prime}}\frac{\partial \widetilde{z}}{\partial x_i} - 2\overline{\rho^D \mathcal{D}_z^D \frac{\partial z^{\prime\prime}}{\partial x_i^D}\frac{\partial z^{\prime\prime}}{\partial x_i^D}} \end{aligned} \tag{D.6}$$

$$
\begin{aligned}
\left\{\frac{\rho_R \Delta U}{H}\right\}\left[\frac{\partial \overline{\rho}\widetilde{z''z''}}{\partial t}+\frac{\partial}{\partial x_i}\left(\overline{\rho}\widetilde{u}_i\widetilde{z''z''}\right)\right] &= -\left\{\frac{\rho_R \Delta U}{H}\right\}\frac{\partial}{\partial x_i}\left(\overline{\rho {u_i}'' z'' z''}\right) \\
&\quad +\left\{\frac{\rho_R \mathcal{D}_R}{H^2}\right\}\frac{\partial}{\partial x_i}\left(\overline{\rho \mathcal{D}_z \frac{\partial z'' z''}{\partial x_i}}\right) \\
&\quad +\left\{\frac{\rho_R \mathcal{D}_R}{H^2}\right\} 2\overline{z''\frac{\partial}{\partial x_i}\left(\rho \mathcal{D}_z \frac{\partial \widetilde{z}}{\partial x_i}\right)} \\
&\quad -\left\{\frac{\rho_R \Delta U}{H}\right\} 2\overline{\rho {u_i}'' z''}\frac{\partial \widetilde{z}}{\partial x_i} \\
&\quad -\left\{\frac{\rho_R \mathcal{D}_R}{H^2}\right\} 2\overline{\rho \mathcal{D}_z \frac{\partial z''}{\partial x_i}\frac{\partial z''}{\partial x_i}} \\
\implies \frac{\partial \overline{\rho}\widetilde{z''z''}}{\partial t}+\frac{\partial}{\partial x_i}\left(\overline{\rho}\widetilde{u}_i\widetilde{z''z''}\right) &= -\frac{\partial}{\partial x_i}\left(\overline{\rho {u_i}'' z'' z''}\right)+\frac{1}{\mathrm{RePr}}\frac{\partial}{\partial x_i}\left(\overline{\rho \mathcal{D}_z \frac{\partial z'' z''}{\partial x_i}}\right) \\
&\quad +\frac{2}{\mathrm{RePr}}\overline{z''\frac{\partial}{\partial x_i}\left(\rho \mathcal{D}_z \frac{\partial \widetilde{z}}{\partial x_i}\right)} \\
&\quad -2\overline{\rho {u_i}'' z''}\frac{\partial \widetilde{z}}{\partial x_i}-\frac{2}{\mathrm{RePr}}\overline{\rho \mathcal{D}_z \frac{\partial z''}{\partial x_i}\frac{\partial z''}{\partial x_i}}\,.
\end{aligned}
\tag{D.7}
$$

Equations for the transport of the Favre-averaged Reynolds stress, $\widetilde{u_i'' u_j''}$, and its trace, the turbulent kinetic energy, k, can be derived as well:

$$
\begin{aligned}
\frac{\partial}{\partial t^D}\left(\overline{\rho^D}\widetilde{u_i^{D''}u_j^{D''}}\right)+\frac{\partial}{\partial x_k^D}\left(\overline{\rho^D}\widetilde{u^D}_k\widetilde{u_i^{D''}u_j^{D''}}\right) &= -\overline{\rho^D}\widetilde{u_i^{D''}u_k^{D''}}\frac{\partial \widetilde{u^D}_j}{\partial x_k^D}-\overline{\rho^D}\widetilde{u_j^{D''}u_k^{D''}}\frac{\partial \widetilde{u^D}_i}{\partial x_k^D} \\
&\quad -\overline{\rho^D}\left(\varepsilon_{ij}^D-\Pi_{ij}^D\right) \\
&\quad -\frac{\partial}{\partial x_k^D}\left\{\overline{\rho^D {u^D}_i'' {u^D}_j'' {u^D}_k''}+\overline{p^{D\prime}u_i^{D''}}\delta_{jk}+\overline{p^{D\prime}u_j^{D''}}\delta_{ik}\right\} \\
&\quad +\frac{\partial}{\partial x_k^D}\left\{\overline{\left(\tau_{jk}^D u_i^{D''}+\tau_{ik}^D u_j^{D''}\right)}\right\}-\overline{u_i^{D''}}\frac{\partial \overline{p^D}}{\partial x_j^D}-\overline{u_j^{D''}}\frac{\partial \overline{p^D}}{\partial x_i^D}
\end{aligned}
\tag{D.8}
$$

$$
\begin{aligned}
\frac{\partial}{\partial t^D}\left(\overline{\rho^D}k^D\right)+\frac{\partial}{\partial x_j^D}\left(\overline{\rho^D}\widetilde{u^D}_j k\right) &= -\overline{\rho^D}\widetilde{u_i^{D''}u_j^{D''}}\frac{\partial \widetilde{u^D}_i}{\partial x_j^D}-\overline{\rho^D}\varepsilon^D \\
&\quad +\frac{\partial}{\partial x_j^D}\left\{\overline{\tau_{ij}^D u_i^{D''}}-\overline{\rho^D u_j^{D''}\frac{1}{2}u_i^{D''}u_i^{D''}\prime\prime}-\overline{p^{D\prime}u_j^{D''}}\right\} \\
&\quad -\overline{u_i^{D''}}\frac{\partial \overline{p^D}}{\partial x_i^D}+\overline{p^{D\prime}\frac{\partial u_i^{D''}}{\partial x_i^D}}
\end{aligned}
\tag{D.9}
$$

$$\begin{aligned}\varepsilon_{ij}^{D} &= \frac{1}{\overline{\rho^{D}}}\overline{\tau_{jk}^{D}\frac{\partial u_{i}^{D\prime\prime}}{\partial x_{k}^{D}} + \tau_{ik}^{D}\frac{\partial u_{j}^{D\prime\prime}}{\partial x_{k}^{D}}} \\ \Pi_{ij}^{D} &= \frac{1}{\overline{\rho^{D}}}\overline{p^{D\prime}\left(\frac{\partial u_{i}^{D\prime\prime}}{\partial x_{j}^{D}} + \frac{\partial u_{j}^{D\prime\prime}}{\partial x_{i}^{D}}\right)}\end{aligned}. \tag{D.10}$$

$$\begin{aligned}\varepsilon_{ij}^{D} &= \left\{\frac{\mu_{R}\Delta U^{2}}{\rho_{R}H^{2}}\right\}\frac{1}{\overline{\rho}}\overline{\tau_{jk}\frac{\partial u_{i}{}''}{\partial x_{k}} + \tau_{ik}\frac{\partial u_{j}{}''}{\partial x_{k}}} \\ \Pi_{ij}^{D} &= \left\{\frac{\Delta U^{3}}{H}\right\}\frac{1}{\overline{\rho}}\overline{p^{\prime}\left(\frac{\partial u_{i}''}{\partial x_{j}} + \frac{\partial u_{j}{}''}{\partial x_{i}}\right)}\end{aligned}. \tag{D.11}$$

Again, substitution gives

$$\begin{aligned}&\left\{\frac{\rho_{R}\Delta U^{3}}{H}\right\}\left[\frac{\partial}{\partial t}\left(\widetilde{\overline{\rho}u_{i}''u_{j}''}\right) + \frac{\partial}{\partial x_{k}}\left(\overline{\rho}\widetilde{u}_{k}\widetilde{u_{i}''u_{j}''}\right)\right] = \\ &\qquad - \left\{\frac{\rho_{R}\Delta U^{3}}{H}\right\}\left[\widetilde{\overline{\rho}u_{i}''u_{k}''}\frac{\partial\widetilde{u}_{j}}{\partial x_{k}} + \widetilde{\overline{\rho}u_{j}''u_{k}''}\frac{\partial\widetilde{u}_{i}}{\partial x_{k}}\right] \\ &\qquad - \left\{\rho_{R}\right\}\overline{\rho}\left(\left\{\frac{\mu_{R}\Delta U^{2}}{\rho_{R}H^{2}}\right\}\varepsilon_{ij} - \left\{\frac{\Delta U^{3}}{H}\right\}\Pi_{ij}\right) \\ &\qquad - \left\{\frac{\rho_{R}\Delta U^{3}}{H}\right\}\frac{\partial}{\partial x_{k}}\left\{\overline{\rho u_{i}''u_{j}''u_{k}''} + \overline{p^{\prime}u_{i}{}''}\delta_{jk} + \overline{p^{\prime}u_{j}{}''}\delta_{ik}\right\} \\ &\qquad + \left\{\frac{\mu_{R}\Delta U^{2}}{H^{2}}\right\}\frac{\partial}{\partial x_{k}}\left\{\overline{\left(\tau_{jk}u_{i}{}'' + \tau_{ik}u_{j}''\right)}\right\} \\ &\qquad - \left\{\frac{\rho_{R}\Delta U^{3}}{H}\right\}\left[\overline{u_{i}{}''}\frac{\partial\overline{p}}{\partial x_{j}} + \overline{u_{j}{}''}\frac{\partial\overline{p}}{\partial x_{i}}\right] \\ \implies &\frac{\partial}{\partial t}\left(\widetilde{\overline{\rho}u_{i}''u_{j}''}\right) + \frac{\partial}{\partial x_{k}}\left(\overline{\rho}\widetilde{u}_{k}\widetilde{u_{i}''u_{j}''}\right) = \widetilde{\overline{\rho}u_{i}''u_{k}''}\frac{\partial\widetilde{u}_{j}}{\partial x_{k}} + \widetilde{\overline{\rho}u_{j}''u_{k}''}\frac{\partial\widetilde{u}_{i}}{\partial x_{k}} \\ &\qquad - \overline{\rho}\left(\frac{1}{\mathrm{Re}}\varepsilon_{ij} - \Pi_{ij}\right) - \frac{\partial}{\partial x_{k}}\left\{\overline{\rho u_{i}''u_{j}''u_{k}''} + \overline{p^{\prime}u_{i}{}''}\delta_{jk} + \overline{p^{\prime}u_{j}{}''}\delta_{ik}\right\} \\ &\qquad + \frac{1}{\mathrm{Re}}\frac{\partial}{\partial x_{k}}\left\{\overline{\left(\tau_{jk}u_{i}{}'' + \tau_{ik}u_{j}''\right)}\right\} - \overline{u_{i}{}''}\frac{\partial\overline{p}}{\partial x_{j}} + \overline{u_{j}{}''}\frac{\partial\overline{p}}{\partial x_{i}}\end{aligned} \tag{D.12}$$

and

$$\left\{\frac{\rho_R\Delta U^3}{H}\right\}\left[\frac{\partial}{\partial t}\left(\overline{\rho}k\right)+\frac{\partial}{\partial x_j}\left(\overline{\rho}\widetilde{u}_jk\right)\right]=-\left\{\frac{\rho_R\Delta U^3}{H}\right\}\widetilde{\overline{\rho}u_i''u_j''}\frac{\partial\widetilde{u}_i}{\partial x_j}-\left\{\frac{\mu_R\Delta U^2}{H^2}\right\}\overline{\rho}\varepsilon$$
$$+\frac{\partial}{\partial x_j}\left\{\left\{\frac{\mu_R\Delta U^2}{H^2}\right\}\overline{\tau_{ij}u_i''}-\left\{\frac{\rho_R\Delta U^3}{H}\right\}\left[\overline{\rho u_j''\frac{1}{2}u_i''u_i''}+\overline{p'u_j''}\right]\right\}$$
$$-\left\{\frac{\rho_R\Delta U^3}{H}\right\}\left[\overline{u_i''}\frac{\partial\overline{p}}{\partial x_i}-\overline{p'\frac{\partial u_i''}{\partial x_i}}\right] \tag{D.13}$$

$$\implies \frac{\partial}{\partial t}\left(\overline{\rho}k\right)+\frac{\partial}{\partial x_j}\left(\overline{\rho}\widetilde{u}_jk\right)=-\overline{\rho}\widetilde{u_i''u_j''}\frac{\partial\widetilde{u}_i}{\partial x_j}-\frac{1}{\mathrm{Re}}\overline{\rho}\varepsilon$$
$$+\frac{\partial}{\partial x_j}\left\{\frac{1}{\mathrm{Re}}\overline{\tau_{ij}u_i''}-\overline{\rho u_j''\frac{1}{2}u_i''u_i''}-\overline{p'u_j''}\right\}-\overline{u_i''}\frac{\partial\overline{p}}{\partial x_i}+\overline{p'\frac{\partial u_i''}{\partial x_i}}\,.$$

In summary, the nondimensionalized equations are

$$
\begin{aligned}
\frac{\partial \overline{\rho}}{\partial t} + \frac{\partial}{\partial x_i}\left(\overline{\rho}\widetilde{u}_i\right) &= 0 \\
\frac{\partial \overline{\rho}\widetilde{u}_i}{\partial t} + \frac{\partial}{\partial x_j}\left(\overline{\rho}\widetilde{u}_i\widetilde{u}_j\right) &= -\frac{\partial \overline{p}}{\partial x_i} + \frac{1}{\mathrm{Re}}\frac{\partial \overline{\tau}_{ij}}{\partial x_j} - \frac{\partial}{\partial x_j}\left(\widetilde{\overline{\rho}u_i''u_j''}\right) \\
\frac{\partial \overline{\rho}\widetilde{z}}{\partial t} + \frac{\partial}{\partial x_i}\left(\overline{\rho}\widetilde{u}_i\widetilde{z}\right) &= \frac{1}{\mathrm{RePr}}\frac{\partial}{\partial x_i}\left(\overline{\rho\mathcal{D}_z\frac{\partial z}{\partial x_i}}\right) - \frac{\partial}{\partial x_i}\left(\widetilde{\overline{\rho}u_i''z''}\right) \\
\frac{\partial \overline{\rho}\widetilde{z''z''}}{\partial t} + \frac{\partial}{\partial x_i}\left(\overline{\rho}\widetilde{u}_i\widetilde{z''z''}\right) &= -\frac{\partial}{\partial x_i}\left(\overline{\rho u_i''z''z''}\right) + \frac{1}{\mathrm{RePr}}\frac{\partial}{\partial x_i}\left(\overline{\rho\mathcal{D}_z\frac{\partial z''z''}{\partial x_i}}\right) \\
&\quad + \frac{2}{\mathrm{RePr}}\overline{z''\frac{\partial}{\partial x_i}\left(\rho\mathcal{D}_z\frac{\partial \widetilde{z}}{\partial x_i}\right)} \\
&\quad - 2\overline{\rho u_i''z''}\frac{\partial \widetilde{z}}{\partial x_i} - \frac{2}{\mathrm{RePr}}\overline{\rho\mathcal{D}_z\frac{\partial z''}{\partial x_i}\frac{\partial z''}{\partial x_i}} \\
\frac{\partial}{\partial t}\left(\widetilde{\overline{\rho}u_i''u_j''}\right) + \frac{\partial}{\partial x_k}\left(\widetilde{\overline{\rho}u_k}\widetilde{u_i''u_j''}\right) &= -\widetilde{\overline{\rho}u_i''u_k''}\frac{\partial \widetilde{u}_j}{\partial x_k} - \widetilde{\overline{\rho}u_j''u_k''}\frac{\partial \widetilde{u}_i}{\partial x_k} \\
&\quad - \overline{\rho}\left(\frac{1}{\mathrm{Re}}\varepsilon_{ij} - \Pi_{ij}\right) \\
&\quad - \frac{\partial}{\partial x_k}\left\{\overline{\rho u_i''u_j''u_k''} + \overline{p'u_i''}\delta_{jk} + \overline{p'u_j''}\delta_{ik}\right\} \\
&\quad + \frac{1}{\mathrm{Re}}\frac{\partial}{\partial x_k}\left\{\overline{\left(\tau_{jk}u_i'' + \tau_{ik}u_j''\right)}\right\} \\
&\quad - \overline{u_i''}\frac{\partial \overline{p}}{\partial x_j} - \overline{u_j''}\frac{\partial \overline{p}}{\partial x_i} \\
\frac{\partial}{\partial t}\left(\overline{\rho}k\right) + \frac{\partial}{\partial x_j}\left(\overline{\rho}\widetilde{u}_jk\right) &= -\widetilde{\overline{\rho}u_i''u_j''}\frac{\partial \widetilde{u}_i}{\partial x_j} - \frac{1}{\mathrm{Re}}\overline{\rho}\varepsilon \\
&\quad + \frac{\partial}{\partial x_j}\left\{\frac{1}{\mathrm{Re}}\overline{\tau_{ij}u_i''} - \overline{\rho u_j''\frac{1}{2}u_i''u_i''} - \overline{p'u_j''}\right\} \\
&\quad - \overline{u_i''}\frac{\partial \overline{p}}{\partial x_i} + \overline{p'\frac{\partial u_i''}{\partial x_i}}\,.
\end{aligned}
\tag{D.14}
$$

D.2 Sampled quantities

Hence, the following quantities are required for the mean equations:

$$\overline{\rho} \quad \widetilde{u}_i \quad \overline{p} \quad \overline{\tau_{ij}} \quad \widetilde{u_i'' u_j''} \quad \widetilde{z} \quad \overline{\rho \mathcal{D}_z \frac{\partial z}{\partial x_i}} \quad \widetilde{u_i'' z''} \quad \widetilde{z'' z''} \quad \overline{z'' \frac{\partial}{\partial x_i}\left(\rho \mathcal{D}_z \frac{\partial \widetilde{z}}{\partial x_i}\right)} \quad \overline{\rho \mathcal{D}_z \frac{\partial z''}{\partial x_i}\frac{\partial z''}{\partial x_i}}$$

$$\overline{\rho u_i'' z'' z''} \quad \overline{\rho \mathcal{D}_z \frac{\partial z'' z''}{\partial x_i}} \quad \overline{p' \frac{\partial u_i''}{\partial x_j}} \quad \widetilde{u_i'' u_j'' u_k''} \quad \overline{p' u_i''} \quad \overline{\tau_{ik} u_j''} \quad \overline{\tau_{ik} \frac{\partial u_j''}{\partial x_k}} \quad \overline{u_i''}\,.$$

These can be obtained solely through raw moments through post-processing steps. Therefore, it is sufficient to sample

$$\overline{\rho} \quad \overline{\rho u_i} \quad \overline{p} \quad \overline{\tau_{ij}} \quad \overline{\rho u_i u_j} \quad \overline{\rho u_i u_j u_k} \quad \overline{\rho z} \quad \overline{\rho \mathcal{D}_z \frac{\partial z}{\partial x_i}} \quad \overline{\rho u_i z} \quad \overline{\rho z^2}$$

$$\overline{\rho u_i z^2} \quad \overline{z \rho \mathcal{D}_z} \quad \overline{\rho \mathcal{D}_z \frac{\partial z}{\partial x_i}\frac{\partial z}{\partial x_i}} \quad \overline{\rho \mathcal{D}_z z \frac{\partial z}{\partial x_i}} \quad \overline{\tau_{ik} u_j} \quad \overline{\tau_{ik} \frac{\partial u_j}{\partial x_k}} \quad \overline{p \frac{\partial u_i}{\partial x_j}} \quad \overline{p u_i} \quad \overline{\rho \mathcal{D}_z}\,.$$

Clearly, for any quantity

$$\widetilde{f} = \frac{\overline{\rho f}}{\overline{\rho}}\,. \tag{D.15}$$

Further,

$$\begin{aligned} \overline{\rho}\widetilde{u_i'' u_j''} &= \overline{\rho\,(u_i - \widetilde{u}_i)\,(u_j - \widetilde{u}_j)} = \overline{\rho u_i u_j} + \overline{\rho \widetilde{u}_i \widetilde{u}_j} - \overline{\rho \widetilde{u}_i u_j} - \overline{\rho u_i \widetilde{u}_j} \\ \implies \widetilde{u_i'' u_j''} &= \widetilde{u_i u_j} + \widetilde{u}_i \widetilde{u}_j - 2\widetilde{u}_i \widetilde{u}_j = \widetilde{u_i u_j} - \widetilde{u}_i \widetilde{u}_j\,. \end{aligned} \tag{D.16}$$

Similarly,

$$\begin{aligned}
\overline{\rho}\widetilde{u_i''z''} &= \overline{\rho\left(u_i-\widetilde{u}_i\right)\left(z-\widetilde{z}\right)} = \overline{\rho u_i z}+\overline{\rho\widetilde{u}_i\widetilde{z}}-\overline{\rho\widetilde{u}_i z}-\overline{\rho u_i\widetilde{z}} \\
\implies \widetilde{u_i''z''} &= \widetilde{u_i z}-\widetilde{u}_i\widetilde{z} \\
\overline{\rho}\widetilde{z''z''} &= \overline{\rho\left(z-\widetilde{z}\right)^2} = \overline{\rho z^2}+\overline{\rho\widetilde{z}^2}-2\overline{\rho\widetilde{z}z} \\
\implies \widetilde{z''z''} &= \widetilde{z^2}-\widetilde{z}^2\,.
\end{aligned} \tag{D.17}$$

These relationships can be extended for arbitrary binary arguments. Also, recognize

$$\widetilde{fg''} = \widetilde{f\left(g-\widetilde{g}\right)} = \widetilde{fg}-\widetilde{f\widetilde{g}} = \widetilde{fg}-\widetilde{f}\widetilde{g} \tag{D.18}$$

$$\overline{fg''} = \overline{f\left(g-\widetilde{g}\right)} = \overline{fg}-\overline{f}\widetilde{g}\,. \tag{D.19}$$

Hence,

$$\begin{aligned}
\widetilde{u_i''u_j''u_k''} &= \overline{\rho}^{-1}\overline{\rho\left(u_i-\widetilde{u}_i\right)\left(u_j-\widetilde{u}_j\right)u_k''} = \widetilde{u_iu_ju_k''}+\widetilde{\widetilde{u}_i\widetilde{u}_ju_k''}-\widetilde{\widetilde{u}_iu_ju_k''}-\widetilde{u_i\widetilde{u}_ju_k''} \\
&= \widetilde{u_iu_ju_k''}+\widetilde{u}_i\widetilde{u}_j\widetilde{u_k''}+-\widetilde{u}_i\widetilde{u_ju_k''}-\widetilde{u}_j\widetilde{u_iu_k''} \\
&= \widetilde{u_iu_ju_k}-\widetilde{u_iu}_j\widetilde{u}_k-\widetilde{u}_i\widetilde{u_ju_k}+\widetilde{u}_i\widetilde{u}_j\widetilde{u}_k-\widetilde{u}_j\widetilde{u_iu_k}+\widetilde{u}_i\widetilde{u}_j\widetilde{u}_k \\
&= \widetilde{u_iu_ju_k}+2\widetilde{u}_i\widetilde{u}_j\widetilde{u}_k-\left(\widetilde{u}_i\widetilde{u_ju_k}+\widetilde{u}_j\widetilde{u_iu_k}+\widetilde{u}_k\widetilde{u_iu_j}\right)\,.
\end{aligned} \tag{D.20}$$

Further, note that unlike Reynolds averages, Favre averages do not commute with differentiation. For example,

$$\begin{aligned}
\frac{\partial \widetilde{f}}{\partial x_i} &= \frac{\partial}{\partial x_i}\left(\frac{\overline{\rho f}}{\overline{\rho}}\right) = \frac{1}{\overline{\rho}}\frac{\partial \overline{\rho f}}{\partial x_i} - \frac{\overline{\rho f}}{\overline{\rho}^2}\frac{\partial \overline{\rho}}{\partial x_i} \\
&= \frac{1}{\overline{\rho}}\overline{\rho \frac{\partial f}{\partial x_i}} + \frac{1}{\overline{\rho}}\overline{f\frac{\partial \rho}{\partial x_i}} - \frac{\widetilde{f}}{\overline{\rho}}\frac{\partial \overline{\rho}}{\partial x_i} \\
&= \widetilde{\frac{\partial f}{\partial x_i}} + \frac{1}{\overline{\rho}}\left(\overline{f\frac{\partial \rho}{\partial x_i}} - \widetilde{f}\frac{\partial \overline{\rho}}{\partial x_i}\right) \\
&= \widetilde{\frac{\partial f}{\partial x_i}} + \frac{1}{\overline{\rho}}\left(\overline{f\frac{\partial \rho}{\partial x_i}} - \overline{\widetilde{f}\frac{\partial \rho}{\partial x_i}}\right) = \widetilde{\frac{\partial f}{\partial x_i}} + \frac{1}{\overline{\rho}}\overline{f''\frac{\partial \rho}{\partial x_i}} \\
&= \widetilde{\frac{\partial f}{\partial x_i}} + \frac{1}{\overline{\rho}}\left(\overline{f\frac{\partial \rho}{\partial x_i}} - \widetilde{f}\overline{\frac{\partial \rho}{\partial x_i}}\right).
\end{aligned} \tag{D.21}$$

These rules can be combined to obtain identities for the more complicated terms. For example,

$$\begin{aligned}
\overline{z''\frac{\partial}{\partial x_i}\left(\rho \mathcal{D}_z \frac{\partial \widetilde{z}}{\partial x_i}\right)} &= \frac{\partial \widetilde{z}}{\partial x_i}\left(\frac{\partial \overline{z\rho\mathcal{D}_z}}{\partial x_i} - \overline{\rho\mathcal{D}_z\frac{\partial z}{\partial x_i}} - \widetilde{z}\frac{\partial \overline{\rho\mathcal{D}_z}}{\partial x_i}\right) + \frac{\partial^2 \widetilde{z}}{\partial x_i \partial x_i}\left(\overline{z\rho\mathcal{D}_z} - \widetilde{z}\overline{\rho\mathcal{D}_z}\right) \\
\overline{\rho\mathcal{D}_z\frac{\partial z''}{\partial x_i}\frac{\partial z''}{\partial x_i}} &= \overline{\rho\mathcal{D}_z\frac{\partial z}{\partial x_i}\frac{\partial z}{\partial x_i}} + \overline{\rho\mathcal{D}_z}\frac{\partial \widetilde{z}}{\partial x_i}\frac{\partial \widetilde{z}}{\partial x_i} - 2\frac{\partial \widetilde{z}}{\partial x_i}\overline{\rho\mathcal{D}_z\frac{\partial z}{\partial x_i}}.
\end{aligned} \tag{D.22}$$

D.3 Probability density functions (PDFs)

Presumed probability density functions play a role in RANS-based modeling for turbulent flames when representing the interaction between the chemistry and the turbulence. Sample PDFs can be computed from the DNS data by creating histograms for each x_1-x_3 plane or the entire domain. The PDF at a point y which falls in the bin of width h is estimated as

$$p_N(y) = \frac{1}{h}\frac{1}{N}\sum_{i=1}^{N}\mathbf{1}_{(y_l, y_l+h]}(y_i) \tag{D.23}$$

where **1** is the indicator function, y_l is the lower edge of the bin, y_i is the i^{th} sample, and N is the total number of samples in the histogram. If averaging only over planes, statistical symmetry in the x_2 direction is employed which helps to lower error. For the PDFs reported in this thesis, $N = 3^8$ was chosen and bins were uniformly spaced (χ PDFs were taking in logspace).

Appendix E

Pressure

The DNS methodology formally eliminates the pressure from playing a dynamic role in the momentum equations. However, for the purpose of gathering statistics or other post-processing, the pressure is required. Taking the divergence of the momentum equations eq. (2.2) gives

$$\begin{aligned} \frac{\partial}{\partial t}\left(\frac{\partial \rho u_i}{\partial x_i}\right) + \frac{\partial^2 \rho u_i u_j}{\partial x_i \partial x_j} &= -\frac{\partial^2 p}{\partial x_i \partial x_i} + \frac{\partial^2 \tau_{ij}}{\partial x_i \partial x_j} \\ \implies \frac{\partial^2 p}{\partial x_i \partial x_i} &= -\frac{\partial}{\partial t}\left(\frac{\partial \rho u_i}{\partial x_i}\right) - \frac{\partial^2 \rho u_i u_j}{\partial x_i \partial x_j} + \frac{\partial^2 \tau_{ij}}{\partial x_i \partial x_j}\,. \\ &= -\frac{\partial}{\partial t}\left(\frac{\partial \rho u_i}{\partial x_i}\right) + \frac{\partial^2 C_{ij}}{\partial x_i \partial x_j} + \frac{\partial F_i^{\tau}}{\partial x_i} \end{aligned} \tag{E.1}$$

A boundary condition on the pressure is implied by the equations as well,

$$\frac{\partial p}{\partial x_2} = -\frac{\partial m_2}{\partial t} + \frac{\partial}{\partial x_j} C_{2j} + \frac{\partial}{\partial x_j} \tau_{2j}\,. \tag{E.2}$$

This is a Poisson problem with a Neumann condition, leading to a singular operator. To rectify this, the mean pressure is set to zero on one side of the domain. During the calculation, the convective and viscous contributions to the residual are formed explicitly at the same time as the pieces for the right hand sides for Ω_2 and ϕ_2.

In line with the RK scheme used in this work, the discretized momentum equation would

be

$$\frac{2}{\Delta t}\left(\frac{\partial \rho {u_i}'}{\partial x_i} - \frac{\partial \rho {u_i}^n}{\partial x_i}\right) = -\frac{\partial^2 \rho u_i {u_j}^n}{\partial x_i \partial x_j} - \frac{\partial^2 p^n}{\partial x_i \partial x_i} + \frac{\partial^2 {\tau_{ij}}^n}{\partial x_i \partial x_j} \tag{E.3}$$

for the first stage. Solving for the pressure at time level n,

$$\frac{\partial^2 p^n}{\partial x_i \partial x_i} = -\frac{\partial^2 \rho u_i {u_j}^n}{\partial x_i \partial x_j} + \frac{\partial^2 {\tau_{ij}}^n}{\partial x_i \partial x_j} - \frac{2}{\Delta t}\left(\frac{\partial \rho {u_i}'}{\partial x_i} - \frac{\partial \rho {u_i}^n}{\partial x_i}\right) . \tag{E.4}$$

Because the source term includes $\partial \rho {u_i}'/\partial t$, the solve cannot be completed until after the substep is completed. Hence, copies of the velocity field and the velocity gradient tensor at level n must be stored when statistics are requested. The constant-coefficient Poisson equation can be solved in the same manner as in the divergence-free momentum reconstruction, see section 3.5.1.2.

Appendix F

Spectra and correlations

The two-point correlation of two fields, u and v, at a point $\boldsymbol{x}$ with separation $\boldsymbol{r}$ is notated as $R_{uv}(\boldsymbol{x},\boldsymbol{r}) = \langle u^*(\boldsymbol{x})v(\boldsymbol{x}+\boldsymbol{r})\rangle$. For a domain $\mathcal{V}$ with two homogeneous directions as presented in this work, consider separation only in the x_1 and x_3 directions. Then, given the spatial discretization,

$$\begin{aligned} R_{uv}(\boldsymbol{x},\boldsymbol{r}) &= \frac{\int_{-L_1/2}^{L_1/2}\int_{-L_3/2}^{L_3/2} u^*(x_1,x_2,x_3)v(x_1+r_1,x_2,x_3+r_3)\,dx_1dx_3}{\int_{-L_1/2}^{L_1/2}\int_{-L_3/2}^{L_3/2} dx_1dx_3} \\ &= \frac{1}{L_1L_3}\int_{-L_1/2}^{L_1/2}\int_{-L_3/2}^{L_3/2} u^*(x_1,x_2,x_3)v(x_1+r_1,x_2,x_3+r_3)\,dx_1dx_3 \\ &= \frac{1}{L_1L_3}\int_{-L_1/2}^{L_1/2}\int_{-L_3/2}^{L_3/2} \left(\sum_{l=-\frac{N_1}{2}+1}^{\frac{N_1}{2}-1}\sum_{n=-\frac{N_3}{2}+1}^{\frac{N_3}{2}-1} \widehat{u}^*_{ln}(x_2)e^{-\mathrm{i}k_lx_1}e^{-\mathrm{i}k_nx_3}\right)\times \\ &\qquad \left(\sum_{l'=-\frac{N_1}{2}+1}^{\frac{N_1}{2}-1}\sum_{n'=-\frac{N_3}{2}+1}^{\frac{N_3}{2}-1} \widehat{v}_{l'n'}(x_2)e^{\mathrm{i}k'_l(x_1+r_1)}e^{\mathrm{i}k'_n(x_3+r_3)}\right)\,dx_1dx_3\,. \end{aligned} \tag{F.1}$$

Using the orthogonality of the Fourier modes means the sums collapse for $l=l'$, $n=n'$,

$$\begin{aligned} R_{uv}(\boldsymbol{x},\boldsymbol{r}) &= \frac{L_1L_3}{L_1L_3}\sum_{l=-\frac{N_1}{2}+1}^{\frac{N_1}{2}-1}\sum_{n=-\frac{N_3}{2}+1}^{\frac{N_3}{2}-1} \widehat{u}^*_{ln}(x_2)\widehat{v}_{ln}(x_2)e^{\mathrm{i}k_lr_1}e^{\mathrm{i}k_nr_3} \\ &= \sum_{l=-\frac{N_1}{2}+1}^{\frac{N_1}{2}-1}\sum_{n=-\frac{N_3}{2}+1}^{\frac{N_3}{2}-1} \widehat{u}^*_{ln}(x_2)\widehat{v}_{ln}(x_2)e^{\mathrm{i}k_lr_1}e^{\mathrm{i}k_nr_3}\,. \end{aligned} \tag{F.2}$$

Hence, the two-point correlation can be calculated readily in wavespace by forming

$$\widehat{R_{uv,ln}} = \widehat{u}^*_{ln}\widehat{v}_{ln} \tag{F.3}$$

and then performing the inverse Fourier transformations. Of particular interest are the one-dimensional separations (when $r_3 = 0$ or $r_1 = 0$). These can be computed by summing over one homogeneous direction then Fourier transforming in the other. That is,

$$\begin{aligned} R_{uv}(\boldsymbol{x}, r_1, 0, 0) = R^{x_1}_{uv}(\boldsymbol{x}, r_1) &= \sum_{l=-\frac{N_1}{2}+1}^{\frac{N_1}{2}-1} \sum_{n=-\frac{N_3}{2}+1}^{\frac{N_3}{2}-1} \widehat{u}^*_{ln}(x_2)\widehat{v}_{ln}(x_2)e^{\mathrm{i}k_l r_1} \\ \implies \widehat{R^{x_1}_{uv,l}} &= \sum_{n=-\frac{N_3}{2}+1}^{\frac{N_3}{2}-1} \widehat{u}^*_{ln}(x_2)\widehat{v}_{ln}(x_2) \end{aligned} \tag{F.4}$$

and

$$\begin{aligned} R_{uv}(\boldsymbol{x}, 0, 0, r_3) = R^{x_3}_{uv}(\boldsymbol{x}, r_3) &= \sum_{l=-\frac{N_1}{2}+1}^{\frac{N_1}{2}-1} \sum_{n=-\frac{N_3}{2}+1}^{\frac{N_3}{2}-1} \widehat{u}^*_{ln}(x_2)\widehat{v}_{ln}(x_2)e^{\mathrm{i}k_n r_3} \\ \implies \widehat{R^{x_3}_{uv,n}} &= \sum_{l=-\frac{N_1}{2}+1}^{\frac{N_1}{2}-1} \widehat{u}^*_{ln}(x_2)\widehat{v}_{ln}(x_2)\,. \end{aligned} \tag{F.5}$$

The one-dimensional energy spectrum is the Fourier transform of the two-point correlations of fluctuations, u' and v'. In the x_1 direction,

$$\begin{aligned} E^{x_1}_{uv}(x_2, k_l) &= \frac{1}{2\pi}\int_{-\frac{L_1}{2}}^{\frac{L_1}{2}} R^{x_1}_{uv}(x_2)e^{-\mathrm{i}k_l r_1}dr_1 \\ &= \frac{1}{2\pi}\int_{-\frac{L_1}{2}}^{\frac{L_1}{2}} \sum_{l'=-\frac{N_1}{2}+1}^{\frac{N_1}{2}-1} \sum_{n=-\frac{N_3}{2}+1}^{\frac{N_3}{2}-1} \widehat{u'}^*_{l'n}(x_2)\widehat{v'}_{ln}(x_2)e^{\mathrm{i}k'_l r_1}e^{-\mathrm{i}k_l r_1}dr_1 \\ &= \frac{L_1}{2\pi}\sum_{n=-\frac{N_3}{2}+1}^{\frac{N_3}{2}-1} \widehat{u'}^*_{ln}(x_2)\widehat{v'}_{ln}(x_2) \end{aligned} \tag{F.6}$$

and similarly

$$E_{uv}^{x_3}(x_2, k_n) = \frac{L_3}{2\pi} \sum_{l=-\frac{N_1}{2}+1}^{\frac{N_1}{2}-1} \widehat{u'}^*_{ln}(x_2)\widehat{v'}_{ln}(x_2)\,. \tag{F.7}$$

The two-dimensional spectrum has an analogous relationship,

$$E_{uv}(x_2, k_l, k_n) = \frac{L_1 L_3}{(2\pi)^2} \widehat{u'}^*_{ln}(x_2)\widehat{v'}_{ln}(x_2)\,. \tag{F.8}$$

F.1 Computational considerations

In the case where u and v are real, the coefficients obey Hermitian symmetry. Hence, from

$$\widehat{u}_{-ln} = \widehat{u}^*_{ln} \tag{F.9}$$

it follows

$$\begin{aligned}
\widehat{u}^*_{ln}\widehat{v}_{ln} + \widehat{u}^*_{-ln}\widehat{v}_{-ln} &= \widehat{u}^*_{ln}\widehat{v}_{ln} + \widehat{u}_{ln}\widehat{v}^*_{ln} \\
&= \mathcal{R}\widehat{u}_{ln}\mathcal{R}\widehat{v}_{ln} + \mathcal{I}\widehat{u}_{ln}\mathcal{I}\widehat{v}_{ln} - \mathrm{i}\mathcal{I}\widehat{u}_{ln}\mathcal{R}\widehat{v}_{ln} + \mathrm{i}\mathcal{I}\widehat{v}_{ln}\mathcal{R}\widehat{u}_{ln} \\
&\quad + \mathcal{R}\widehat{u}_{ln}\mathcal{R}\widehat{v}_{ln} + \mathcal{I}\widehat{u}_{ln}\mathcal{I}\widehat{v}_{ln} + \mathrm{i}\mathcal{I}\widehat{u}_{ln}\mathcal{R}\widehat{v}_{ln} - \mathrm{i}\mathcal{I}\widehat{v}_{ln}\mathcal{R}\widehat{u}_{ln} \\
&= 2\left(\mathcal{R}\widehat{u}_{ln}\mathcal{R}\widehat{v}_{ln} + \mathcal{I}\widehat{u}_{ln}\mathcal{I}\widehat{v}_{ln}\right)\,.
\end{aligned} \tag{F.10}$$

Spectra are often reported in terms of the wavenumber magnitude so eq. (F.10) can be used to simplify computation of the folded eq. (F.6). For example, if $l \neq 0$,

$$\begin{aligned}
E_{uv}^{x_1}(x_2, |k_l|) &= \frac{L_1}{2\pi} \sum_{n=-\frac{N_3}{2}+1}^{\frac{N_3}{2}-1} \widehat{u'}^*_{ln}(x_2)\widehat{v'}_{ln}(x_2) + \widehat{u'}^*_{-ln}(x_2)\widehat{v'}_{-ln}(x_2) \\
&= \frac{2L_1}{2\pi} \sum_{n=-\frac{N_3}{2}+1}^{\frac{N_3}{2}-1} \mathcal{R}\widehat{u'}_{ln}\mathcal{R}\widehat{v'}_{ln} + \mathcal{I}\widehat{u'}_{ln}\mathcal{I}\widehat{v'}_{ln}\,.
\end{aligned} \tag{F.11}$$

When $l = 0$,

$$\frac{L_1}{2\pi} \sum_{n=-\frac{N_3}{2}+1}^{\frac{N_3}{2}-1} \mathcal{R}\widehat{u'}_{0n}\mathcal{R}\widehat{v'}_{0n} + \mathcal{I}\widehat{u'}_{0n}\mathcal{I}\widehat{v'}_{0n} \tag{F.12}$$

is taken (must also be real). Symmetry also collapses the sum in eq. (F.7),

$$\sum_{l=-\frac{N_1}{2}+1}^{\frac{N_1}{2}-1} \widehat{u'}^{*}_{ln}\widehat{v'}_{ln} = \mathcal{R}\widehat{u'}_{0n}\mathcal{R}\widehat{v'}_{0n} + \mathcal{I}\widehat{u'}_{0n}\mathcal{I}\widehat{v'}_{0n} + 2\sum_{l=1}^{\frac{N_1}{2}-1} \mathcal{R}\widehat{u'}_{ln}\mathcal{R}\widehat{v'}_{ln} + \mathcal{I}\widehat{u'}_{ln}\mathcal{I}\widehat{v'}_{ln}\,. \tag{F.13}$$

In an analogous sense, exploiting symmetry about the point $\boldsymbol{x}$ means we can report the one-dimensional correlations in terms of the magnitude of the separation. That is,

$$\begin{aligned}
R^{x_1}_{uv}(x_2, |r_1|) &= \frac{1}{2}\left(R^{x_1}_{uv}(x_2, r_1) + R^{x_1}_{uv}(x_2, -r_1)\right) \\
&= \frac{1}{2}\sum_{l=-\frac{N_1}{2}+1}^{\frac{N_1}{2}-1}\sum_{n=-\frac{N_3}{2}+1}^{\frac{N_3}{2}-1} \widehat{u'}^{*}_{ln}\widehat{v'}_{ln}\left(e^{\mathrm{i}k_l r_1} + e^{-\mathrm{i}k_l r_1}\right) \\
&= \sum_{l=-\frac{N_1}{2}+1}^{\frac{N_1}{2}-1}\sum_{n=-\frac{N_3}{2}+1}^{\frac{N_3}{2}-1} \widehat{u'}^{*}_{ln}\widehat{v'}_{ln}\cos(k_l r_1) \\
&= \sum_{n=-\frac{N_3}{2}+1}^{\frac{N_3}{2}-1} \widehat{u'}^{*}_{0n}\widehat{v'}_{0n} \\
&\quad + \sum_{l=1}^{\frac{N_1}{2}-1}\sum_{n=-\frac{N_3}{2}+1}^{\frac{N_3}{2}-1} \left\{\widehat{u'}^{*}_{ln}(x_2)\widehat{v'}_{ln}(x_2) + \widehat{u'}^{*}_{-ln}\widehat{v'}_{-ln}\right\}\cos(k_l r_1) \\
&= \sum_{n=-\frac{N_3}{2}+1}^{\frac{N_3}{2}-1} \mathcal{R}\widehat{u'}_{0n}\mathcal{R}\widehat{v'}_{0n} + \mathcal{I}\widehat{u'}_{0n}\mathcal{I}\widehat{v'}_{0n} \\
&\quad + 2\sum_{l=1}^{\frac{N_1}{2}-1}\sum_{n=-\frac{N_3}{2}+1}^{\frac{N_3}{2}-1} \left\{\mathcal{R}\widehat{u'}_{ln}\mathcal{R}\widehat{v'}_{ln} + \mathcal{I}\widehat{u'}_{ln}\mathcal{I}\widehat{v'}_{ln}\right\}\cos(k_l r_1)\,,
\end{aligned} \tag{F.14}$$

hence, $R_{uv}^{x_1}(x_2, |r_1|)$ is the inverse Fourier cosine transform of $2\pi/L_1 E_{uv}^{x_1}(x_2, |k_l|)$. Similarly,

$$
\begin{aligned}
R_{uv}^{x_3}(x_2, |r_3|) &= \frac{1}{2}\left(R_{uv}^{x_3}(x_2, r_3) + R_{uv}^{x_3}(x_2, -r_3)\right) \\
&= \sum_{n=-\frac{N_3}{2}+1}^{\frac{N_3}{2}-1} \sum_{l=-\frac{N_1}{2}+1}^{\frac{N_1}{2}-1} \widehat{u'}_{ln}^{\,*} \widehat{v'}_{ln} \cos(k_n r_3) \\
&= \sum_{n=-\frac{N_3}{2}+1}^{\frac{N_3}{2}-1} \Bigg\{ \mathcal{R}\widehat{u'}_{0n} \mathcal{R}\widehat{v'}_{0n} + \mathcal{I}\widehat{u'}_{0n} \mathcal{I}\widehat{v'}_{0n} \\
&\qquad + 2 \sum_{l=1}^{\frac{N_1}{2}-1} \mathcal{R}\widehat{u}_{ln} \mathcal{R}\widehat{v'}_{ln} + \mathcal{I}\widehat{u'}_{ln} \mathcal{I}\widehat{v'}_{ln} \Bigg\} \cos(k_n r_3) \qquad \text{(F.15)} \\
&= \mathcal{R}\widehat{u'}_{00} \mathcal{R}\widehat{v'}_{00} + \mathcal{I}\widehat{u}_{00} \mathcal{I}\widehat{v'}_{00} \\
&\quad + \sum_{n=1}^{\frac{N_3}{2}-1} \Bigg\{ \mathcal{R}\widehat{u'}_{0n} \mathcal{R}\widehat{v'}_{0n} + \mathcal{I}\widehat{u'}_{0n} \mathcal{I}\widehat{v'}_{0n} + 2 \sum_{l=1}^{\frac{N_1}{2}-1} \mathcal{R}\widehat{u'}_{ln} \mathcal{R}\widehat{v'}_{ln} + \mathcal{I}\widehat{u'}_{ln} \mathcal{I}\widehat{v'}_{ln} \\
&\qquad + \mathcal{R}\widehat{u'}_{0-n} \mathcal{R}\widehat{v'}_{0-n} + \mathcal{I}\widehat{u'}_{0-n} \mathcal{I}\widehat{v'}_{0-n} \\
&\quad + 2 \sum_{l=1}^{\frac{N_1}{2}-1} \mathcal{R}\widehat{u'}_{l-n} \mathcal{R}\widehat{v'}_{l-n} + \mathcal{I}\widehat{u'}_{l-n} \mathcal{I}\widehat{v'}_{l-n} \Bigg\} \cos(k_n r_3)\,,
\end{aligned}
$$

hence, $R_{uv}^{x_3}(x_2, |r_3|)$ is the inverse Fourier cosine transform of $2\pi/L_3 E_{uv}^{x_3}(x_2, |k_n|)$.

Finally, note that $\widehat{u'}_{ln} = \widehat{u}_{ln}$ unless $l = n = 0$. Therefore, the computations of the spectra can be done using the full fields u and v and then the contribution of the means to the zero modes, $\langle u \rangle \langle v \rangle$, can be removed.

Appendix G

χ-dependent flamelet equation of state

Unlike in a RANS simulation where flamelet solutions are integrated against a probability density function to obtain averaged properties, the flamelet DNS directly uses the interpolated/extrapolated data from a family of laminar flames. Hence, the smoothing nature of integration does not mask discontinuities or problematic extrapolations in the (z, χ) space. The χ-dependent flamelet equation of state (which revealed a fundamental flaw in the steady laminar flamelet assumptions detailed in section 4.4) was created from the laminar flames as follows. To avoid issues for large and small χ where formally extinction occurs and where data is not available, respectively, we are willing to alter the underlying data since modifying the flamelet in these regions should have a negligible effect on the average thermochemical properties and is necessary since these are accessible states to the instantaneous turbulent flame. Along these lines the raw flamelet data first undergoes an admittedly empirical transformation. $\chi^* = 2\nabla z \cdot \nabla z$ is used as the second parameter instead of χ to avoid an implicit solve during runtime as χ is explicitly dependent on ν. Firstly, the uniqueness of the mapping from $(z, \chi^*) \rightarrow \rho$ is checked by plotting contours from the laminar flame data. Then, let $y = \log_{10}(\chi^*)$ and $y_{max}(z)$ be the y found in the flamelet with the highest strain rate. The data is rescaled according to

$$\log_{10}(s) = \begin{cases} y & \text{if } y < \delta y_{max} \\ y \times \{1 + (y - \delta y_{max})\}^{-.3\delta y_{max}+2.7} & \text{if } y > \delta y_{max} \end{cases} \tag{G.1}$$

which effectively stretches the data for large χ^*, doing so more severely where y_{max} is relatively small, but leaves the data relatively unchanged at moderate values of χ^*. Then to handle small strain rates, define

$$\zeta = \log(Cs + 1) \tag{G.2}$$

which behaves logarithmically until s is small when $\zeta \approx Cs$. In this case, $C = 10^7$. This ensures the data is continuous as $\chi \to 0$. B-spline interpolation is done in the (z, ζ) space.

Appendix H

Chemistry modeling details

H.1 Mixture fraction equation

Let W_k be the molecular weight of species k. From Poinsot [4], the j^{th} reaction is summarized as

$$\sum_k \nu_{kj}^{'} \mathcal{M}_k \rightleftharpoons \sum_k \nu_{kj}^{''} \mathcal{M}_k \tag{H.1}$$

where $\nu_{kj}^{'}$ and $\nu_{kj}^{''}$ are the molar stoichiometric coefficients. Let $\nu_{kj} = \nu_{kj}^{''} - \nu_{kj}^{'}$; then by conservation of mass

$$\sum_k \nu_{kj} W_k = 0\,. \tag{H.2}$$

The balanced equation for n-heptane/air combustion is

$$C_7H_{16} + 11O_2 \rightarrow 7CO_2 + 8H_2O \tag{H.3}$$

which gives

$$\beta = \frac{1}{7}\frac{Z_C}{W_C} + \frac{1}{16}\frac{Z_H}{W_H} - \frac{1}{11}\frac{Z_O}{W_O} \tag{H.4}$$

when defining Bilger's mixture fraction [91]

$$z = \frac{\beta - \beta_{ox}}{\beta_{fuel} - \beta_{ox}} \tag{H.5}$$

where β_{ox} and β_{fuel} signify the value of β in the oxidizer and fuel stream, respectively. This definition uses the elemental mass fractions which are given by

$$Z_p = \sum_k a_{kp} \frac{W_p}{W_k} Y_k \tag{H.6}$$

with a_{kp} the number of atoms of element p in species k. For convenience, let

$$\beta = \sum_p b_p \frac{Z_p}{W_p} \tag{H.7}$$

where p indexes over the elements (C, H, O).

Under the standard steady laminar flamelet assumptions, the species all have the same diffusion coefficient ($\mathcal{D}$) and experience Fickian diffusion. Hence, the k^{th} species transport equation is

$$\frac{\partial \rho Y_k}{\partial t} + \frac{\partial}{\partial x_i}\left(\rho u_i Y_k\right) = \frac{\partial}{\partial x_i}\left(\rho \mathcal{D} \frac{\partial Y_k}{\partial x_i}\right) + \dot{\omega}_k \tag{H.8}$$

with

$$dot\omega_k = \sum_j \dot{\omega}_{kj} = W_k \sum_j \nu_{kj} \mathcal{Q}_j \tag{H.9}$$

where $\mathcal{Q}_j$ is the net progress rate of reaction j. Weighting eq. (H.8) by $a_{kp} W_p / W_k$ and summing over k gives

$$\frac{\partial \rho Z_p}{\partial t} + \frac{\partial}{\partial x_i}\left(\rho u_i Z_p\right) = \frac{\partial}{\partial x_i}\left(\rho \mathcal{D} \frac{\partial Z_p}{\partial x_i}\right) + \sum_k a_{kp} \frac{W_p}{W_k} \dot{\omega}_k \tag{H.10}$$

since, for example,

$$\begin{aligned} \frac{\partial}{\partial x_i}\left(\rho \mathcal{D} \frac{\partial}{\partial x_i}\left(\sum_k a_{kp} \frac{W_p}{W_k} Y_k\right)\right) &= \frac{\partial}{\partial x_i}\left(\rho \mathcal{D} \sum_k a_{kp} \frac{W_p}{W_k} \frac{\partial Y_k}{\partial x_i}\right) \\ = \frac{\partial}{\partial x_i}\left(\sum_k a_{kp} \frac{W_p}{W_k} \rho \mathcal{D} \frac{\partial Y_k}{\partial x_i}\right) &= \sum_k a_{kp} \frac{W_p}{W_k} \frac{\partial}{\partial x_i}\left(\rho \mathcal{D} \frac{\partial Y_k}{\partial x_i}\right) . \end{aligned} \tag{H.11}$$

Also,

$$\sum_k a_{kp}\frac{W_p}{W_k}\dot{\omega}_k = \sum_j\sum_k a_{kp}\frac{W_p}{W_k}W_k\nu_{kj}\mathcal{Q}_j$$
$$= \sum_j \mathcal{Q}_j \sum_k a_{kp}\nu_{kj} = 0 \tag{H.12}$$

because the inner sum represents conservation of elements. This means no source term appears in this transport equation for Z_p. z is a normalized linear combination of these Z_p and, in a similar manner, rescaling and combining the equations for Z_p gives the mixture fraction equation

$$\frac{\partial \rho z}{\partial t} + \frac{\partial}{\partial x_i}\left(\rho u_i z\right) = \frac{\partial}{\partial x_i}\left(\rho\mathcal{D}\frac{\partial z}{\partial x_i}\right). \tag{H.13}$$

The complex chemistry DNS has a different transport model and the diffusive term in the species equation is

$$\frac{\partial}{\partial x_i}\left(\rho D_k\frac{W_k}{W}\frac{\partial X_k}{\partial x_i} - \rho V_i^c Y_k\right) \tag{H.14}$$

where D_k is the mixture-averaged diffusion coefficient, X_k is the mole fraction of species k, and

$$W = \frac{1}{\sum_k Y_k/W_k} = \sum_k X_k W_k \tag{H.15}$$

is the mean molecular weight. Also included is the Hirschfelder and Curtiss velocity correction

$$V_i^c = \sum_k D_k\frac{W_k}{W}\frac{\partial X_k}{\partial x_i} \tag{H.16}$$

which is used to ensure the conservation of mass equation is recovered when all the species equations are summed. The resulting Z_p equation is

$$\frac{\partial \rho Z_p}{\partial t} + \frac{\partial}{\partial x_i}\left(\rho u_i Z_p\right) = \frac{\partial}{\partial x_i}\left(\rho\sum_k a_{kp}D_k\frac{W_p}{W}\frac{\partial X_k}{\partial x_i} - \rho V_i^c Z_p\right) \tag{H.17}$$

which implies

$$\frac{\partial \rho z}{\partial t} + \frac{\partial}{\partial x_i}\left(\rho u_i z\right) = \frac{\partial}{\partial x_i}\left(\frac{\rho}{\beta_{fuel} - \beta_{ox}} \sum_k \sum_p b_p \frac{a_{kp}}{W} D_k \frac{\partial X_k}{\partial x_i} - \rho V_i^c z\right) . \tag{H.18}$$

Sutherland *et al.* [92] quantify differential diffusion through examining the discrepancy between "exact" diffusion and "approximate" diffusion found in flamelet models, i.e.

$$\frac{\partial}{\partial x_i}\left(\frac{\rho}{\beta_{fuel} - \beta_{ox}} \sum_k \sum_p b_p \frac{a_{kp}}{W} D_k \frac{\partial X_k}{\partial x_i} - \rho V_i^c z\right) - \frac{\partial}{\partial x_i}\left(\rho \mathcal{D} \frac{\partial z}{\partial x_i}\right) \tag{H.19}$$

where $\mathcal{D}$ is chosen according to the flamelet assumptions.

H.2 Error analysis

Broadly, the flamelet assumptions result in simplified transport as identified in eq. (H.19) as well as a projection which allows for the thermodynamic state to be described solely by the mixture fraction field. Hence, there exist two separate sources of error present. Consider the molecular diffusion term in eq. (H.17). Denote a thermodynamic or transport property (e.g. the density, species diffusivities, mean molecular weight, and mole fractions) evaluated with the true, full state (using the entirety of the mass fractions) with the subscript *true*. Then let the subscript z_{true} indicate a thermodynamic property evaluated with the true mixture fraction (computed from the mass fractions) but with the underlying flamelet model (i.e. $z \rightarrow \rho(z)$). Then

$$\begin{aligned}
&\delta_{proj,DD} = \\
&\frac{\partial}{\partial x_i}\left(\frac{\rho^{true}}{\beta_{fuel} - \beta_{ox}} \sum_k \sum_p b_p \frac{a_{kp}}{W^{true}} D_k^{true} \frac{\partial X_k^{true}}{\partial x_i} - \rho^{true} V_i^{c,true} z_{true}\right) - \\
&\frac{\partial}{\partial x_i}\left(\frac{\rho^{z_{true}}}{\beta_{fuel} - \beta_{ox}} \sum_k \sum_p b_p \frac{a_{kp}}{W^{z_{true}}} D_k^{z_{true}} \frac{\partial X_k^{z_{true}}}{\partial x_i} - \rho^{z_{true}} V_i^{c,z_{true}} z_{true}\right)
\end{aligned} \tag{H.20}$$

defines the discrepancy in the differential diffusion model due to the projection of the thermochemical state onto the low-dimensional flamelet manifold. Similarly, a discrepancy for the simplified Fickian model for diffusion used in the flamelet approach can be taken as

$$\delta_{proj,FD} = \frac{\partial}{\partial x_i}\left(\rho^{true}\mathcal{D}^{true}\frac{\partial z_{true}}{\partial x_i}\right) - \frac{\partial}{\partial x_i}\left(\rho^{z_{true}}\mathcal{D}^{z_{true}}\frac{\partial z_{true}}{\partial x_i}\right). \tag{H.21}$$

As in [92], eq. (H.19) can be evaluated entirely in an *a priori* sense, that is

$$\begin{aligned}&\delta_{model,diff} = \\ &\frac{\partial}{\partial x_i}\left(\frac{\rho^{true}}{\beta_{fuel}-\beta_{ox}}\sum_k\sum_p b_p\frac{a_{kp}}{W^{true}}D_k^{true}\frac{\partial X_k^{true}}{\partial x_i} - \rho^{true}V_i^{c,true}z_{true}\right) - \\ &\frac{\partial}{\partial x_i}\left(\rho^{true}\mathcal{D}^{true}\frac{\partial z_{true}}{\partial x_i}\right)\end{aligned} \tag{H.22}$$

defines the model form error incurred by the simplified Fickian diffusion. The flamelet DNS gives access to

$$\frac{\partial}{\partial x_i}\left(\rho^{z_f}\mathcal{D}^{z_f}\frac{\partial z_f}{\partial x_i}\right) \tag{H.23}$$

where z_f is the flamelet DNS mixture fraction, which makes an *a posteriori* comparison natural. Let

$$\begin{aligned}\varepsilon_{diff} = &\frac{\partial}{\partial x_i}\left(\frac{\rho^{true}}{\beta_{fuel}-\beta_{ox}}\sum_k\sum_p b_p\frac{a_{kp}}{W^{true}}D_k^{true}\frac{\partial X_k^{true}}{\partial x_i} - \rho^{true}V_i^{c,true}z_{true}\right) - \\ &\frac{\partial}{\partial x_i}\left(\rho^{z_f}\mathcal{D}^{z_f}\frac{\partial z_f}{\partial x_i}\right)\end{aligned} \tag{H.24}$$

represent the error in that case.

H.2.1 Computational considerations

In order to do the type of analysis discussed above, it is convenient to work entirely with the mass fractions rather than carrying both Y_k and X_k. The differential diffusion diffusive term can be rewritten as

$$\begin{aligned}\frac{\partial}{\partial x_i}\left(\rho D_k \frac{W_k}{W}\frac{\partial X_k}{\partial x_i} - \rho V_i^c z\right) &= \frac{\partial}{\partial x_i}\left(\rho D_k \frac{W_k}{W}\frac{\partial \frac{W}{W_k}Y_k}{\partial x_i} - \rho V_i^c z\right) \\ &= \frac{\partial}{\partial x_i}\left(\rho D_k \frac{Y_k}{W}\frac{\partial W}{\partial x_i} + \rho D_k \frac{\partial Y_k}{\partial x_i} - \rho V_i^c z\right) .\end{aligned} \tag{H.25}$$

V_i^c is rewritten in the same manner, i.e.

$$V_i^c = \sum_k D_k \frac{W_k}{W}\frac{\partial X_k}{\partial x_i} = \sum_k \left(D_k \frac{Y_k}{W}\frac{\partial W}{\partial x_i} + D_k \frac{\partial Y_k}{\partial x_i}\right) \tag{H.26}$$

Therefore, only Y_k, W, and ∇W are stored. Averaging eq. (H.18) gives

$$\begin{aligned}\frac{\partial \overline{\rho}\widetilde{z}}{\partial t} + \frac{\partial}{\partial x_i}\left(\overline{\rho}\widetilde{u_i}\widetilde{z}\right) &= \frac{\partial}{\partial x_i}\left(\frac{1}{\beta_{fuel}-\beta_{ox}}\overline{\rho \sum_k \sum_p b_p \frac{a_{kp}}{W} D_k \frac{\partial X_k}{\partial x_i}} - \overline{\rho}\widetilde{V_i^c}\widetilde{z} - \overline{\rho}\widetilde{u_i'' z''}\right) \\ &= \frac{\partial}{\partial x_i}\left(\frac{1}{\beta_{fuel}-\beta_{ox}}\overline{\rho \sum_k \sum_p b_p \frac{a_{kp}}{W} D_k \left(\frac{Y_k}{W}\frac{\partial W}{\partial x_i} + \frac{\partial Y_k}{\partial x_i}\right)} - \overline{\rho}\widetilde{V_i^c}\widetilde{z} - \overline{\rho}\widetilde{u_i'' z''}\right) .\end{aligned} \tag{H.27}$$

To obtain the terms in this averaged equation the necessary raw moments are

$$\overline{\rho} \qquad \overline{\rho u_i} \qquad \overline{\rho z} \qquad \overline{\rho u_i z} \qquad \overline{\rho \sum_k \sum_p b_p \frac{a_{kp}}{W} D_k \left(\frac{Y_k}{W}\frac{\partial W}{\partial x_i} + \frac{\partial Y_k}{\partial x_i}\right)} \qquad \overline{\rho V_i^c}$$

and $\overline{\mu}$ is also desired.

H.3 Arrhenius law for progress rates

For the j^{th} reaction in a chemical mechanism

$$\mathcal{Q}_j = K_{fj}\Pi_{k=1}^{N_s}\left(\rho\frac{Y_k}{W_k}\right)^{\nu'_{kj}} - K_{rj}\Pi_{k=1}^{N_s}\left(\rho\frac{Y_k}{W_k}\right)^{\nu''_{kj}} \tag{H.28}$$

where K_{fj} and K_{rj} are the forward and reverse reaction rates, respectively. For solving the steady laminar flamelet equations (system (H.32)) and the complex chemistry DNS of Attili, Bisetti, *et al.* [23], the reaction rates are modeled with the Arrhenius law [4] which states

$$K_{fj} = A_{fj}T^{n_j}\exp\left(-\frac{E_j}{\mathcal{R}T}\right). \tag{H.29}$$

A_{fj} is known as the preexponential constant, n_j is the temperature exponent, E_j the activation energy, and $\mathcal{R}$ is the universal gas constant. The reverse rate is computed as

$$K_{rj} = \frac{k_{fj}}{\left(\frac{p_0}{\mathcal{R}T}\right)^{\sum_{k=1}^{N_s}\left(\nu'_{kj}-\nu''_{kj}\right)}\exp\left(\frac{\Delta S_j^0}{\mathcal{R}} - \frac{\Delta H_j^0}{\mathcal{R}T}\right)} \tag{H.30}$$

where ΔS_j^0 and ΔH_j^0 are the entropy and enthalpy change for reaction j, respectively. The chemical source terms are computed from eq. (H.9). The coefficients required to obtain all necessary thermodynamic and transport properties for the chemical mechanism are included with [41].

H.4 Laminar flamelet equations

Under the laminar flamelet assumptions, the species and temperature equations simplify dramatically (see section 2.2.1 for the key assumptions). The direction in which the flame

structure varies is the same direction in which the mixture fraction varies, so a coordinate transformation can be introduced and the result is the so-called flamelet equations [4, 12],

$$\begin{cases} \rho \dfrac{\partial Y_{\beta,\mathrm{lam}}}{\partial t} = \dot{\omega}_k + \dfrac{1}{2}\rho_{\mathrm{lam}}\chi_{\mathrm{lam}}\dfrac{\partial^2 Y_{\beta,\mathrm{lam}}}{\partial {z_{\mathrm{lam}}}^2} \\ \rho \dfrac{\partial T_{\mathrm{lam}}}{\partial t} = \dot{\omega}_T + \dfrac{1}{2}\rho_{\mathrm{lam}}\chi_{\mathrm{lam}}\dfrac{\partial^2 T_{\mathrm{lam}}}{\partial {z_{\mathrm{lam}}}^2}\,, \end{cases} \tag{H.31}$$

where $Y_{\beta,\mathrm{lam}}$ is the β^{th} species mass fraction and T_{lam} is the temperature. The subscript "lam" emphasizes these variables are tied to the laminar flamelet problem. System (H.31) is further simplified by assuming the laminar flamelets are steady:

$$\begin{cases} 0 = \dot{\omega}_\beta + \dfrac{1}{2}\rho_{\mathrm{lam}}\chi_{\mathrm{lam}}\dfrac{\partial^2 Y_{\beta,\mathrm{lam}}}{\partial {z_{\mathrm{lam}}}^2} \\ 0 = \dot{\omega}_T + \dfrac{1}{2}\rho_{\mathrm{lam}}\chi_{\mathrm{lam}}\dfrac{\partial^2 T_{\mathrm{lam}}}{\partial {z_{\mathrm{lam}}}^2}\,. \end{cases} \tag{H.32}$$

These equations have one independent variable, z_{lam}, and the effect of the surrounding turbulent flowfield is encapsulated entirely by the imposed scalar dissipation rate. Hence, the resulting laminar flame structure is described entirely by z_{lam} and χ_{lam}. The chemical source terms $\dot{\omega}_\beta$ and $\dot{\omega}_T$ are obtained in the same fashion as in the complex chemistry DNS and the same chemical mechanism is employed. System (H.32) can be solved in mixture fraction space directly or indirectly by mapping the solution of steady axisymmetric stagnation flows (as is done in Cantera [79], see chapters 6 and 7 in [39]) to mixture fraction space. With the latter option, opposing fuel and oxidizer streams create a solution in physical space in which the mixture fraction increases monotonically from zero on the oxidizer side to one on the fuel side. The flamelet library is built by solving the equations for different imposed scalar dissipation rate profiles $\{\chi^i_{\mathrm{lam}}\}$.

Appendix I

Supplemental figures

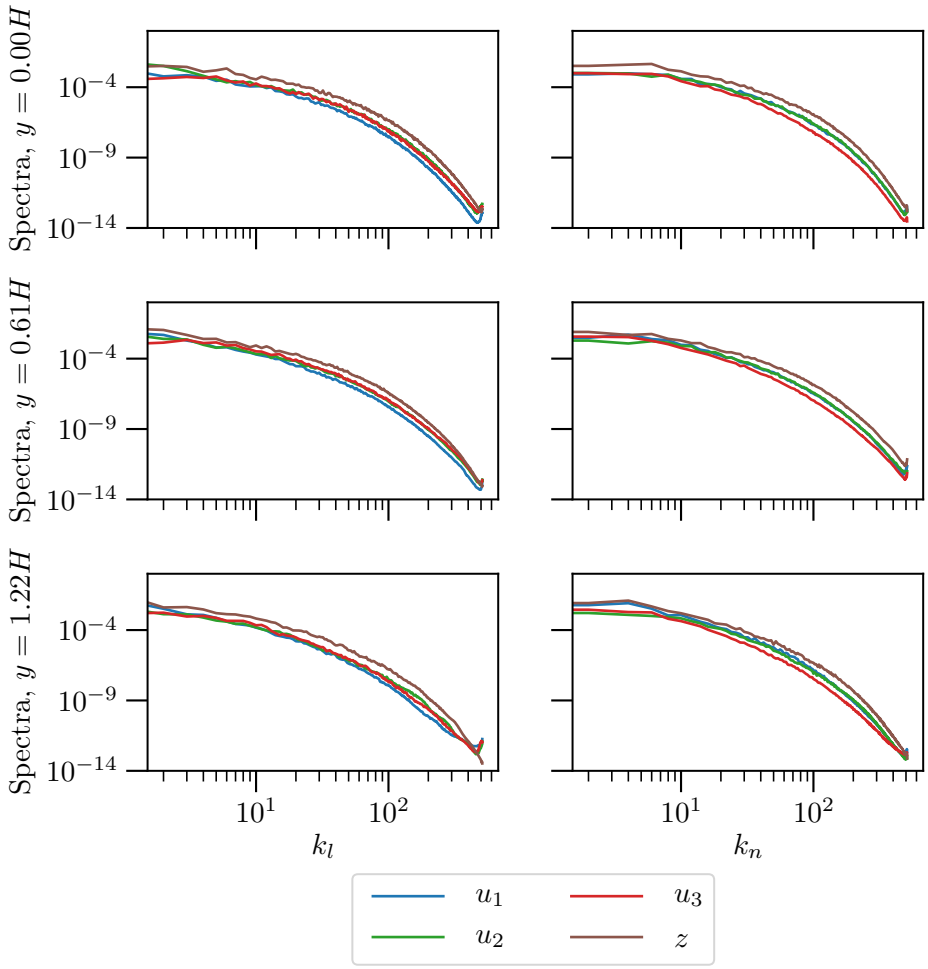

Figure I.1: Energy spectra at 15 ms in the flamelet DNS.

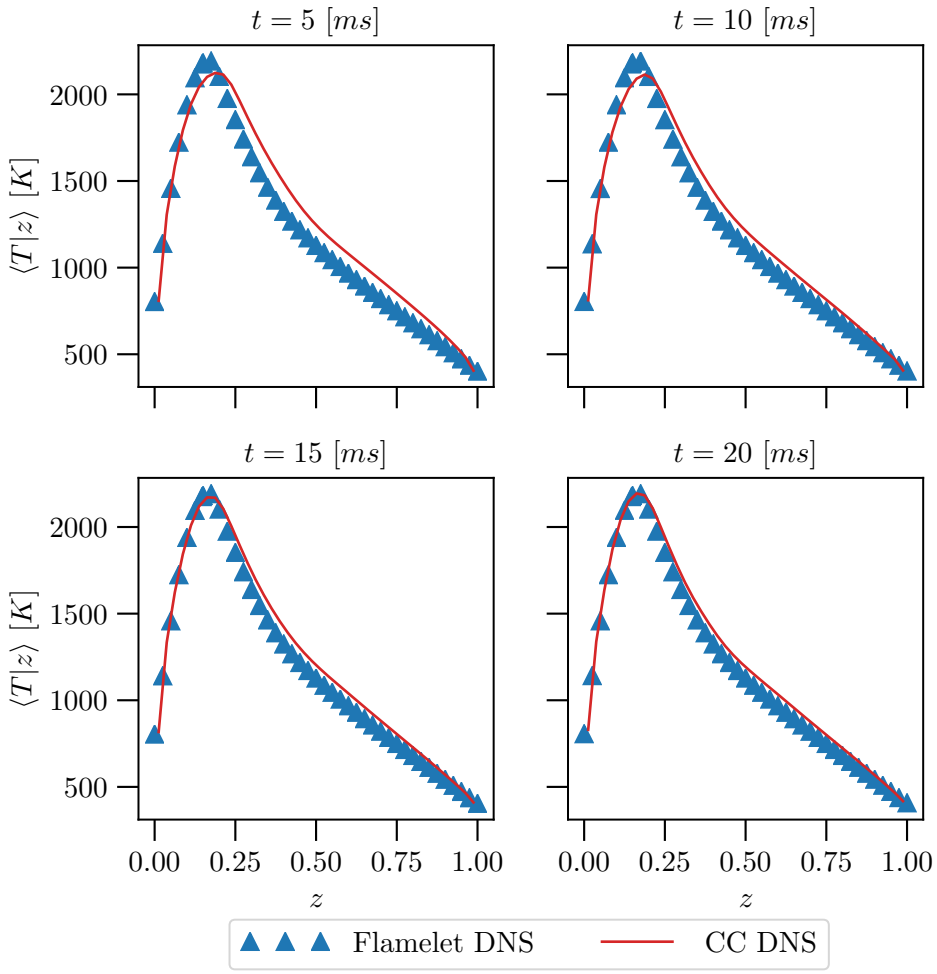

Figure I.2: Conditionally averaged temperature, conditioned on mixture fraction.

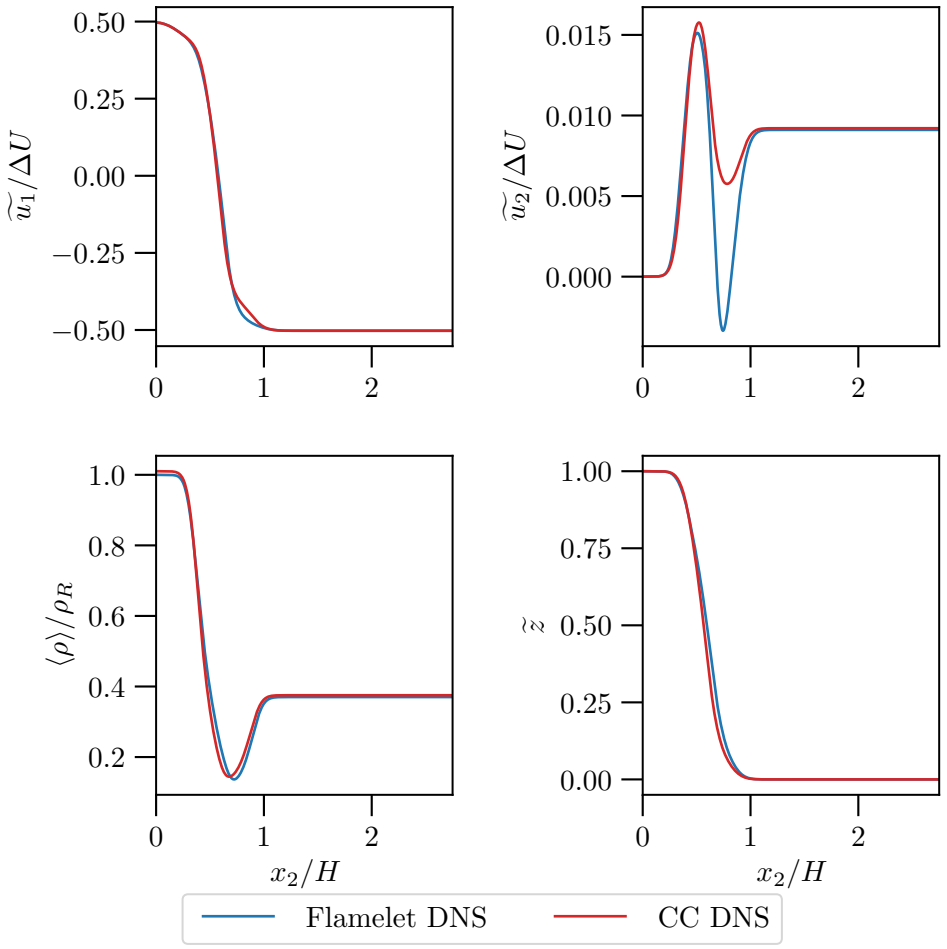

Figure I.3: Profiles of the flamelet DNS mean state variables at 5 ms as a function of the crosswise coordinate x_2/H for the flamelet DNS conducted here and the complex chemistry DNS (CC DNS) of [23].

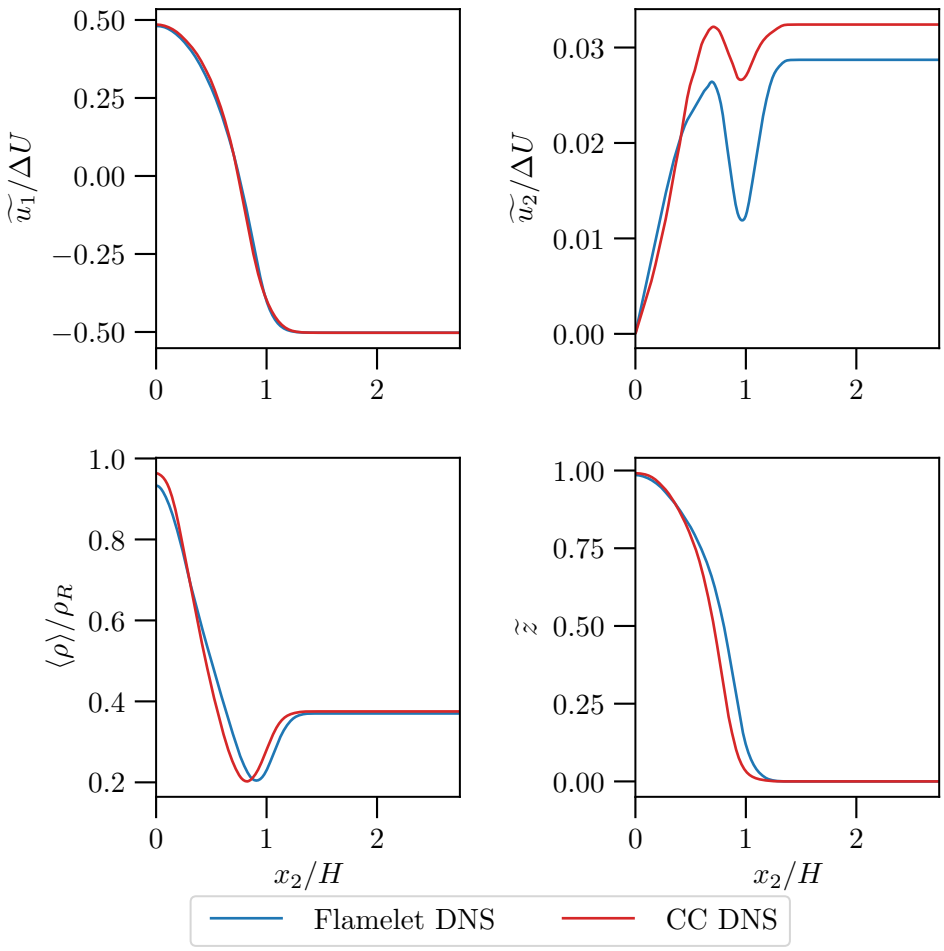

Figure I.4: Profiles of the flamelet DNS mean state variables at 10 ms as a function of the crosswise coordinate x_2/H for the flamelet DNS conducted here and the complex chemistry DNS (CC DNS) of [23].

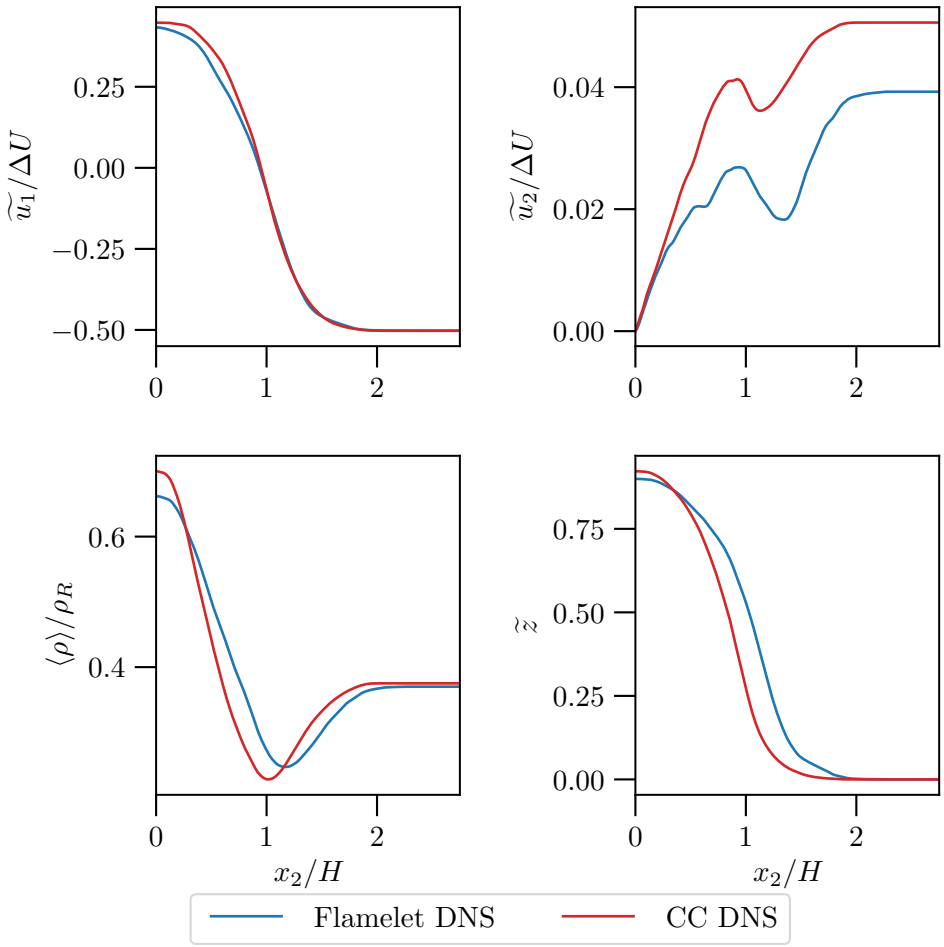

Figure I.5: Profiles of the flamelet DNS mean state variables at 15 ms as a function of the crosswise coordinate x_2/H for the flamelet DNS conducted here and the complex chemistry DNS (CC DNS) of [23].

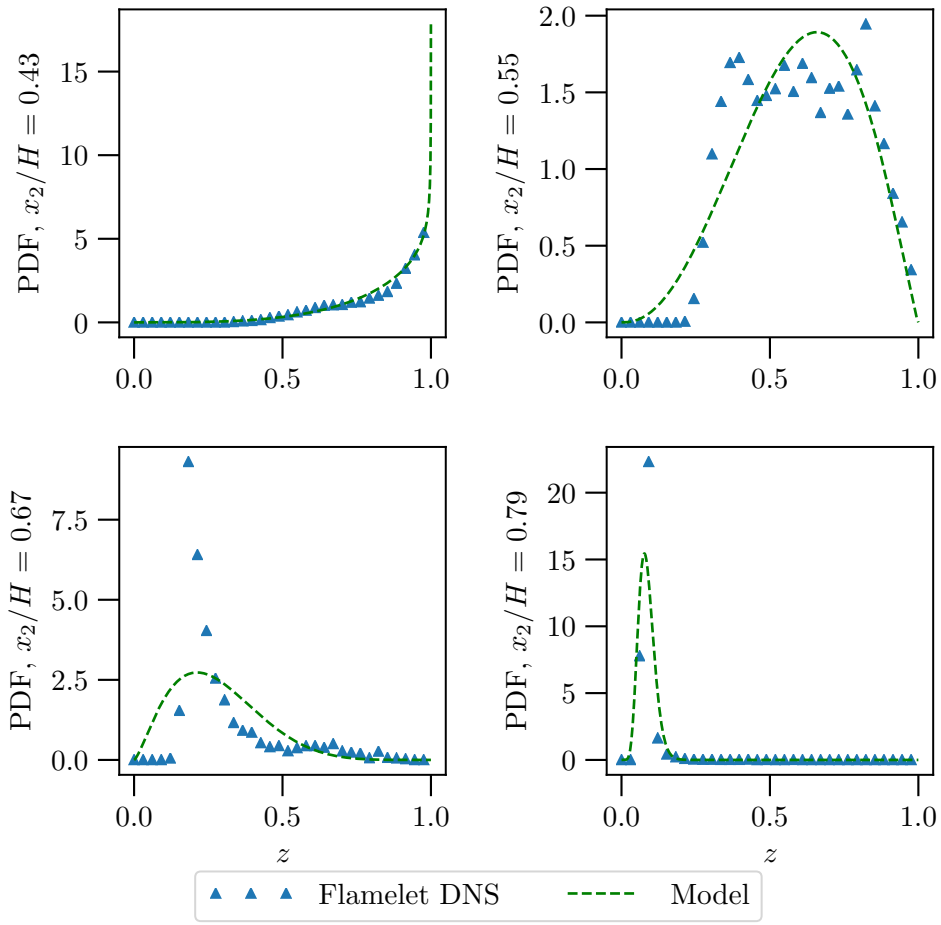

Figure I.6: Sample PDFs of mixture fraction at various x_2 locations at 5 ms. Also shown is the β-PDF (eq. (2.25)) matching the first two sample moments of z at each location.

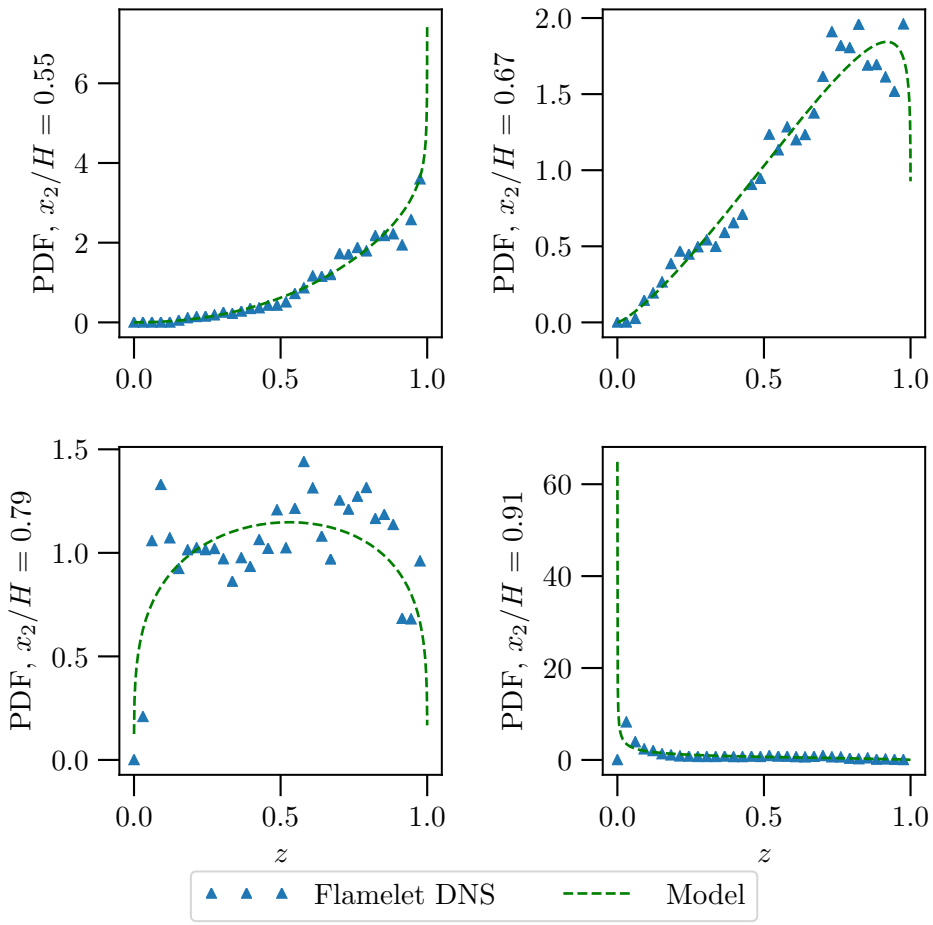

Figure I.7: Sample PDFs of mixture fraction at various x_2 locations at 10 ms. Also shown is the β-PDF (eq. (2.25)) matching the first two sample moments of z at each location.

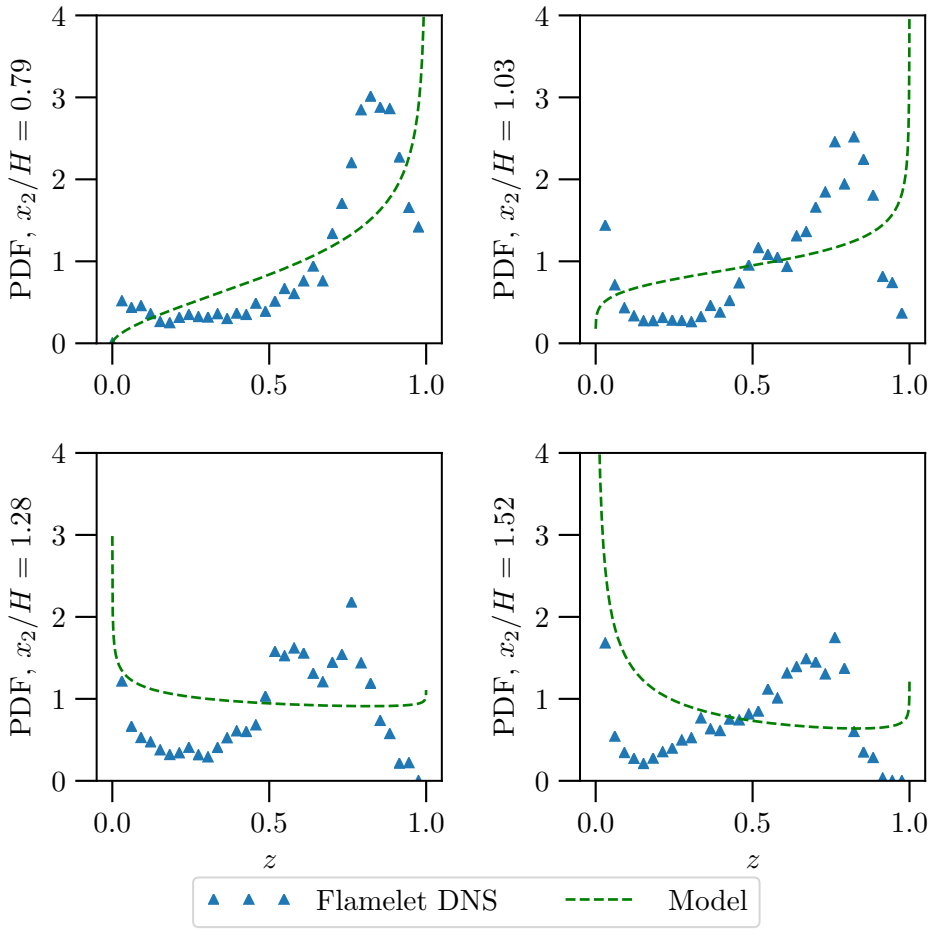

Figure I.8: Sample PDFs of mixture fraction at various x_2 locations at 20 ms. Also shown is the β-PDF (eq. (2.25)) matching the first two sample moments of z at each location.

Bibliography

[1] John Kim, Parviz Moin, and Robert Moser. Turbulence statistics in fully developed channel flow at low Reynolds number. *Journal of fluid mechanics*, 177:133–166, 1987.

[2] Stephen B. Pope. Small scales, many species and the manifold challenges of turbulent combustion. *Proceedings of the Combustion Institute*, 34(1):1–31, 2013.

[3] Denis Veynante and Luc Vervisch. Turbulent combustion modeling. *Progress in energy and combustion science*, 28(3):193–266, 2002.

[4] Thierry Poinsot and Denis Veynante. *Theoretical and numerical combustion*. Self-published, Third edition, 2012.

[5] P. Trisjono and H. Pitsch. Systematic analysis strategies for the development of combustion models from DNS: a review. *Flow, Turbulence and Combustion*, 95(2-3):231–259, 2015.

[6] Joseph C. Oefelein, Guilhem Lacaze, Rainer N. Dahms, and Ramanan Sankaran. High-fidelity large eddy simulation (LES) of combustion for propulsion and power. In *Proceedings of SciDAC 2011*, 2011.

[7] Paul A. Durbin. Some recent developments in turbulence closure modeling. *Annual Review of Fluid Mechanics*, 50:77–103, 2018.

[8] Amsini Sadiki, A. Maltsev, B. Wegner, F. Flemming, A. Kempf, and J. Janicka. Unsteady methods (URANS and LES) for simulation of combustion systems. *International Journal of Thermal Sciences*, 45(8):760–773, 2006.

[9] R. S. Barlow, editor. *Proceedings of the 7th TNF workshop*, 2004.

[10] R. S. Barlow, editor. *Proceedings of the 8th TNF workshop*, 2006.

[11] Heinz Pitsch. Large-eddy simulation of turbulent combustion. *Annual Review of Fluid Mechanics*, 38(1):453–482, 2006.

[12] N. Peters. Laminar flamelet concepts in turbulent combustion. *Symposium (International) on Combustion*, 21(1):1231–1250, 1988.

[13] Hendrik Forkel and Johannes Janicka. Large eddy simulation of a turbulent hydrogen diffusion flame. In *1st International Symposium on Turbulence and Shear Flow Phenomena, TSFP 1999*, 1999.

[14] Kilian Altimira. *Numerical Simulation of Non-premixed Laminar and Turbulent Flames by Means of Flamelet Modelling Approaches*. PhD thesis, Universitat Politècnica de Catalunya, 2005.

[15] Adel Alghamdi. RANS-SLFM and LES-SLFM numerical simulations of turbulent non-premixed oxy-fuel jet flames using CO2/O2 mixture. Master's thesis, Iowa State University, 2017.

[16] Pusheng Zhang. Laminar flamelet modeling of pilot jet methane/air flames. Master's thesis, University of Windsor, 2008.

[17] Reni De Meester, Bertrand Naud, and Bart Merci. Hybrid RANS/PDF calculations of Sydney swirling flames. In *4th European Combustion Meeting*, 2009.

[18] F. C. Christo and B. B. Dally. Modeling turbulent reacting jets issuing into a hot and diluted coflow. *Combustion and Flame*, 142(1-2):117–129, 2005.

[19] Guoxiu Li, Bertrand Naud, and Dirk Roekaerts. Numerical investigation of a bluff-body stabilised nonpremixed flame with differential Reynolds-stress models. *Flow, Turbulence and Combustion*, 70(1-4):211–240, 2003.

[20] Hong Im. Direct numerical simulations for combustion science: Past, present, and future. In Santu De, Avinash Agarwal, Swetaprovo Chaudhuri, and Swarnendu Sen, editors, *Modeling and Simulation of Turbulent Combustion*, pages 99–132. 2018.

[21] Evatt R. Hawkes, Ramanan Sankaran, James C. Sutherland, and Jacqueline H. Chen. Scalar mixing in direct numerical simulations of temporally evolving plane jet flames with skeletal CO/H2 kinetics. *Proceedings of the Combustion Institute*, 31 I:1633–1640, 2007.

[22] Chun Sang Yoo, Edward S. Richardson, Ramanan Sankaran, and Jacqueline H. Chen. A DNS study on the stabilization mechanism of a turbulent lifted ethylene jet flame in highly-heated coflow. *Proceedings of the Combustion Institute*, 33(1):1619–1627, 2011.

[23] Antonio Attili, Fabrizio Bisetti, Michael E. Mueller, and Heinz Pitsch. Formation, growth, and transport of soot in a three-dimensional turbulent non-premixed jet flame. *Combustion and Flame*, 161(7):1849–1865, 2014.

[24] Antonio Attili, Fabrizio Bisetti, Michael E. Mueller, and Heinz Pitsch. Damköhler number effects on soot formation and growth in turbulent nonpremixed flames. *Proceedings of the Combustion Institute*, 35(2):1215–1223, 2015.

[25] David O. Lignell, Jacqueline H. Chen, and Hans A. Schmutz. Effects of Damköhler number on flame extinction and reignition in turbulent non-premixed flames using DNS. *Combustion and Flame*, 158(5):949–963, 2011.

[26] R. Knikker. A comparative study of high-order variable-property segregated algorithms for unsteady low Mach number flows. *International Journal for Numerical Methods in Fluids*, 66(4):403–427, 2011.

[27] Franck Nicoud. Conservative high-order finite-difference schemes for low-Mach number flows. *Journal of Computational Physics*, 158(1):71–97, 2000.

[28] Pieter Rauwoens, Jan Vierendeels, and Bart Merci. A stable pressure-correction scheme for time-accurate non-premixed combustion simulations. *Flow, Turbulence and Combustion*, 82(2):249–269, 2009.

[29] E. Motheau and J. Abraham. A high-order numerical algorithm for DNS of low-Mach-number reactive flows with detailed chemistry and quasi-spectral accuracy. *Journal of Computational Physics*, 313:430–454, 2016.

[30] Habib N. Najm, Peter S. Wyckoff, and Omar M. Knio. A semi-implicit numerical scheme for reacting flow: I. Stiff chemistry. *Journal of Computational Physics*, 143(2):381–402, 1998.

[31] Clifton Wall, Charles D. Pierce, and Parviz Moin. A semi-implicit method for resolution of acoustic waves in low Mach number flows. *Journal of Computational Physics*, 181(2):545–563, 2002.

[32] Y. Jang and S. M. de Bruyn Kops. Pseudo-spectral numerical simulation of miscible fluids with a high density ratio. *Computers and Fluids*, 36(2):238–247, 2007.

[33] John Bell. AMR for low Mach number reacting flow. In *Adaptive Mesh Refinement-Theory and Applications*, pages 203–221. Springer, 2005.

[34] Michael S. Dodd and Antonino Ferrante. A fast pressure-correction method for incompressible two-fluid flows. *Journal of Computational Physics*, 273:416–434, 2014.

[35] Steven A. Orszag, Moshe Israeli, and Michel O. Deville. Boundary conditions for incompressible flows. *Journal of Scientific Computing*, 1(1):75–111, 1986.

[36] C. D. Pierce. *Progress-Variable Approach For Large-Eddy Simulation Of Turbulent Combustion*. PhD thesis, Stanford University, 2001.

[37] L. Shunn and F. Ham. Consistent and accurate state evaluations in variable-density flow simulations. *Annual Research Briefs*, pages 135–147, 2006.

[38] Myoungkyu Lee and Robert D. Moser. Direct numerical simulation of turbulent channel flow up to Re_τ=5200. *Journal of Fluid Mechanics*, 774:395–415, 2015.

[39] Robert J. Kee, Michael E. Coltrin, Peter Glarborg, and Huayang Zhu. *Chemically Reacting Flow: Theory, Modeling, and Simulation*. John Wiley & Sons, 2017.

[40] Bonnie J. McBride, Michael J. Zehe, and Sanford Gordon. NASA Glenn coefficients for calculating thermodynamic properties of individual species. Technical Report NASA/TP—2002-211556, NASA, 2002.

[41] Fabrizio Bisetti, Guillaume Blanquart, Michael E. Mueller, and Heinz Pitsch. On the formation and early evolution of soot in turbulent nonpremixed flames. *Combustion and Flame*, 159(1):317–335, 2012.

[42] Luc Vervisch and Thierry Poinsot. Direct numerical simulation of non-premixed turbulent flames. *Annual Review of Fluid Mechanics*, 30(1):655–691, 1998.

[43] N. Peters and A. M. Kanury. *Turbulent combustion*. 2000.

[44] K. Claramunt, R. Consul, D. Carbonell, and C. D. Pérez-Segarra. Analysis of the laminar flamelet concept for nonpremixed laminar flames. *Combustion and Flame*, 145(4):845–862, 2006.

[45] Paul A. Libby and Forman A. Williams, editors. *Turbulent reacting flows*. Springer-Verlag, 1980.

[46] Rodney O. Fox and Herbert L. Stiles. *Computational models for turbulent reacting flows*, volume 419. Cambridge University Press, 2003.

[47] John M. Richardson, Henry C. Howard Jr, and Robert W. Smith Jr. The relation between sampling-tube measurements and concentration fluctuations in a turbulent gas jet. In *Symposium (International) on Combustion*, volume 4, pages 814–817. Elsevier, 1953.

[48] E. Effelsberg and N. Peters. Scalar dissipation rates in turbulent jets and jet diffusion flames. *Symposium (International) on Combustion*, 22(1):693 – 700, 1989.

[49] Werner J. A. Dahm and Kenneth A. Buch. Lognormality of the scalar dissipation pdf in turbulent flows. *Physics of Fluids A: Fluid Dynamics*, 1(7):1290–1293, 1989.

[50] Bénédicte Cuenot. The flamelet model for non-premixed combustion. In *Turbulent combustion modeling*, pages 43–61. Springer, 2011.

[51] Daniel P. Combest, Palghat A. Ramachandran, and Milorad P. Dudukovic. On the gradient diffusion hypothesis and passive scalar transport in turbulent flows. *Industrial & Engineering Chemistry Research*, 50(15):8817–8823, 2011.

[52] David C. Wilcox. *Turbulence modeling for CFD (Third Edition)*. 2006.

[53] Sigfried W. Haering, Todd A. Oliver, and Robert D. Moser. Active model split hybrid RANS/LES. *arXiv e-prints*, page arXiv:2006.13118, June 2020.

[54] D. B. Spalding. Concentration fluctuations in a round turbulent free jet. In *Numerical prediction of flow, heat transfer, turbulence and combustion*, pages 41–53. Elsevier, 1983.

[55] C. Beguier, I. Dekeyser, and B. E. Launder. Ratio of scalar and velocity dissipation time scales in shear flow turbulence. *The Physics of Fluids*, 21(3):307–310, 1978.

[56] Paul A. Durbin and Bjorn A. Pettersson Reif. *Statistical theory and modeling for turbulent flows*. Wiley, 2nd edition, 2011.

[57] Antonio Almagro, Manuel García-Villalba, and Oscar Flores. A numerical study of a variable-density low-speed turbulent mixing layer. *Journal of Fluid Mechanics*, 830:569–601, 2017.

[58] Carl de Boor. A practical guide to splines - revised edition. *Springer-Verlag, New York*, 2001.

[59] Olivier Botella and Karim Shariff. B-spline methods in fluid dynamics. *International Journal of Computational Fluid Dynamics*, 17(2):133–149, 2003.

[60] Prem Venugopal, Robert D. Moser, and Fady M. Najjar. Direct numerical simulation of turbulence in injection-driven plane channel flows. *Physics of Fluids*, 20(10):105103, 2008.

[61] R. D. Ulerich. *Reducing Turbulence- and Transition-Driven Uncertainty in Aerothermodynamic Heating Predictions for Blunt-Bodied Reentry Vehicles*. PhD thesis, The University of Texas-Austin, 2014.

[62] Yong Yi Bay, Daniel J. Bodony, and Jonathan B. Freund. Boundary-consistent b-spline filtering schemes and application to high-fidelity simulations of turbulence. *Journal of Computational Physics*, 419:109680, 2020.

[63] Wai Y. Kwok, Robert D. Moser, and Javier Jiménez. A critical evaluation of the resolution properties of B-Spline and compact finite difference methods. *Journal of Computational Physics*, 174:510–551, 2001.

[64] Claudio Canuto, M. Yousuff Hussaini, Alfio Quarteroni, and Thomas A. Zang. *Spectral methods: fundamentals in single domains*. Springer Science & Business Media, 2007.

[65] John P. Boyd. *Chebyshev and Fourier spectral methods*. Courier Corporation, 2001.

[66] Richard W. Johnson. Higher order b-spline collocation at the greville abscissae. *Applied Numerical Mathematics*, 52(1):63–75, 2005.

[67] Steven A. Orszag. On the elimination of aliasing in finite-difference schemes by filtering high-wavenumber components. *Journal of the Atmospheric Sciences*, 28(6):1074, 1971.

[68] Carla Manni and Hendrik Speleers. Standard and non-standard CAGD tools for isogeometric analysis: a tutorial. In *IsoGeometric Analysis: A New Paradigm in the Numerical Approximation of PDEs*, pages 1–69. Springer International Publishing, 2016.

[69] Parviz Moin and Krishnan Mahesh. Direct numerical simulation: a tool in turbulence research. *Annual review of fluid mechanics*, 30(1):539–578, 1998.

[70] Ranjan K. Mallik. Solutions of linear difference equations with variable coefficients. *Journal of Mathematical Analysis and Applications*, 222(1):79–91, 1998.

[71] Myoungkyu Lee, Nicholas Malaya, and Robert D. Moser. Petascale direct numerical simulation of turbulent channel flow on up to 786k cores. In *Proceedings of the International Conference on High Performance Computing, Networking, Storage and Analysis*, page 61. ACM, 2013.

[72] Roque Corral and Javier Jiménez. Fourier/chebyshev methods for the incompressible navier-stokes equations in infinite domains. *Journal of Computational Physics*, 121(2):261–270, 1995.

[73] Claudio Canuto. Boundary conditions in Chebyshev and Legendre methods. *SIAM Journal on Numerical Analysis*, 23(4):815–831, 1986.

[74] Nicholas Malaya, Kemelli C. Estacio-Hiroms, Roy H. Stogner, Karl W. Schulz, Paul T. Bauman, and Graham F. Carey. Masa: a library for verification using manufactured and analytical solutions. *Engineering with Computers*, 29(4):487–496, 2013.

[75] Xiaoyi He, Raoyang Zhang, Shiyi Chen, and Gary D. Doolen. On the three-dimensional Rayleigh–Taylor instability. *Physics of Fluids*, 11(5):1143–1152, 1999.

[76] V. N. Goncharov. Analytical model of nonlinear, single-mode, classical Rayleigh-Taylor instability at arbitrary Atwood numbers. *Physical Review Letters*, 88(13):4, 2002.

[77] Pauli Virtanen, Ralf Gommers, Travis E. Oliphant, Matt Haberland, Tyler Reddy, David Cournapeau, Evgeni Burovski, Pearu Peterson, Warren Weckesser, Jonathan Bright, Stéfan J. van der Walt, Matthew Brett, Joshua Wilson, K. Jarrod Millman, Nikolay Mayorov, Andrew R. J. Nelson, Eric Jones, Robert Kern, Eric Larson, C. J. Carey, İlhan Polat, Yu Feng, Eric W. Moore, Jake VanderPlas, Denis Laxalde, Josef Perktold, Robert Cimrman, Ian Henriksen, E. A. Quintero, Charles R. Harris, Anne M. Archibald, Antônio H. Ribeiro, Fabian Pedregosa, Paul van Mulbregt, and SciPy 1.0 Contributors. SciPy 1.0: Fundamental algorithms for scientific computing in Python. *Nature Methods*, 17:261–272, 2020.

[78] Vicente Hernandez, Jose E. Roman, and Vicente Vidal. SLEPc: A scalable and flexible toolkit for the solution of eigenvalue problems. *ACM Trans. Math. Software*, 31(3):351–362, 2005.

[79] David G. Goodwin, Raymond L. Speth, Harry K. Moffat, and Bryan W. Weber. Cantera: An object-oriented software toolkit for chemical kinetics, thermodynamics, and transport processes. `https://www.cantera.org`, 2018. Version 2.4.0.

[80] Mark Galassi, Jim Davies, James Theiler, Brian Gough, Gerard Jungman, Patrick Alken, Michael Booth, Fabrice Rossi, and Rhys Ulerich. *GNU scientific library*. Citeseer, 2002.

[81] Bart J. Daly and Francis H. Harlow. Transport equations in turbulence. *The Physics of Fluids*, 13(11):2634–2649, 1970.

[82] E. Effelsberg and N. Peters. A composite model for the conserved scalar pdf. *Combustion and Flame*, 50:351–360, 1983.

[83] Ji Ryong Cho and Myung Kyoon Chung. A k-ε-γ equation turbulence model. *Journal of Fluid Mechanics*, 237:301–322, 1992.

[84] R. F. Alvani and Michael Fairweather. Prediction of the ignition characteristics of flammable jets using intermittency-based turbulence models and a prescribed pdf approach. *Computers & Chemical Engineering*, 32(3):371–381, 2008.

[85] Dominik Denker, Antonio Attili, Michael Gauding, Kai Niemietz, Mathis Bode, and Heinz Pitsch. A new modeling approach for mixture fraction statistics based on dissipation elements. *Proceedings of the Combustion Institute*, 2020.

[86] Todd A. Oliver, Gabriel Terejanu, Christopher S. Simmons, and Robert D. Moser. Validating predictions of unobserved quantities. *Computer Methods in Applied Mechanics and Engineering*, 283:1310–1335, 2015.

[87] Teresa N. Portone. *Representing model-form uncertainty from missing microstructural information*. PhD thesis, The University of Texas-Austin, 2019.

[88] Rebecca E. Morrison, Todd A. Oliver, and Robert D. Moser. Representing model inadequacy: A stochastic operator approach. *SIAM/ASA Journal on Uncertainty Quantification*, 6(2):457–496, 2018.

[89] J. Janicka and N. Peters. Prediction of turbulent jet diffusion flame lift-off using a pdf transport equation. *Symposium (International) on Combustion*, 19(1):367 – 374, 1982. Nineteenth Symposium (International) on Combustion.

[90] R. F. Alvani and M. Fairweather. Ignition characteristics of turbulent jet flows. *Chemical Engineering Research and Design*, 80(8):917–923, 2002.

[91] R. W. Bilger, S. H. Stårner, and R. J. Kee. On reduced mechanisms for methane-air combustion in nonpremixed flames. *Combustion and Flame*, 80(2):135–149, 1990.

[92] J. C. Sutherland, P. J. Smith, and J. H. Chen. Quantification of differential diffusion in nonpremixed systems. *Combustion Theory and Modelling*, 9(2):365–383, 2005.